Phase Behavior, Adsorption Behavior and Interfacial Properties of Fluids in Shale Reservoirs

by

Yueliang Liu

A thesis submitted in partial fulfillment of the requirements for the degree of

Doctor of Philosophy

in

Petroleum Engineering

Department of Civil and Environmental Engineering
University of Alberta

ABSTRACT

Shale oil/gas resources are becoming an increasingly important energy resource. Compared to conventional reservoirs, shale generally consists of a large proportion of organic matters. Organic matter is mainly comprised of kerogen, within which a significant amount of nanopores may reside. Due to the presence of kerogen, the distribution of fluid molecules in shale can be strongly affected by the fluid/pore wall interactions, leading to significant fluid adsorption on pore surface and thus resulting in a quite different phase behavior in shale reservoirs from that in conventional ones. In addition to the fluid/pore wall interactions, capillary pressure comes into play an important role in affecting the two-phase equilibria, whenever two-phase equilibrium appears in the confined spaces in shale. Understanding of phase behavior, adsorption behavior, and interfacial properties of fluids in shale is of critical importance for more accurately determining the macroscopic and microscopic distribution of fluids in shale reservoirs as well as understanding the mechanisms governing the fluid transport in shale reservoirs.

In this thesis, we first investigate the phase behavior of pure hydrocarbons and hydrocarbon mixtures in nanopores by applying the Peng-Robinson equation of state (PR-EOS) (Peng and Robinson, 1976) with capillary pressure model (Nojabaei *et al.*, 2013) and by applying the engineering density functional theory (DFT), respectively. The capillary pressure between vapor phase and liquid phase is incorporated into PR-EOS. The computed results using the PR-EOS with capillary pressure model show that: phase behavior of hydrocarbons in nanopores deviates from that in bulk; the dew-points and the critical points vary in pores with different sizes. Comparison with the engineering DFT shows that the widely used PR-EOS with capillary pressure model is not reliable in describing confined fluid phase behavior. Considering that pores with different sizes generally coexist in shale samples, we further investigate the phase

behavior of fluid in a double-pore system using molecular dynamic (MD) simulations. We observe that as system pressure decreases, heavier hydrocarbons tend to accumulate in smaller pores, while lighter ones can be readily recovered from the organic pores. CO_2 can readily recover C_1 from both micro- and meso-pores, but cannot effectively replace nC_4 from these pores. Hydrocarbons generally exhibit different fluid-distribution patterns in different nanoscale pores due to the different levels of fluid/pore wall interactions.

Fluid molecules can strongly adsorb on shale surface due to their strong affinity to organic pore walls. To investigate the adsorption behavior of hydrocarbons on shale samples, we initially measure the excess adsorption isotherms of pure hydrocarbons on shale samples. A pragmatic method is proposed to determine the adsorption-phase density yielded by the GCMC simulation method; this leads to the more accurate determination of absolute adsorption isotherms based on the measured excess ones. According to grand canonical Monte Carlo (GCMC) simulation results, absolute adsorption is always higher than the measured excess adsorption. It is also found that individual hydrocarbons exhibit distinct adsorption capacities towards organic pore surface, which leads to the competitive adsorption of hydrocarbon species towards organic pore surface. An experimental study is further conducted to investigate the effect of competitive adsorption on bulk-fluid phase behavior; specifically, phase equilibrium of gas mixtures with the presence of actual shale samples is measured with a PVT setup. We observe that competitive adsorption of different species on shale alters the bubble-point pressure of the original fluid mixtures, confirming competitive adsorption affects the phase behavior of fluids in shale reservoirs.

Although the PR-EOS with capillary pressure model is not precise in describing the in-situ phase behavior of shale fluids, the convenience of using it to quickly describe the confined phase behavior makes this approach still widely used in the shale industry. However, the interfacial

tension (IFT) used in such model needs to be accurately determined. Targeting the vapor-liquid equilibria of gas/brine mixtures, IFTs for the CO_2+CH_4/brine systems are measured using the axisymmetric drop shape analysis (ADSA) under shale reservoir conditions. We find that the presence of CO_2 reduces the IFT of the CO_2+CH_4/brine systems, while salts can increase the IFT of this system. These findings will be also useful for achieving a better understanding on the mechanisms of enhanced shale gas recovery using CO_2 injection.

PREFACE

A version of Chapter 2 has been published as Liu, Y., Jin, Z., and Li, H. (2018), Comparison of Peng-Robinson equation of state with capillary pressure model with engineering density-functional theory in describing the phase behavior of confined hydrocarbons, *SPE Journal*, Preprint. Liu, Y., Jin, Z., and Li, H. are responsible for the simulation results and analysis. Li, H. is the supervisory author and gets involved in the concept formation and manuscript composition.

A version of Chapter 3 was submitted to *Industrial & Engineering Chemistry Research* for publication as Liu, Y., Li, H., and Ma, X., Competitive adsorption behavior of hydrocarbon(s)/CO_2 mixtures in a double-nanopore system using molecular simulations. Liu, Y. is responsible for the simulation results and data analysis as well as the manuscript composition. Ma, X. contributes in conducting the simulation work. Li, H. is the supervisory author and gets involved in the concept formation and manuscript composition.

A version of Chapter 4 has been published as Liu, Y., Li, H., Tian, Y., Jin, Z., and Deng, H., (2018), Determination of the absolute adsorption/desorption isotherms of CH_4 and *n*-C_4H_{10} on shale from a nano-scale perspective, *Fuel*, 218: 67-77. Liu, Y. is responsible for the data measurements, simulation results, and data analysis. Tian, Y. contributes to the simulation work. Jin, Z. and Deng, H. contribute to the manuscript composition and edits. Li, H. is the supervisory author and gets involved in the concept formation and manuscript composition.

A version of Chapter 5 has been published as Liu, Y., Li, H., and Okuno, R. (2018), Phase behavior of N_2/*n*-C_4H_{10} in a partially confined space derived from shale sample, *Journal of Petroleum Science and Engineering*, 160: 442-451. Liu, Y. is responsible for the experimental results and analysis. Li, H. and Okuno, R. contribute to the formation of the research idea and manuscript edits. Li, H. is the supervisory author and gets involved in the concept formation and manuscript composition.

A version of Chapter 6 has been published as Liu, Y., Li, H., and Okuno, R. (2018), Measurements and modeling of interfacial tension for CO_2/CH_4/brine systems under reservoir conditions, *SPE Journal*, Preprint. Liu, Y. is responsible for the experimental data, simulation results, and analysis. Li, H. and Okuno, R. contribute to the formation of the research idea and

manuscript edits. Li, H. is the supervisory author and gets involved in the concept formation and manuscript composition.

Chapter 1 summarizes the research background, problem statement, research objectives, and thesis structure. Chapters 1 and 7 are originally written by Yueliang Liu and have never been published elsewhere.

DEDICATION

This dissertation is dedicated to my dearest parents, my mom Mrs. Hongyun Zhang, my dad Mr. Xianzhang Liu, and my dear brother Mr. Wei Liu.

ACKNOWLEDGMENTS

I would like to express my sincere appreciations to my supervisor Dr. Huazhou Andy Li for providing me a precious opportunity working with him as well as his technical and financial support during my PhD study. I am thankful to Dr. Ryosuke Okuno at the University of Texas at Austin and Dr. Zhehui Jin at the University of Alberta for their many good technical suggestions on my PhD research. I also thank my committee members Dr. Lesley James, Dr. Ergun Kuru, Dr. Zhehui Jin, and Dr. Zukui Li for their excellent comments and suggestions on my PhD thesis.

I also wish to acknowledge the following individuals or organizations during my PhD study at the University of Alberta:

- China Scholarship Council (CSC) for a four-year PhD Scholarship provided to me;
- Past and present group members in Dr. Li's research group;
- Natural Sciences and Engineering Research Council (NSERC) of Canada for a Discovery Grant to Dr. H. Li;
- Dr. Tayfun Babadagli and Dr. Juliana Leung for serving as my candidacy exam committee members;
- Lab technicians Mrs. Mihaela Istratescu, Mr. Todd Kinee, and Mr. Lixing Lin for their technical assistance in the lab works.

Table of Contents

List of Tables

List of Figures

CHAPTER 1 INTRODUCTION

1.1 Research background

In shale reservoirs, pore size is generally falling in the range of nanometers (Wang *et al.*, 2016). In these nanopores, fluid flow and phase behavior can be highly affected by surface attractions and capillarity (Gelb *et al.*, 1999). Understanding of fluid phase behavior confined in nanopores is of great significance for revealing the essential mechanisms of hydrocarbons recovery from shale reservoirs. A number of theoretical and computational approaches have been applied to the study of phase behavior of confined fluids. The PR-EOS with capillary pressure model is one popular choice and has been widely used in the shale industry due to its high-calculation efficiency (Nojabaei *et al.,* 2013). But this model cannot take into account the fluid-pore wall interactions, which, however, plays a key role in affecting the phase behavior of nano-confined hydrocarbons (Jin and Firoozabadi, 2016a).

Recently, molecular simulations and statistical thermodynamics have been proposed to study the phase behavior of confined fluids. Among them, GCMC simulations (Neimark and Vishnyakov, 2000; Singh *et al.,* 2009; Wongkoblap *et al.,* 2011; Jin and Nasrabadi, 2016) and engineering DFT (Li *et al.,* 2014; Jin and Firoozabadi, 2016a; Jin and Firoozabadi, 2016b) are mostly used. These approaches explicitly consider the intermolecular and fluid-pore wall interactions (Lev *et al.,* 1999), which have shown excellent agreement with experimental data on the gas adsorption and interfacial phenomena (Li and Firoozabadi, 2009; Singh *et al.,* 2009; Li *et al.,* 2014; Jin and Firoozabadi, 2016b). Currently, there is no explicit comparison between the statistical thermodynamic based method and the PR-EOS with capillary pressure model on the phase behavior of confined fluids. Moreover, many phase-behavior models are only using a single-pore size to describe the effect of nano-confinement on phase behavior, while shale sample generally

comprises of pores with pore size distribution. However, fluid phase behavior in porous media or with the presence of multiple pores is rarely investigated.

It has been known that the surface attraction dominates phase behavior when pores are in nano-scale, which results in strong adsorption of molecules on pore surface. To study the adsorption behavior of gases in shale, adsorption isotherms of pure hydrocarbons are usually measured on shale samples. As the most abundant component in shale gas reservoirs, CH_4 is thus mostly measured. However, due to the limitations of the experimental setups, the adsorption of heavier hydrocarbons on shale is scarcely tested. The directly measured adsorption isotherms are excess adsorption, which is equal to the difference between the total amount of gas in pores and the amount of free gas in total accessible pore volume (Tian *et al.*, 2017). To accurately evaluate the adsorbed amount of gas on shale, the measured excess adsorption isotherms needs to be converted to the absolute adsorption isotherms. The absolute adsorption reflects the amount of adsorbed gas in the adsorbed state on shale samples (Tian *et al.*, 2017; Liu *et al.*, 2018). In previous works (Rexer *et al.*, 2013; Ren *et al.*, 2017), the conversion between the absolute adsorption (M_a) and excess adsorption (M_{ex}) is done with the following formula,

$$M_a = \frac{M_{ex}}{1 - \frac{\rho}{\rho_a}} \tag{1-1}$$

where ρ_a represents the adsorbed gas density; ρ is the gas density in bulk. Therefore, the key to obtain the absolute adsorption is to accurately determine the adsorbed gas density in nanopores.

Previously, constant values have been normally used to represent the adsorbed gas density. Dubinin (1960) suggested that the adsorbed CH_4 density correlates with the van der Waals

constant *b*, which is a constant value in CH_4. Later, the density of adsorbed CH_4 is argued to be equal to the liquid density of CH_4 at normal boiling point, 420 kg/m^3 (Lewis *et al.*, 1950; Grant and Mane, 1964; Menon, 1968; Tsai *et al.*, 1985; Wang *et al.*, 2017). However, it has been proved that the adsorbed CH_4 density is affected by pressure and temperature (Ambrose *et al.*, 2012; Jin and Firoozabadi, 2013; Liu *et al.*, 2018). Recently, by assuming a constant adsorbed CH_4 density, the Dubinin-Radushkevitch (DR) equation, Supercritical DR (SDR), Ono-Kondo model, and the modified Langmuir equation were used to obtain the absolute adsorption after correcting the measured excess adsorption (Gensterblum 2009; Gensterblum 2010; Ambrose *et al.*, 2012; Gasparik *et al.*, 2012; Xiong *et al.*, 2017). These models match the excess adsorption data by adjusting the adsorbed CH_4 density, which are only a curve fitting job without detailing the underlying physical mechanisms. Molecular simulations specifically take into consideration the fluid/pore wall interactions, which could be used to determine the adsorbed CH_4 density accurately. Recently, using molecular simulations, Ambrose *et al.* (2012) proposed that the adsorbed CH_4 density is related with the bulk temperature, pressure, and pore size. Molecular simulations could be a good choice in determining the adsorbed CH_4 density and calculate the absolute adsorption isotherms based on the measured excess isotherms.

Shale fluids are usually gas mixtures; individual components in shale fluids generally exhibit selective adsorption behavior on shale, while few efforts have been devoted to understanding how the individual components of a gas mixture become selectively adsorbed on shale and how such selective adsorption alters its phase behavior in confined spaces. It is mainly because the measurements of adsorption equilibrium of gas mixtures are difficult to be conducted (Walton and Sholl, 2015). Adsorption equilibrium data of gas mixtures are, however, critical to shale hydrocarbon-in-place estimation and the design of adsorption separation (Walton and Sholl,

2015). Therefore, new experimental approaches need to be designed to obtain the fundamental data in order to reveal the essential mechanisms of the adsorption effect on phase behavior.

In addition to the fluid/pore wall interactions, capillary pressure due to the interfacial tension between two equilibrating vapor-liquid phases comes into play an important role in affecting the two-phase equilibria, whenever two-phase equilibrium appears in tiny pore spaces in shale. An accurate determination of the interfacial tension between two equilibrating phases helps to make sure that the capillarity in pores can be properly captured. Extensive experimental studies are conducted on pure gas-water systems over wide ranges of pressure and temperature. Most of the existing studies did not address how non-hydrocarbon contaminants affect the gas-water IFT, especially at high pressure/temperature conditions. In addition, the gas/water IFT are mostly measured between pure hydrocarbons and water (or brine), rather than gas mixtures/water systems. An accurate IFT model is also needed to be developed to predict the IFT of gas/brine systems under reservoir conditions. To date, numerous correlations have been proposed, and some of them are used in commercial reservoir simulators for estimating the IFT in the petroleum industry. Because of their simplicity, the Parachor model (Macleod, 1923; Weinaug and Katz, 1943) and the scaling law (Lee and Chien, 1984) have gained more use than other predictive methods (Danesh, 1998). However, both methods are not recommended for the prediction of IFT of hydrocarbon/water systems due to their low accuracy.

1.2 Problem statement

Although extensive efforts have been made to investigate the phase behavior, adsorption behavior, and interfacial properties of fluids in shale reservoirs, the following important questions remain to be addressed or further clarified:

- What are the limitations of the PR-EOS with capillary pressure model in describing phase

behavior of confined fluids? What will the fluid phase behavior calculated with DFT look like in nanopores? Furthermore, how to describe the phase behavior of fluid in porous media and how will the pore size distribution affect the fluid phase behavior?

- How to obtain the excess adsorption isotherms of heavier hydrocarbons on shale samples? Based on the directly measured excess adsorption isotherms, how to calculate the adsorption-phase density and then obtain the absolute adsorption isotherms?
- In shale reservoirs, how do the individual components adsorb towards organic shale surface? How does the competitive adsorption affect the fluid phase behavior under the shale reservoir conditions? How to directly measure the fluid phase equilibrium with the presence of shale samples to demonstrate the effect of competitive adsorption on phase behavior?
- How does the addition of CO_2 will affect the IFT between CH_4 and water at high pressure/temperature conditions? How does salinity of water phase affect the gas-water IFT? How to improve the existing IFT model or develop a new IFT model that can more accurately determine the IFTs of gas-brine systems?

1.3 Research objectives

The objective of this research is to achieve a better understanding of the phase behavior, adsorption behavior, and interfacial properties of fluids under the shale reservoir conditions; both experimental and theoretical efforts are invested to achieve this objective. More specifically, the detailed research objectives are summarized as follows:

- From molecular perspective, to determine the fluid phase behavior of pure hydrocarbons and hydrocarbon mixtures in nanopores; to clarify the limitations of the PR-EOS with capillary pressure model in describing phase behavior of confined fluids; and, to describe

the fluid phase behavior in porous media, understanding the effect of pore size distribution on fluid phase behavior;

- To measure the excess adsorption isotherms of heavier hydrocarbons on shale samples; then, to calculate the adsorption-phase density from molecular perspective; and to obtain accurate absolute adsorption isotherms of hydrocarbons on shale samples;
- To design an experimental method to measure the fluid phase behavior with the presence of shale samples; to reveal how the competitive adsorption affects the fluid phase behavior;
- To measure the IFTs between gas mixtures and brine at high pressure/temperature conditions; to understand the effect of the presence of non-hydrocarbons or salinity on gas-water IFT; and to develop a new IFT model to calculate the IFTs of gas-brine systems.

1.4 Thesis structure

There are seven chapters in this dissertation. In **Chapter 1**, we introduce the research background, together with the problem statement, and its major research objectives. **Chapter 2** presents the study on the comparison of the PR-EOS with capillary pressure model with the engineering DFT in determining the phase behavior of confined hydrocarbons. In this chapter, we determine the fluid phase behavior of pure hydrocarbons and hydrocarbon mixtures in nanopores with the PR-EOS with capillary pressure model and the engineering DFT, respectively. And then, we clarify the limitations of the PR-EOS with capillary pressure model in describing phase behavior of confined fluids. **Chapter 3** presents the study of investigating the competitive adsorption behavior of hydrocarbons mixtures in a double-nanopore system with molecular simulations. In this chapter, the effect of the presence of double nanopores on

adsorption behavior is investigated. In **Chapter 4**, we investigate the phase behavior of mixtures with the presence of shale samples. With this study, we intend to clarify the effect of competitive adsorption on the bulk phase behavior. **Chapter 5** presents the study on the determination of absolute adsorption/desorption isotherms of CH_4 and n-C_4H_{10} on shale from a nanopore-scale perspective; the excess adsorption isotherms of CH_4 and n-C_4H_{10} on shale are initially measured; we then apply GCMC simulations to obtain the adsorption-phase density and determine the absolute adsorption isotherms. **Chapter 6** presents the measurements and modeling of IFT of CO_2+CH_4/brine systems at reservoir conditions. Finally, conclusions of the current research and recommendations for future work are presented in **Chapter 7**.

1.5 References

Ambrose, R.J., Hartman, R.C., Diaz-Campos, M. *et al.* 2012. Shale Gas-in-place Calculations Part I: New Pore-scale Considerations. *SPE J.* 17 (1): 219-229.

Danesh, A. 1998. PVT and Phase Behaviour of Petroleum Reservoir Fluids. Ph.D. Dissertation, Herriot Watt University, Edinburgh, SCO.

Dubinin, M.M. 1960. The Potential Theory of Adsorption of Gases and Vapors for Adsorbents with Energetically Nonuniform Surfaces. *Chem. Rev.* 60 (2): 235-241.

Gasparik, M., Ghanizadeh, A., Bertier, P. *et al.* 2012. High-pressure Methane Adsorption Isotherms of Black Shales from the Netherlands. *Energy Fuel* 26: 4995-5004.

Gelb, L.D., Gubbins, K.E., Radhakrishnan, R. *et al.* 1999. Phase Separation in Confined Systems. *Rep. Prog. Phys.* 62: 1573-1659.

Gensterblum, Y., Hemert, P., Billemont, P. *et al.* 2009. European Inter-laboratory Comparison of High Pressure CO_2 Sorption Isotherms. I: Activated Carbon. *Carbon* 47: 2958-2969.

Gensterblum, Y., Hemert, P., Billemont, P. *et al.* 2010. European Inter-laboratory Comparison

of High Pressure CO_2 Sorption Isotherms II: Natural Coals. *Int. J. Coal Geol.* 84: 115-124.

Grant, R.J., Manes, M. 1964. Correlation of Some Gas Adsorption Data Extending to Low Pressures and Supercritical Temperatures. *Ind. Eng. Chem. Fundam.* 3: 221-224.

Jin, B., Nasrabadi, H. 2016. Phase Behavior of Multi-component Hydrocarbon Systems in Nano-pores using Gauge-GCMC Molecular Simulation. *Fluid Phase Equilib.* 425: 324-334.

Jin, Z., Firoozabadi, A. 2016a. Thermodynamic Modeling of Phase Behavior in Shale Media. *SPE J.* 21 (1): 190-207.

Jin, Z., Firoozabadi, A. 2016b. Phase Behavior and Flow in Shale Nanopores from Molecular Simulations. *Fluid Phase Equilibr.* 430: 156-168.

Lee, S.T., Chien, M.C.H. 1984. A New Multicomponent Surface Tension Correlation Based on Scaling Theory. Presented at the SPE/DOE Improved Oil Recovery Conference. Tulsa.

Lewis, W.K., Gilliland, E.R., Chertow, B. *et al.* 1950. Pure Gas Isotherms. *Ind. Eng. Chem.* 42: 1326-1332.

Liu, Y., Li, H., Tian, Y. *et al.* 2018. Determination of the Absolute Adsorption/Desorption Isotherms of CH_4 and n-C_4H_{10} on Shale from a Nano-scale Perspective. *Fuel* 218: 67-77.

Li, Z., Firoozabadi, A. 2009. Interfacial Tension of Nonassociating Pure Substances and Binary Mixtures by Density Functional Theory Combined with Peng–Robinson Equation of State. *J. Chem. Phys.* 130 (15): 154108.

Li, Z., Jin, Z., Firoozabadi, A. 2014. Phase Behavior and Adsorption of Pure Substances and Mixtures and Characterization in Nanopore Structures by Density Functional Theory. *SPE J.* 19 (6): 1096-1109.

Ren, W., Li, G., Tian, S. *et al.* 2017. Adsorption and Surface Diffusion of Supercritical Methane

in Shale. *Ind. Eng. Chem. Res.* 56: 3446-3455.

Rexer, T.F.T., Benham, M.J., Aplin, A.C. *et al.* 2013. Methane Adsorption on Shale under Simulated Geological Temperature and Pressure Conditions. *Energy Fuels* 27: 3099-3109.

Macleod, D.B. 1923. On a Relation between Surface Tension and Density. *Trans. Faraday. Soc.* 19: 38-41.

Menon, P.G. 1968. Adsorption at High Pressures. *J. Phys. Chem.* 72: 2695-2696.

Neimark, A.V., Vishnyakov, A. 2000. Gauge Cell Method for Simulation Studies of Phase Transitions in Confined Systems. *Phys. Rev. E* 62 (4): 4611-4622.

Nojabaei, B., Johns, R.T., Chu, L. 2013. Effect of Capillary Pressure on Phase Behavior in Tight Rocks and Shales. *SPE Res. Eval. Eng*. 16 (3): 289-281.

Singh, S.K., Sinha, A., Deo, G. *et al.* 2009. Vapor-Liquid Phase Coexistence, Critical Properties, and Surface Tension of Confined Alkanes. *J. Phys. Chem. C* 113 (17): 7170-7180.

Tian, Y., Yan, C., Jin, Z. 2017. Characterization of Methane Excess and Absolute Adsorption in Various Clay Nanopores from Molecular Simulation. *Sci. Rep.* 7: 12040.

Tsai, M.C., Chen, W.N., Cen, P.L. *et al.* 1985. Adsorption of Gas Mixture on Activated Carbon. Carbon. 23 (2): 167-173.

Walton, K.S., Sholl, D.S. 2015. Predicting Multicomponent Adsorption: 50 Years of the Ideal Adsorbed Solution Theory. *J. AIChE*. 61 (9): 2757-2762.

Wang, L., Yin, X., Neeves, K.B. *et al.* 2016. Effect of Pore-size Distribution on Phase Transition of Hydrocarbon Mixtures in Nanoporous Media. *SPE J*. 21 (6): 1981-1995.

Wang, Y., Zhu, Y., Liu, S. *et al.* 2016. Methane Adsorption Measurements and Modeling for Organic-Rich Marine Shale Samples. *Fuel* 172: 301-309.

Weinaug, C.F., Katz, D.L. 1943. Surface Tension of Methane-Propane Mixtures. *Ind. Eng. Chem.* 35: 239.

Wongkoblap, A., Do, D.D., Birkett, G. *et al.* 2011. A Critical Assessment of Capillary Condensation and Evaporation Equations: A Computer Simulation Study. *J. Colloid Interface Sci.* 356 (2): 672-680.

Xiong, F., Wang, X., Amooie, N. *et al.* 2017. The Shale Gas Sorption Capacity of Transitional Shales in the Ordos Basin, NW China. *Fuel* 208: 236-246.

CHAPTER 2 COMPARISON OF PR-EOS WITH CAPILLARY PRESSURE MODEL WITH ENGINEERING DENSITY FUNCTIONAL THEORY IN DESCRIBING THE PHASE BEHAVIOR OF CONFINED HYDROCARBONS

A version of this chapter was presented at the SPE Annual Technical Conference and Exhibition held on 9-11 October 2017 in San Antonio, TX, USA and has been accepted for publication in *SPE Journal*.

Abstract

Peng-Robinson equation of state (PR-EOS) with capillary effect has been extensively used to describe the phase behavior of hydrocarbons under nano-confinement in shale reservoirs. In nanopores, surface adsorption may be significant and molecular distribution is heterogeneous. While PR-EOS cannot take into account these effects, statistical thermodynamic approaches such as density functional theory (DFT) can explicitly consider the intermolecular and fluid-surface interactions. In this work, we compare the phase behavior of pure hydrocarbons and mixtures in nanopores from PR-EOS with capillary effect and engineering DFT. We apply the Young-Laplace (YL) equation assuming zero contact angle to calculate the capillary pressure in PR-EOS with capillary effect. On the other hand, we extend the PR-EOS to inhomogeneous conditions by using weighted density approximation (WDA) in engineering DFT.

For pure components, both approaches predict that the dew-point temperature increases in hydrocarbon-wet nanopores. While engineering DFT predicts that the confined dew-point temperature approaches bulk saturation point when pore size approaches 30 nm, the saturation point obtained from PR-EOS with capillary effect approaches bulk only when the pore size is as large as 1,000 nm. With engineering DFT, the critical points in nanopores deviate from that in bulk, but no change is observed from PR-EOS with capillary effect model. The difference between PR-EOS with capillary effect and engineering DFT on the dew-point temperature decreases as the system pressure approaches the critical pressure. At low pressure conditions, PR-EOS with capillary effect model becomes unreliable.

For binary mixtures, both approaches predict that the lower dew-point decreases and the upper dew-point increases. More interestingly, phase transition can still occur when the system temperature is higher than the bulk cricondentherm point. Engineering DFT predict that the

confined lower dew-point approaches bulk when pore size approaches 20 nm, whereas the dew-point obtained from PR-EOS with capillary effect approaches bulk only when the pore size is as large as 100 nm. This work illustrates that assuming homogeneous distributions in nanopores may not be applicable to predict the phase behavior of hydrocarbons under nano-confinement.

Keywords: Peng-Robinson equation of state (PR-EOS) with capillary effect, density functional theory (DFT), phase behavior, nanoconfinement, dew-point

2.1 Introduction

In nanopores, the thermodynamic properties of confined fluids can be very different from that in bulk (Alfi *et al.* 2016, Jin and Firoozabadi 2016). The saturation points of confined fluids are shifted (Luo *et al.* 2016, Luo *et al.* 2016) and strong fluid-surface interaction may result in significant surface adsorption and inhomogeneous density distributions (Cabral *et al.* 2005, Li *et al.* 2014). Advancing the understanding of phase behavior of confined fluids is not only crucial to the shale/tight gas and oil recovery (Civan *et al.* 2012), but also of fundamental importance to many industrial applications, such as heterogeneous catalysis (Cervilla *et al.* 1994), pollution control (Volzone 2007) and separation processes (Basaldella *et al.* 2007).

A number of theoretical and computational approaches have been applied to the study of phase behavior of confined fluids. One popular choice is to use Peng-Robinson equation of state (PR-EOS) by combining the capillary effect. The capillary effect relates the pressure difference between two phases (Travalloni *et al.* 2010, Travalloni *et al.* 2010, Nojabaei *et al.* 2013), which can be evaluated from the Kelvin equation by using the Young-Laplace (YL) equation. The PR-EOS with capillary pressure model predicted that the bubble-point and lower dew-point of hydrocarbon mixtures decreases in nanopores, while the upper dew-point increases (Nojabaei *et*

al. 2013, Jin and Firoozabadi 2016). Within the framework of PR-EOS with capillary pressure model, the fluid distribution in nanopore is considered to be homogeneous and confinement effect is taken into account by considering the capillary pressure. PR-EOS with capillary pressure model cannot consider the intermolecular and fluid-surface interactions which play key roles in the phase behavior of nano-confined hydrocarbons (Jin and Firoozabadi 2016). The assumption of phase equilibrium between an ideal gas and an incompressible liquid phase from the Kelvin equation becomes invalid in nanoscale (Tan and Piri 2015). In addition, the capillary pressure is usually obtained from the bulk interfacial tensions between two phases and the curvature (Nojabaei *et al.* 2013). In nanoscale, the interfacial tensions can be very different from the bulk (Singh and Kwak 2007, Bruot and Caupin 2016). To improve the capability of PR-EOS with capillary pressure model, Travalloni *et al.* (2010a and 2010b) employed two parameters describing fluid-surface interactions to study the phase behavior of confined fluids in porous media. Although this model can calculate the capillary condensation in nanopores, its prediction has a large deviation from molecular simulations. Despite of above-mentioned deficiencies, PR-EOS with capillary pressure model is still a popular choice among engineers and scientists because it is simple and can be easily incorporated into reservoir simulations. However, the reliability of this approach has not been calibrated by more sophisticated statistical thermodynamic approaches yet.

Recently, molecular simulations and theoretical computations based on statistical thermodynamics have been widely used to study the phase behavior of confined fluids. Among them, grand canonical Monte Carlo (GCMC) simulations (Walton and Quirke 1989, Neimark and Vishnyakov 2000, Singh *et al.* 2009, Wongkoblap *et al.* 2011, Jin and Nasrabadi 2016) and density functional theory (DFT) (Li *et al.* 2014, Jin and Firoozabadi 2016, Jin and Firoozabadi

2016) are popular choices. These approaches can explicitly consider the intermolecular and fluid-surface interactions from molecular perspective (Lev *et al.* 1999). Within the framework of GCMC simulations and DFT, the equilibrium properties of confined fluids are determined by the grand potential minimization (Li *et al.* 2014). These statistical thermodynamic approaches have shown excellent agreement with experimental data on the gas adsorption and interfacial phenomena (Li and Firoozabadi 2009, Singh *et al.* 2009, Li *et al.* 2014, Jin and Firoozabadi 2016). Currently, there is no explicit comparison between the statistical thermodynamic based method and the PR-EOS with capillary pressure model on the phase behavior of confined fluids.

In this work, we will compare the PR-EOS with capillary pressure model and engineering DFT (Li *et al.* 2014) on the phase behavior of confined hydrocarbons. We investigate the phase behavior of pure nC_8 and C_1-nC_6 mixtures in nanopores. These hydrocarbons are commonly seen in shale gas and oil reservoirs (Gasparik *et al.* 2012, Luo *et al.* 2016). In our previous works (Li *et al.* 2014, Jin and Firoozabadi 2016, Jin and Firoozabadi 2016), we have used an engineering DFT with PR-EOS to study the hydrocarbon adsorption-desorption isotherms as well as gas sorption in shale media and achieved good agreement with experimental data. Recently, we have calibrated the engineering DFT by comparing to GCMC simulations on the saturation properties of confined pure and hydrocarbons mixtures (Jin 2017). Comparing to GCMC simulations, engineering DFT can significantly reduce the computational cost. For simplicity, we use a structureless carbon slit-pore model to describe nanopores. Carbon surface is oil-wet and can provide underlying mechanisms on the effect of nano-confinement on the phase behavior of hydrocarbons in shale nanoporous media. By comparing to engineering DFT, we can assess the validity of the PR-EOS with capillary pressure model in describing the phase behavior of confined fluids.

2.2 Molecular Model and Theory

In this work, engineering DFT extends bulk PR-EOS to inhomogeneous conditions by using weighted density approximation (WDA) (Rosenfeld 1989). On the other hand, we use the YL equation to describe the capillary pressure in the PR-EOS with capillarity. We compared two approaches by studying the dew-point and other thermodynamic properties of hydrocarbons under nano-confinement.

2.2.1 Engineering Density Functional Theory

Within the framework of the engineering DFT, the phase behavior of hydrocarbons in nanopores is studied in an open system setting. An open system can freely exchange matter and energy with the outside reservoir of given properties. In engineering DFT, the system is in equilibrium with an infinite fictitious reservoir in which the chemical potential μ and temperature T are fixed. The equilibrium thermodynamic properties such as the adsorption and phase behaviors can be obtained by the minimization of the grand potential functional which is a function of density distributions (Ebner *et al.* 1976). The grand potential functional $\Omega\left[\{\rho_k(\mathbf{r})\}\right]$ of the system is related to the Helmholtz free energy functional $F\left[\{\rho_k(\mathbf{r})\}\right]$ by,

$$\Omega\left[\{\rho_k(\mathbf{r})\}\right] = F\left[\{\rho_k(\mathbf{r})\}\right] + \sum_k \int \rho_k(\mathbf{r})\left[\Psi_k(\mathbf{r}) - \mu_k\right] d\mathbf{r}, \tag{2-1}$$

where $d\mathbf{r}$ presents the differential volume; $\rho_k(\mathbf{r})$ is the number density distribution of the component k at the position $\mathbf{r}$; $\Psi_k(\mathbf{r})$ is the solid-surface external potential of the component k at the position $\mathbf{r}$; μ_k is the chemical potential of component k in bulk (Li and Firoozabadi 2009). At equilibrium, the grand potential functional is at minimum. In other words, the first-order derivative of the grand potential functional over density distributions is zero,

$$\frac{\delta\Omega\left[\left\{\rho_k(\mathbf{r})\right\}\right]}{\delta\rho_k(\mathbf{r})}=0. \tag{2-2}$$

With an accurate representation of the excess Helmholtz free energy functional $F^{ex}\left[\left\{\rho_k(\mathbf{r})\right\}\right]$, the Euler-Lagrange equation can be yielded by minimizing the grand potential functional,

$$\rho_k(\mathbf{r})=\exp\left[\beta\mu_k-\beta\Psi_k(\mathbf{r})-\delta\beta F^{ex}\left[\left\{\rho_k(\mathbf{r})\right\}\right]/\delta\rho_k(\mathbf{r})\right], \tag{2-3}$$

where $\beta=1/k_BT$; k_B is the Boltzmann constant and T is the absolute temperature.

In our engineering DFT model, the excess Helmholtz free energy functional is divided into two parts: one is obtained from the PR-EOS (Peng and Robinson 1976, Robinson *et al.* 1985), in which the weighted density approximation (WDA) (Rosenfeld 1989) is adopted to account for the physical interactions between fluid molecules; the other part is supplemented by the quadratic density expansion to account for the long-range interactions (Ebner *et al.* 1976, Ebner and Saam 1977). The detailed expressions for the excess Helmholtz free energy functional can be found in the literature by Li and Firoozabadi (2009).

The chemical potentials of fluids are obtained from the PR-EOS. To obtain an accurate equilibrium density distribution, the dimensionless volume shift parameter (VSP) (Jhaveri and Youngren 1988) is applied by fitting the equilibrium liquid density at $T=0.7T_c$. The parameters used in the PR-EOS can be found in Table 2-1. The binary interaction coefficient between CH_4 and nC_6 is fixed as 0.005 (Nojabaei *et al.* 2013). We use the structureless carbon to simulate the pores. In a carbon-slit pore, the density distributions were assumed to only vary in the z direction perpendicular to the solid surfaces, i.e. $\rho_k(\mathbf{r})=\rho_k(z)$. The fluid-surface interactions φ_{wk} are described by the 10-4-3 Steele potentials (Steele 1973),

$$\varphi_{wk}(z)=2\pi\rho_w\varepsilon_{wk}\sigma_{wk}^2\Delta\left[\frac{2}{5}\left(\frac{\sigma_{wk}}{z}\right)^{10}-\left(\frac{\sigma_{wk}}{z}\right)^{4}-\frac{\sigma_{wk}^4}{3\Delta\left(0.61\Delta+z\right)^3}\right], \tag{2-4}$$

where $\rho_w=114$ nm^{-3} and $\Delta=0.335$ nm. Unlike interactions σ_{wk} and ε_{wk} are computed using the standard Lorentz-Berthelot combining rules: $\sigma_{wk}=(\sigma_w+\sigma_k)/2$ and $\varepsilon_{wk}=\sqrt{\varepsilon_w\varepsilon_k}$ with $\varepsilon_w=28$ K and $\sigma_w=0.3345$ nm, respectively. The external potential Ψ_k in a slit pore is expressed as,

$$\Psi_k(z)=\varphi_{wk}(z)+\varphi_{wk}(W-z), \tag{2-5}$$

where W is the slit-pore size.

In our engineering DFT calculations, the external potentials for C_1, nC_6, and nC_8 are modeled as one CH_4-wall interaction, sum of two CH_3-wall and four CH_2-wall interactions, and sum of two CH_3-wall and six CH_2-wall interactions, respectively, as done in our previous works (Jin and Firoozabadi 2016, Jin 2017). We use the modified Buckingham exponential-6 intermolecular potential to describe the energy and size parameters of methyl group (-CH_3), methylene group (-CH_2-), and CH_4. This force field combined with united atom model has shown excellent agreement with experimental data on interfacial tension of various hydrocarbons (Singh *et al.* 2009). We have shown that by using the modified Buckingham exponential-6 intermolecular potential, engineering DFT has excellent agreement with GCMC simulations on the saturation properties and critical points of confined hydrocarbons (Jin and Firoozabadi 2016, Jin 2017). The parameters σ_k and ε_k are 0.3679 nm and 129.63 K, respectively, for -CH_3 group, 0.4 nm and 73.5 K, respectively, for -CH_2- group, and 0.373 nm and 160.3 K, respectively, for CH_4.

The average density ($\rho_{ave,k}$) of the component k in pores is given as,

$$\rho_{ave,k} = \frac{\int_0^W \rho_k(z)\,dz}{W}. \tag{2-6}$$

Table 2-1 Critical temperature T_c, critical pressure P_c, acentric factor ω, molar weight M_w, VSP, and attraction energy parameter ε_g for C_1, nC_6, and nC_8 in the engineering DFT and PR-EOS with capillary pressure model.

Species	T_c (K)	P_c (bar)	ω	M_w (g/mol)	VSP	ε_g / k_B (K)
C_1	190.56	45.99	0.011	16.04	-0.1533	1178
nC_6	507.40	30.12	0.296	86.18	-0.01478	2765
nC_8	568.70	24.90	0.398	114.2	0.04775	3192

2.2.2 PR-EOS with Capillary Pressure Model

Within the PR-EOS with capillary pressure model, the pressure difference between the vapor and liquid phases is described by the capillary pressure P_{cap}, which is related to the interfacial tension γ, contact angle θ, and pore curvature $1/r$,

$$P_{cap} = \frac{2\gamma\cos\theta}{r}, \tag{2-7}$$

We assume that liquid phase completely wets the surface and the contact angle is zero. The interfacial tension of pure component was obtained from National Institute of Standards and Technology Chemistry WebBook (NIST). For mixtures, the interfacial tension is computed by (Weinaug and Katz 1943),

$$\gamma = \left[\sum_{i=1}^{2} PAC_i\left(x_i\rho_L - y_i\rho_V\right)\right]^4, \tag{2-8}$$

where PAC_i represents the Parachor number of component i; ρ_L and ρ_V denote molar densities of liquid and vapor phases, respectively; x_i and y_i are the mole fractions of

component i in liquid and vapor phases, respectively. As presented by previous studies (Santiso and Firoozabadi 2006, Bui and Akkutlu 2015), the Parachor model is valid only when the pore radius is larger than 5 nm. Thus, in this study, the phase behavior description by the PR-EOS with capillary pressure model is conducted in pores down to 10 nm.

The phase equilibrium is obtained by achieving the equality of fugacity for each component across the vapor/liquid interface. In pores, the phase pressures used for evaluating the fugacities are different due to the presence of capillary pressure. Thereby, the expression at equilibrium is given as,

For a binary mixture,

$$f_i^V\left(P_V,T,y_i\right)=f_i^L\left(P_L,T,x_i\right),\ \ i=1,2, \tag{2-9}$$

For a pure component,

$$f^V\left(P_V,T\right)=f^L\left(P_L,T\right), \tag{2-10}$$

where f_i^V and f_i^L are the fugacities of component i in vapor and liquid phases, respectively; T is absolute temperature; P_V and P_L are vapor and liquid pressures, respectively. Dew-point is identified as the formation of first droplet.

The above equations for the dew-point calculations are solved by the standard negative flash algorithm; the successive substitution (SS) is initially applied to update the *K-values*, and then followed by the Newton iterations for convergence.

2.3 Dew-Point Calculation

For a pure component, phase description is conducted at an isobaric condition. Within the engineering DFT simulations, starting from a sufficiently high temperature, we gradually lower

the temperature to observe the capillary condensation of confined fluids (sudden jump in average densities in pores); at each temperature, fluid configurations in pores at the previous temperature are used as the initial condition. We use successive substitution iteration to update the density distributions by using the output of Eq. (2-3) as a new input (Li *et al.* 2014, Jin 2017). At the first temperature where the initial guess is not available, the bulk density is then used for the initialization.

For the mixtures, phase description is conducted at isothermal conditions. Within engineering DFT, the lower dew-point of confined fluids is calculated by gradually increasing the bulk pressure while using fluid configurations in pores at the previous pressure condition as the initial condition. The successive substitution iteration is used to update the density distributions by using the output of Eq. (2-3) as a new input. At the first pressure, where the initial guess is not available, the bulk density is used for the initialization. The calculation of lower dew-point is started at a sufficiently low pressure, and ended at a sufficiently high pressure. Similarly, for upper dew-point calculations, we start from sufficiently high pressure and gradually lower the bulk pressure. We monitor the capillary condensation to detect both lower and upper dew-points. As we will discuss later, the capillary condensation refers to sudden jump in the averaged density of confined heavier component.

Engineering DFT can reveal the hysteresis in nanopores and the process of increasing/decreasing pressure would provide different results. However, for PR-EOS with capillary pressure model, there is no hysteresis and the dew-point for the mixture can be obtained either by increasing or decreasing the pressure.

2.4 Critical Properties of Pure Components

We also calculate the critical points of confined pure hydrocarbons. The critical temperature of the confined pure component T_c^c is estimated by fitting the liquid-vapor coexistence densities to the following scaling law (Rowlinson and Widom 1982),

$$\rho_L - \rho_V = A\left(1-\frac{T}{T_c^c}\right)^{\eta}, \tag{2-11}$$

where A and η are the fitting parameter and the characteristic exponent, respectively.

The obtained confined critical temperature is then used to calculate the confined critical density (ρ_c^c) with the assumption that the coexisting vapor-liquid densities obey the so-called rectilinear law (Rowlinson and Swinton 1982),

$$\frac{\rho_L + \rho_V}{2} - \rho_c^c = B\left(1-\frac{T}{T_c^c}\right), \tag{2-12}$$

where B is the fitting parameter.

Practically, ρ_c^c and T_c^c are regressed by the least-square fit minimizing the average deviation between the above equations and the simulated coexisting vapor-liquid densities. Once these critical properties are obtained, the confined critical pressure P_c^c can then be estimated by extrapolating the Clapeyron plot to $1/T_c^c$ (Singh and Kwak 2007),

$$\ln P_c^c = C - \frac{D}{T_c^c}. \tag{2-13}$$

where *C* and *D* are the fitting parameters.

2.5 Results and Discussion

In this section, we use the engineering DFT and PR-EOS with capillary `effect` model to study the phase behavior and critical properties of confined pure nC_8 and the confined dew-points of binary mixture of C_1-nC_6 (bulk mole fraction C_1 is 0.7). By comparing with the engineering DFT, the performance of PR-EOS with capillary effect model is evaluated.

2.5.1 Phase Behavior and Critical Properties of Confined Pure *n*C_8

With the engineering DFT, we present the average density (ρ_{ave}) of pure nC_8 in nanopores of $W = 5$, 8, and 12 nm at $P = 8$ atm in Figure 2-1. The results are obtained by decreasing the system temperature. For 5-nm nanopore, ρ_{ave} continuously increases as temperature decreases, but for 8-nm and 12-nm nanopores, ρ_{ave} has a sudden jump from gas-phase-like density to liquid-phase-like density. This behavior is so-called capillary condensation (Li *et al.* 2014) and the temperature is defined as the dew-point temperature of confined fluids. We use these two densities to represent the vapor phase and liquid phase densities in phase coexistence curve. As indicated in Figure 2-1, the calculated dew-point temperatures of nC_8 in 8-nm, and 12-nm nanopores are around 502.0 K, and 495.5 K, respectively, which is about 8.0 K, and 1.5 K higher than the bulk saturation temperature (494.0 K) as obtained from the PR-EOS (1978). The increase in dew-point temperature is in agreement with the experimental measurements by Luo *et al.* (2016b). For confined pure component, the engineering DFT can calculate the average density in nanopores for the entire temperature range, while the PR-EOS with capillary effect model can have vapor-liquid equilibrium only at the saturation point.

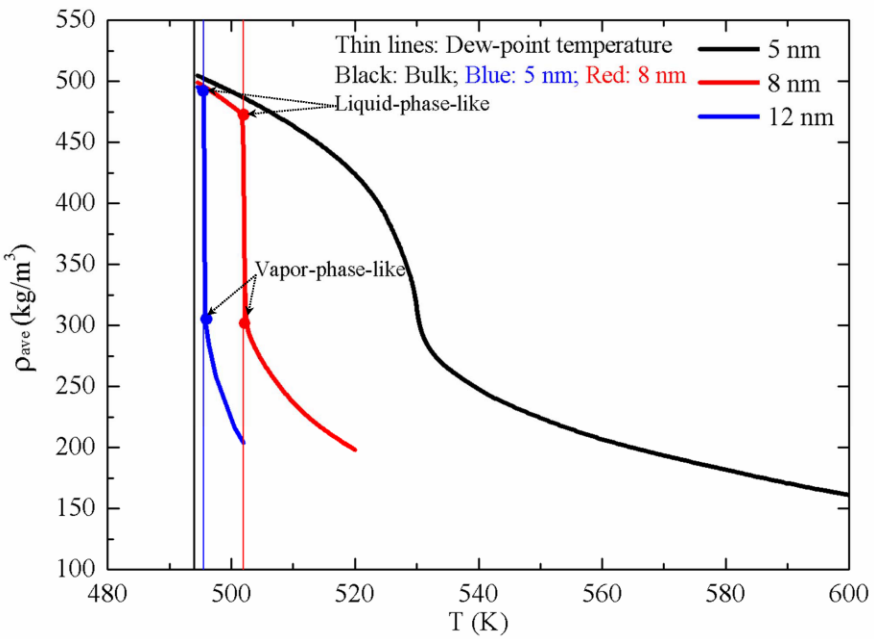

Figure 2-1 The average density ρ_{ave} of pure nC_8 in nanopores of W = 5, 8, and 12 nm at the condition of P = 8 atm from the engineering DFT.

Figure 2-2 depicts the density-temperature ($\rho - T$) vapor-liquid coexistence envelopes of nC_8 in nanopores of various pore sizes from the PR-EOS with capillary effect model and the engineering DFT. In engineering DFT, the vapor and liquid phase densities are identified as ρ_{ave} right before and at the capillary condensation as shown in Figure 1. We observe that T_c^c obtained from the engineering DFT is shifted to a lower value and approaches T_c as pore size increases, which is in line with previous simulation works (Singh *et al.* 2009, Didar and Akkutlu 2013), while no shift is observed from the PR-EOS with capillary effect model. The PR-EOS with capillary effect model predicts that the vapor-phase density in nanopores is similar to that in bulk, while the density obtained from the engineering DFT is significantly higher. While engineering DFT takes into account the fluid-surface interactions and surface adsorptions, the PR-EOS with capillary effect ignores these effects. As a result, the vapor and liquid phase densities obtained from engineering DFT can be higher than that of bulk vapor and liquid phases,

respectively. As pore size increases, the PR-EOS with capillary effect predicts that vapor-liquid coexistence curve of confined nC_8 approaches bulk. It also predicts that the liquid phase coexistence density first increases as temperature decreases, but after a certain point then decreases. It is because the liquid phase pressure at coexistence is lower than the bulk pressure. As bulk pressure decreases, the capillary pressure increases due to higher interfacial tension. As a result, PR-EOS with capillary effect becomes less reliable at low pressure conditions. Additionally, the PR-EOS with capillary effect model calculates the dew-point with the assumption of vapor-liquid coexistence as a priori. The calculated liquid phase would be in a superheated state with the lower pressure and density. This behavior is completely opposite to the findings from engineering DFT. It implies that stability test with capillary effect should be employed to evaluate phase stability in naopores when using the PR-EOS with capillary effect model, especially in low pressure region. (Zhong *et al.* 2017)

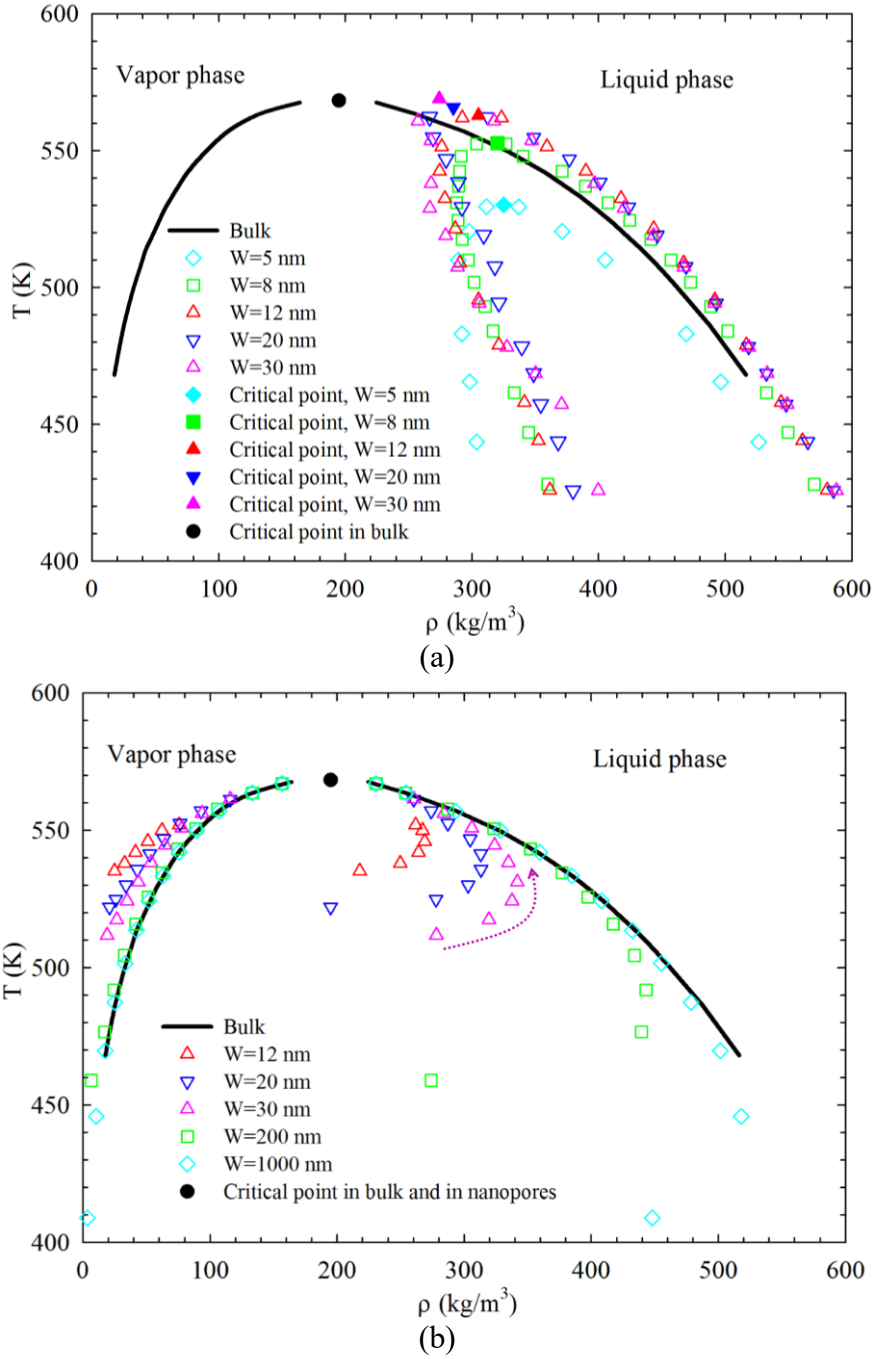

Figure 2-2 The density-temperature vapor-liquid coexistence curve for nC_8 from (a) the engineering DFT at W = 5, 8, 12, and 20 nm and from (b) the PR-EOS with capillary effect at W = 12, 20, 30, 200, and 1000 nm. The bulk vapor-liquid density is calculated by the PR-EOS (1978). The filled symbols represent the estimated critical temperatures and densities from Eq. (2-11) to Eq. (2-13). The dashed arrow highlights the region where the liquid phase density is lowered due to lower liquid phase pressure from the PR-EOS with capillary effect.

To further investigate the phase behavior of confined fluids, in Figure 2-3 we present the dew-point temperatures of pure nC_8 at isobaric conditions of 1 atm, 5 atm, and 20 atm from the

engineering DFT, and at 5 atm, and 20 atm from the PR-EOS with capillary effect model. For comparison, we also depict the bulk saturation point obtained from the PR-EOS (1978). From two approaches, we observe that as pore size increases, dew-point in nanopores decreases and approaches the bulk saturation temperature. When pore size is smaller than a certain value, there is no capillary condensation from engineering DFT. It indicates confinement-induced supercriticality of hydrocarbons in small nanopores, which is in line with previous experimental measurements (Luo *et al.* 2016). As pressure increases, the supercriticality shifts to larger pores from engineering DFT. The PR-EOS with capillary pressure predicts that when the pore size is sufficiently small, there is no equality of fugacities of vapor and liquid phase. Unlike engineering DFT, the area of non-fugacity equality moves toward a smaller pore size with an increase in pressure. At 5 atm, while engineering DFT predicts that the dew-point temperature of confined nC_8 approaches bulk in 30 nm pores, within the PR-EOS with capillary effect it is only the case in 1,000 nm pores. Zhao *et al.* (2017) found that the dew-point pressure of confined propane is very close to bulk saturation point when the pore size is around 70 nm. Parsa *et al.* (2015) claimed that the capillary condensation pressure in 50 nm pores is close to bulk saturation point.

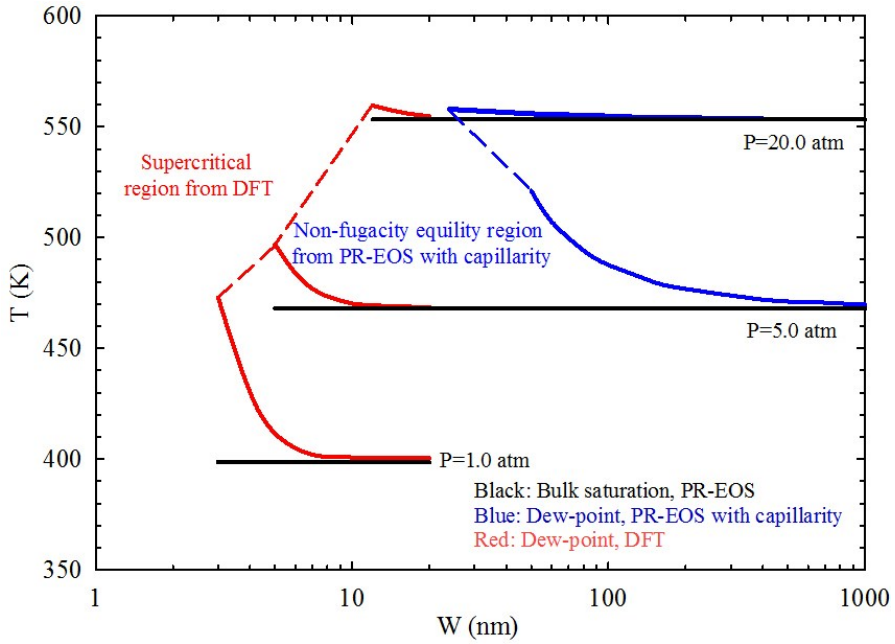

Figure 2-3 The saturation temperatures of pure nC_8 in nanopores and the corresponding bulk saturation temperatures from the engineering DFT at isobaric conditions of 1 atm, 5 atm and 20 atm (red lines) and the PR-EOS with capillary effect model (blue lines) at isobaric conditions of 5 atm and 20 atm. The black lines represent the bulk saturation temperature from the PR-EOS (1978).

Based on the dew-point temperature calculations, we depict the $P-T$ diagram of nC_8 in nanopores from the engineering DFT and the PR-EOS with capillary effect model in Figure 2-4. For comparison, we also present the bulk $P-T$ diagram calculated from the PR-EOS (1978). Both approaches predict that as pore size increases, saturation pressure in nanopores increases. At a given system temperature, phase transitions of hydrocarbons in oil-wet nanopores take place at lower pressures than that in the bulk. As for the engineering DFT, fluid-surface interaction may facilitate the phase transitions of confined hydrocarbons. On the other hand, using Monte Carlo simulations, Singh *et al.* (2009) predicted that in small oil-wet nanopores (pore less than 2 nm), the saturation pressure of confined hydrocarbons can be higher than the bulk saturation point. Engineering DFT predicts that the *P-T* diagram of nC_8 approaches bulk for W=30 nm, while the *P-T* diagram from the PR-EOS with capillary effect model approaches the bulk only

when W is as large as 1,000 nm. Although the PR-EOS with capillary effect model is in qualitative agreement with the engineering DFT, there is orders of magnitude difference in the critical pore sizes between these two approaches.

While engineering DFT predicts that the confined $P-T$ diagram deviates from the bulk as pressure increases, the opposite is true for the PR-EOS with capillary pressure effect. As pressure increases, the effect of capillary pressure becomes less significant. In addition, the critical pressure from the PR-EOS with capillary effect model does not deviate from the bulk critical pressure. On the other hand, the critical pressure from engineering DFT is lowered in nanopores, which is in line with previous works (Balbuena and Gubbins 1993, Lev *et al.* 1999). Due to the lowered critical point, engineering DFT predicts that the supercriticality shifts toward lower pressure and temperature. The supercriticality remains intact for the PR-EOS with capillary effect. We also find that there is non-fugacity equality region from PR-EOS with capillary effect model at low pressure conditions. The PR-EOS with capillary effect model is based on the assumption that confined phase behavior is only affected by capillary pressure, which is dependent on the pore size and surface tension. We use the bulk surface tension for pure nC_8 from the National Institute of Standards and Technology Chemistry WebBook (NIST). However, in nanopores, the surface tension can be very different from that in bulk (Bruot and Caupin 2016). As suggested by Singh and Kwak (2007), vapor-liquid surface tension under confinement is significantly lower than the bulk value; they proposed that the fluid-pore surface interaction greatly affects the surface tension.

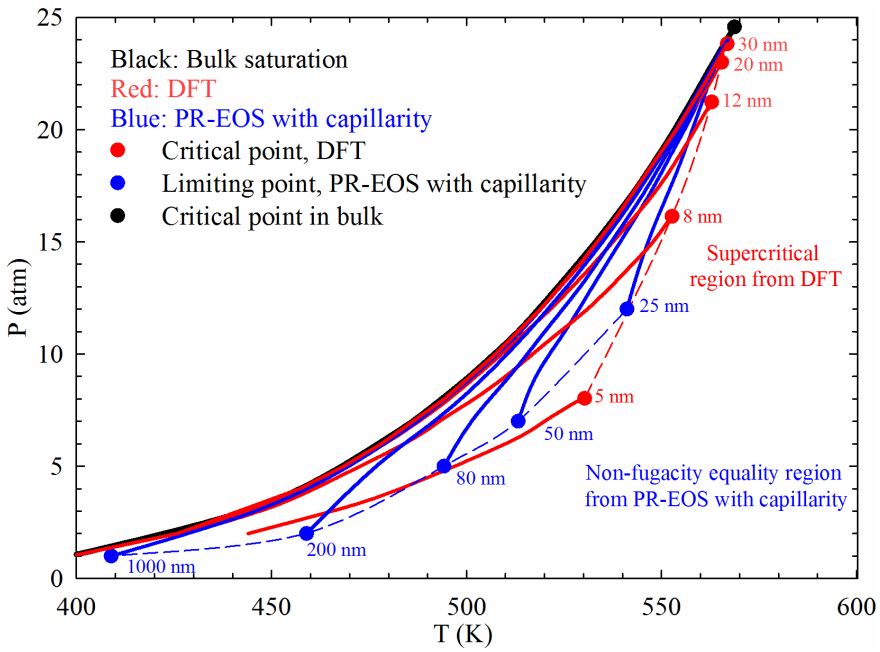

Figure 2-4 The Pressure-Temperature (*P*-*T*) diagram of nC_8 in nanopores from engineering DFT and PR-EOS with capillary effect model and the corresponding bulk *P*-*T* diagram from the PR-EOS (1978).

We depict the shifts in the critical pressure from engineering DFT in terms of $1/W$ in Figure 2-5. The shift in the critical pressure is calculated from $\Delta P = \left(P_{cb} - P_{cp}\right)/P_{cb}$, where P_{cb} is the bulk critical pressure and P_{cp} is the confined critical pressure. While the PR-EOS with capillary effect model predicts that there is no deviation on the critical pressure, the engineering DFT shows negative deviation. In other words, the critical pressure is lowered in oil-wet nanopores. Singh *et al.* (2009) studied the shift in the critical pressure of nC_8 with pore confinement in graphite using the configurational-biased grand-canonical transition-matrix Monte Carlo simulations. They observed that when the W is larger than 3 nm, the deviation can be positive, which means that the confined critical pressure increases as illustrated in Figure 2-5. The shifted critical points by Singh *et al.* (2009) have been widely used in the so-called EOS modeling with shifted critical properties (Sapmanee 2011, Devegowda *et al.* 2012, Alharthy *et al.* 2013, Jin *et al.* 2013, Zhang *et al.* 2013). However, Didar and Akkutulu (2013) have shown that the critical

pressure of methane in carbon nanopores decreases by using Monte Carlo simulation. The lower critical pressure is also confirmed by simulation works by Balbuena and Gubbins (1993) and Lev *et al.* (1999) on Lennard-Jones fluids confined in an attractive pore.

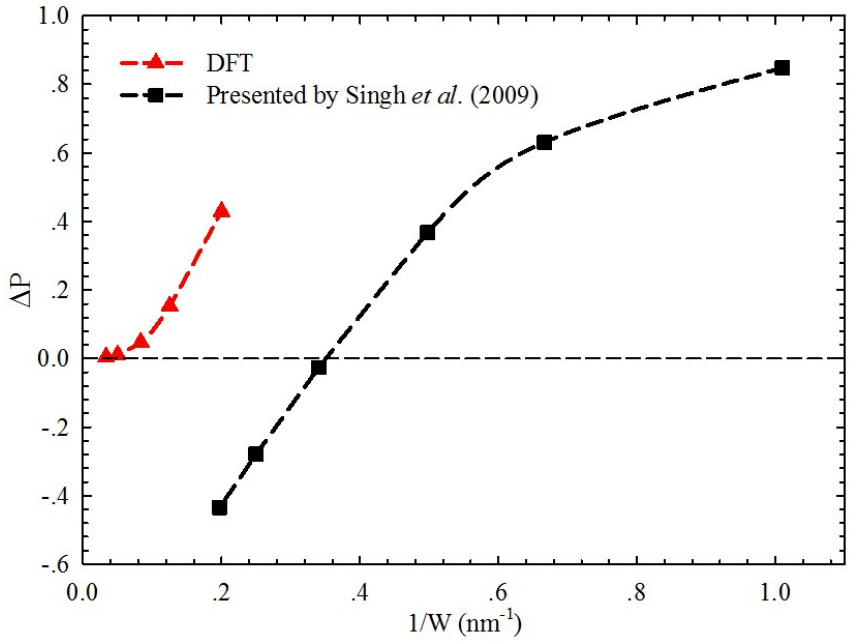

Figure 2-5 The shift in the critical pressure ΔP of nC_8 versus $1/W$ as calculated by the engineering DFT and the prediction results from Singh *et al.* (2009).

2.5.2 Phase Behavior of Confined C_1-nC_6 Mixture

After studying the phase behavior of pure nC_8 in nanopores, in this subsection, we use engineering DFT and PR-EOS with capillary effect model to investigate the phase behavior of confined C_1-nC_6 mixture. We will study the lower and upper dew-point pressure of this mixture at isothermal conditions. The molar fraction of C_1 in the bulk C_1-nC_6 mixture is fixed at 0.7.

We firstly investigate the lower dew-point pressure. By increasing the system pressure, we obtain the change in the average density (ρ_{ave}) of C_1-nC_6 mixture obtained from the engineering DFT in nanopores of $W = 3$, 5, and 20 nm at three isothermal conditions of $T = 410$, 435, and 445 K, respectively, as shown in Figures 2-6 to 2-8. Note that $T = 445$ K is higher than the bulk

cricondentherm $T_{cric} = 440.73$ K, which is the highest temperature at which phase transitions can occur in bulk. As bulk pressure increases, the average density of nC_6 shows a sudden jump at the capillary condensation pressure. When $T < T_{cric}$, the lower dew-point pressure with confinement is lower than the bulk and approaches bulk value as pore size increases. In nanopores, the average density of nC_6 has a nonlinear correlation with system pressure. However, the average density of C_1 has a linear behavior. Compared to nC_6, C_1 shows a density drop at the dew-point pressure, as indicated in Figures 2-6b to 2-8b. This opposite behavior is due to the selective adsorption between C_1 and nC_6 molecules; nC_6 molecules have stronger affinity to the pore surface than C_1 molecules. We also found that, as pore size increases, the average density of nC_6 decreases due to the weaker fluid-surface interactions. On the other hand, for C_1, this is true only when the mixture forms vapor-like structure in nanopores. At $T = 435$ K, the average density profile of C_1 and nC_6 in 3-nm nanopore is continuous and no sudden jump/drop is observed, indicating supercriticality. The same phenomenon is also observed in the 20-nm nanopore at $T = 445$ K. In Figures 2-6 to 2-8, we also include the results on the variation of the average mixture density with the pore size. We observe that the as bulk pressure increases, the average mixture density also shows a sudden jump at the capillary condensation pressure; such capillary condensation pressure is the same as that obtained from the average density curves of C_1 and nC_6 of C_1-nC_6 mixture.

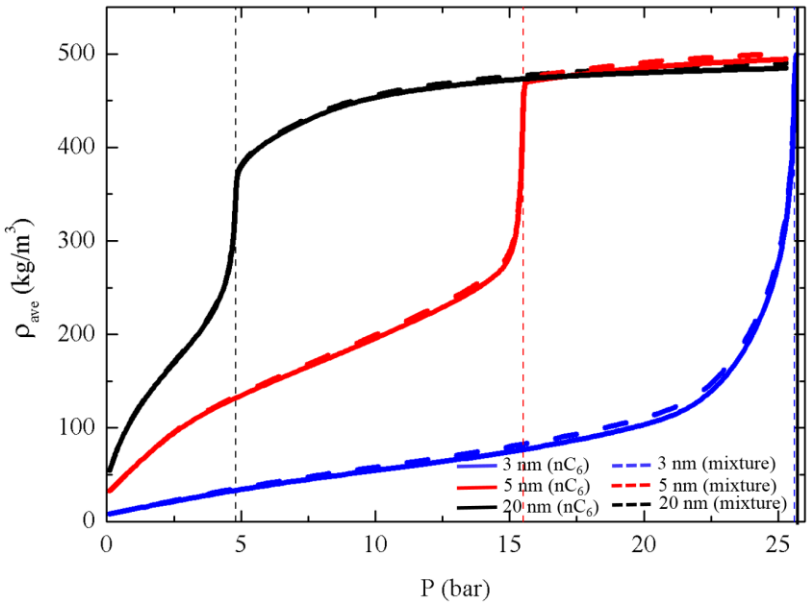

(a)

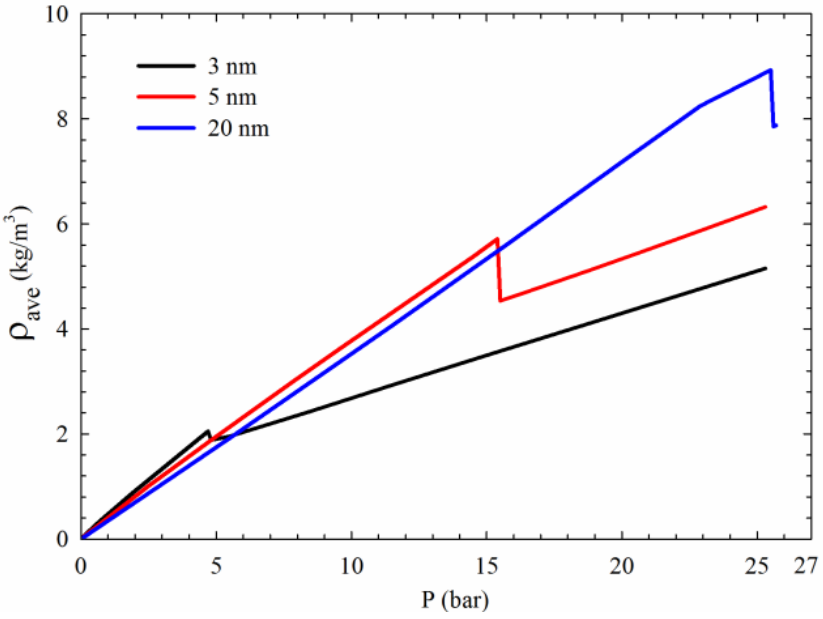

(b)

Figure 2-6 The average density of C_1 and nC_6 of C_1-nC_6 mixture (solid lines) and the average mixture density (dashed lines) in nanopores of pore sizes of 3 nm (black), 5 nm (red), and 20 nm (blue) at isothermal condition of T = 410 K: (a) nC_6; and (b) C_1. The thin solid line (black) presents lower dew-point pressure in bulk; the thin dash lines (black), (red), and (blue) present lower dew-point pressures in 3 nm, 5 nm, and 20 nm nanopores, respectively.

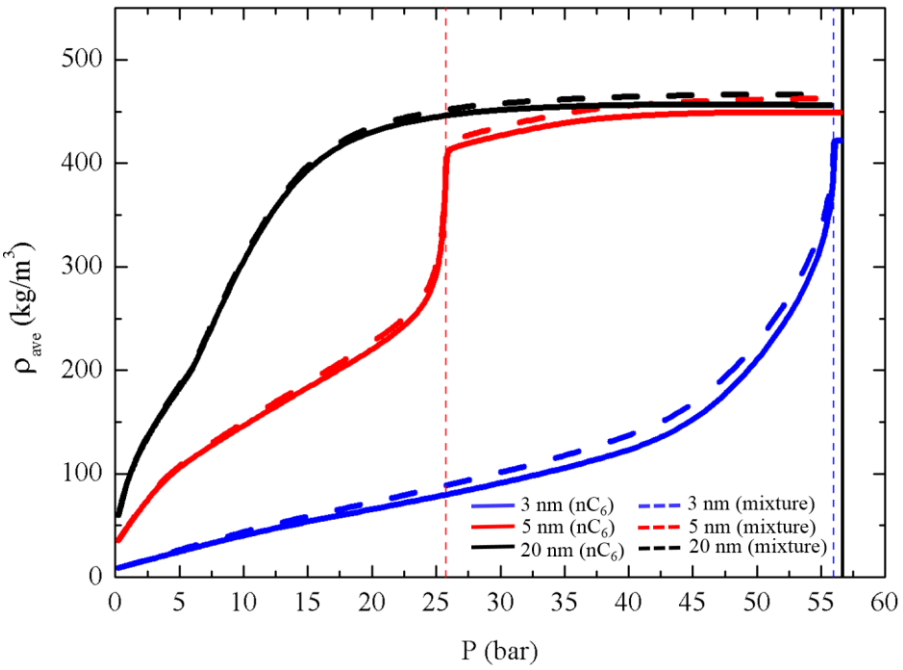

(a)

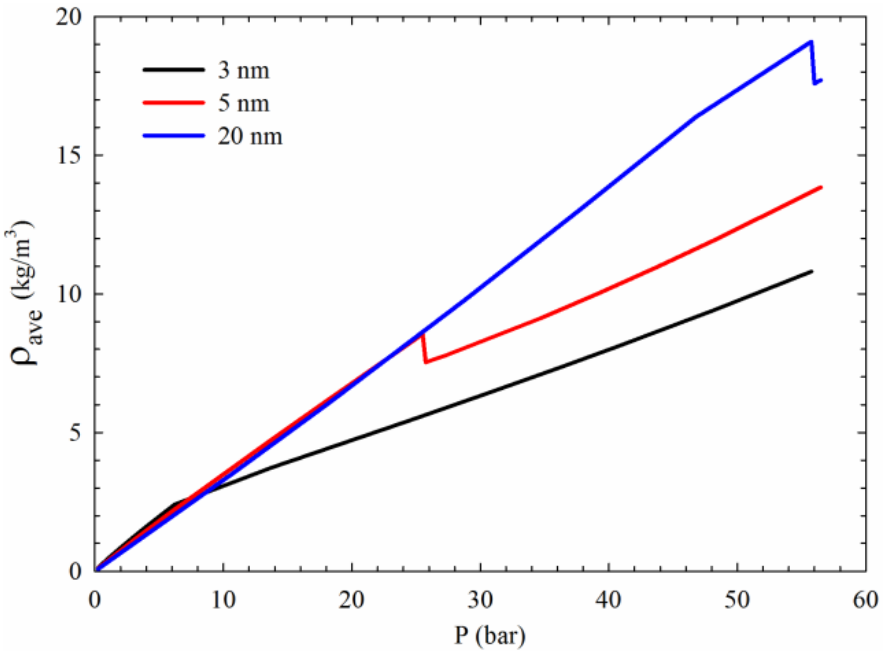

(b)

Figure 2-7 The average density of C_1 and nC_6 of C_1-nC_6 mixture (solid lines) and the average mixture density (dashed lines) in nanopores of pore sizes of 3 nm (black), 5 nm (red), and 20 nm (blue) at isothermal condition of T = 435 K: (a) nC_6; and (b) C_1. The thin solid line (black) presents lower dew-point pressure in bulk; the thin dash lines (red), and (blue) present lower dew-point pressures in 5 nm, and 20 nm nanopores, respectively.

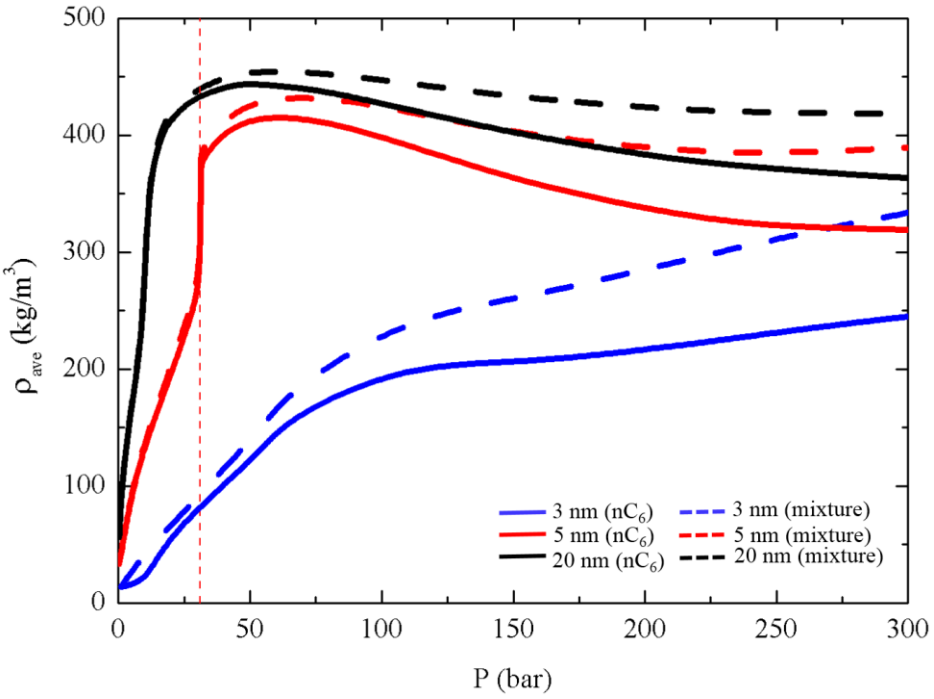

(a)

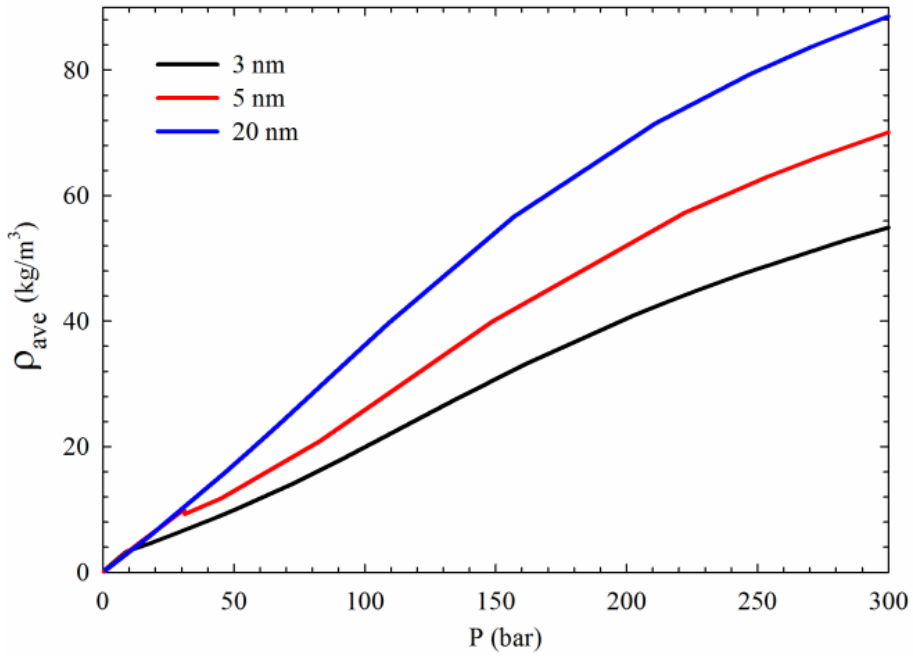

(b)

Figure 2-8 The average density of C_1 and nC_6 of C_1-nC_6 mixture (soline lines) and the average mixture density (dashed lines) in nanopores of pore sizes of 3 nm (black), 5 nm (red), and 20 nm (blue) at isothermal condition of T = 445 K: (a) nC_6; and (b) C_1. The thin dash line (red) presents lower dew-point pressure in 5 nm nanopore.

In Figure 2-9, we depict the $P-T$ diagrams of the C_1-nC_6 mixture in nanopores of varying pore sizes in the lower dew-point region from the engineering DFT and the PR-EOS with capillary effect model. For comparison, we also present the bulk $P-T$ diagram from the PR-EOS (1978). We observe that, when $T < T_{cric}$, the lower dew-point pressures obtained from both engineering DFT and PR-EOS with capillary effect model are shifted to lower pressures. As pore size increases, the confined lower dew-point pressures approach the bulk. When $T > T_{cric}$, we observe that phase transition still can occur from the calculations by the PR-EOS with capillary effect model and engineering DFT, which agrees with the previous works (Sandoval *et al.* 2016). As for the engineering DFT, we define the highest temperature at which the lower dew-point of confined fluids can be observed as the critical temperature of lower dew-point. As shown in Figure 2-9a, we observe that the critical temperature of lower dew-point increases till 5 nm and then decreases from the engineering DFT. As for the PR-EOS with capillary effect model, the cricondentherm of lower dew-point decreases with pore size, as presented in Figure 2-9b. With both approaches, we observe that the critical temperature and the cricondentherm approach the bulk cricondentherm point as pore size increases.

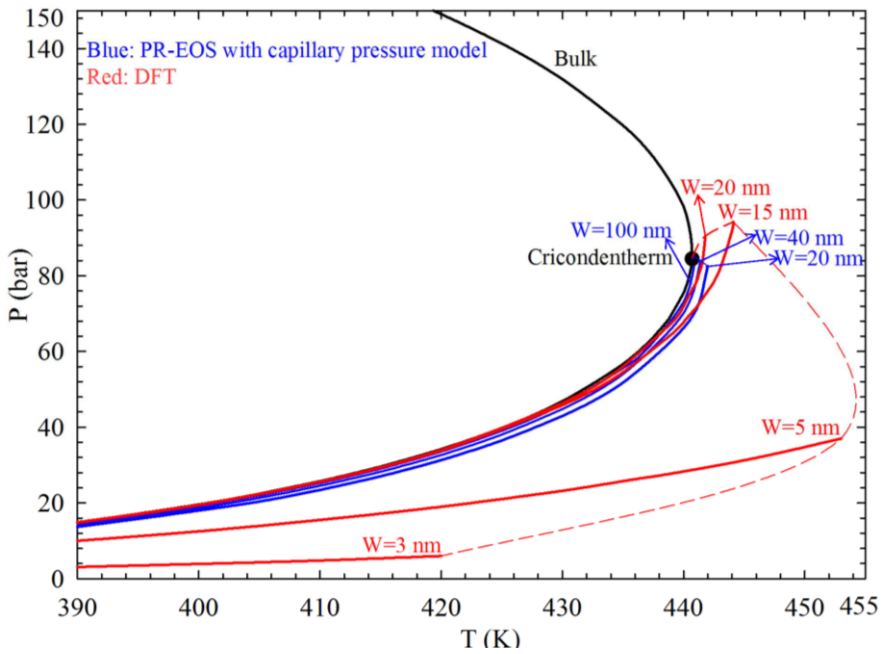

(a)

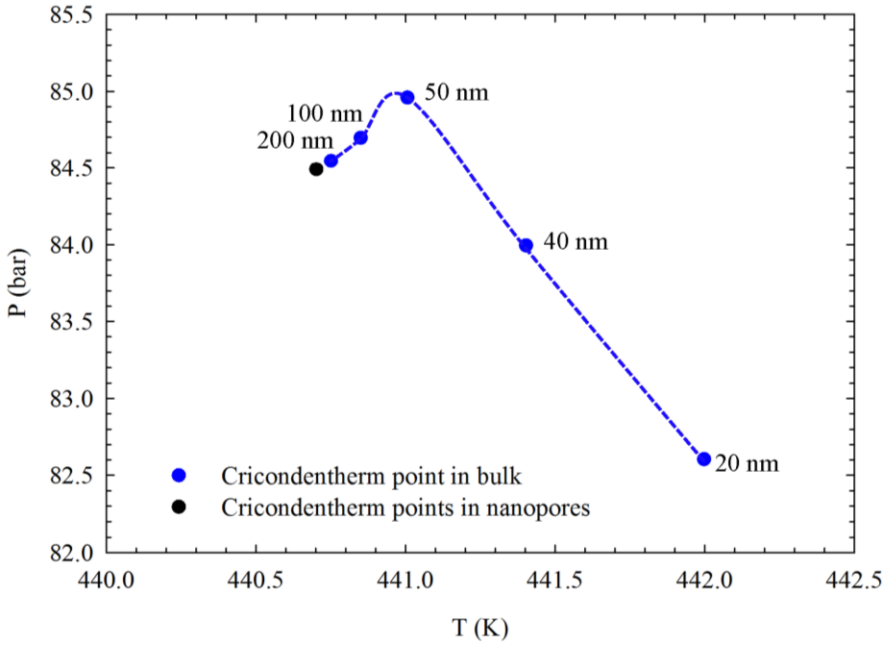

(b)

Figure 2-9 (a) The lower dew-point lines of C_1-nC_6 mixture in nanopores from the PR-EOS with capillary effect model and engineering DFT and the corresponding bulk *P-T* diagram from the PR-EOS (1978); (b) Cricondentherm of the lower dew-point with pore size as obtained from the PR-EOS with capillary pressure model.

We then focus on the upper dew-point pressure. By decreasing the system pressure, we present

the average density (ρ_{ave}) of C_1 and nC_6 of C_1-nC_6 mixture obtained from the engineering DFT in nanopores of $W = 20$, 30, and 50 nm at three isothermal conditions of $T = 430$, 435, and 439 K, respectively, as shown in Figures 2-10a to 2-12a. Note that these temperatures are all lower than the bulk cricondentherm $T_{cric} = 440.73$ K. The desorption isotherms of C_1-nC_6 mixture are obtained by decreasing the system pressure, which represents the calculations of upper dew-point pressures of confined fluids. As bulk pressure decreases, the average density of nC_6 decreases first and then increases. It also shows a sudden jump at the capillary condensation pressure at 439 K for all pore sizes. The upper dew-point pressure with confinement is higher than that in the bulk and approaches the bulk value as pore size increases. As pore size increases, the average density of nC_6 decreases due to weaker fluid-surface interactions. At $T = 435$ K, the average density profile of nC_6 in 20-nm pores is continuous and no sudden jump is observed over the entire pressure range, while in 30-nm and 50-nm pores there is capillary condensation. The non-capillary condensation indicates confinement-induced supercriticality of hydrocarbons in small nanopores. The same phenomenon is also observed in the 20-nm and 30-nm pores at $T = 430$ K. In other words, supercriticality shifts toward higher pore size as temperature drops. Similar to the adsorption process, in nanopores, the average density of nC_6 has a non-linear correlation with system pressure and the average density of C_1 has a linear behavior during desorption process. Compared to nC_6, C_1 shows a density drop at the lower dew-point pressure, as indicated in Figures 2-10b to 2-12b. This opposite behavior can be attributed to the selective adsorption between C_1 and nC_6 molecules; nC_6 molecules have stronger affinity to the pore surface than C_1 molecules.

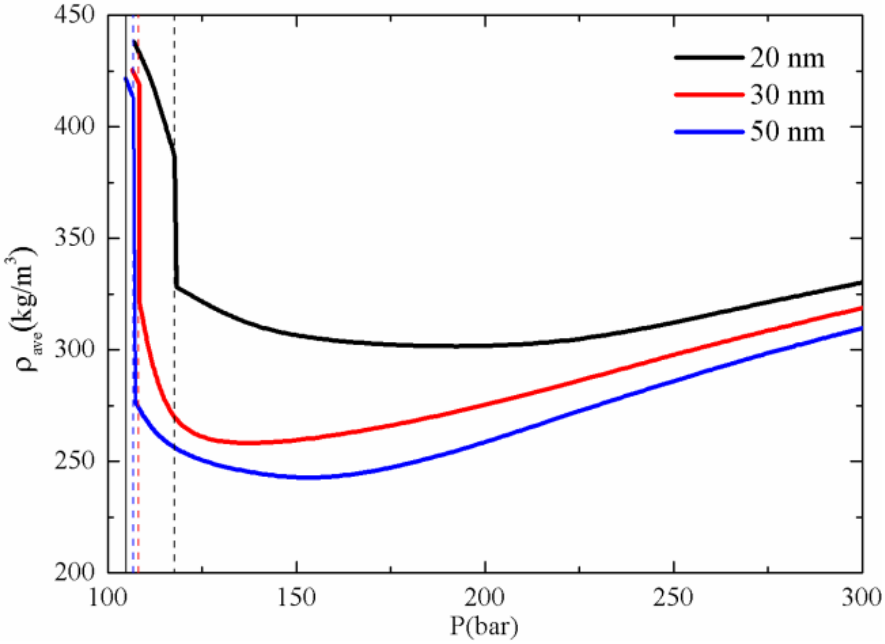

(a)

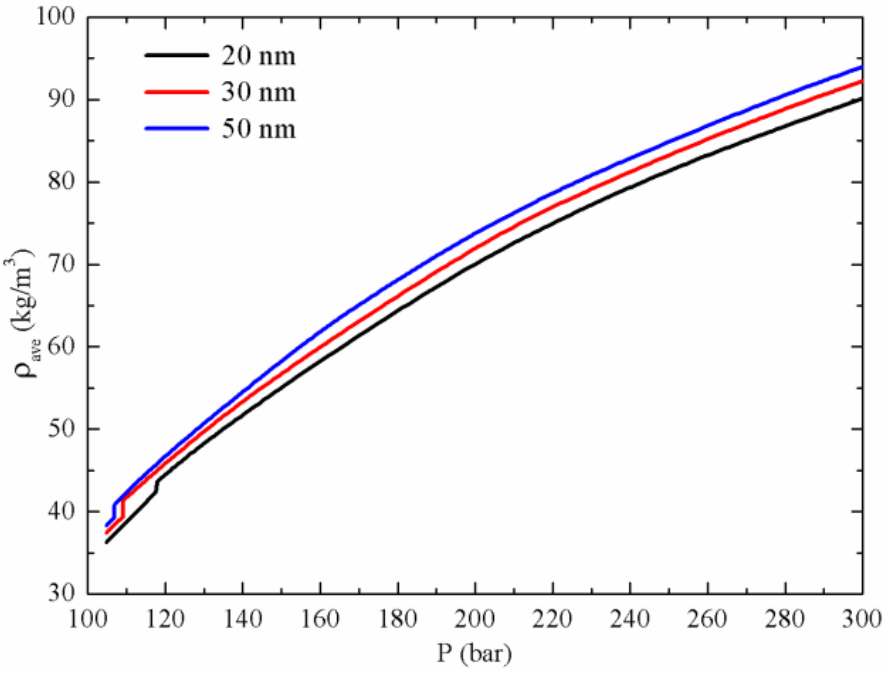

(b)

Figure 2-10 The average density of C_1 and nC_6 of C_1-nC_6 mixture in nanopores of pore sizes of 20 nm (black), 30 nm (red), and 50 nm (blue) at isothermal condition of T=439 K: (a) nC_6; and (b) C_1; the thin solid line (black) presents upper dew-point pressure in bulk; the thin dash lines (black), (red), and (blue) present upper dew-point pressures in 20 nm, 30 nm, and 50 nm nanopores, respectively.

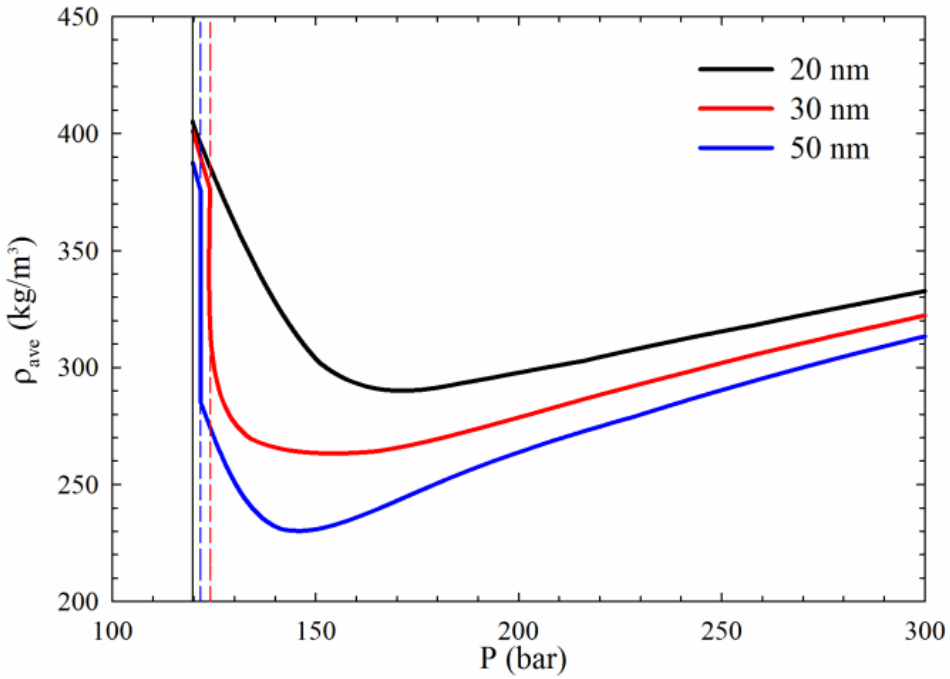

(a)

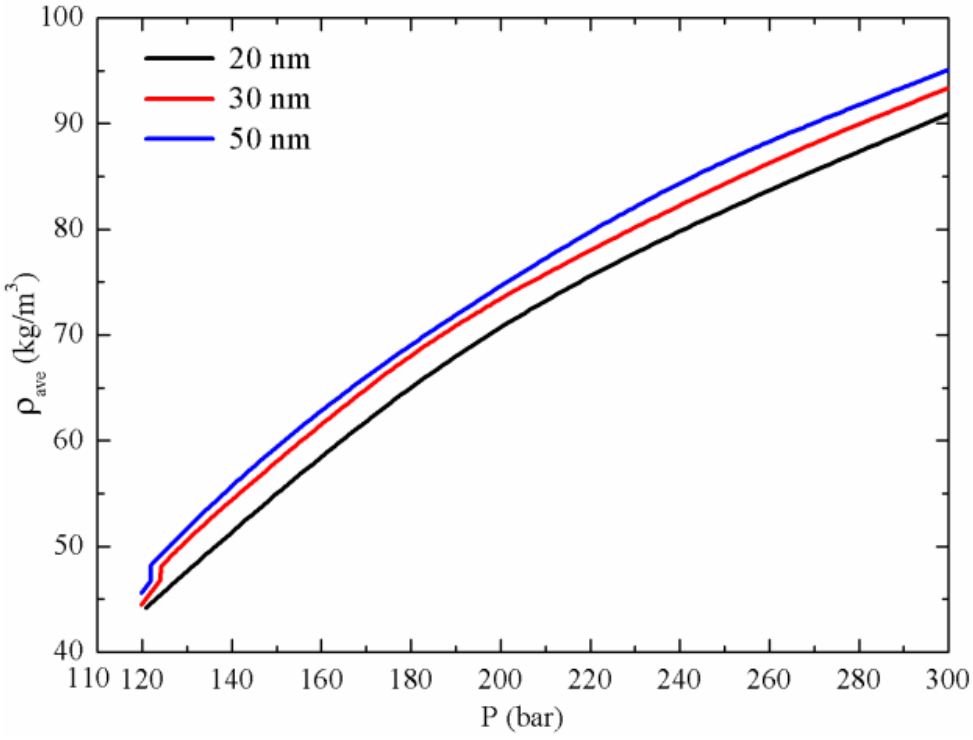

(b)

Figure 2-11 The average density of C_1 and nC_6 of C_1-nC_6 mixture in nanopores of pore sizes of 20 nm (black), 30 nm (red), and 50 nm (blue) at isothermal condition of T=435 K: (a) nC_6; and (b) C_1; the thin solid line (black) presents upper dew-point pressure in bulk; the thin dash lines (red), and (blue) present upper dew-point pressures in 30 nm, and 50 nm nanopores, respectively.

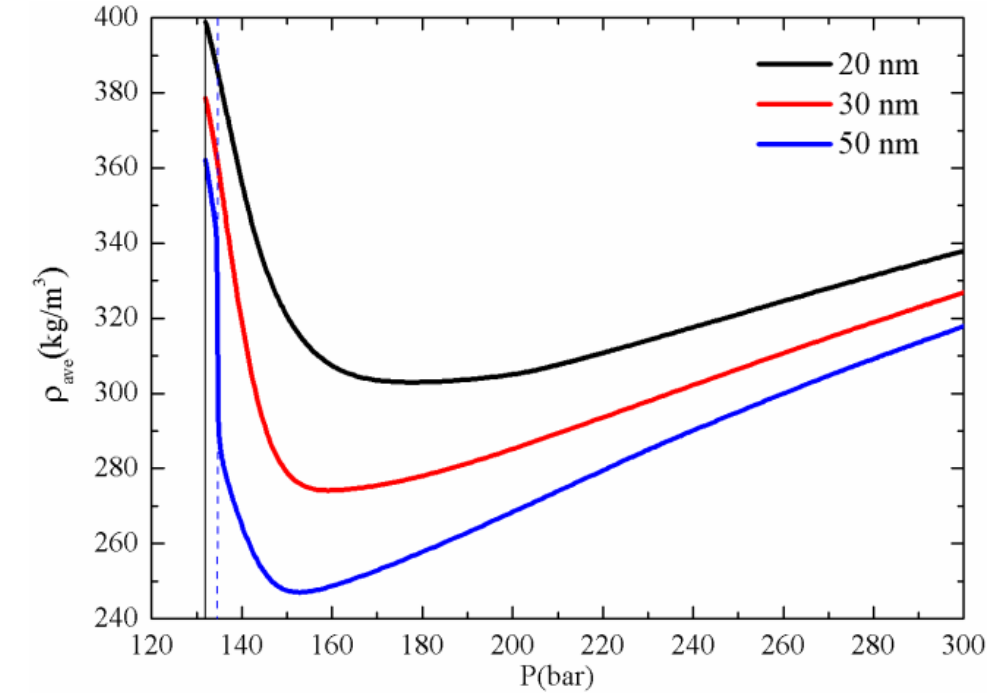

(a)

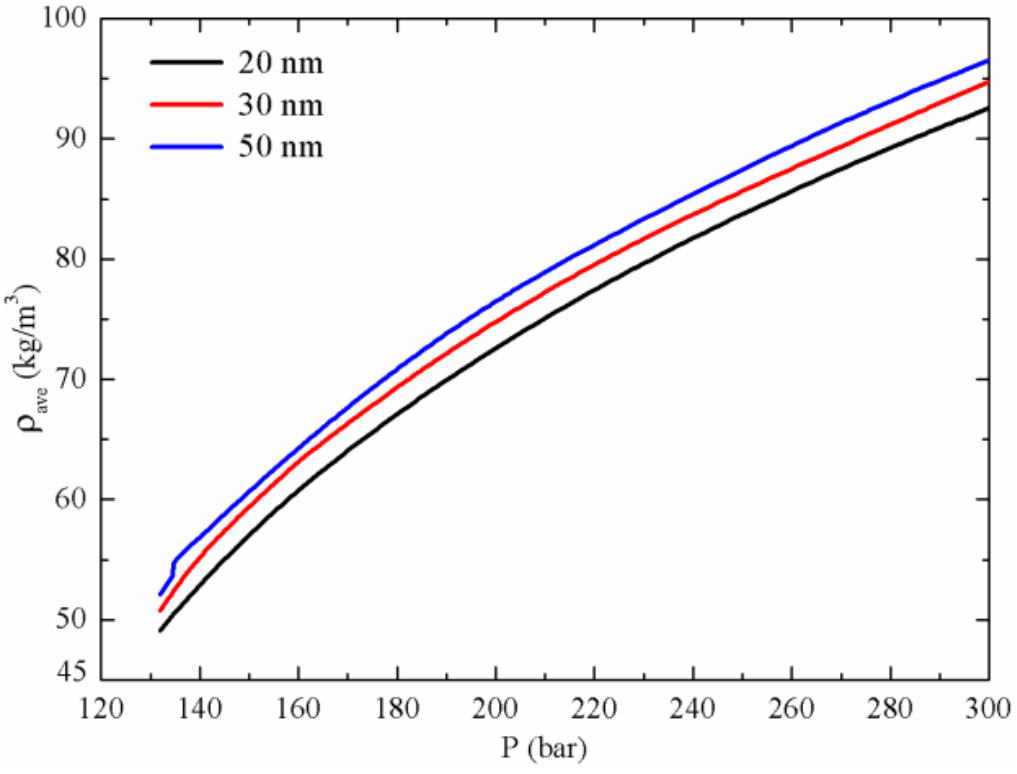

(b)

Figure 2-12 The average density of C_1 and nC_6 of C_1-nC_6 mixture in nanopores of pore sizes of 20 nm (black), 30 nm (red), and 50 nm (blue) at isothermal condition of T=430 K: (a) nC_6; and (b) C_1; the thin solid line (black) presents upper dew-point pressure in bulk; the thin dash line (blue) presents upper dew-point pressure in 50 nm nanopores.

Figure 2-13 presents the adsorption and desorption isotherms of nC_6 of C_1-nC_6 mixtures in a nanopores with $W = 20$ nm at various temperatures. The confined fluids experience capillary condensation and then evaporation in adsorption and desorption isotherms at $T = 441$ and 441.8 K. These temperatures are higher than T_{cric}. Interestingly, the condensation behaviors from adsorption and desorption isotherms coincide at around 441.8 K. At $T = 442$ K, the adsorption and desorption isotherms overlap in the entire range, indicating supercriticality. During pressure drop, capillary condensation in nanopores can be understood as retrograde condensation. As a result, such dew-point corresponds to the upper dew-point, which is different from the lower dew-point observed from adsorption process. During desorption, after forming liquid-like phases within nanopores, heavier component can have capillary evaporation as pressure further drops. On the other hand, during adsorption, heavier component first experiences capillary condensation and then evaporation as pressure further increases.

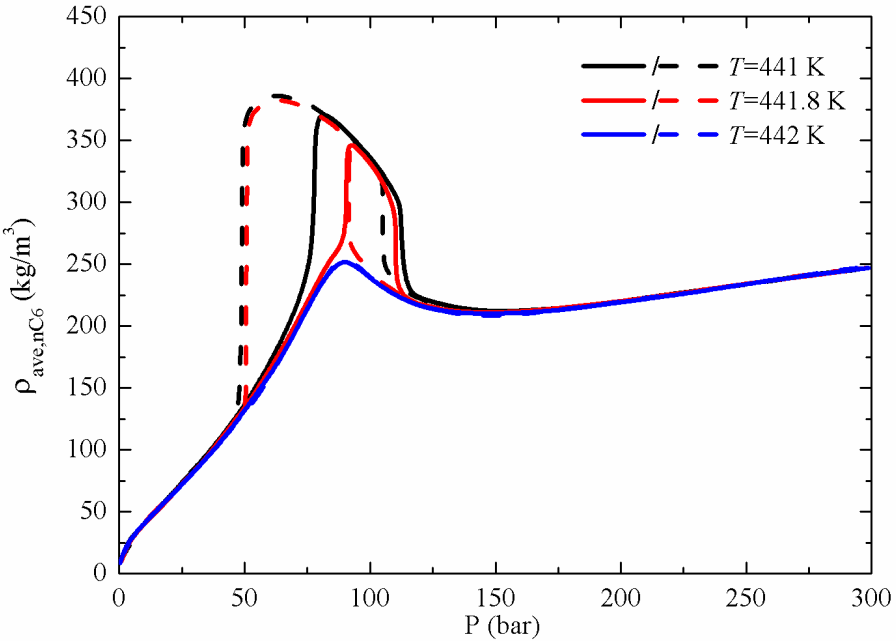

Figure 2-13 The adsorption isotherms (solid lines) and desorption isotherms (dash lines) of nC_6 in the C_1-nC_6 mixtures in nanopores with a pore size of 20 nm at various temperatures.

In Figure 2-14, we present the $P-T$ diagram of C_1-nC_6 mixture in nanopores of varying pore sizes in the upper and lower dew-point regions. Both Engineering DFT and the PR-EOS with capillary pressure model predict that upper dew-point pressure increases. As pore size increases, the upper dew-point of confined fluids approaches the bulk. Interestingly, engineering DFT predicts that the upper dew-point line coincides with the lower dew-point line at one point, as shown in Figure 2-14. We can define this point as the cricondentherm point of confined fluids. To our knowledge, this is the first time this phenomenon is ever reported. As temperature decreases, the confined upper dew-points show departure from the corresponding bulk values. If temperature further drops, there is supercritical region predicted from engineering DFT, where no capillary condensation is observed as pressure drops. On the other hand, the PR-EOS with capillary effect model does not show such supercriticality and the upper dew-point line passes through the bulk critical point due to zero capillary pressure at the critical point.

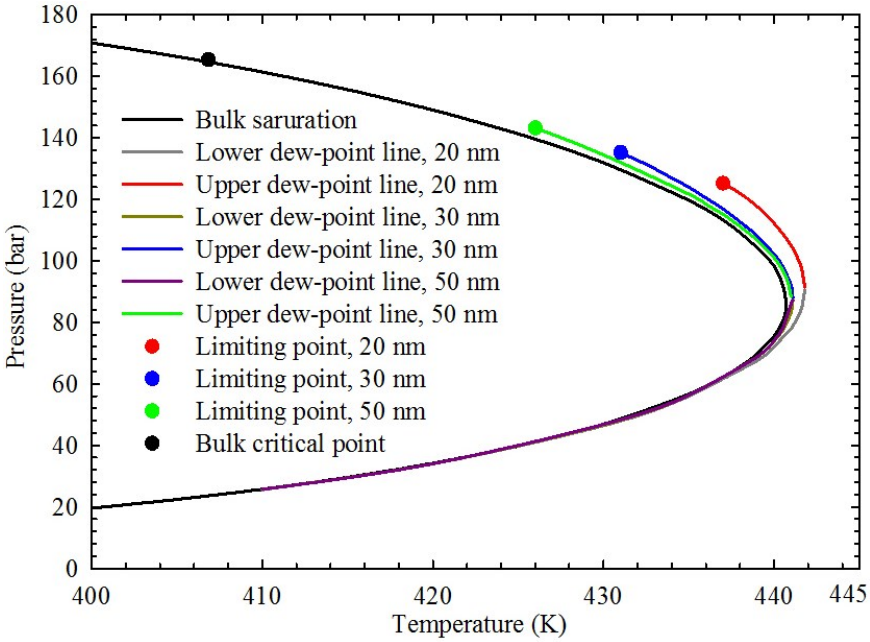

(a)

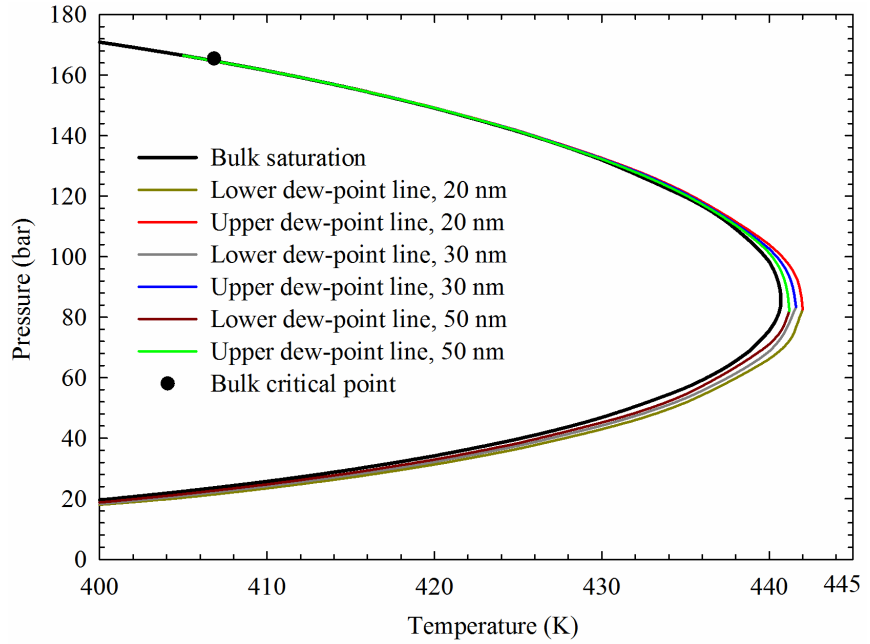

(b)

Figure 2-14 The dew-point lines of C_1-nC_6 mixture in nanopores from (a) engineering DFT and (b) PR-EOS with capillary effect model.

Figure 2-15 depicts the deviations of the confined dew-point pressures for the C_1-nC_6 mixture as predicted from the PR-EOS with capillary effect model and engineering DFT. Both approaches

predict that deviation of the confined dew-point pressures decreases as pore size increases. For the PR-EOS with capillary effect model, we observe that the dew-point pressure difference increases as system temperature increases. At the bulk critical temperature, the upper dew-point pressure remains unchanged. However, as illustrated in Figure 2-15a, engineering DFT predicts that, as temperature increases, the upper dew-point pressure difference decreases first, and then increases in 30-nm and 50-nm nanopores. Besides, in the vincinity of the upper dew-point, engineering DFT calculation indicates that, when temperature is lower than a certain value, there is no capillary condensation. As pore size increases, the supercriticality shifts to a lower temperature. Nojabaei *et al.* (2013) proposed that phase transition cannot happen beyond the cricondentherm. However, both PR-EOS with capillary effect model and engineering DFT predict that phase transitions can still occur at temperatures beyond the bulk cricondentherm point.

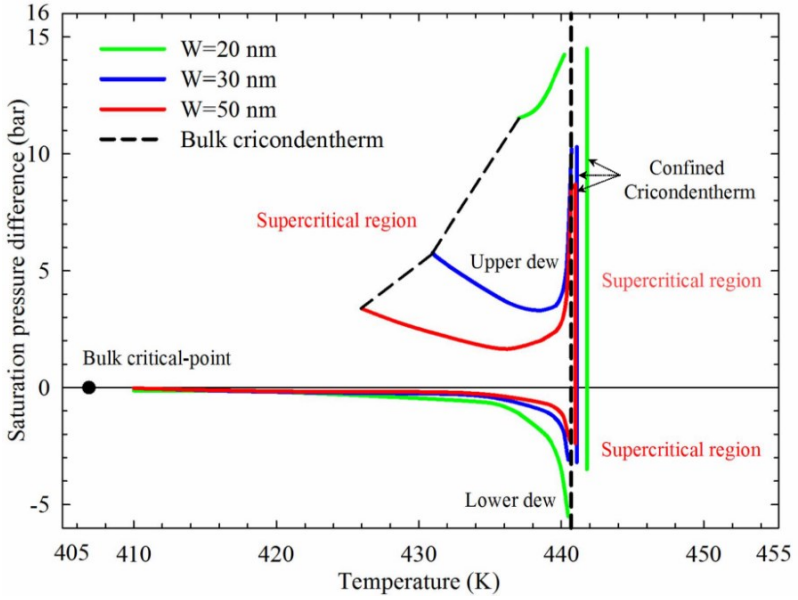

(a)

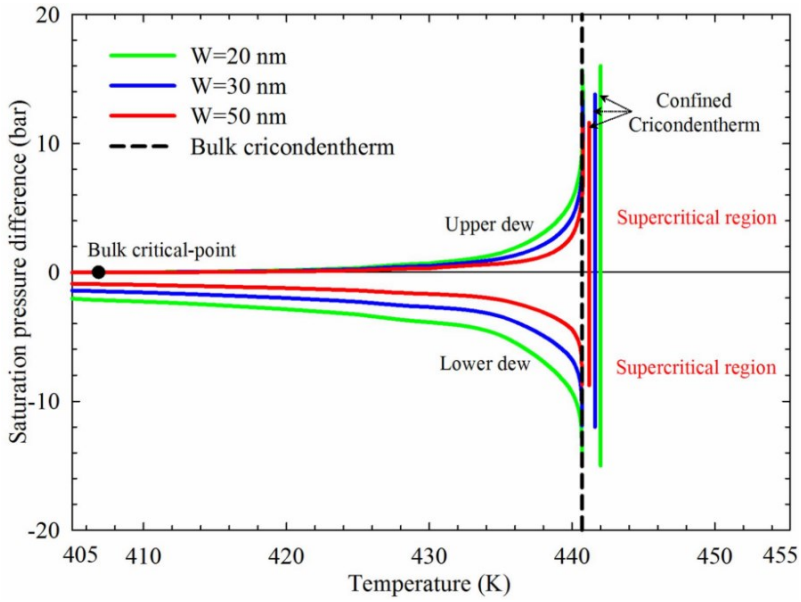

(b)

Figure 2-15 Dew-point pressure differences of C1-nC6 mixture in various nanopores from (a) engineering DFT and (b) PR-EOS with capillary effect model. The confined cricondentherm correspond to the highest temperatures when phase transition in nanopore occurs.

2.6 Conclusions

In this work, we use PR-EOS with capillary pressure model and engineering DFT to study the

phase behavior and critical properties of confined pure hydrocarbon nC_8 and dew-points of hydrocarbon mixture of C_1-nC_6. Engineering DFT, which extends PR-EOS to inhomogeneous conditions using WDA, can faithfully capture vapor-liquid equilibrium in nanopores. By comparing with engineering DFT, the performance of PR-EOS with capillary effect model is evaluated. The specific conclusions can be drawn as follows:

- For pure nC_8, both engineering DFT and PR-EOS with capillary effect model predicts that, at isobaric conditions, as nanopore size increases, the dew-point temperature approaches the bulk saturation temperature. The difference between PR-EOS with capillary effect and engineering DFT on the dew-point temperature decreases as the system pressure approaches the critical pressure. At low pressure conditions, PR-EOS with capillary effect model becomes unreliable.
- Under different isobaric conditions, engineering DFT predicts that the confined dew-point of pure nC_8 approaches the bulk saturation point when pore size is 30 nm, while the PR-EOS with capillary effect model predicts that the confined dew-point approaches the bulk only when the pore size is as large as 1,000 nm. It emphasizes the importance of considering the fluid-surface interactions and surface adsorption for accurately describing the phase behavior of confined fluids.
- Under different isobaric conditions, engineering DFT predicts that the confined lower dew-point of C_1-nC_6 mixture approaches the bulk saturation point when pore size is 20 nm, while for this pore size the upper dew-point shows larger deviation from the bulk value. On the other hand, the dew-point obtained from the PR-EOS with capillary effect model approaches the bulk only when the pore size is as large as 100 nm.

- For the C_1-nC_6 mixture tested, both PR-EOS with capillary effect model and engineering DFT predict that the confined fluids can have phase transition at temperature higher than the cricondentherm point. Engineering DFT also predicts that supercriticality of the upper dew-point can occur when the temperature is lower than a certain point.

Engineering DFT can provide important insights into the phase behavior modeling in unconventional shale reservoir. It can also provide necessary corrections and guidance to the conventional EOS modeling (i.e., correct shifted saturation properties and hysteresis). Engineering DFT can also possibly be coupled into reservoir simulations by obtaining the phase behavior of confined fluids of various composition, pressure, and temperature as priori. Pore size distribution can also affect the phase behavior modeling. There have been some conventional EOS modeling (Wang *et al.* 2016, Luo *et al.* 2017) and Monte Carlo (MC) simulations works (Jin *et al.* 2017) on the effect of pore size distributions on the phase behavior of pure and hydrocarbon mixtures in nanoporous media. However, inhomogeneous density distributions and surface adsorption are still ignored in conventional EOS modeling and MC simulation is greatly hampered by expensive computational cost, especially for heavy hydrocarbons. In addition, based on the SEM imaging, it has been revealed that pore structures in shale may not only be slit-shaped, but also include cylindrical and ink-bottle shapes (de Boer and Lippens 1964, Sing *et al.* 2008). The adsorption-desorption isotherms of hydrocarbons in these shaped pores can be different from the slit-shaped. For example, within ink-bottle model, depending on the pore diameter ratio of "ink" and "bottle", nitrogen adsorption-desorption isotherms may behave differently due to pore-blocking and cavitation effects (Fan *et al.* 2011, Klomkliang *et al.* 2013). In future, we will also explore the effect of pore size distribution and pore geometry on the phase behavior of nano-confined pure and hydrocarbon mixtures.

Nomenclature

$\Omega\left[\{\rho_k(\mathbf{r})\}\right]$ = Grand potential functional

$F\left[\{\rho_k(\mathbf{r})\}\right]$ = Helmholtz free energy functional

μ = Chemical potential

T = Temperature

$d\mathbf{r}$ = Differential volume

$\rho_k(\mathbf{r})$ = Number density distribution of the component k at the position $\mathbf{r}$

$\Psi_k(\mathbf{r})$ = Solid surface external potential of the component k at the position $\mathbf{r}$

k_B = Boltzmann constant

$\rho_{ave,k}$ = Average density of the component k in pores

T_c = Critical temperature

P_c = Critical pressure

ω = Acentric factor

M_w = Molar weight

VSP = Volume shift parameter

ε_g = Attraction energy parameter

P_{cap} = Capillary pressure

γ = Interfacial tension

θ = Contact angle

r = Pore radius

PAC_i = Parachor number of component i

ρ_L = Molar density of liquid phase

ρ_V = Molar density of liquid phase

x_i = Mole fractions of component i in liquid phase

y_i = Mole fractions of component i in vapor phase

f_i^V = Fugacities of component i in vapor phase

f_i^L = Fugacities of component i in liquid phase

P_V = Vapor pressures

P_L = Liquid pressure

T_c^c = Critical temperature of the confined pure component

A = Fitting parameter

η = Characteristic exponent

ρ_c^c = Confined critical density

B = Fitting parameter

P_c^c = Confined critical pressure

C = Fitting parameter

D = Fitting parameter

ρ_{ave} = Average density

W = Pore size

P_{cb} = Bulk critical pressure

P_{cp} = Confined critical pressure

T_{cric} = Bulk cricondentherm

2.7 References

Alfi, M., Nasrabadi, H. and Banerjee, D. 2016. Experimental Investigation of Confinement Effect on Phase Behavior of Hexane, Heptane and Octane Using Lab-on-a-chip Technology. *Fluid Phase Equilibr.* **423**: 25-33.

Alharthy, N. S., Nguyen, T., Teklu, T. *et al.* 2013. Multiphase Compositional Modeling in Small-Scale Pores of Unconventional Shale Reservoirs. Presented at the SPE Annual Technical Conference and Exhibition, New Orleans, Louisiana, USA, 30 September-2 October.

Balbuena, P. B., and Gubbins, K. E. 1993. Theoretical interpretation of adsorption behavior of simple fluids in slit pores. *Langmuir* **9** (7): 1801-1814.

Basaldella, E. I., Tara, J. C., Armenta, G. A. *et al.* 2007. Cu/SBA-15 as Adsorbent for Propane/Propylene Separation. *J. Porous Mat*. **14** (3): 273-278.

Bruot, N., and Caupin, F. 2016. Curvature Dependence of the Liquid-Vapor Surface Tension beyond the Tolman Approximation. *Phys. Rev. Lett*. **116** (5): 056102.

Bui, K., and Akkutlu, I. Y. 2015. Nanopore Wall Effect on Surface Tension of Methane. *Mol. Phys.* **113** (22): 3506-3513.

Cabral, V. F., Alfradique, M. F., Tavares, F. W. *et al.* 2005. Thermodynamic Equilibrium of Adsorbed Phases. *Fluid Phase Equilibr.* **233** (1): 66-72.

Cervilla, A., Corma, A., Fornes, V. *et al.* 1994. Intercalation of $[MoVIO_2(O_2CC(S)Ph_2)_2]_2$-in a Zn (II)-Al (III) Layered Double Hydroxide Host: A Strategy for the Heterogeneous Catalysis of the Air Oxidation of Thiols. *J. Am. Chem. Soc.* **116** (4): 1595-1596.

Civan, F., Devegowda, D., Sigal, R. *et al.* 2012. Theoretical Fundamentals, Critical Issues, and Adequate Formulation of Effective Shale Gas and Condensate Reservoir Simulation. *AIP Conference Proceedings* **1453** (1): 155-160.

de Boer, J. H., and Lippens, B. C. 1964. Studies on Pore Systems in Catalysts II. The Shapes of Pores in Aluminum Oxide Systems. *J. Catal.* **3** (1): 38-43.

Devegowda, D., Sapmanee, K., Civan, F. *et al.* 2012. Phase Behavior of Gas Condensates in Shales Due to Pore Proximity Effects: Implications for Transport Reserves and Well Productivity. Presented at the SPE Annual Technical Conference and Exhibition, San Antonio, Texas, USA, 8-10 October.

Didar, B. R., and Akkutlu, I. Y. 2013. Pore-size Dependence of Fluid Phase Behavior and Properties in Organic-Rich Shale Reservoirs. Presented at the SPE International Symposium on Oilfield Chemistry, The Woodlands, Texas, USA, 8-10 April.

Ebner, C., and Saam, W. F. 1977. New Phase-Transition Phenomena in Thin Argon Films. *Phys. Rev. Lett.* **38** (25): 1486-1489.

Ebner, C., Saam, W. F., and Stroud, D. 1976. Density-functional Theory of Simple Classical Fluids. I. Surfaces. *Phys. Rev. A* **14** (6): 2264-2273.

Fan, C., Do, D. D., and Nicholson, D. 2011. On the Cavitation and Pore Blocking in Slit-Shaped Ink-Bottle Pores. *Langmuir* **27** (7): 3511-3526.

Gasparik, M., Ghanizadeh, A., Gensterblum, Y. *et al.* 2012. The Methane Storage Capacity of Black Shales. *3rd EAGE Shale Wrokshop-Shale Physics and Shale Chemistry*.

Jhaveri, B. S., and Youngren, G. K. 1988. Three-Parameter Modification of the Peng-Robinson Equation of State To Improve Volumetric Predictions. *SPE Reserv. Eng.* **3** (3): 1033-1040.

Jin, B., Bi, R., and Nasrabadi, H. 2017. Molecular Simulation of the Pore Size Distribution

Effect on Phase Behavior of Methane Confined in Nanopores. *Fluid Phase Equilibr.* **452** (Supplement C): 94-102.

Jin, B., and Nasrabadi, H. 2016. Phase Behavior of Multi-component Hydrocarbon Systems in Nano-pores Using Gauge-GCMC Molecular Simulation. *Fluid Phase Equilibr.* **425**: 324-334.

Jin, L., Ma, Y., and Jamili, A. 2013. Investigating the Effect of Pore Proximity on Phase Behavior and Fluid Properties in Shale Formations. Presented at the SPE Annual Technical Conference and Exhibition, New Orleans, Louisiana, 30 September-2 October.

Jin, Z. 2017. Bubble/Dew Point and Hysteresis of Hydrocarbons in Nanopores from Molecular Perspective. *Fluid Phase Equilibr.* **458**: 177-185.

Jin, Z., and Firoozabadi, A. 2016. Phase Behavior and Flow in Shale Nanopores from Molecular Simulations. *Fluid Phase Equilibr.* **430**: 156-168.

Jin, Z., and Firoozabadi, A. 2016. Thermodynamic Modeling of Phase Behavior in Shale Media. *SPE J.* **21** (1): 190-207.

Klomkliang, N., Do, D. D., and Nicholson, D. 2013. On the Hysteresis Loop and Equilibrium Transition in Slit-shaped Ink-bottle Pores. *Adsorption* **19** (6): 1273-1290.

Gelb, L. D., Gubbins, K. E., Radhakrishnan, R. *et al.* 1999. Phase Separation in Confined Systems. *Rep. Prog. Phys.* **62** (12): 1573-1659.

Li, Z., and Firoozabadi, A. 2009. Interfacial Tension of Nonassociating Pure Substances and Binary Mixtures by Density Functional Theory Combined with Peng-Robinson Equation of State. *J. Chem. Phys*. **130** (15): 154108.

Li, Z., Jin, Z., and Firoozabadi, A. 2014. Phase Behavior and Adsorption of Pure Substances and Mixtures and Characterization in Nanopore Structures by Density Functional Theory. *SPE*

J. **19** (6): 1096-1109.

Luo, S., Lutkenhaus, J. L., and Nasrabadi, H. 2016. Confinement-Induced Supercriticality and Phase Equilibria of Hydrocarbons in Nanopores. *Langmuir* **32** (44): 11506-11513.

Luo, S., Lutkenhaus, J. L., and Nasrabadi, H. 2016. Use of Differential Scanning Calorimetry to Study Phase Behavior of Hydrocarbon Mixtures in Nano-scale Porous Media. *J. Petrol. Sci. Eng.* **163**: 731-738.

Luo, S., Lutkenhaus, J. L., and Nasrabadi, H. 2017. Multi-Scale Fluid Phase Behavior Simulation in Shale Reservoirs by a Pore-Size-Dependent Equation of State. Presented at the SPE Annual Technical Conference and Exhibition, San Antonio, USA, 9-11 October.

Luo, S., Nasrabadi, H., and Lutkenhaus, J. L. 2016. Effect of confinement on the bubble points of hydrocarbons in nanoporous media. *AIChE J.* **62** (5): 1772-1780.

Neimark, A. V., and Vishnyakov, A. 2000. Gauge Cell Method for Simulation Studies of Phase Transitions in Confined Systems. *Phys. Rev. E* **62** (4): 4611-4622.

NIST Chemistry WebBook, NIST Standard Reference Database Number 69, National Institute of Standards and technology, Gaithersburg, MD, 20899, http://webbook.nist.gov.

Nojabaei, B., Johns, R. T., and Chu, L. 2013. Effect of Capillary Pressure on Phase Behavior in Tight Rocks and Shales. *SPE Reserv. Eval. Eng.* **16** (3): 281-289.

Parsa, E., Yin, X., and Ozkan, E. 2015. Direct Observation of the Impact of Nanopore Confinement on Petroleum Gas Condensation. Presented at the SPE Annual Technical Conference and Exhibition, Houston, Texas, USA, 28-30 September.

Peng, D. Y., and Robinson, D. B. 1976. A New Two-Constant Equation of State. *Ind. Eng. Chem. Fund.* **15** (1): 59-64.

Robinson, D. B., Peng, D. Y., and Chung, S. Y. K. 1985. The Development of the Peng-

Robinson Equation and Its Application to Phase Equilibrium in A System Containing Methanol. *Fluid Phase Equilibr.* **24** (1-2): 25-41.

Rosenfeld, Y. 1989. Free-energy Model for the Inhomogeneous Hard-sphere Fluid Mixture and Density-Functional Theory of Freezing. *Phys. Rev. Lett.* **63** (9): 980-983.

Rowlinson, J. S., and Swinton, F. L. 1982. Liquids and Liquid Mixtures, London, U.K., Butterworth.

Rowlinson, J. S., and Widom, B. 1982. Molecular Theory of Capillarity, Oxford, U.K., Clarendon.

Sandoval, D. R., Yan, W., Michelsen, M. L. *et al.* 2016. The Phase Envelope of Multicomponent Mixtures in the Presence of a Capillary Pressure Difference. *Ind. Eng. Chem. Res.* **55** (22): 6530-6538.

Santiso, E., and Firoozabadi, A. 2006. Curvature Dependency of Surface Tension in Multicomponent Systems. *AIChE J.* **52** (1): 311-322.

Sapmanee, K. 2011. Effects of pore proximity on behavior and production prediction of gas/condensate, University of Oklahoma.

Sing, K. S. W., Everett, D. H., Haul, R. A. W. *et al.* 2008. Reporting Physisorption Data for Gas/Solid Systems. Handbook of Heterogeneous Catalysis, Wiley-VCH Verlag GmbH & Co. KGaA.

Singh, J. K., and Kwak, S. K. 2007. Surface Tension and Vapor-liquid Phase Coexistence of Confined Square-well Fluid. *J. Chem. Phys.* **126** (2): 024702.

Singh, S. K., Sinha, A., Deo, G. *et al.* 2009. Vapor-Liquid Phase Coexistence, Critical Properties, and Surface Tension of Confined Alkanes. *J. Chem. Phys. C* **113** (17): 7170-7180.

Steele, W. A. 1973. The Physical Interaction of Gases with Crystalline Solids: I. Gas-solid Energies and Properties of Isolated Adsorbed Atoms. *Surf. Sci.* **36** (1): 317-352.

Tan, S. P., and Piri, M. 2015. Equation-of-state Modeling of Confined-fluid Phase Equilibria in Nanopores. *Fluid Phase Equilibr.* **393**: 48-63.

Travalloni, L., Castier, M., Tavares, F. W. *et al.* 2010. Critical Behavior of Pure Confined Fluids from an Extension of the van der Waals Equation of State. *J. Supercrit. Fluid* **55** (2): 455-461.

Travalloni, L., Castier, M., Tavares, F. W. *et al.* 2010. Thermodynamic Modeling of Confined Fluids Using an Extension of the Generalized van der Waals Theory. *Chem. Eng. Sci.* **65** (10): 3088-3099.

Volzone, C. 2007. Retention of Pollutant Gases: Comparison between Clay Minerals and their Modified Products. *Appl. Clay Sci.* **36** (1-3): 191-196.

Walton, J. P. R. B., and Quirke, N. 1989. Capillary Condensation: A Molecular Simulation Study. *Mol. Simulat.* **2** (4-6): 361-391.

Wang, L., Yin, X., Neeves, K. B. *et al.* 2016. Effect of Pore-Size Distribution on Phase Transition of Hydrocarbon Mixtures in Nanoporous Media. *SPE J.* **21** (6): 1981-1995.

Weinaug, C. F., and Katz, D. L. 1943. Surface Tensions of Methane-Propane Mixtures. *Ind. Eng. Chem.* **35** (2): 239-246.

Wongkoblap, A., Do, D. D., Birkett, G. *et al.* 2011. A Critical Assessment of Capillary Condensation and Evaporation Equations: A Computer Simulation Study. *J. Colloid Interf. Sci.* **356** (2): 672-680.

Zhang, Y., Civan, F., Devegowda, D. *et al.* 2013. Improved Prediction of Multi-Component Hydrocarbon Fluid Properties in Organic Rich Shale Reservoirs. Presented at the SPE

Annual Technical Conference and Exhibition, New Orleans, Louisiana, 30 September-2 October.

Zhong, J., Zandavi, S. H., Li, H. *et al.* 2017. Condensation in One-Dimensional Dead-End Nanochannels. *ACS Nano.* **11** (1): 304-313.

CHAPTER 3 COMPETITIVE ADSORPTION BEHAVIOR OF HYDROCARBON(S)/CO_2 MIXTURES IN A DOUBLE-NANOPORE SYSTEM USING MOLECULAR SIMULATIONS

A version of this chapter will be submitted to *Journal of Industrial & Engineering Chemistry Research*.

Abstract

CO_2 injection into shale reservoirs has been recently proposed as a promising method that can be used to enhance hydrocarbon recovery from shale reservoirs. Adsorption behavior of hydrocarbon(s)/CO_2 mixtures under shale-reservoir conditions plays an important role in affecting the efficiency of CO_2-enhanced hydrocarbon recovery from shale. In organic pores residing in shale reservoirs, the adsorption behavior of hydrocarbon(s)/CO_2 mixtures can be significantly affected by the strong fluid/pore-wall interactions. In this work, a double-nanopore system comprising of two pores with sizes of 1 nm and 3 nm is built; then the competitive adsorption behavior of hydrocarbon(s)/CO_2 mixtures (i.e., C_1/nC_4, C_1/CO_2, nC_4/CO_2, and C_1/nC_4/CO_2 mixtures) is investigated in this double-nanopore system using the molecular dynamic (MD) simulations. Firstly, the competitive adsorption behavior of C_1/nC_4 mixture in double-nanopore system is studied with a depressurization manner. The effects of pressure and pore size distribution on competitive adsorption between hydrocarbons and CO_2 are discussed. To investigate the efficiency of CO_2 in replacing C_1 or nC_4 molecules from organic pores, dynamic distribution characteristics of C_1/CO_2, nC_4/CO_2, and C_1/nC_4/CO_2 mixtures in the double-nanopore system are further investigated. The competitive adsorption behavior of C_1/nC_4 mixture indicates that, in both nanopores, as pressure decreases, adsorption of lighter hydrocarbon (i.e., C_1) decreases significantly, but adsorption of heavier component (i.e., nC_4) increases slightly. It suggests that as pressure decreases, the lighter hydrocarbons can be easily extracted from nanopores, while the heavier hydrocarbons may not be readily produced. Adsorption behavior of C_1/CO_2 indicates that CO_2 can help the C_1 recovery from nanopores; meanwhile, the recovery efficiency in the larger pore, (i.e., 3 nm), is much higher than that in the smaller pore (i.e., 1 nm). On the contrary, as pressure decreases, adsorption of nC_4 in nC_4/CO_2

mixtures in both nanopores is becoming stronger with the presence of CO_2; the same behavior is also observed for $C_1/nC_4/CO_2$ mixture. This implies that, although CO_2 injection may help the recovery of lighter hydrocarbons (e.g., C_1), but may not be an efficient agent for the recovery of heavier hydrocarbons (e.g., nC_4).

Keywords: Competitive adsorption; Molecular dynamics simulations; Pore size distribution; Hydrocarbon recovery; CO_2 injection

3.1 Introduction

Shale oil/gas resources, as one kind of unconventional hydrocarbon resource, have been attracting global attention in recent years due to their considerable abundance [1-5]. However, the unique characteristics of shale reservoirs, such as extremely low permeability and heterogeneity, make it difficult to recover shale resources from such reservoirs [6]. Unlike conventional reservoirs, pores in shale matrix are generally in the nanometer range. In nanopores, the fluid-pore surface interactions are significant, leading to strong adsorption of components on the pore surface. Moreover, individual components generally exhibit different levels of adsorption capacity on the pore surface, resulting in the competitive adsorption phenomenon [7]. Understanding of the competitive adsorption of fluids in shale is of critical importance for more accurately determining the macroscopic and microscopic distribution of fluids in shale reservoirs as well as the mechanisms governing the fluid transport in shale reservoirs.

A number of theoretical methods have been employed to study the adsorption behavior of fluid on shale. Langmuir adsorption model and Brunnauer-Emmet-Teller (BET) method were initially adopted to describe the adsorption behavior in shale media [8-13]. Although the Langmuir model

with tuned parameters can give a satisfying match with experimental data, this model is derived from the assumption that the fluid molecules form single-adsorption layer on pore surface, while the remaining molecules distribute in pores homogeneously [14]. Moreover, the single adsorption-layer assumption may not be valid in nanopores. It has been found that molecules can exhibit multi-layered adsorption on pore surface due to the strong interactions between molecules and pore surface [14]. The BET model is proposed under the assumption that the fluid molecules can form an infinite number of adsorption layers, while it still assumes homogeneous fluid distributions by neglecting the fluid-pore surface interactions [14]. The ideal adsorbed solution theory (IAST) was proposed to estimate the mixture adsorption in porous media, with which the single-component adsorption data is solely used to obtain the multicomponent adsorption isotherms [15-16]. However, this method only works well for ideal systems [17].

The grand canonical Monte Carlo (GCMC) simulations [18-22], density functional theory (DFT) [23-25], and molecular dynamics (MD) simulations [26-27] have been recently adopted to study the adsorption of fluids in nano-scale pores. These statistical thermodynamic approaches can explicitly consider the fluid-pore surface interactions and have shown excellent agreement with the experimental data on gas adsorption and interfacial phenomena [28-29]. On the basis of the calculations made with molecular simulation methods, density distribution of molecules in nanopores is heterogeneous: near the pore surface, the density is significantly higher than that in the pore center, while the density in pore center approaches the density in bulk [30]. But these existing molecule-based models use a single pore size to describe the adsorption behavior. However, in shale reservoirs, the sizes of nanopores are generally not uniform, exhibiting different pore size distributions in different parts of the reservoir. Thereof, to better understand the adsorption of fluids in nanopores, the effect of pore size distribution should be considered.

Injection of CO_2 into shale reservoirs has been proposed as a promising method that can not only enhance shale oil/gas recovery but also sequestrate CO_2 in shale reservoirs [31-35]. Since C_1 is generally the dominant component in shale fluids, studies regarding enhancing C_1 recovery with CO_2 are mostly conducted. Recently, experimental measurements at the laboratory scale are conducted to investigate the adsorption behavior of C_1/CO_2 mixtures on shale rocks [36-43]. It is found that CO_2 has a higher adsorption capacity than C_1, indicating that CO_2 injection can be an effective method for enhancing shale C_1 recovery in shale reservoirs. Numerical simulations have also been conducted to validate the feasibility of this technique [44-61]. Results of these numerical studies indicated that CO_2 injection into depleted shale gas reservoirs for enhanced gas recovery is technically feasible. Although these studies can provide us some insights on the competitive adsorption behaviors of C_1/CO_2 mixtures, the effect of the presence of CO_2 on the recovery of heavier hydrocarbons is scarcely studied. Recently, Jin and Firoozabadi [23] investigated the competitive adsorption of nC_4/CO_2 mixture in organic pores, finding that using CO_2 to recover nC_4 from organic pores is more significant at high pressure conditions. However, again, this study only investigates adsorption behavior in single nanopore without the consideration of pore size distribution.

The study on adsorption behavior of hydrocarbon(s)/CO_2 mixtures in shale is still at a preliminary stage. In this study, we built a double-nanopore system comprising of two pores with different pore sizes and investigate the competitive adsorption behavior of hydrocarbon(s)/CO_2 mixtures in this double-nanopore system using the MD method. The adsorption behavior of hydrocarbon(s)/CO_2 mixtures is studied with a depressurization method.

3.2 Methodology and Simulation Model

3.2.1 Molecular Dynamic Simulation

In this work, we employ the Forcite Module Package in the MATERIAL STUDIO software [62-65]. Within the MD simulations, the condensed-phased-optimized molecular potential for atomistic simulation studies (COMPASS) force field is applied to describe the interatomic interactions in the Force Module. The COMPASS force field has been recognized as the first force-field that can make an accurate simultaneous prediction for wide ranges of molecules, including polymers [65-66]. In the COMPASS force field, the total potential energy (E^{total}) is given as [66]:

$$E^{total} = E^{internal} + E^{cross-coupling} + E^{vanderWaals} + E^{electrostatic} \tag{3-1}$$

$$E^{internal} = \sum E^{(b)} + \sum E^{(\theta)} + \sum E^{(\phi)} + \sum E^{(\gamma)} \tag{3-2}$$

$$E^{cross-coupling} = \sum E^{(b\theta)} + \sum E^{(b\phi)} + \sum E^{(b'\phi)} + \sum E^{(\theta\theta')} + \sum E^{(\theta\phi)} + \sum E^{(\theta\theta'\phi)} \tag{3-3}$$

where b and b' represent the lengths of two adjacent bonds, respectively; θ and θ' represent the angles between two adjacent bonds, respectively; ϕ is the angle resulted from dihedral torsion; and γ represents the out of the plane angle [65]. $E^{internal}$ is the energy derived from each of the internal valence coordinates; $E^{cross-coupling}$ is the summation of the cross-coupling terms between internal coordinates. $E^{vanderWaals}$ is the summation of attractive and repulsive Lennard-Jones terms [67]. Based on the atom-based method, we can obtain the $E^{vanderWaals}$ and $E^{electrostatic}$ with a cutoff distance of 12.5 Å and an initial charge of 0 [68]. Additionally, the Andersen thermostat [69] is used for temperature conversion.

3.2.2 Simulation Model

Carbon materials have been widely used to simulate kerogen in shale considering that kerogen is hydrophobic [14, 23]. In this work, the full atomistic structure of graphite layers is applied to simulate the organic pores. The graphic layers are formed by carbon atoms. As shown in **Figure 3-1**, two carbon-slit pores are placed in parallel and are connected by a space with given volume. The graphene layers located in the left-hand of the pore system create a confined space (which can represent organic pores in shale), while the space in the right-hand of the pore system corresponds to a bulk space (which can represent a micro-fracture). Overall, this double-nanopore system consists of three regions, i.e., the 1-nm pore, the 3-nm pore, and a bulk space connecting the two pores. As for this pore system, the periodic boundary condition is applied in all three directions. In this simulation box, four graphic layers are used to form one carbon sheet and three carbon sheets are used to construct the two carbon-slit pores. In this pore system, the separation between two carbon-atom centers residing in the two graphite layers is 0.335 nm. **Figure 3-2** presents the schematic of the carbon sheet. As shown in Figure 3-2, in the same graphite layer, the distance between two adjacent carbon-atom centers is 0.142 nm. During the simulation, the position of carbon sheets is fixed. The size of the simulation box is $(L_c + L_b)$ nm × 3.69 nm × $(4 + 5W_c)$ nm in the x, y, and z directions, respectively (L_c represents the length of the two pores, 6.619 nm; L_b represents the length of the connecting space; and W_c represents the separation between the two carbon-atom centers in the two graphite layers, 0.335 nm).

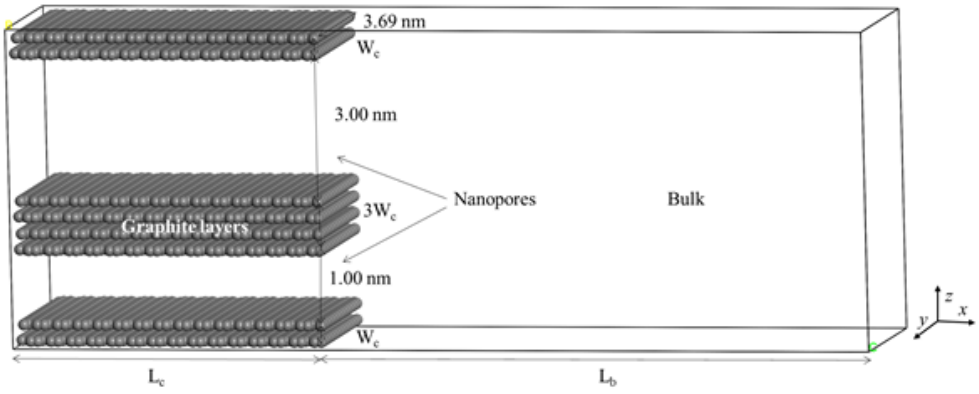

Figure 3-1 Schematic of the double-pore system.

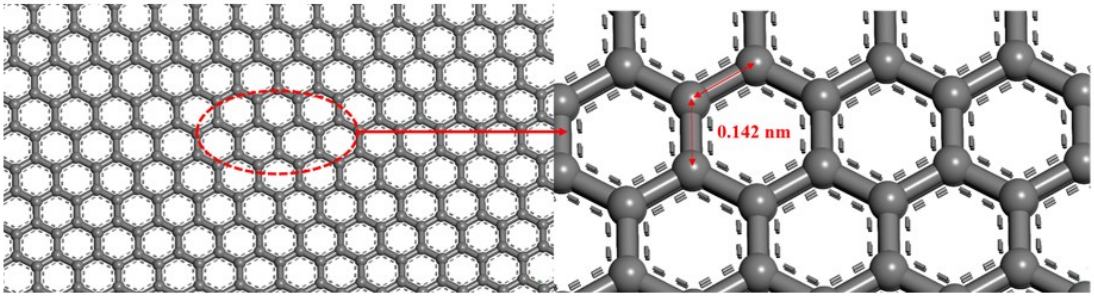

Figure 3-2 Schematic of the carbon sheet in the x-y plane view.

MD simulations are performed in the canonical *NVT* ensemble; such an ensemble has fixed number of particles (*N*), volume (*V*), and temperature (*T*). We initially load a mixture composed of given number of molecules in the *NVT* ensemble. The pressure of the system is decreased by increasing the length of the bulk space. In this study, three pressure conditions (i.e., 3.97 MPa, 5.66 MPa, and 7.94 MPa) are created by changing L_b to be 3.322 nm, 11.381 nm, and 26.381 nm, respectively. Based on the known system volume, system temperature and mole numbers of the molecules in the system, we calculate the system pressure using Peng-Robinson equation of state (1978) [70]. The basic inputs used for MD simulations are summarized in **Table 3-1**.

Table 3-1 Summary of the parameter values used in the MD simulations.

Mixtures	Molar fraction	Simulation pressure (MPa)	Simulation time (ns)	Simulation temperature (K)
C_1/nC_4	0.7:0.3	3.97, 5.66, 7.94	35	333.15
C_1/CO_2	0.5:0.5	3.97, 5.66, 7.94	35	333.15
nC_4/CO_2	0.5:0.5	3.97, 5.66, 7.94	35	333.15
$nC_4/C_1/CO_2$	0.15:0.35:0.5	3.97, 5.66, 7.94	35	333.15

When placed in this pore system, C_1, nC_4, and CO_2 molecules in the C_1/nC_4, C_1/CO_2, and nC_4/CO_2 mixtures generally display competitive adsorption on pore surface at given temperature and pressure conditions. In this work, we use selectivity coefficient to characterize the competitive adsorption of C_1, nC_4, and CO_2 molecules in organic pores [52]. As for binary mixtures, the selectivity coefficient ($S_{A/B}$) is defined as [52],

$$S_{A/B} = \frac{(x_A / x_B)}{(y_A / y_B)} \tag{3-4}$$

where A and B are the species in binary mixtures; x_A and x_B are the molar fractions of adsorbates A and B in the adsorbed phase, respectively; y_A and y_B are the molar fractions of adsorbates A and B in the space connecting two pores, respectively. If $S_{A/B}$ is less than 1, it indicates that the adsorption capacity of A is lower than that of B; that is, B is easier to adsorb on pore surface than A [71].

3.3 Results and Discussion

In this section, we first show the dynamic distributions of C_1/nC_4, C_1/CO_2, nC_4/CO_2, and $nC_4/C_1/CO_2$ mixtures in the double-nanopore system at a given temperature (T) of 333.15 K. The dynamic distributions of species in the double-nanopore system are studied at three different pressure conditions. Then, adsorption selectivity of individual components in binary mixtures of C_1/nC_4, C_1/CO_2, and nC_4/CO_2 is calculated to compare the adsorption capacity on organic pore

surface. Finally, we analyze the replacement of C_1 and nC_4 molecules by CO_2 in the nanopores.

3.3.1 Adsorption Behavior of Mixtures in the Double-nanopore System

1) Competitive adsorption behavior of C_1/nC_4 mixture. Figure 3-3 presents the density profiles of C_1/nC_4 mixture (70 mol%:30 mol%) in the two pores at T=333.15 K and three different pressures. Near the pore wall, the *in-situ* density of C_1 and nC_4 molecules is much higher than that at the pore center, indicating the formation of adsorption layers near the pore wall. The density of C_1 and nC_4 molecules at the pore center of 1 nm pore is significantly higher than the density at the center of 3 nm pore. In smaller pores, the adsorbed molecules at the pore center become tighter due to the enhanced association forces from both sides of the pore, leading to the much higher density at the central location of the pore [71-73]. Compared to C_1, nC_4 molecules tend to more readily saturate the nanopores due to the stronger surface attractions, resulting in higher adsorption densities in the adsorption layers. It indicates that nC_4 molecules have a higher adsorption capacity on organic pore surface than C_1 molecules. This observation agrees well with the previous experimental measurements [73].

In the 3 nm pore, C_1 molecules form one stronger adsorption layer and the second relatively weaker layers. We observe that the adsorption density of C_1 molecules in the second adsorption layer is slightly lower than that in the first adsorption layer. However, adsorption density of the second adsorption layer formed by nC_4 molecules is much lower than that of the first stronger adsorption layer. C_1 molecule has a smaller molecular diameter than nC_4, which results in that the adsorption layer formed by C_1 molecules stay much closer to pore surface than that formed by nC_4 molecules. In the 1 nm pore, in addition to being adsorbed on the pore surface, many C_1 molecules are highly packed at the pore center, while fewer nC_4 molecules stay at the pore center; this behavior is probably caused by the competitive adsorption between C_1 and nC_4

molecules on organic pore surface.

As pressure drops, C_1 adsorption decreases in both pores, but nC_4 adsorption becomes stronger in both pores. It is because as pressure decreases, a significant amount of C_1 molecules are released and more spare space is created, rendering nC_4 molecules being with stronger affinity to the pore surface at lower pressures. It thus causes the enhanced adsorption of nC_4 in organic pores as pressure decreases. In previous studies [74-75], similar trend has also been found for other adsorbate materials, such as zeolites and pillared layered materials. These results imply that as reservoir pressure decreases during production, lighter components are more readily produced, while the heavier components tend to stay within nanopores and become difficult to be recovered.

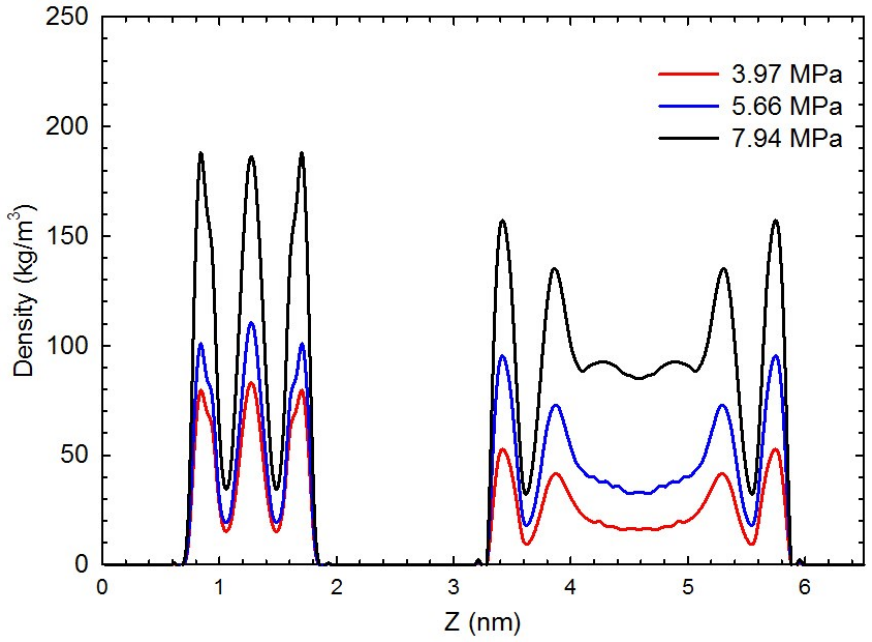

(a)

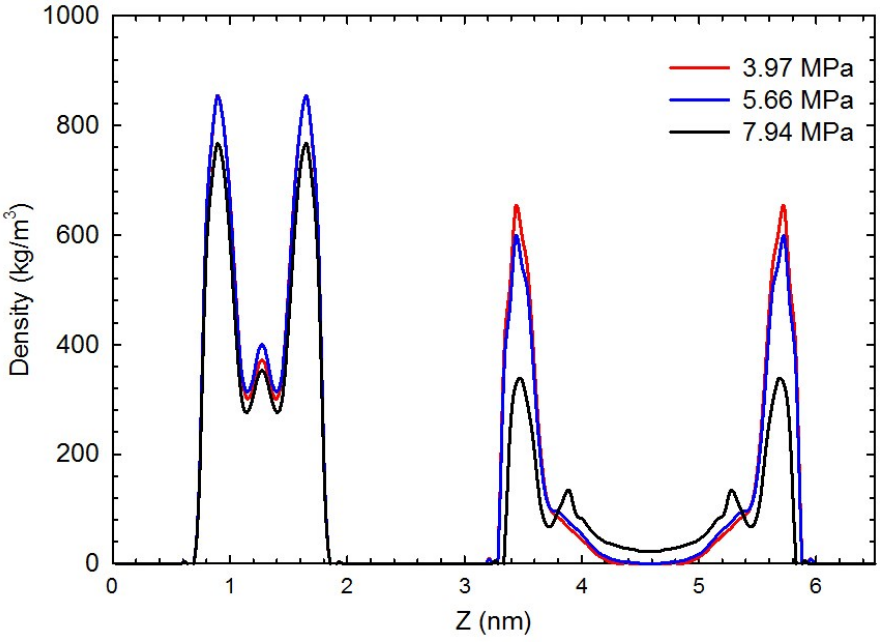

(b)

Figure 3-3 Density profiles of (a) C_1 and (b) nC_4 molecules in C_1/nC_4 (70 mol%:30 mol%) mixture in 1 nm and 3 nm pores at 333.15 K and three different pressures.

2) Competitive adsorption behavior of C_1/CO_2 mixture. In **Figure 3-4**, we present the density distributions of an equimolar mixture of C_1/CO_2 in the two nanopores at 333.15 K and three different pressures. Compared to CO_2, C_1 molecules exhibit a more pronounced second

adsorption layer under the same pressure. It was found that the second adsorption layer is caused by the clustering of molecules [76]. Therefore, the clustering of C_1 molecules should be much stronger than that of CO_2 molecules, which enhances the adsorption of C_1 molecules in the second adsorption layer.

As pressure drops, density of C_1 in the adsorption layers as well as at the pore center decreases in both nanopores. A similar trend is also observed for CO_2 molecules. Compared to C_1, the density decrement of CO_2 due to pressure drop is less pronounced. Adsorption capacity of species highly correlates with the system pressure: adsorption capacity is generally lowered as pressure decreases. When pressure is lowered, the previously adsorbed C_1 and CO_2 molecules are released from pore surface. With the release of the adsorbed molecules, more adsorption sites are liberated, which, on the other hand, enhances the adsorption capacity of other species. Therefore, the competitive adsorption between C_1 and CO_2 is mainly affected by the coupling effects of pressure and the liberated adsorption sites due to desorption. This coupling effect leads to a relatively less pronounced decrease in the density of the CO_2 adsorption layer.

At 7.94 MPa, we place pure C_1 molecules in the double-nanopore system and obtain the density profiles in the two pores at 333.15 K. We observe that the *in-situ* density of pure C_1 in the double-nanopores is significantly higher than that of C_1 in C_1/CO_2 mixture. CO_2 has stronger adsorption capacity than C_1 on the organic pore surface; thereby, when CO_2 is introduced into the organic pores, C_1 can be replaced by CO_2, especially in the 1 nm pore. Based on this finding, it can be inferred that CO_2 injection is helpful for C_1 recovery from organic pores.

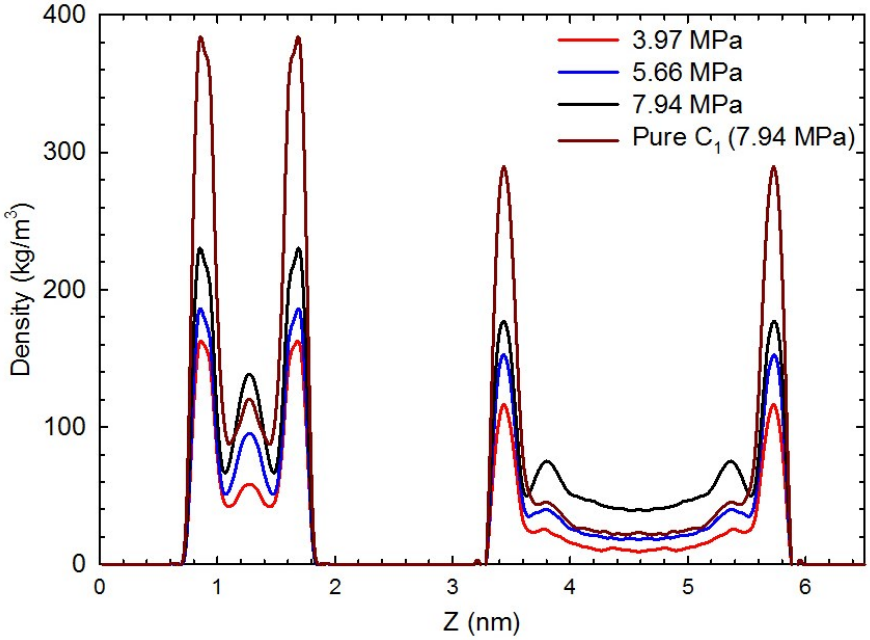

(a)

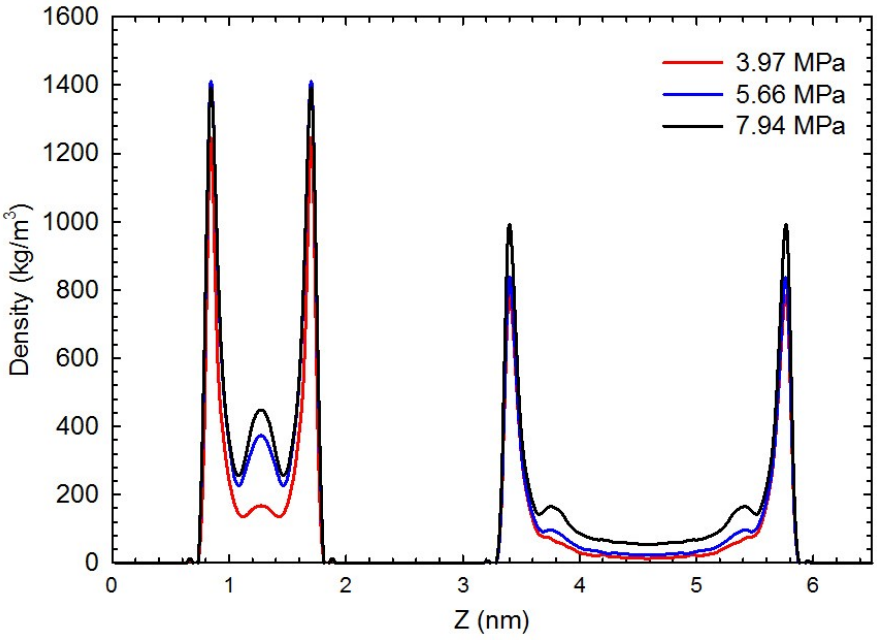

(b)

Figure 3-4 Density profiles of (a) C_1 and (b) CO_2 molecules in C_1/nC_4 mixture (50 mol%:50 mol%) in 1 nm and 3 nm pores at 333.15 K and three different pressures.

3) Competitive adsorption behavior of nC_4/CO_2 mixture. Figure 3-5 presents the density profiles of nC_4 and CO_2 in an equimolar mixture of nC_4/CO_2 mixture in the double nanopores at 333.15 K and three different pressures. nC_4 and CO_2 molecules have multi-layer adsorption in

the 3 nm pore; this observation is in line with the previous study conducted in single pores [23]. However, in the 1 nm pore, nC$_4$ and CO$_2$ molecules exhibit single-layer adsorption; meanwhile, the density at the pore center is high due to the packing effect. Moreover, the adsorption density of nC$_4$ in the equimolar nC$_4$/CO$_2$ mixture is significantly higher than CO$_2$, indicating its stronger adsorption capacity than CO$_2$. Figure 3-5 also presents the density profile of pure nC$_4$ in the double-nanopores at 7.94 MPa. We can observe that density of the adsorption layer of pure nC$_4$ is higher than that of nC$_4$ in the nC$_4$/CO$_2$ mixture in both nanopores, especially in the 1 nm pore. That is, with the presence of CO$_2$, adsorption of pure nC$_4$ is reduced due to the competitive adsorption between nC$_4$ and CO$_2$ molecules on pore surface.

As pressure decreases, density of the adsorption layer of CO$_2$ in the nC$_4$/CO$_2$ mixture decreases. Interestingly, density of the adsorption layer of nC$_4$ in nC$_4$/CO$_2$ mixture increases as pressure drops. When pressure decreases, CO$_2$ molecules desorb from the organic pores surface, liberating more adsorption sites on the pore surface. Although a decrease in the system pressure weakens the adsorption of nC$_4$, adsorption of nC$_4$ is enhanced as more liberated adsorption sites are created due to CO$_2$ desorption. It thereby results in an increasing adsorption of nC$_4$ molecules in nanopores as pressure decreases. Thereby, when CO$_2$ is introduced, it may not be effective to use the depressurization approach to recover nC$_4$ from organic pores.

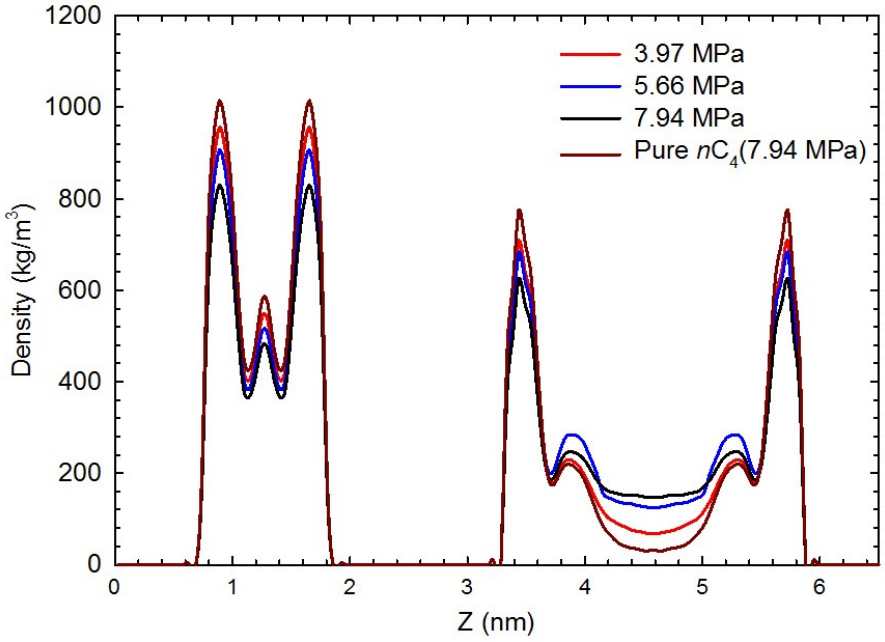

(a)

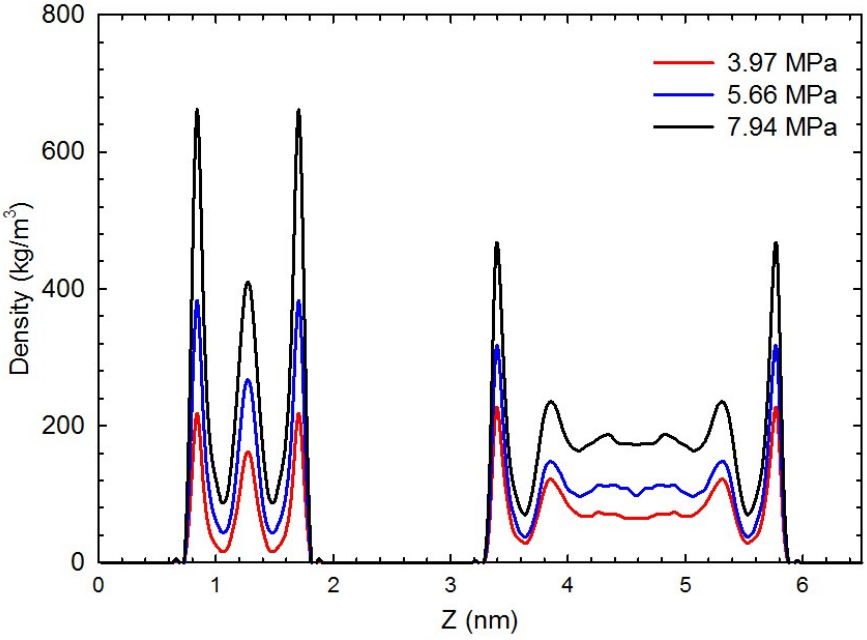

(b)

Figure 3-5 Density profiles of (a) nC_4 and (b) CO_2 molecules in nC_4/CO_2 mixture (50 mol%:50 mol%) in 1 nm and 3 nm pores at 333.15 K and three different pressures.

In **Figure 3-6**, we show the snapshots of molecular distributions of CH_4/CO_2 (50 mol%:50 mol%) and nC_4/CO_2 (50 mol%:50 mol%) mixtures in the double-pore system at 333.15 K and at 5.66 MPa. As shown in Figure 3-6 (a), when CO_2 molecules are introduced into the double-nanopore

system which is initially saturated with C_1, CO_2 molecules strongly adsorb on the pore surface due to the interactions between CO_2 and pore surface. On the contrary, C_1 molecules are replaced by CO_2 molecules and mainly appear in the pore center and the bulk space. We also observe that molecules are packed more tightly in the 1 nm pore than that in the 3 nm pore due to the confining effect. In Figure 3-6 (b), we introduce CO_2 molecules into the double-nanopore system which is initially saturated with nC$_4$ molecules. Compared to CH_4/CO_2 mixture, CO_2 molecules in the nC$_4$/CO_2 mixture mainly appear in the pore center and the bulk space. Based on the above results, we can infer that the introduction of CO_2 to C_1-rich shale reservoirs can result in a relatively higher concentration of C_1 in the bulk space than in the nanopores. In comparison, the introduction of CO_2 to nC$_4$-rich shale reservoirs can result in a relatively higher concentration of CO_2 in the bulk space than in the nanopores. The higher concentration of the lighter component in the bulk space tends to yield a higher bubble point or dew point for the fluids in the bulk space.

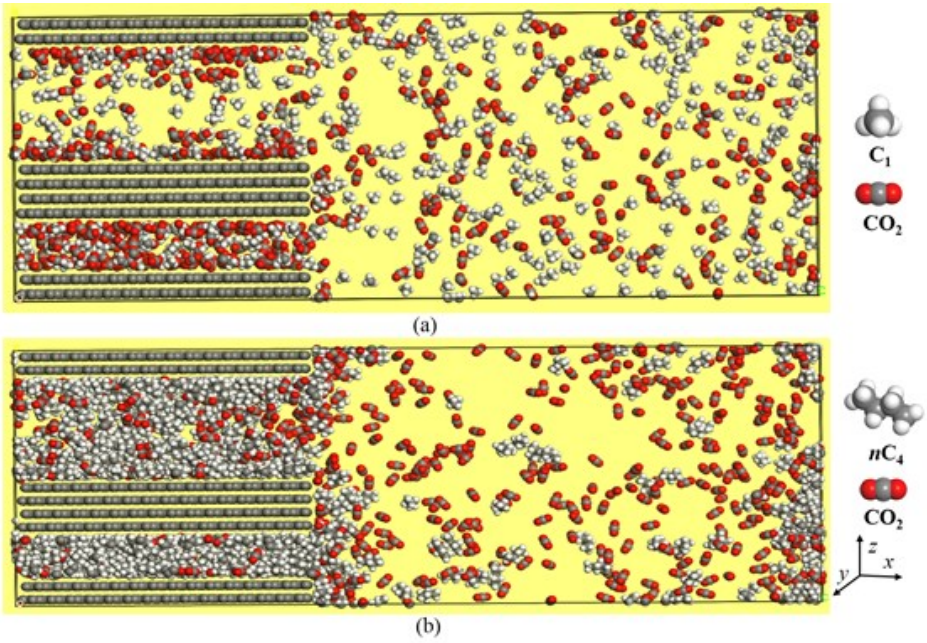

Figure 3-6 Snapshots of the molecule distributions of (a) CH_4/CO_2 (50 mol%:50 mol%) and (b) nC$_4$/CO_2 (50 mol%:50 mol%) mixtures in the double-nanopore system at 333.15 K and 5.66 MPa.

4) Competitive adsorption behavior of $C_1/nC_4/CO_2$ mixture. In this subsection, we further investigate the competitive adsorption behavior of $C_1/nC_4/CO_2$ mixture in the double-nanopore system based on the consideration that fluid in shale reservoirs generally comprises of multiple hydrocarbons. **Figure 3-7** presents the density profiles of C_1, nC_4, and CO_2 in $C_1/nC_4/CO_2$ mixture (35 mol%:15 mol%:50 mol%) in the two nanopores at 333.15 K and three different pressures. As shown in Figure 3-7, CO_2 exhibits the strongest adsorption capacity in both pores, followed by nC_4 and C_1. The higher adsorption capacity of CO_2 than nC_4 is mainly caused by the dominance of CO_2 molecules in the $C_1/nC_4/CO_2$ mixture. As observed from Figure 3-7 (b), nC_4 in the $C_1/nC_4/CO_2$ mixture mainly adsorb on the pore surface, exhibiting single-layer adsorption. However, C_1 and CO_2 molecules can form a second weaker adsorption layer in addition to the first stronger adsorption layer. The different adsorption behavior is resulted from the competitive adsorption capacity among C_1, nC_4, and CO_2 molecules on the organic pore surface. As pressure decreases, a significant reduction in the adsorption density is observed for C_1 and CO_2 molecules. Interestingly, as pressure decreases, adsorption density of nC_4 in the 3 nm pore is almost unchanged, while adsorption density of nC_4 in the 1 nm pore is enhanced. During depressurization, C_1 and CO_2 molecules can be suddenly released from nanopores, but nC_4 would not be produced from organic pores. It further validates the former findings that CO_2 can efficiently recover C_1 from organic pores, but tends to be less efficient for enhancing nC_4 recovery.

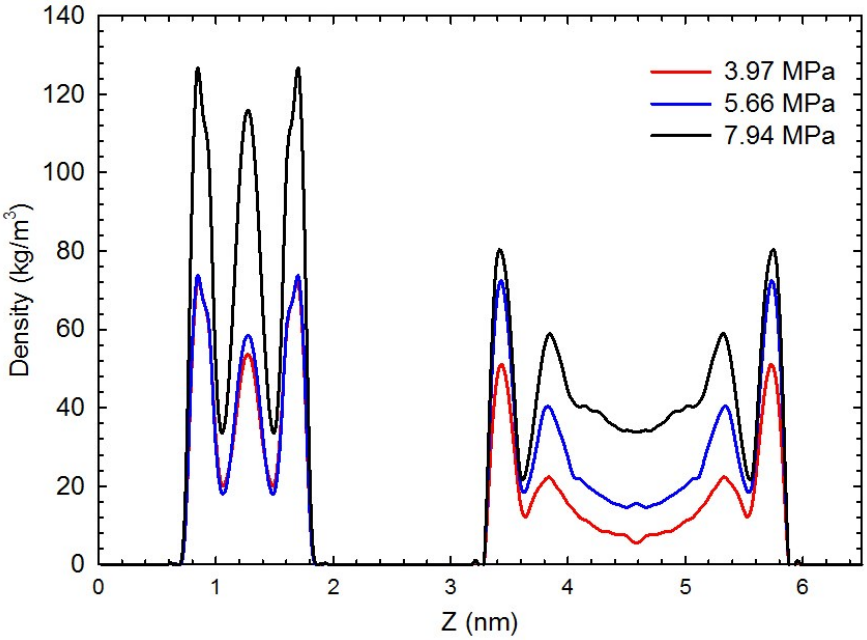
3.97 MPa
5.66 MPa
7.94 MPa
Density (kg/m3)
Z (nm)
0
20
40
60
80
100
120
140
0
1
2
3
4
5
6

(a)

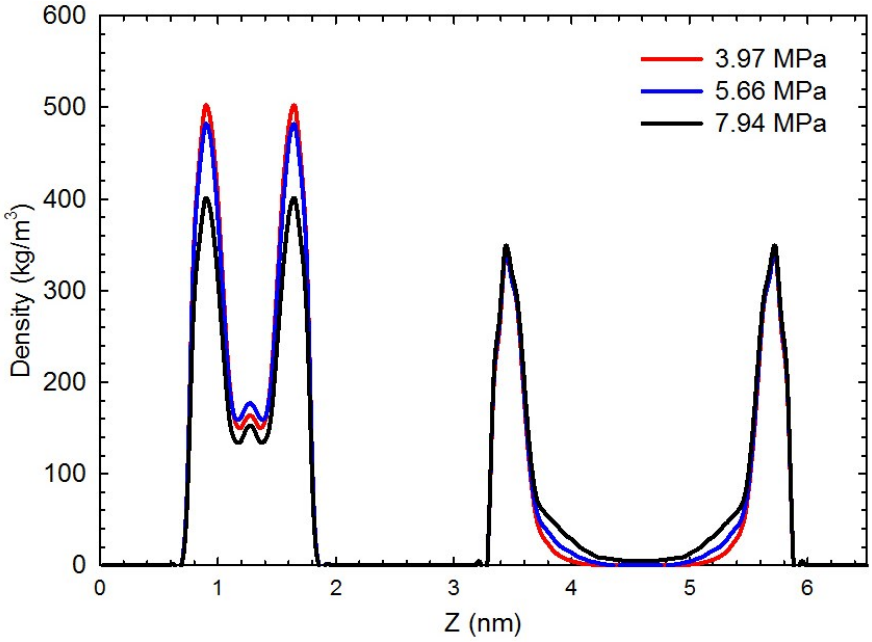
3.97 MPa
5.66 MPa
7.94 MPa
Density (kg/m3)
Z (nm)
0
100
200
300
400
500
600
0
1
2
3
4
5
6

(b)

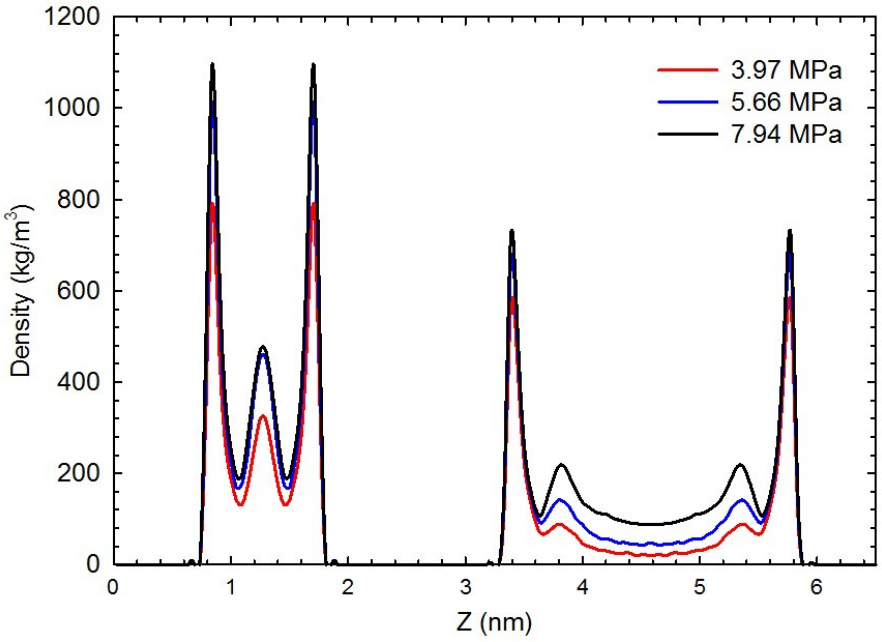

(c)

Figure 3-7 Density profiles of (a) C_1, (b) nC_4, and (c) CO_2 molecules in $C_1/nC_4/CO_2$ (35 mol%:15 mol%:50 mol%) mixture in 1 nm and 3 nm pores at 333.15 K and three different pressures.

3.3.2 Adsorption Selectivity of Species in Organic Pores

Figures 3-8 to 3-10 show the adsorption selectivity of nC_4 over C_1 (in the C_1/nC_4 mixture), C_1 over CO_2 (in the C_1/CO_2 mixture), and nC_4 over CO_2 (in the CO_2/nC_4 mixture) in the 1 nm and 3 nm pores, respectively. As shown in Figure 3-8, adsorption selectivity of nC_4 over C_1 is always higher than 1, suggesting that adsorption capacity of nC_4 on organic pore surface is stronger than that of C_1. This is due to the fact that nC_4 molecules have stronger affinity to the organic surface than C_1 as pressure decreases. In both pores, the adsorption selectivity of both C_1 and nC_4 increases as pressure decreases. Moreover, we observe that adsorption selectivity for either C_1 or nC_4 in the 1 nm pore is always higher than that in the 3 nm pore.

Figure 3-9 shows that the adsorption selectivity of C_1 over CO_2 is always lower than 1, indicating that CO_2 molecule has stronger adsorption capacity on pore surface than C_1 molecule. In the 3 nm pore, adsorption selectivity first increases and then decreases with a decreasing

pressure. This observation is in line with the findings by Kurniawan *et al.* [52]. However, in the 1 nm pore, adsorption selectivity initially decreases to a minimum value and then increases with a decreasing pressure. As shown in Figure 3-10, the adsorption selectivity of nC_4 over CO_2 is always higher than 1; it suggests that adsorption capacity of nC_4 is stronger than CO_2. Again, the adsorption selectivity in the 1 nm pore is observed to be higher than that in the 3 nm pore.

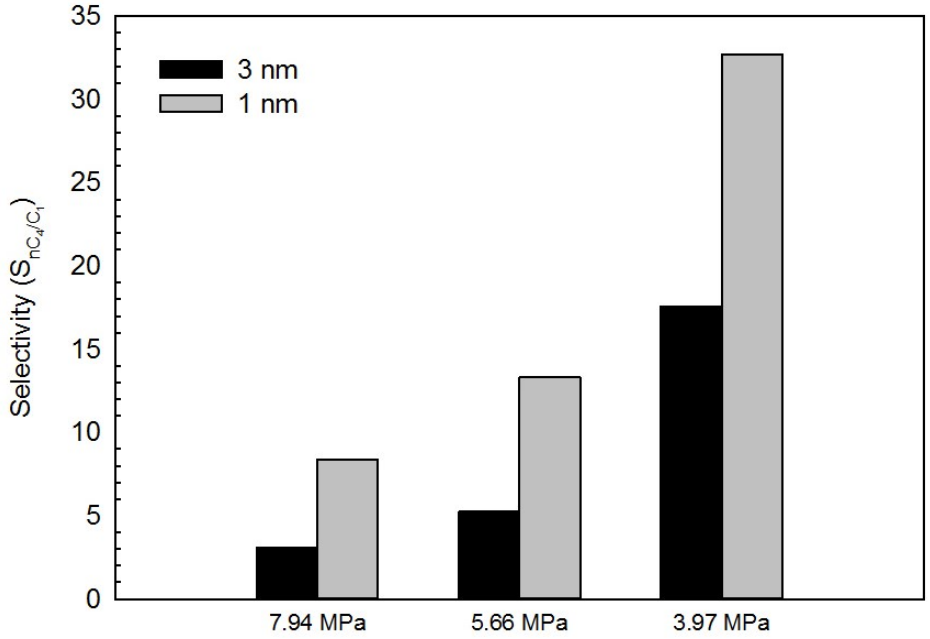

Figure 3-8 Adsorption selectivity of nC_4 over C_1 (in the C_1/nC_4 mixture) at different pressures in 1 nm and 3 nm pores.

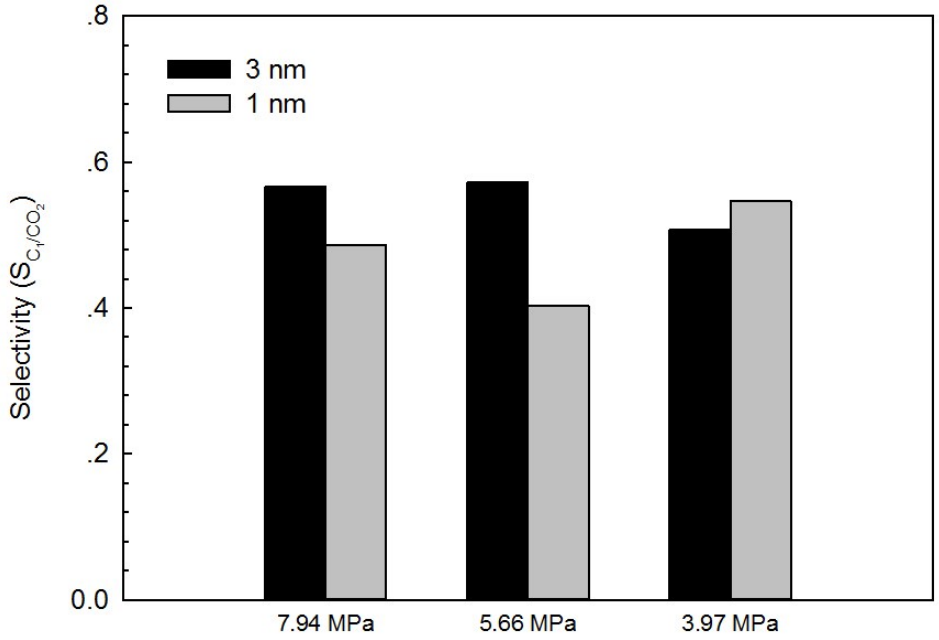

Figure 3-9 Adsorption selectivity of C_1 over CO_2 (in the C_1/CO_2 mixture) at different pressures in 1 nm and 3 nm pores.

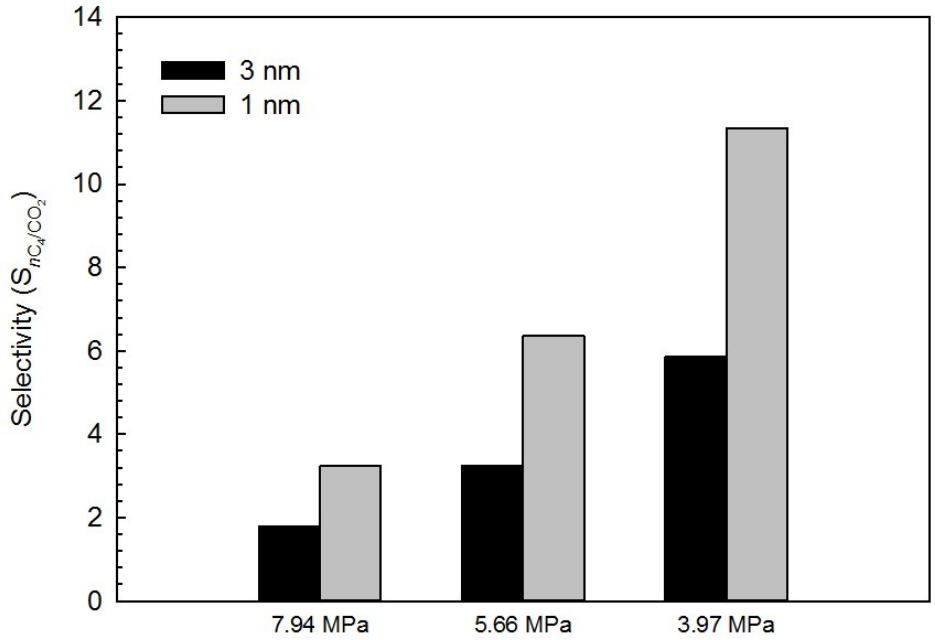

Figure 3-10 Adsorption selectivity of nC_4 over CO_2 (in the CO_2/nC_4 mixture) at different pressures in 1 nm and 3 nm pores.

3.3.3 Replacement of C_1 and nC_4 from Nanopores with CO_2 Injection

In order to see how CO_2 effectively replaces C_1 and nC_4 from organic nanopores, we calculate the molar fractions of C_1 and nC_4 in the C_1/CO_2 and nC_4/CO_2 mixtures in the 1 nm and 3 nm pores at different pressures. **Figure 3-11** presents the molar fractions of C_1 in C_1/CO_2 mixture in both nanopores at three different pressures. As pressure decreases, molar fraction of C_1 decreases in both nanopores, implying that, as pressure decreases, CO_2 expels more C_1 molecules from organic pores. Moreover, the molar fraction of C_1 in the 1 nm pore is lower than that in the 3 nm pore, suggesting CO_2 is more effective in recovering C_1 molecules from smaller pores. **Figure 3-12** presents molar fractions of nC_4 in nC_4/CO_2 mixture in both nanopores at three different pressures. We can observe that the molar fraction of nC_4 in the two pores is not affected by the system pressure, which is quite different that for C_1. Thereby, in shale industry, CO_2 is a suitable agent to recover lighter hydrocarbons (i.e., C_1) from organic pores, but would not be efficient in recovering heavier hydrocarbons (i.e., nC_4) because the recovery efficiency is strongly affected by the competitive adsorption behavior between hydrocarbons and CO_2 on the organic pore surface.

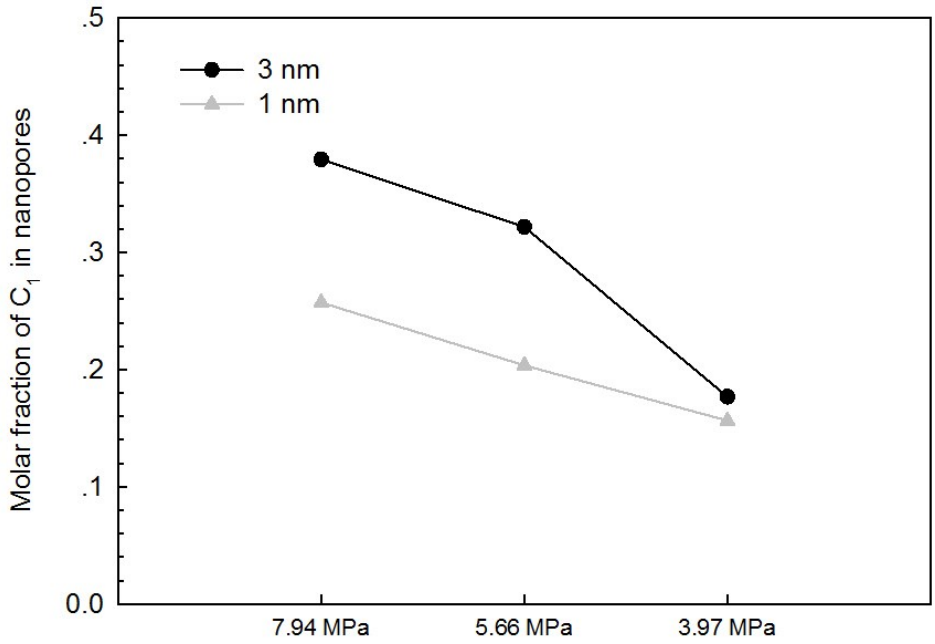

Figure 3-11 Molar fraction of C_1 in the C_1/CO_2 mixture in nanopores at three different pressures.

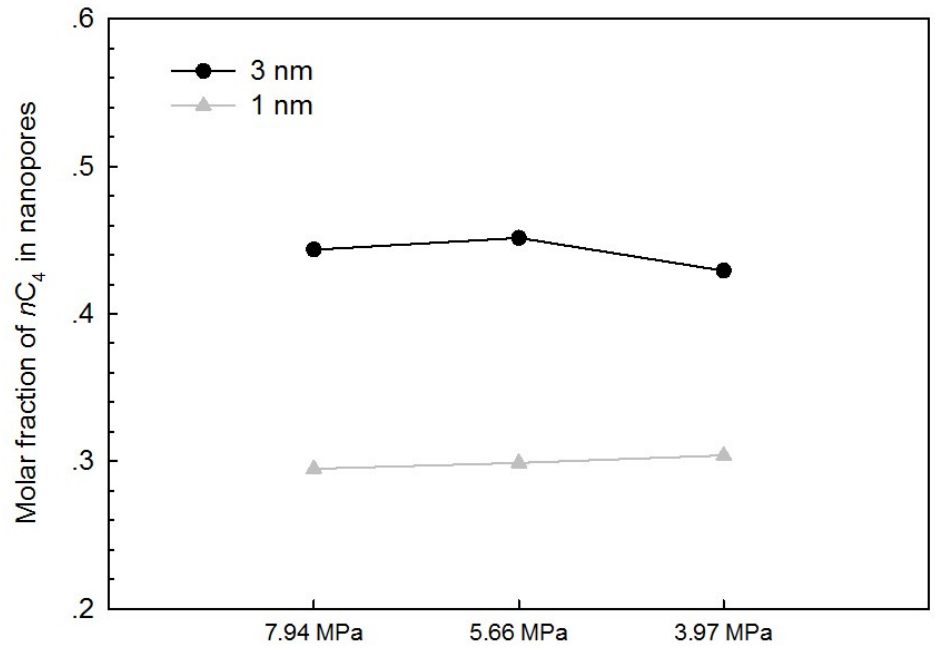

Figure 3-12 Molar fraction of nC_4 in the nC_4/CO_2 mixture in nanopores at three different pressures.

3.4 Conclusions

In this study, we use MD simulations to study the competitive adsorption behavior of hydrocarbon(s)/CO_2 mixtures in a double-nanopore system. The potential usage of CO_2 for enhanced hydrocarbon recovery from nanopores is discussed. The conclusions can be drawn as

follows:

- The dynamic distributions of C_1/nC_4 mixture in the double-nanopore system illustrates that as pressure decreases, adsorption of C_1 tends to decrease, while adsorption of nC_4 is improved. It indicates that lighter components may be readily produced from organic pores as pressure drops, while heavier components have a tendency to remain in organic nanopores, rendering them being difficult to be produced.
- The dynamic distributions of C_1/CO_2 mixture in the double-nanopore system show that as pressure drops, part of the adsorbed C_1 molecules in nanopores are replaced by CO_2 due to the stronger adsorption capacity of CO_2 on organic pore surface. As observed from the dynamic distributions of nC_4/CO_2 mixture in the double-nanopore system, adsorption of CO_2 decreases with a decreasing pressure, while adsorption of nC_4 increases as a decreasing pressure; it indicates that CO_2 is inefficient in recovering nC_4 with the depressurization approach.
- Based on the calculated adsorption selectivity on organic pore surface, it is found that nC_4 and CO_2 exhibit stronger adsorption capacity than C_1. Moreover, the adsorption capacity of CO_2 is generally weaker than nC_4.
- Based on the calculated molar fractions of C_1 and nC_4 in C_1/CO_2 and nC_4/CO_2 mixtures in nanopores, it is found that CO_2 can work as a suitable agent to recover C_1 from organic pores but would not be efficient in recovering nC_4 from nanopores.
- According to the calculated density distributions of mixtures in the double-nanopore system, it is found that fluid tends to get more accumulated in the smaller pore than in the larger pore. Compared to those in the smaller pore, hydrocarbons residing in the larger pore can be more readily recovered by CO_2.

3.5 References

[1] Huang, L.; Ning, Z.; Wang, Q. *et al.* Effect of Organic Type and Moisture on CO_2/CH_4 Competitive Adsorption in Kerogen with Implications for CO_2 Sequestration and Enhance CH_4 Recovery. *Appl. Energy* **2018**, 210, 28.

[2] Yuan, J.; Luo, D.; Feng L. A Review of the Technical and Economic Evaluation Techniques for Shale Gas Development. *Appl. Energy* **2015**, 148, 49.

[3] Weijermars, R. US Shale Gas Production Outlook Based on Well Roll-out Rate Scenarios. *Appl. Energy* **2014**, 124, 283.

[4] Yamazaki, T.; Aso, K.; Chinju, J. Japanese Potential of CO_2 Sequestration in Coal Seams. *Appl. Energy* **2006**, 83(9), 911.

[5] Karacan, C.Ö.; Ruiz, F.; Cotè, M.; Phipps, S. Coal Mine Methane: A Review of Capture and Utilization Practices with Benefits to Mining Safety and to Greenhouse Gas Reduction. *Int. J. Coal Geol.* **2011**, 86, 121.

[6] Weijermars, R. Economic Appraisal of Shale Gas Plays in Continental Europe. *Appl. Energy* **2013**, 106, 100.

[7] Wang, Y.; Tsotsis, T.T.; Jessen, K. Competitive Sorption of Methane/Ethane Mixtures on Shale: Measurements and Modeling. *Ind. Eng. Chem. Res.* **2015**, 54, 12178.

[8] Ambrose, R.J.; Hartman, R.C.; Campos, M.D. *et al.* New Pore-scale Considerations for Shale Gas in Place Calculations. Presented at the SPE Unconventional Gas Conference, Pittsburgh, Pennsylvania, USA, 23-25 February, **2010**.

[9] Weniger, P.; Kalkreuth, W.; Busch A. *et al.* High-pressure Methane and Carbon Dioxide Sorption on Coal and Shale Samples from the Parana Basin, Brazil. *International J. Coal Geology* **2010**, 84(3-4), 190.

[10] Brunauer, S.; Emmett, P.H.; Teller E. Adsorption of Gases in Multimolecular Layers. *J. Am. Chem. Soc*. **1938**, 60(2), 309.

[11] Langmuir, I. The Constitution and Fundamental Properties of Solids and Liquids. Part I. Solids. *J. Am. Chem. Soc*. **1916**, 38(11), 2221.

[12] Halsey, G.D. Physical Adsorption on Non-uniform Surfaces. *J. Chem. Phys.* **1948**, 16: 931.

[13] Roque-Malherbe, R.M.A. Adsorption and Diffusion in Nanoporous Materials. Boca Raton, Florida: CRC Press, **2007**.

[14] Li, Z.; Jin, Z.; Firoozabadi, A. Phase Behavior and Adsorption of Pure Substances and Mixtures and Characterization in Nanopore Structures by Density Functional Theory. *SPE J*. **2014**, 19(6), 1096.

[15] Myers, A.L.; Prausnitz, J.M. Thermodynamics of Mixed-gas Adsorption. *AIChE J*. **1965**, 11(1), 121.

[16] Cessford, N.; Seaton, N.; Düren T. Evaluation of Ideal Adsorbed Solution Theory as A Tool for the Design of Metal-organic Framework Materials. *Ind. Eng. Chem. Res*. **2012**, 51, 4911.

[17] Sweatman, M.B.; Quirke, N. Predicting the Adsorption of Gas Mixtures: Adsorbed Solution Theory versus Classical Density Functional Theory. *Langmuir* **2002**, 18(26), 10443.

[18] Jin, B.; Nasrabadi, H. Phase Behavior of Multi-component Hydrocarbon Systems in Nano-pores Using Gauge-GCMC Molecular Simulation. *Fluid Phase. Equilibr.* **2016**, 425, 324.

[19] Neimark, A.V.; Vishnyakov, A. Gauge Cell Method for Simulation Studies of Phase Transitions in Confined Systems. *Phys. Rev. E* **2000**, 62(4), 4611.

[20] Singh, S.K.; Sinha, A.; Deo, G. *et al.* Vapor Liquid Phase Coexistence, Critical Properties, and Surface Tension of Confined Alkanes. *J. Phys. Chem. C* **2009**, 113(17), 7170.

[21] Walton, J.P.R.B.; Quirke, N. Capillary Condensation: A Molecular Simulation Study. *Mol. Simulat.* **1989**, 2(4-6), 361.

[22] Wongkoblap, A.; Do, D.D.; Birkett, G. *et al.* A Critical Assessment of Capillary Condensation and Evaporation Equations: A Computer Simulation Study. *J. Colloid Interface Sci.* **2011**, 356(2), 672.

[23] Jin, Z.; Firoozabadi, A. Phase Behavior and Flow in Shale Nanopores from Molecular Simulations. *Fluid Phase Equilibr.* **2016**a, 430, 156.

[24] Jin, Z.; Firoozabadi, A. Thermodynamic Modeling of Phase Behavior in Shale Media. *SPE J.* **2016**b, 21(1), 190.

[25] Li, Z.; Jin, Z.; Firoozabadi, A. Phase Behavior and Adsorption of Pure Substances and Mixtures and Characterization in Nanopore Structures by Density Functional Theory. *SPE J.* **2014**, 19(6), 1096.

[26] Jin, Z.; Firoozabadi, A. Phase Behavior and Flow in Shale Nanopores from Molecular Simulations. Presented at the *SPE Annual Technical Conference and Exhibition* in Houston, Texas, USA, 28-30 September **2015**.

[27] Shirono, K.; Daiguiji, H. Molecular Simulation of the Phase Behavior of Water Confined in Silica Nanopores. *J. Phys. Chem. C* **2007**, 111(22), 7938.

[28] Liu, Y.; Jin, Z.; Li, H. Comparison of PR-EOS with Capillary Pressure Model with Engineering Density Functional Theory on Describing the Phase Behavior of Confined Hydrocarbons. Presented at the *SPE Annual Technical Conference and Exhibition* in San Antonio, Texas, USA, 9-11 October **2017**.

[29] Li Z.; Firoozabadi A. Interfacial Tension of Nonassociating Pure Substances and Binary Mixtures by Density Functional Theory Combined with Peng-Robinson Equation of State.

J. Chem. Phys. **2009**, 130(15), 154108.

[30] Tian, Y.; Yan, C.; Jin, Z. Characterization of Methane Excess and Absolute Adsorption in Various Clay Nanopores from Molecular Simulation. *Sci. Rep.* **2017**, 7: 12040.

[31] White, C.M.; Smith, D.H.; Jones, K.L. *et al.* Sequestration of Carbon Dioxide in Coal with Enhanced Coalbed Methane Recovery-A Review. *Energy Fuels* **2005**, 19(3), 659.

[32] Chatterjee, R.; Paul, S. Classification of Coal Seams for Coal Bed Methane Exploitation in Central Part of Jharia Coalfield, India Statistical Approach. *Fuel* **2013**, 111, 20.

[33] Vishal, V.; Singh, T.N.; Ranjith, P.G. Influence of Sorption Time in CO_2-ECBM Process in Indian Coals Using Coupled Numerical Simulation. *Fuel* **2015**, 139, 51.

[34] Jiang, X. A review of physical modelling and numerical simulation of long-term geological storage of CO_2. *Appl. Energy* **2011**, 88(11), 3557.

[35] Luo, X.; Wang, S.; Wang, Z. *et al.* Adsorption of Methane, Carbon Dioxide and Their Binary Mixtures on Jurassic Shale from the Qaidam Basin in China. *Int. J. Coal Geol.* **2015**, 150-151, 210.

[36] Gensterblum, Y.; Busch, A.; Krooss, B.M. Molecular Concept and Experimental Evidence of Competitive Adsorption of H_2O, CO_2 and CH_4 on Organic Material. *Fuel* **2014**, 115: 581.

[37] Ottiger, S.; Pini, R.; Storti, G. *et al.* Measuring and Modeling the Competitive Adsorption of CO_2, CH_4, and N_2 on a Dry Coal. *Langmuir* **2008**, 24(17), 9531.

[38] Bhowmik, S.; Dutta, P. Investigation into the Methane Displacement Behavior by Cyclic, Pure Carbon Dioxide Injection in Dry, Powdered, Bituminous Indian Coals. *Energy Fuels* **2011**, 25(6), 2730.

[39] Faiz, M.M.; Saghafi, A.; Barclay, S.A. *et al.* Evaluating Geological Sequestration of CO_2 in Bituminous Coals: The Southern Sydney Basin, Australia as A Natural Analogue. *Int. J.*

Greenh. Gas Con. **2007**, 1(2): 223-235.

[40] Khosrokhavar, R.; Wolf, K.H.; Bruining, H. Sorption of CH_4 and CO_2 on a Carboniferous Shale from Belgium using a Manometric Setup. *Int. J. Coal Geol.* **2014**, 128, 153.

[41] Busch, A.; Gensterblum, Y.; Krooss, B.M. Methane and CO_2 Sorption and Desorption Measurements on Dry Argonne Premium Coals: Pure Components and Mixtures. *Int. J. Coal Geol*. **2003**, 55(2), 205.

[42] Majewska, Z.; Ceglarska-Stefańsk, G.; Majewski, S. *et al.* Binary Gas Sorption/Desorption Experiments on a Bituminous Coal: Simultaneous Measurements on Sorption Kinetics, Volumetric Strain and Acoustic Emission. *Int. J. Coal Geol.* **2009**, 77(1), 90.

[43] Ross, D.J.; Bustin, R.M. Impact of Mass Balance Calculations on Adsorption Capacities in Microporous Shale Gas Reservoirs. *Fuel* **2007**, 86(17), 2696.

[44] Kim, T.H.; Cho, J.; Lee, K.S. Evaluation of CO_2 Injection in Shale Gas Reservoirs with Multi-component Transport and Geomechanical Effects. *Appl. Energy* **2017**, 190, 1195.

[45] Luo, F.; Xu, R.N.; Jiang, P.X. Numerical Investigation of the Influence of Vertical Permeability Heterogeneity in Stratified Formation and of Injection/Production Well Perforation Placement on CO_2 Geological Storage with Enhanced CH_4 Recovery. *Appl. Energy* **2013**, 102, 1314.

[46] Yu, W.; Al-Shalabi, E.W.; Sepehrnoori, K. A Sensitivity Study of Potential CO_2 Injection for Enhanced Gas Recovery in Barnett Shale Reservoirs. In: Proceedings of the SPE unconventional resources conference. Society of Petroleum Engineers, Woodlands, Texas, April 1-3, **2014**.

[47] Jiang, J.; Shao, Y.; Younis, R.M. Development of a Multi-continuum Multicomponent Model for Enhanced Gas Recovery and CO_2 Storage in Fractured Shale Gas Reservoirs. In:

Proceedings of the SPE improved oil recovery symposium. Society of Petroleum Engineers, Tulsa, Oklahoma, April 12-16, **2014**.

[48] Godec, M.; Koperna, G.; Petrusak, R. *et al.* Potential for Enhanced Gas Recovery and CO_2 Storage in the Marcellus Shale in the Eastern United States. *Int. J. Coal Geol.* **2013**, 118, 95.

[49] Liu, F.; Ellett, K.; Xiao, Y. *et al.* Assessing the Feasibility of CO_2 Storage in the New Albany Shale (Devonian-Mississippian) with Potential Enhanced Gas Recovery using Reservoir Simulation. *Int. J. Greenh. Gas Conl.* **2013**, 17, 111.

[50] Zhang, J.; Liu, K.; Clennell, M.B. *et al.* Molecular Simulation of CO_2-CH_4 Competitive Adsorption and Induced Coal Swelling. *Fuel* **2015**, 160, 309.

[51] Kazemi, M.; Takbiri-Borujeni, A. Molecular Dynamics Study of Carbon Dioxide Storage in Carbon-based Organic Nanopores. Presented at the *SPE Annual Technical Conference and Exhibition* in Dubai, UAE, September 26-28, **2016**.

[52] Kurniawan, Y.; Bhatia, S.K.; Rudolph, V. Simulation of Binary Mixture Adsorption of Methane and CO_2 at Supercritical Conditions in Carbons. *AIChE J.* **2006**, 52(3), 957.

[53] Yuan, Q.; Zhu, X.; Lin, K. *et al.* Molecular Dynamics Simulations of the Enhanced Recovery of Confined Methane with Carbon Dioxide. *Phys. Chem. Chem. Phys.* **2015**, 17, 31887.

[54] Brochard, L.; Vandamme, M.; Pellenq, R. *et al.* Adsorption-Induced Deformation of Microporous Materials: Coal Swelling Induced by CO_2-CH_4 Competitive Adsorption. *Langmuir* **2012**, 28, 2659.

[55] Wang, X.; Zhai, Z.; Jin, X. *et al.* Molecular Simulation of CO_2/CH_4 Competitive Adsorption in Organic Matter Pores in Shale under Certain Geological Conditions. *Petrol. Explor. Dev.*

2016, 43(5), 841.

[56] Lu, X.; Jin, D.; Wei, S. *et al.* Competitive Adsorption of a Binary CO_2-CH_4 Mixture in Nanoporous Carbons: Effects of Edge-Functionalization. *Nanoscale* **2015**, 7(3), 1002.

[57] Liu, X.; He, X.; Qiu, N. *et al.* Molecular Simulation of CH_4, CO_2, H_2O and N_2 Molecules Adsorption on Heterogeneous Surface Models of Coal. *Appl. Surf. Sci.* **2016**, 389, 894.

[58] Sun, H.; Zhao, H.; Qi, N. *et al.* Molecular Insights into the Enhanced Shale Gas Recovery by Carbon Dioxide in Kerogen Slit Nanopores. *J. Phys. Chem. C* **2017**, 121(18), 10233.

[59] Huang, L.; Ning, Z.; Wang, Q. *et al.* Molecular Simulation of Adsorption Behaviors of Methane, Carbon Dioxide and Their Mixtures on Kerogen: Effect of Kerogen Maturity and Moisture Content. *Fuel* **2018**, 211, 159.

[60] Wu, H.; Chen, J.; Liu, H. Molecular Dynamics Simulations about Adsorption and Displacement of Methane in Carbon Nanochannels. *J. Phys. Chem. C* **2015**, 119(24), 13652.

[61] Kowalczyk, P.; gauden, P.A.; Terzyk, A.P. *et al.* Displacement of Methane by Coadsorbed Carbon Dioxide Is Facilitated in Narrow Carbon Nanopores. *J. Phys. Chem. C* **2012**, 116(25), 13640.

[62] Yu, S.; Yanming, Z.; Wu, L. Macromolecule Simulation and CH_4 Adsorption Mechanism of Coal Vitrinite. *Appl. Surf. Sci.* **2017**, 396, 291.

[63] Zhao, Y.; Feng, Y.; Zhang, X. Molecular Simulation of CO_2/CH_4 Self- and Transport Diffusion Coefficients in Coal. *Fuel* **2016**, 165, 19.

[64] Valentini, P.; Schwartzentruber, T.E.; Cozmuta I. ReaxFF Grand Canonical Monte Carlo Simulation of Adsorption and Dissociation of Oxygen on Platinum (111). *Surf. Sci.* **2011**, 605(23), 1941.

[65] Li, Y.; Wang, S.; Wang, Q. *et al.* Molecular Dynamics Simulations of Tribology Properties of NBR (nitrile-butadiene rubber)/Carbon Nanotube Composites. *Compos. Part B* **2016**, 97, 62.

[66] Rigby, D.; Sun, H.; Eichinger, B.E. Computer Simulations of Poly (ethylene oxide): Force Field, PVT Diagram and Cyclization Behaviour. *Polym. Int.* **1997**, 44(3), 311.

[67] Jones, J.E. On the Determination of Molecular Field-OII from the Equation of State of a Gas. *Proc. R. Soc. Lond. Ser. A* **1924**, 106, 463.

[68] Song, Y.; Jiang, B.; Li, W. Molecular Simulations of $CH_4/CO_2/H_2O$ Competitive Adsorption on Low Rank Coal Vitrinite. *Phys. Chem. Chem. Phys*. **2017**, 19, 17773.

[69] Andersen, H.C. Molecular Dynamics at Constant Pressure and/or Temperature. *J. Chem. Phys*. **1980**, 72: 2384.

[70] Robinson, D.B.; Peng, D.Y. The Characterization of the Heptanes and Heavier Fractions for the GPA Peng-Robinson Programs. Research Report RR-28, Gas Processors Association, Tulsa, **1978**.

[71] Liu, Y.; Wilcox, J. Molecular Simulations of CO_2 Adsorption in Micro- and Mesoporous Carbons with Surface Heterogeneity. *Int. J. Coal Geol*. **2012**, 104, 83.

[72] Chen, G.; Zhang, J.; Lu, S. *et al.* Adsorption Behavior of Hydrocarbon on Illite. *Energy Fuels* **2016**, 30, 9114.

[73] Liu, Y.; Li, H.; Tian, Y. *et al.* Determination of the Absolute Adsorption/Desorption Isotherms of CH_4 and n-C_4H_{10} on Shale from A Nano-scale Perspective. *Fuels* **2018**, 218, 67.

[74] Lu, L.; Wang, Q.; Liu, Y. Adsorption and Separation of Ternary and Quaternary Mixtures of Short Linear Alkanes in Zeolites by Molecular Simulation. *Langmuir* **2003**, 19(25),

10617.

[75] Li, W.Z.; Liu, Z.Y.; Chen, Y.L. *et al.* Molecular Simulation of Adsorption and Separation of Mixtures of Short Linear Alkanes in Pillared Layered Materials at Ambient Temperature. *J. Colloid Interf. Sci.* **2007**, 312(2), 179.

[76] Jin, Z.; Firoozabadi, A. Methane and Carbon Dioxide Adsorption in Clay-like Slit Pores by Monte Carlo Simulations. *Fluid Phase Equilibr.* **2013**, 360, 456.

CHAPTER 4 DETERMINATION OF THE ABSOLUTE ADSORPTION/DESORPTION ISOTHERMS OF CH_4 AND n-C_4H_{10} ON SHALE FROM A NANO-SCALE PERSPECTIVE

A version of this chapter has been accepted for publication in *Fuel*.

Abstract

Accurate description of absolute adsorption/desorption behavior for hydrocarbons on shale is of critical importance to the understanding of the fundamental mechanisms governing the storage, transport, and recovery of shale gas or shale gas condensate in shale reservoirs. By applying a thermogravimetric method, we first measure the excess adsorption/desorption isotherms of pure CH_4 and *n*-C_4H_{10} on shale samples over the temperature range of 303.15-393.15 K. The maximum test pressures considered for CH_4 and *n*-C_4H_{10} are 50 bar and 2 bar, respectively. Grand Canonical Monte Carlo (GCMC) simulations are then applied to calculate the density of the adsorption phase by considering the fluid-pore surface interactions. We use such calculated density of the adsorption phase to calibrate the excess adsorption/desorption isotherms, which enables us to eventually obtain the absolute adsorption/desorption isotherms. Such approach for estimating the density of the adsorption phase is essentially different from the commonly used approaches in which the density of the adsorption phase is considered to be independent of temperature, pressure, and pore size.

The adsorption/desorption test results show that both CH_4 and *n*-C_4H_{10} exhibit more adsorption as temperature decreases or pressure increases. Their adsorption/desorption isotherms exhibit hysteresis phenomenon and this phenomenon weakens as temperature increases. Comparatively, the hysteresis behavior observed for *n*-C_4H_{10} is more obvious than that for CH_4. Compared with CH_4, *n*-C_4H_{10} has higher adsorption capacity under the same condition, indicating its higher affinity towards the shale with organic matters. As for the conventional approaches, the density calculated from the van der Waals constant *b* or the liquid hydrocarbon density can be used to reasonably well evaluate the absolute adsorption isotherms of *n*-C_4H_{10} on shale, but tends to underestimate the absolute adsorption of CH_4 on shale. GCMC simulations show that the density

of the adsorption phase is strongly correlated with system pressure, temperature, and pore size. Compared to the conventional approaches, GCMC simulations can better capture the *in-situ* density of adsorption phase; on the basis of the *in-situ* density of adsorption phase, we can then achieve more accurate determination of the absolute adsorption isotherms of a given hydrocarbon on shale. This study raises the imperativeness of leveraging more sophisticated simulation tools (such as GCMC) for more accurate determination of absolute adsorption isotherms.

Keywords: Density of the adsorption phase; Absolute adsorption/desorption isotherms; Hysteresis phenomenon; Grand Canonical Monte Carlo simulations; Thermogravimetric analysis

4.1 Introduction

Shale resources (such as shale gas or shale gas condensate) have emerged as a key energy resource in recent years. Shale rocks generally have higher total organic carbon (TOC) content than the conventional ones, resulting in hydrocarbons being more apt to adsorb on shale surface [1]. Thereof, a significant proportion of reserves in shale reservoirs can be in the adsorbed state. During the production of shale gas or shale gas condensate, desorption plays an important role. Adsorption/desorption of hydrocarbons usually exhibits an interesting phenomenon of hysteresis, and the knowledge about the adsorption/desorption behavior of hydrocarbons in shale is crucial for estimating the hydrocarbon storage capacity and understanding the mechanisms of the subsequent hydrocarbon recovery.

Adsorbed hydrocarbons can account for 20-85 vol% of the total reserves in shale reservoirs [2]. Many previous researches focused on investigating the adsorption capacity of hydrocarbons on shale rocks [3,4,5]. CH_4, known to be the most abundant component in shale gas reservoirs, was

mostly studied. Some heavier hydrocarbons, e.g., C_2H_6, C_3H_8, and *n*-C_4H_{10}, can be also present with a large quantity in shale reservoirs, up to 20 vol% [6]. But adsorptions of these heavier components in shale rocks are scarcely measured in the literature. Pedram *et al.* (1984) [7] measured the adsorption isotherms of C_2H_6, C_3H_8, and *n*-C_4H_{10} in two oil-shale samples and found that *n*-C_4H_{10} has the highest adsorption capacity, followed by C_3H_8 and C_2H_6. But it is noted that the oil-shale they used still have residual oil left in the samples, which can affect the gas adsorption on shale due to the large solubility of various hydrocarbons in shale oil. Therefore, such measured adsorption isotherms could not represent the actual adsorption capacity of gases on shale. Recently, Wang *et al.* (2015) [6] measured the excess adsorption isotherms of pure CH_4 and C_2H_6 on shale samples. C_2H_6 is shown to have a higher adsorption capacity than CH_4, and Wang *et al.* (2015) [6] attributed this finding to that C_2H_6 is more apt to get adsorbed on shale samples than CH_4. But this conclusion is made based on the measured excess adsorption isotherms, rather than the absolute adsorption isotherms; excess adsorption isotherms are generally not accurate enough as it neglects the adsorbed-phase volume occupied by the adsorbed gas.

By knowing the pore volume from the helium adsorption, volumetric method is commonly used to measure the adsorption isotherms of hydrocarbons on shale samples [8,9]. Recently, some scholars used the thermogravimetric analysis (TGA) technique to measure the adsorption isotherms [6]. Compared with the volumetric method, TGA loads a smaller sample amount into the setup; the magnetic suspension balance mounted in the TGA setup is capable of measuring the weight change down to 1 μg, rendering the TGA technique more accurate than the volumetric method. However, the adsorption isotherms directly measured by TGA technique are excess adsorption isotherms, which neglects the adsorbed-phase volume and thereby

underestimates the total adsorption amount. The density of the adsorption phase is commonly used to correct the excess adsorption isotherms, yielding the absolute adsorption isotherms. In the adsorption phase, gas molecules are in an adsorbed state; to our knowledge, few efforts are dedicated to quantifying the density of the adsorption phase. Previously, constant density values are normally used to pragmatically represent the density of the adsorption phase. Dubinin (1960) [10] suggested that the density of the adsorption phase is a constant value which correlates with the van der Waals constant *b*. Later, the density of adsorption phase is argued to be equal to the liquid adsorbate density [5,11,12]. Li *et al.* (2002) [13] compared the aforementioned methods and claimed that the density of the adsorption phase is a function of the system temperature, but its value approaches that proposed by Dubinin (1960) [10]. Recently, with molecular simulations, Ambrose *et al.* (2012) [14] suggested that the density of the adsorption phase correlates with the system temperature, pressure, and pore size. Actually, fluids in confined space are strongly affected by fluid/pore surface interactions, especially in shale samples which are usually abundant in nanoscale pores. It is, thereby, of critical importance to precisely capture the density of the adsorption phase in order to more accurately determine the absolute adsorption isotherms.

The objectives of this study are multifold: 1) to use GCMC simulations to capture the *in-situ* density distribution in carbon-slit pores under the effects of the system pressure, temperature, and pore size; 2) to determine the absolute adsorption/desorption isotherms of hydrocarbons on shale samples by knowing the *in-situ* density of the adsorption phase; and 3) to further analyze and compare the characteristics of the absolute adsorption/desorption isotherms of CH_4 and *n*-C_4H_{10}. As part of a comprehensive study on the adsorption/desorption behavior of hydrocarbons in shale reservoirs, we measure the adsorption/desorption isotherms of CH_4 and *n*-C_4H_{10} on two

shale samples using the TGA technique, and then determine the absolute adsorption/desorption isotherms based on GCMC simulations. CH_4 is selected with the consideration that CH_4 is the most abundant component in shale gas, while *n*-C_4H_{10} adsorption/desorption isotherms are measured to represent the adsorption/desorption behavior of heavier hydrocarbons in shale reservoirs.

4.2 Experimental Section

4.2.1 Materials and Shale Sample Preparation

The purities of CH_4 and *n*-C_4H_{10} (Chongqing Tianke Gas Company, China) used in this study are 99.999 mol% and 99.998 wt%, respectively. The uncertainty of the adsorption/desorption measurements as a result of the gas purities can be negligible. Two shale samples, labeled with #1 and #2, are retrieved from the Longmaxi formation located at the depth of 1,836 m and 1,562 m, respectively, in the southeastern of Sichuan Basin (China). The temperature of the Longmaxi formation is in the range of 355.13-363.15 K and the pressure in this formation is in the range of 100-150 bar. The two shale samples are selected with different TOC contents to clarify the effect of TOC content on the adsorption capacity of hydrocarbons. Considering that adsorption can be affected by the particle size, shale particles used in the adsorption/desorption measurements have the same particle size for different hydrocarbons. In this experiment, the shale samples are crushed into small particles with diameters in the range of 1.00-1.18 mm (US Mesh 16-18). Then, to remove the moisture and *in-situ* gas, the shale particles are placed in an oven at 423.15 K, and being vacuumed for 48 hours. Prior to their use in the adsorption/desorption measurements, the shale samples are stored in a zip-locked bag to avoid oxidation and water uptake.

4.2.2 Characterization of Shale Sample

This section presents the procedures used to characterize the shale samples as well as the characterization results. Various techniques, including the TOC measurement, the scanning election microscopy (SEM), and the N_2 adsorption/desorption test are adopted to characterize the shale samples.

The TOC content of two shale samples is measured by a combustion elemental analyzer. In this measurement, the organic carbon in shale samples are sparged with oxygen, forming carbon dioxide; then the TOC content is determined by detecting the amount of the carbon dioxide with the non-dispersive infrared detector. The TOC contents of the two shale samples are shown in Table 4-1. We observe shale sample #1 has a higher TOC content of 3.71 wt%, 3.78 times of that in shale sample #2. The measured TOC contents are in good agreement with the reported values for Longmaxi shale which ranges from 0.52 to 6.05 wt% [2].

Table 4-1 TOC contents and BET surface areas of the two shale samples used in this study.

Shale sample ID	TOC content (wt%)	R_o (%)	BET surface area (m^2/g)
#1	3.71	2.35	2.98
#2	0.98	1.82	2.06

The Hitachi TM-300 SEM setup is used to characterize the surface morphology at an accelerating voltage of 20.0 kV. Prior to scanning, shale surface is polished with argon ion. Subsequently, the polished shale surface is coated with a golden film with a thickness of 10 nm to improve the conductivity. Fig. 4-1 shows the FE-SEM images taken on the two shale samples. We then further conduct the energy-dispersive X-ray spectroscopy (EDX) analysis on the chosen points “a” and “b” in shale samples #1 and #2, respectively, as marked in Fig. 4-1. Fig. 4-2 shows the EDX test results. As seen from Fig. 4-2, a high concentration of carbon element is present at both sites, indicating that organic matter, i.e., kerogen, is residing in both sites. It can

be also seen from Fig. 4-1 that the kerogen is surrounded by mesopores, which is a typical characteristic observed for kerogen in shale.

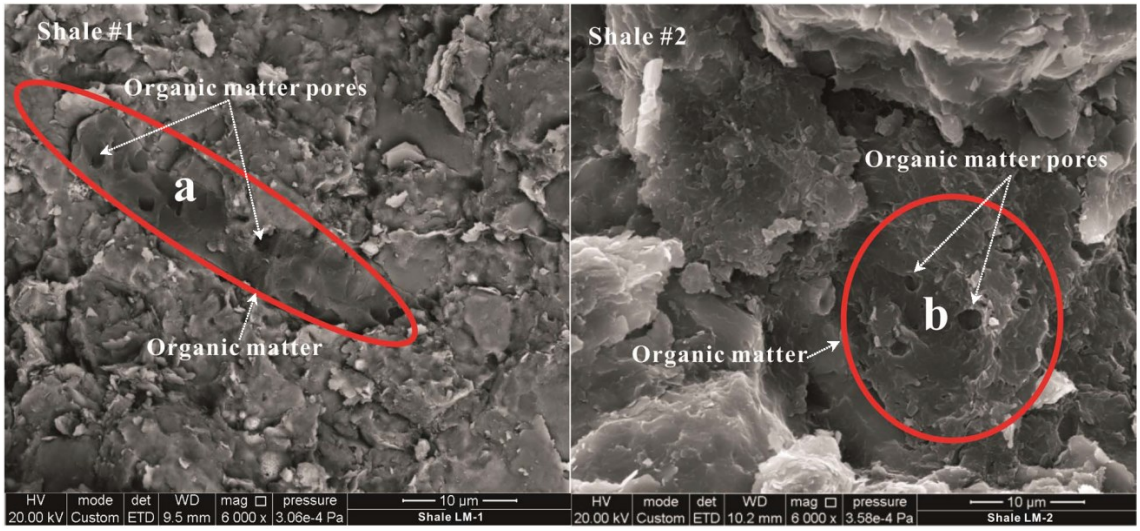

Figure 4-1 The FE-SEM images of the two shale samples. Energy-dispersive X-ray spectroscopy (EDX) analysis has been conducted at the sites marked by "*a*" and "*b*".

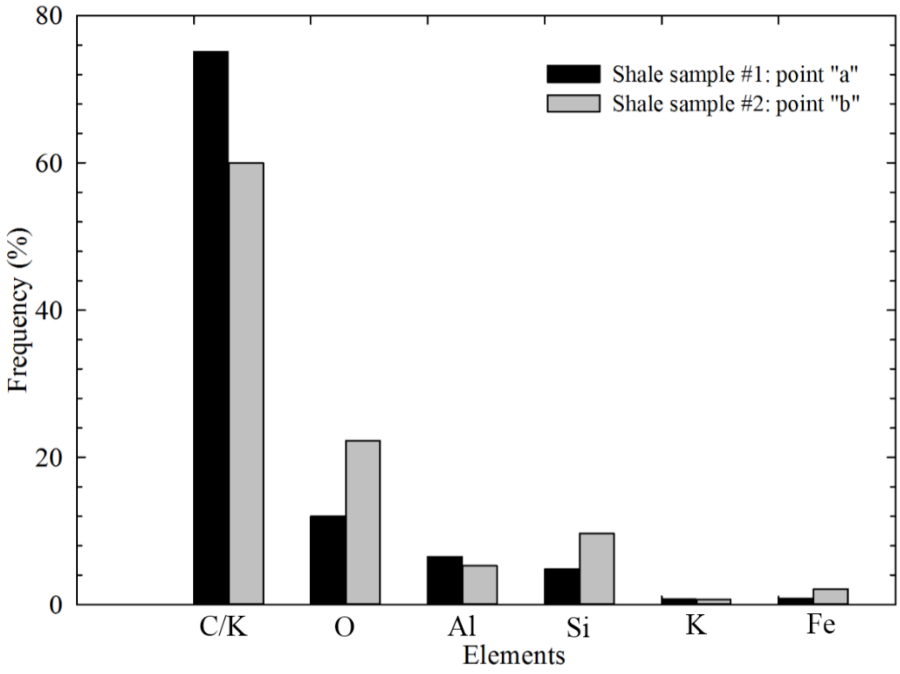

Figure 4-2 Energy-dispersive X-ray spectroscopy (EDX) analysis results for points "*a*" and "*b*" shown in Fig. 4-1.

Pore size distribution and Brunauer-Emmett-Teller (BET) surface area are characterized by the N_2 adsorption/desorption tests conducted with the Autosorb iQ-Chemiadsorption & Physi-

adsorption Gas Adsorption Analyzer (Quantachrome Instruments, USA). In a wide range of testing pressure, N_2 adsorption isotherms can characterize pore size distributions in the micro-, meso- and macro-porosity range (approximately 0.5-200 nm) [15]. Therefore, in view of the nature of our shale samples, we select N_2 as the adsorptive to obtain the PSD of two shale samples. Fig. 4-3 presents the pore size distribution of the two shale samples as obtained by analyzing the N_2 isotherm data measured at 77.0 K with the non-local density functional theory (NLDFT). With the NLDFT method, the networking effects and transition from the models of independent pores to the pore networks cannot be addressed. Furthermore, the swelling effect caused by adsorption is not considered in the NLDFT method. However, the whole region of micro- and mesopores can be properly characterized [16]. The dominant pore size of shale sample #1 is around 4.2 nm, while the dominant pore size of shale sample #2 is around 3.3 nm. Shale sample #1 possesses more mesopores (2-50 nm) and macropores (larger than 50 nm) than shale sample #2, indicating a higher thermal maturity of the organic matter in shale sample #1. We further measure the R_o value for each shale sample, while such R_o value represents the thermal maturity of organic matter in shale samples. The R_o values for shale samples # 1 and #2 are 2.35% and 1.82%, respectively, which validate our former statement. As measured in this study, the BET surface area obtained for shale sample #1 is higher than that for shale sample #2.

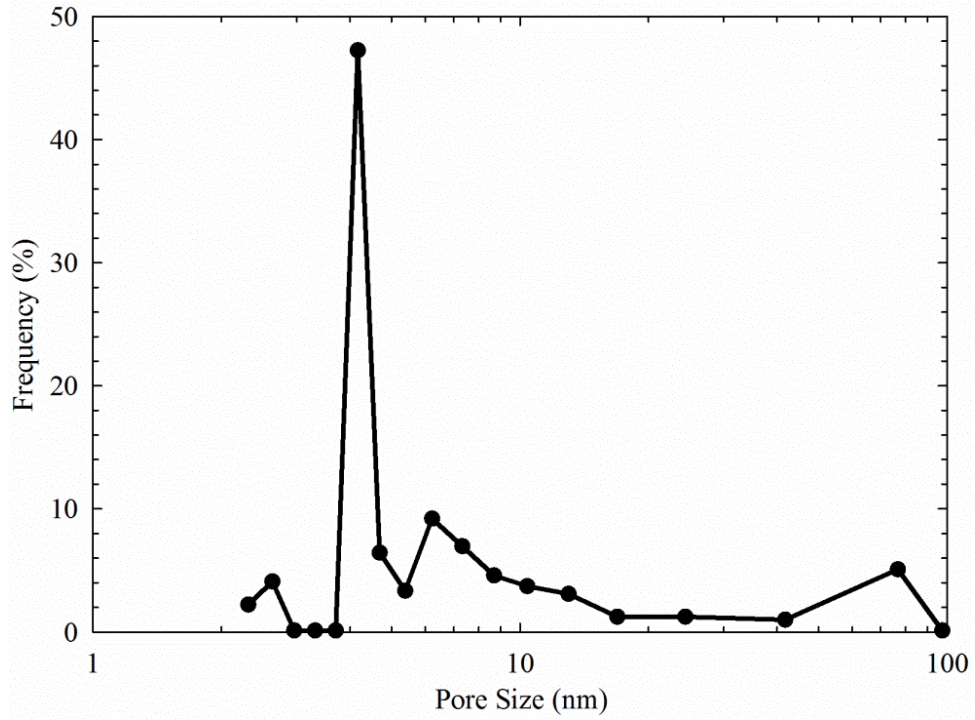

(a)

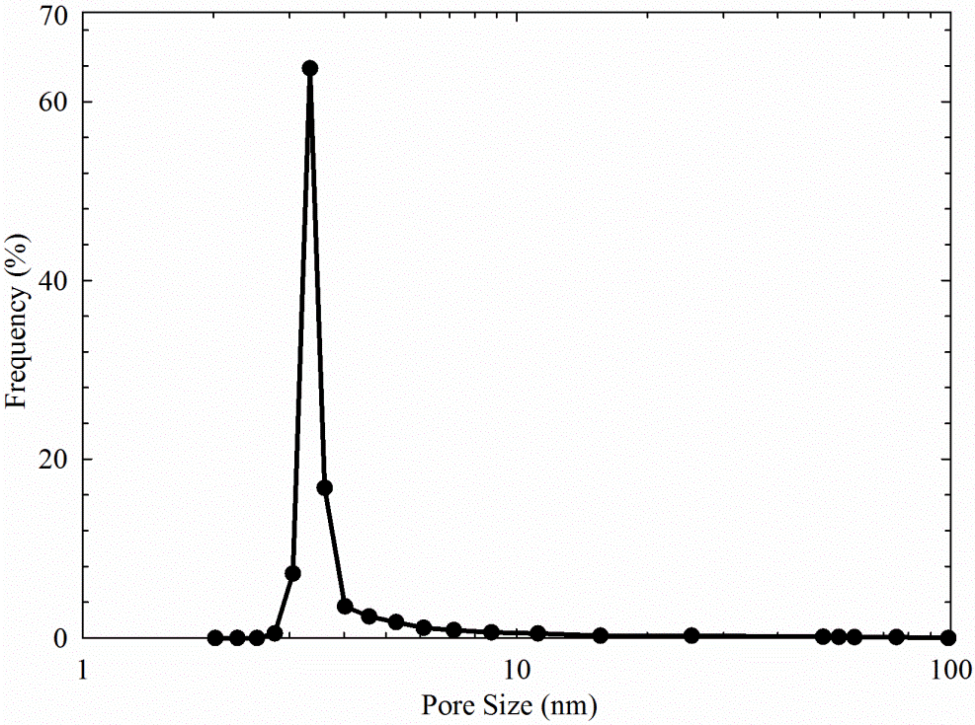

(b)

Figure 4-3 Pore size distributions of (a) shale sample #1 and (b) shale sample #2 as obtained from N_2 adsorption/desorption test.

4.2.3 Excess and Absolute Adsorption/Desorption

We measure the excess adsorption/desorption isotherms of CH_4 and *n*-C_4H_{10} using a thermogravimetric analyzer (TGA) (IEA-100B, Hiden Isochema Ltd., U.K). The key component of TGA is a magnetic suspension balance with 1.0 μg accuracy in weight measurement. In this study, the test pressures are set up to 50 bar for CH_4 and up to 2 bar for *n*-C_4H_{10}, respectively, while the test temperatures are set at 303.15, 333.15, 368.15, and 393.15 K. An electrical heater is applied to keep a constant temperature during the adsorption/desorption measurements. It should be noted that 2 bar is the highest pressure value we can reach due to the low vapor pressure of *n*-C_4H_{10} at room temperature. Each test is repeated twice to make sure the measured results are reliable and reproducible. The maximum deviation between two consecutive runs is found to be less than ±1.56%.

With TGA technique, the measured excess adsorption uptake (M_{ex}) is obtained by [6],

$$M_{ex} = M_a - \rho V_a = M_{app} - \left(M_s + M_{sc}\right) + \rho\left(V_s + V_{sc}\right) \tag{4-1}$$

where M_a is the adsorbed uptake on the shale sample, which is defined as the absolute adsorption uptake (M_{abs}), kg; ρ is the bulk gas density, kg/m^3; V_a is the adsorption-phase volume, m^3; M_{app} is the apparent weight measured by TGA, kg; M_s and M_{sc} are the weight of shale sample and the weight of the sample container, respectively, kg; and (V_s + V_{sc}) is the total volume of the shale sample and the sample container, m^3.

It has been found that, when pore size is large enough, the gas density in the pore center approaches that in bulk [14]. Thereof, in nanopores, the distribution of CH_4 or *n*-C_4H_{10} molecules can be divided into free-gas region and adsorption-phase region. Fig. 4-4 schematically shows

the absolute adsorption uptake, the excess adsorption uptake, the free-gas region, and the adsorption-phase region in a nanopore. As shown in Fig.4-4, the density of the adsorption phase (ρ_{ads}) is higher than bulk free-gas phase density (ρ). The green area depicted in Fig. 4-4 shows the absolute adsorption. Based on knowledge of the density of the adsorption phase and absolute adsorption uptake (M_{abs}), the adsorption-phase volume (V_a) can be calculated using the following equation,

$$V_a = \frac{M_{abs}}{\rho_{ads}} \tag{4-2}$$

Therefore, the actual adsorbed amount on the shale sample, i.e., absolute adsorption uptake, can be obtained by,

$$M_{abs} = \frac{M_{ex}}{1 - \frac{\rho}{\rho_{ads}}} \tag{4-3}$$

Thereof, the key to obtain an accurate absolute adsorption uptake is to accurately calculate the density of the adsorption phase. It is known that the density of the adsorption phase is a function of system pressure, temperature, and pore size [14]. However, in previous works, the density of the adsorption phase was provided as a constant which was either calculated from van der Waals constant *b* [10] or obtained from the liquid density [5,11,12]. From a nanopore-scale perspective, molecular simulations can faithfully capture the properties of the adsorption phase over a wide pressure and temperature range due to the consideration of fluid/pore surface interactions. In this study, we calculate the density of the adsorption phase using the GCMC simulations.

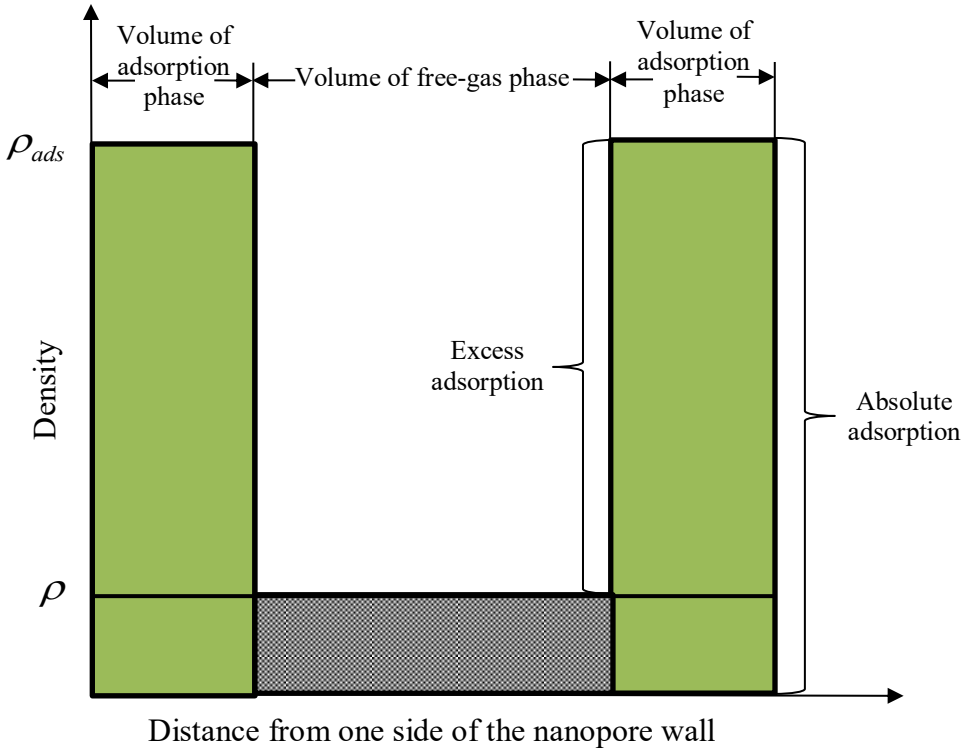

Figure 4-4 Schematic of the absolute adsorption and excess adsorption in nanopores. ρ_{ads} is the density of the adsorption phase, and ρ is the density of the free-gas phase, which is equal to the bulk gas density.

4.3 Grand Canonical Monte Carlo (GCMC) Simulations

Within grand canonical (GC) ensemble, the entire system has fixed volume (V) and temperature (T) and chemical potential (μ). Since the number of molecules in the system fluctuates during the simulations, the average number of molecules in the ensemble is fully determined by the chemical potential.

In our model, the united atom model [17] is used to simulate different hydrocarbon molecules. The modified Buckingham exponential-6 intermolecular potential [18] is applied to describe non-bonded site-site interactions among functional groups on different molecules, as well as

among functional groups belonging to the same molecule separated by more than three bonds. The pairwise interaction potential $U(r)$ for the non-bonded site-site interactions is given as [18],

$$U(r) = \left\{ \frac{\varepsilon}{1-\frac{6}{\alpha}} \left[\frac{6}{\alpha} \exp\left(\alpha \left[1 - \frac{r}{r_m} \right] \right) - \left(\frac{r_m}{r} \right)^6 \right] \right\}, \quad r > r_{\max}$$
$$= \infty, \quad r < r_{\max} \tag{4-4}$$

where r is the inter-particle separation distance, r_m is the radial distance at which $U(r)$ reaches a minimum, and the cutoff distance $r_{\max}$ is the smallest radial distance for which $dU(r)/dr = 0$ [19]. Since the original Buckingham exponential-6 potential can be negative at very short distances, the cutoff distance is thus defined to avoid negative potentials [18]. The radial distance at which $U(r) = 0$ is defined as σ. The values of the exponential-6 parameters ε, σ and α are 129.63 K, 0.3679 nm, and 16, respectively, for the methyl group (-CH_3), 73.5 K, 0.4 nm, and 22, respectively, for the methylene group (-CH_2-), and 160.3 K, 0.373 nm, 15, respectively, for CH_4 [19]. The cross parameters are determined by the following combining rules [19],

$$\sigma_{ij} = \frac{1}{2}(\sigma_i + \sigma_j) \tag{4-5}$$

$$\varepsilon_{ij} = (\varepsilon_i \varepsilon_j)^{1/2} \tag{4-6}$$

$$\alpha_{ij} = (\alpha_i \alpha_j)^{1/2} \tag{4-7}$$

The bond lengths for CH_3-CH_2 and CH_2-CH_2 are taken as 0.1687 nm and 0.1535 nm, respectively. The torsion potential ($U_{tor}(\varphi)$) is expressed as [20],

$$U_{tor}(\varphi) = V_0 + \frac{V_1}{2}(1 + \cos\varphi) + \frac{V_2}{2}(1 - \cos 2\varphi) + \frac{V_3}{2}(1 + \cos 3\varphi) \tag{4-8}$$

where φ is the torsional angle from equilibrium, V_0, V_1, V_2, and V_3 are 0, 355.03, -68.19, and

791.32 K, respectively. The bond bending potential $U_{bend}(\theta)$ is calculated by [21],

$$U_{bend}(\theta) = \frac{K_\theta}{2}(\theta - \theta_{eq})^2 \tag{4-9}$$

where parameter K_θ is equal to 62500 K/rad^2, θ is the bond angle from equilibrium, and θ_{eq} is the equilibrium bond angle (114°).

It has been found that the higher organic carbon content enables hydrocarbons to be more apt to adsorb on shale surface [22]. Thereby, in this model, nanopores are selected as slit geometry with smooth and structureless carbon surfaces. 10-4-3 Steele potentials are used to describe the fluid-pore surface interactions φ_{wf} [23],

$$\varphi_{wf}(z) = 2\pi\rho_w\varepsilon_{wf}\sigma_{wf}^2\Delta\left[\frac{2}{5}\left(\frac{\sigma_{wf}}{z}\right)^{10} - \left(\frac{\sigma_{wf}}{z}\right)^4 - \frac{\sigma_{wf}^4}{3\Delta(0.61\Delta + z)^3}\right] \tag{4-10}$$

where z is the distance of the fluid particle from the pore surface, ρ_{wf} is the density of carbon atom per unit surface area of the graphite layer (114 nm^{-3}), The molecular parameters of an atom in the graphite layer are ε_{wf} =28 K, and σ_{wf} =0.3345 nm [24], and Δ is the spacing between two adjacent graphene layers (0.335 nm), respectively. The external potential ψ in a slit pore is given as [23],

$$\psi(z) = \varphi_{wf}(z) + \varphi_{wf}(W - z) \tag{4-11}$$

where W is the size of the slit pore.

In each MC cycle, a trial random displacement is applied to all CH_4 molecules; with equal probability, a CH_4 molecule is randomly removed from or inserted into the simulations box depending on the chemical potential of CH_4. For simulations of *n*-C_4H_{10} molecules in slit pores,

in addition to the MC moves as mentioned above, a trial random rotation is applied to all *n*-C_4H_{10} molecules. We use a configurational-biased GCMC algorithm to insert and remove *n*-C_4H_{10} molecules [25]. The Widom insertion method [26] is used to obtain the chemical potentials of bulk CH_4 and *n*-C_4H_{10} molecules in canonical ensemble. The PR-EOS [27] is applied to calculate the bulk densities of CH_4 and *n*-C_4H_{10} at given pressure and temperature. The MC moves are implemented by using the Metropolis algorithm [28]. During the simulations, 0.1 million of MC cycles per each adsorbate molecule is required to reach an equilibrium state, while 0.5 million of MC cycles per adsorbate molecule is required to sample the density profiles.

The average density (ρ_{ave}) of component *i* in carbon-slit pores is expressed as,

$$\rho_{ave} = \frac{\langle N_i \rangle M_i}{V N_A} \tag{4-12}$$

where $\langle N_i \rangle$ is the ensemble averaged number of molecules of component *i* in nanopores, V is the volume, *M* is molecular weight of components *i*, and N_A is Avogadro constant, 6.022×10^{23}.

4.4 Results and Discussion

In the following section, we first explore the detailed density distributions of pure CH_4 or *n*-C_4H_{10} in single carbon-slit pores using GCMC simulations. Then, we calculate the density of the adsorption phase under given conditions. Such density values are subsequently employed to calibrate the excess adsorption/desorption isotherms of CH_4 and *n*-C_4H_{10} which are directly measured by the TGA apparatus. To our knowledge, it is the first time that adsorption/desorption isotherms of *n*-C_4H_{10} on dried shale are measured.

4.4.1 Density Distributions in Nanopores

To calculate the density of the adsorption phase, density distributions in nanopores should be known a priori. We investigate the density distributions of pure CH_4 or *n*-C_4H_{10} in a single carbon-slit pore. The effects of the system pressure, temperature, and pore size are examined. In the GCMC framework, CH_4 molecules are regarded as spherical particles, while *n*-C_4H_{10} molecules are represented considering the orientation and configuration [29].

4.4.1.1 Effect of System Pressure

With molecular simulations, Ambrose *et al.* (2012) [14] found that the CH_4 adsorption behavior in nanopores is sensitive to changes in pressure. To illustrate the effect of system pressure on adsorption behavior of CH_4 and *n*-C_4H_{10}, in Fig. 4-5, we present the density distributions of CH_4 and *n*-C_4H_{10} in 4.2 nm pore at 368.15 K and different system pressures. It is noted that the 4.2 nm is the dominant pore size of shale sample #1. At all bulk pressure conditions, both CH_4 and *n*-C_4H_{10} molecules can form one strong adsorption layer and the density in the pore center approaches the bulk density obtained from NIST [30]. Thereby, the gas in the adsorption layer can be stated as the adsorbed gas, while the gas located in the pore center can be taken as the free gas. As for CH_4, when pressure is larger than 35 bar, a second weak adsorption layer can form in the location adjacent to the first adsorption layer, while *n*-C_4H_{10} forms such a second adsorption layer when system pressure is larger than 0.4 bar. As the bulk pressure increases, the second adsorption layer becomes more pronounced due to the stronger interactions between molecules, as depicted in Fig. 4-5. Compared with CH_4, the second adsorption layer of *n*-C_4H_{10} is stronger due to the stronger molecule/molecule interactions. On the contrary, at a relatively lower pressure, CH_4 or *n*-C_4H_{10} molecules form only one adsorption layer; beyond this adsorption layer, the density is slightly higher than the bulk density, which corresponds to a transition zone

in the density profiles [31,34]. Furthermore, we observe that, the density of the adsorption layers of CH_4 and n-C_4H_{10} increases with pressure. Therefore, it may not be appropriate to use a constant density value to represent the density of the adsorption phase [5,8].

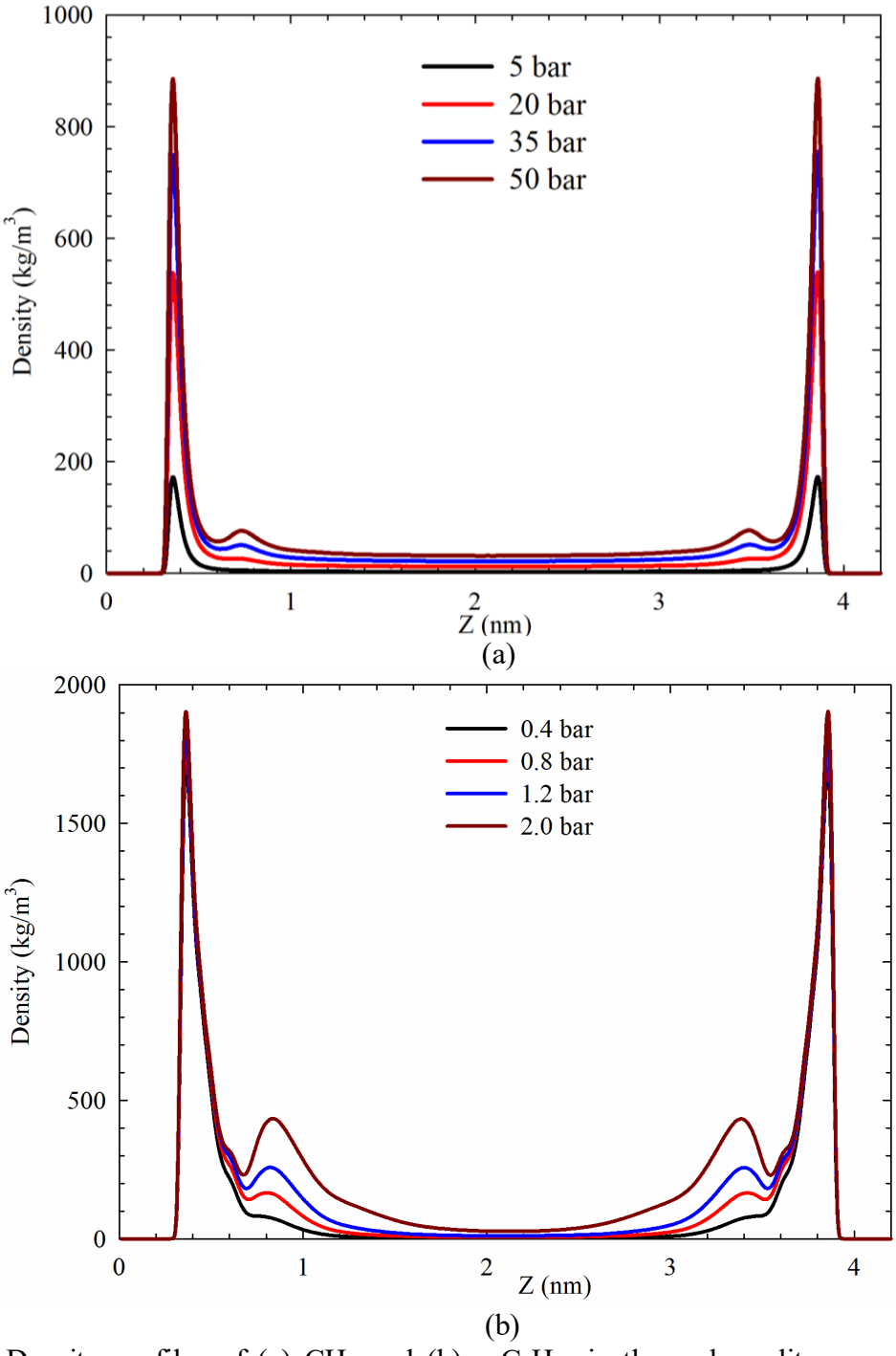

Figure 4-5 Density profiles of (a) CH_4 and (b) n-C_4H_{10} in the carbon-slit pore of 4.2 nm at 368.15 K and different pressures.

4.4.1.2 Effect of System Temperature

Fig. 4-6 shows the density distributions of CH_4 or *n*-C_4H_{10} molecules in a carbon-slit pore of 4.2 nm under different system temperatures. As the system temperature decreases, the density of the adsorption layer increases. However, as temperature increases, adsorption of CH_4 or *n*-C_4H_{10} is significantly suppressed, which is manifested by the drops in the density of the two adsorption layers; this observation is in line with a previous study by Ambrose *et al.* (2012) [14]. It is due to the weaker fluid/surface interaction at higher temperatures. Comparatively, the density of the two adsorption layers of *n*-C_4H_{10} is higher than that of CH_4. It is probably because the surface attraction of the carbon wall to *n*-C_4H_{10} is stronger than that to CH_4, which greatly enhances the adsorption of the heavier alkane, *n*-C_4H_{10}.

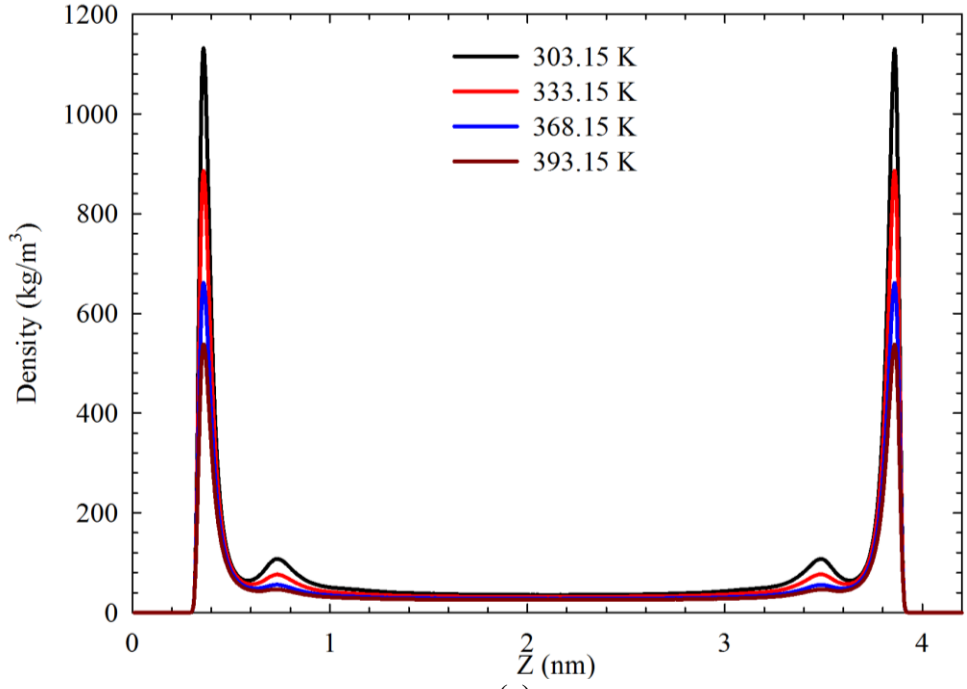

(a)

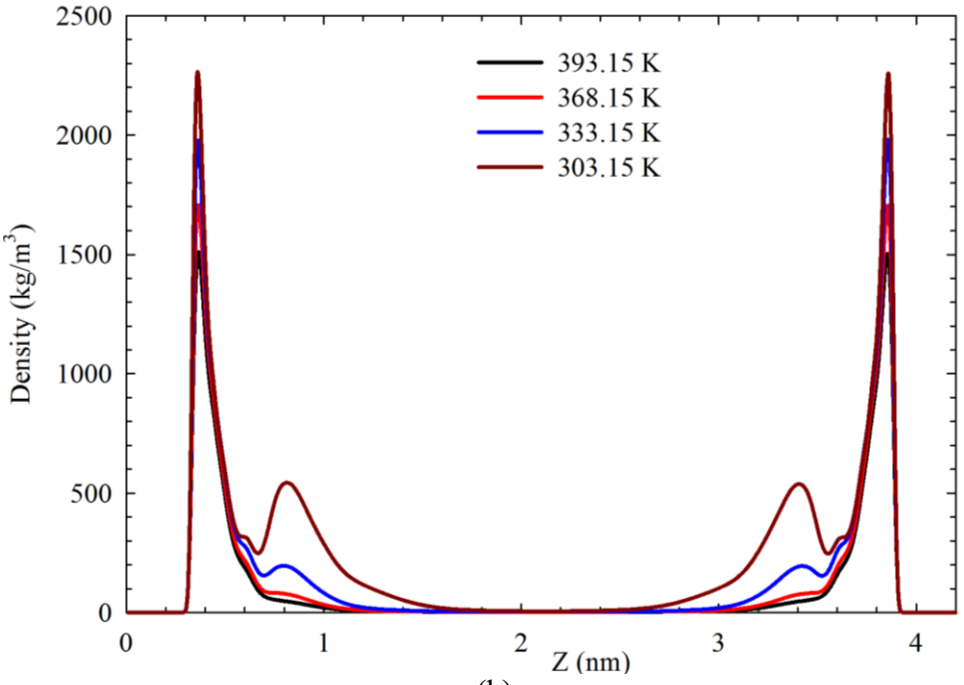

(b)

Figure 4-6 Density profiles of (a) CH_4 in the carbon-slit pore of 4.2 nm at 50 bar and (b) n-C_4H_{10} in the carbon-slit pore of 4.2 nm at 0.4 bar.

4.4.1.3 Effect of Pore Size

To reveal the effect of pore size on density profiles, in Fig. 4-7, we present the density distributions of CH_4 and n-C_4H_{10} molecules in carbon-slit pores of 1.0, 3.3, 4.2, and 5.0 nm. In

pores with a size larger than 1.0 nm, CH_4 and *n*-C_4H_{10} molecules can form two adsorption layers, while, in the 1.0 nm pore, only one adsorption layer forms on the pore surface due to the limited pore space. In addition, the density in the center of 4.2 nm and 5.0 nm pores approaches the bulk, while the density in the center of 1.0 nm pore is much higher than the bulk value. As the pore size becomes as narrow as 1.0 nm, the packing of molecules in the pore center becomes tighter due to the enhanced attraction forces from the both sides of the pore, leading to the much higher density in the central location of the pore [32,33]. It indicates that there is no free-gas region in such nanopores. It is interesting to observe from Fig. 4-7 that the density profiles exhibited by CH_4 molecules in the 3.3 nm pore well resemble those in the 4.2 nm and 5.0 nm pores. It implies that once the pore size is larger than a certain value, a change in the pore size will not affect the configuration of the adsorption layers formed by the CH_4 molecules. As for *n*-C_4H_{10}, the density of the free-gas phase in 3.3 nm pore is much higher than those in 4.2 nm and 5.0 nm pores, while the adsorption phase in the 3.3 nm pore well resembles that in the 4.2 nm and 5.0 nm pores. It is clear that the fluid distributions in nanopores can be greatly affected by the pore size. Our results indicate that fluid distributions of CH_4 and *n*-C_4H_{10} vary in response to the changes in system pressure, temperature, and pore size.

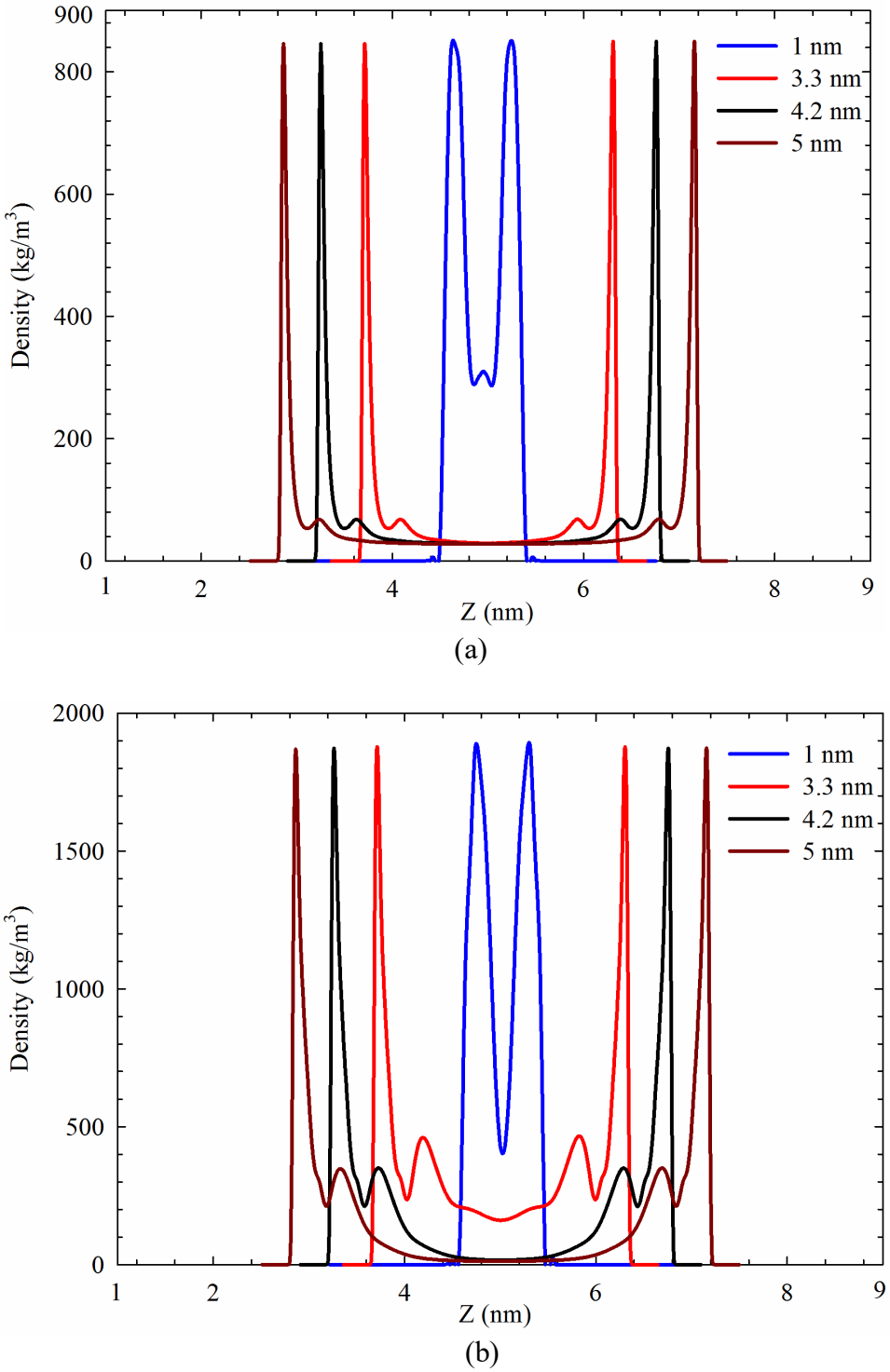

Figure 4-7 Density profiles of (a) CH_4 in the carbon-slit pores of 1.0, 3.3, 4.2, and 5.0 nm at 333.15 K and 45 bar and (b) *n*-C_4H_{10} in the carbon-slit pores of 1.0, 3.3, 4.2, and 5.0 nm at 368.15 K and 1.6 bar.

4.4.1.4 Identification of the Adsorption Phase

One issue needs to be addressed herein, i.e., how to determine the cutoff distance that separates the free-gas phase and the adsorption phase. As can be observed from Fig. 4-7, in mesopores (2-50 nm), two adsorption layers are formed, and the density in the pore center approaches that in the bulk. However, in micropores (<2 nm), only one adsorption layer is formed and the density in the pore center is much higher than bulk. This observation is in line with the previous study by Tian *et al.* (2017) [34]. As a result, in micropores, it is not justifiable to use the adsorption model in Fig. 4-4. Considering the two studied shale cores mainly contain mesopores, we thus can define the free-gas phase and the adsorption phase.

We use CH_4 adsorption in 4.2 nm carbon-slit pore as an example to illustrate the methodology for determining the adsorption phase. Fig. 4-8 presents the density distributions of CH_4 confined in the carbon-slit pore of 4.2 nm at 333.15 K and 50 bar. As shown in this figure, the adsorption phase is defined as the region between *a* (or *a*') and *b* (or *b*'). The volume between points *a* and *a'* is depicted as the all accessible pore volume of the bulk free gas [34]. Point *b* (or *b*') is the saddle point between the first adsorption layer and the second weak adsorption layer. The width of the adsorption phase of CH_4 (*ab*), around 0.37 nm, is similar to the diameter of CH_4 molecule. For *n*-C_4H_{10}, the width of the adsorption phase, around 0.42 nm, is also similar to the diameter of *n*-C_4H_{10} molecules. It indicates that CH_4 and *n*-C_4H_{10} generally exhibits single-layered Langmuir adsorption on pore surface under the experimental conditions, which agrees well with the previous studies [35,36]. Using this methodology, we can determine the width of the adsorption phase for CH_4 or *n*-C_4H_{10} in 3.3 nm and 4.2 nm pores under the experimental pressure/temperature conditions. It is noted that 4.2 and 3.3 nm are the dominant pore sizes of shale sample #1 and #2, respectively. As shown in Fig. 4-5, it is found that, at a given

temperature, the width of the adsorption phase remains almost unchanged as the system pressure increases. However, Fig. 4-6 shows that, at a given pressure, the width of the adsorption phase increases as the system temperature increases. At a higher temperature, the larger width is probably resulted from the weaker carbon surface/gas interactions.

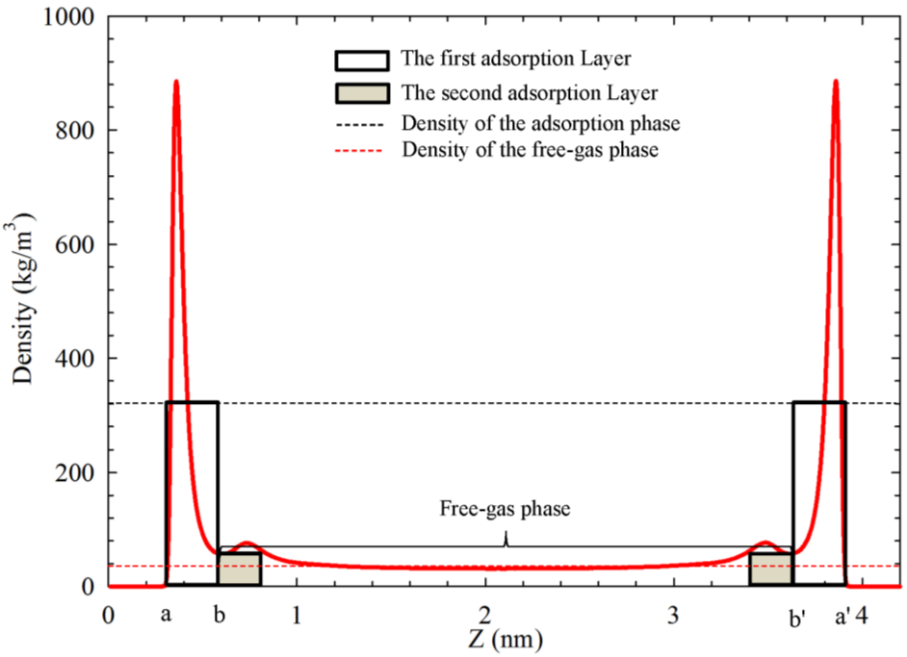

Figure 4-8 Density profile of CH_4 in the carbon-slit pore of 4.2 nm at 368.15 K and 50 bar.

4.4.2 Average Density of the Adsorption Phase

By knowing the width of the adsorption phase, the average density of the adsorption phase for CH_4 or n-C_4H_{10} can be thereby calculated by $\rho_{ave} = \int_a^b \rho_{ads}(z)dz / z_{ab}$ (ρ_{ave} is the average density of the adsorption phase; ρ_{ads} is the *in-situ* density of the adsorption phase; and z_{ab} is the distance between *a* and *b*) (See Fig. 4-8). Figs. 4-9 and 4-10 show the average density of the adsorption phase for CH_4 and n-C_4H_{10}, respectively; we calculate the density of the adsorption phase of CH_4 or n-C_4H_{10} in carbon-slit pores of 3.3 and 4.2 nm at different pressures and temperatures. We find that the average density of the adsorption phase of CH_4 or n-C_4H_{10} in 3.3 nm pore is identical to that in 4.2 nm pore. Furthermore, as for CH_4 and n-C_4H_{10}, the average

density of the adsorption phase strongly correlates with the system pressure and temperature: it increases as the system pressure increases (or as the system temperature decreases).

Fig. 4-9 also shows the density of liquid CH_4, 421 kg/m^3 [5] and another constant density of CH_4 calculated from the van der Waals constant *b* [10,13,37]. It is noted that the liquid CH_4 density has been extensively used as the density of the adsorption phase to obtain the absolute adsorption isotherms [5] or fit empirical models to the adsorption isotherms [3,37,38]. The constant value of 421 kg/m^3 is mostly used. The constant density of CH_4 based on the van der Waals constant *b* is also heavily used to represent the density of the adsorption phase, i.e., 1/*b* [10,13,37]. Fig. 4-10a also shows the density of liquid *n*-C_4H_{10} calculated from the van der Waals constant *b*, 502 kg/m^3. Since the saturated liquid density of *n*-C_4H_{10} is known to correlate with system temperature, the following correlation can be used to calculate the saturated liquid density of *n*-C_4H_{10}, as depicted in Fig. 4-10b [39],

$$\log_{10}\left(\frac{\rho_{nC_4H_{10}}}{1000}\right)=\log_{10}(h)-\log_{10}(l)\left(1-\frac{T}{T_c}\right)^n \tag{4-13}$$

where $\rho_{nC_4H_{10}}$ is saturated density of *n*-C_4H_{10}, kg/m^3; T_c is the critical temperature of *n*-C_4H_{10}; *h*, *l*, and *n* are coefficients with values of 0.2283, 0.2724, and 0.2863, respectively. The critical pressure and temperature of *n*-C_4H_{10} used are listed in Table 4-2. It is clear that, as for either CH_4 or *n*-C_4H_{10}, the density of the adsorption phase should be a variable which depends on the *in-situ* temperature/pressure, rather than a constant value.

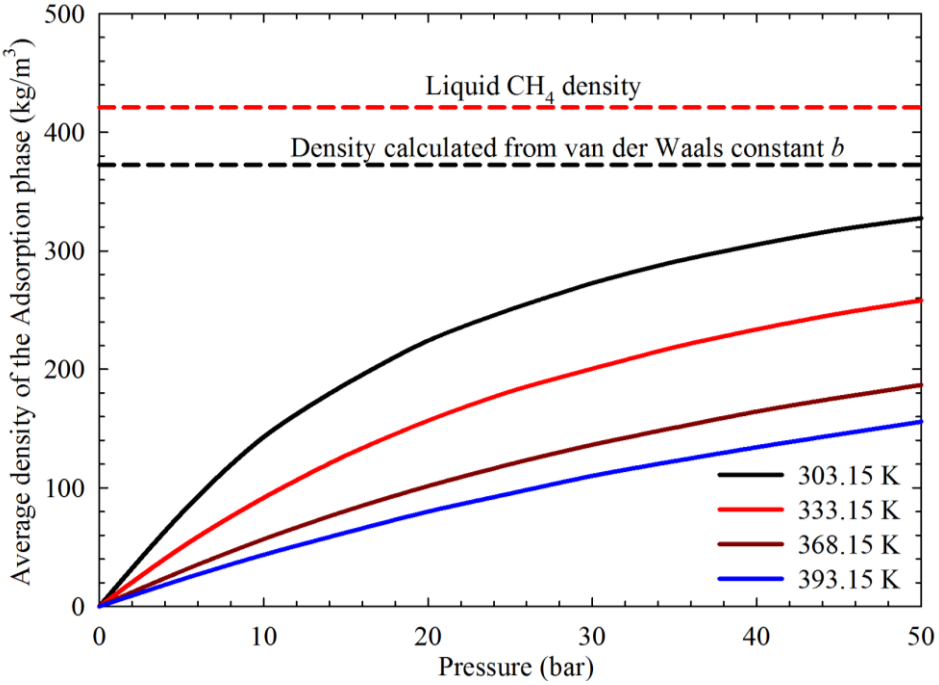

Figure 4-9 Average density of the adsorption phase of CH_4 confined in the carbon-slit pore of 3.3 nm and 4.2 nm at different temperatures and pressures. The constant density of liquid CH_4 and the density calculated from van der Waals constant *b* are also shown in this figure. It should be noted that the average density of the adsorption phase of CH_4 confined in 3.3 nm pore is identical to that in the 4.2 nm pore.

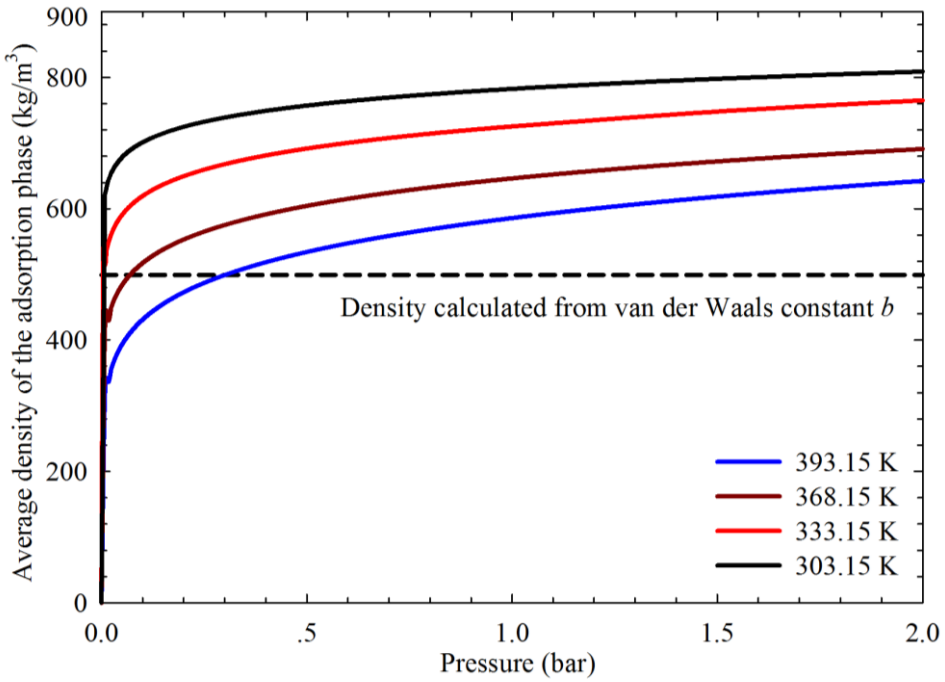

(a)

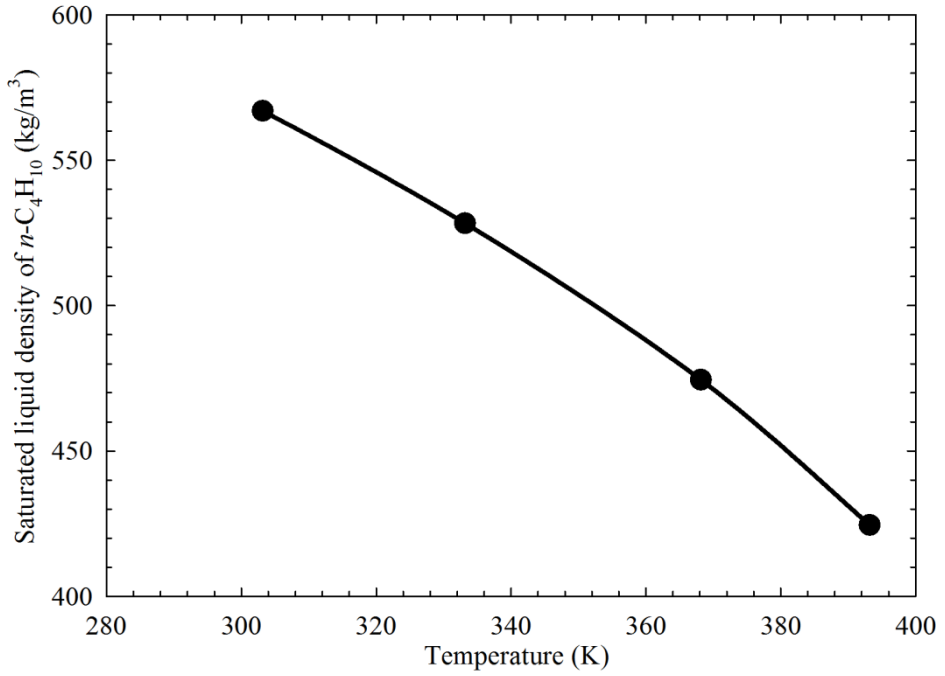

(b)

Figure 4-10 (a) Average density of the adsorption phase of *n*-C_4H_{10} confined in the carbon-slit pore of 3.3, and 4.2 nm at different temperatures and pressures: The constant density of liquid *n*-C_4H_{10} calculated from van der Waals constant *b* is also shown in this figure; (b) Saturated liquid density of *n*-C_4H_{10} as a function of temperature is calculated by Equation (4-13). It should be noted that the average density of the adsorption phase of *n*-C_4H_{10} confined in 3.3 nm pore is identical to that in the 4.2 nm pore.

Table 4-2 Critical properties of *n*-C_4H_{10} used for density calculation [40].

Adsorbate	T_c (K)	P_c (bar)
n-C_4H_{10}	425.18	37.97

As shown in Fig. 4-8, the free-gas is defined as the region between points *b* and *b*', which covers the second weak adsorption layer. In Fig. 4-11, we compare the average density of the free-gas region of CH_4 in a 4.2 nm pore calculated by the GCMC simulations with the bulk density from NIST [30]. The average density of the free-gas region for CH_4 is calculated by $\rho_f = \int_b^{b'} \rho(z)dz / z_{bb'}$ (ρ_f is the average density of the free-gas phase; ρ is the *in-situ* density of the free-gas phase; and $z_{bb'}$ is the distance between *b* and *b*') (see Fig. 4-8). Fig. 4-11 shows the comparative results at 333.15 K, demonstrating that the density values calculated from GCMC simulations is in a good agreement with the NIST data, especially at relatively low pressures. This proves the reliability of the GCMC simulations. But deviation shows up at pressures larger than 30 bar and increases as pressure further increases. Such deviation can be attributed to the presence of the transition zone [34] (See Fig. 4-5).

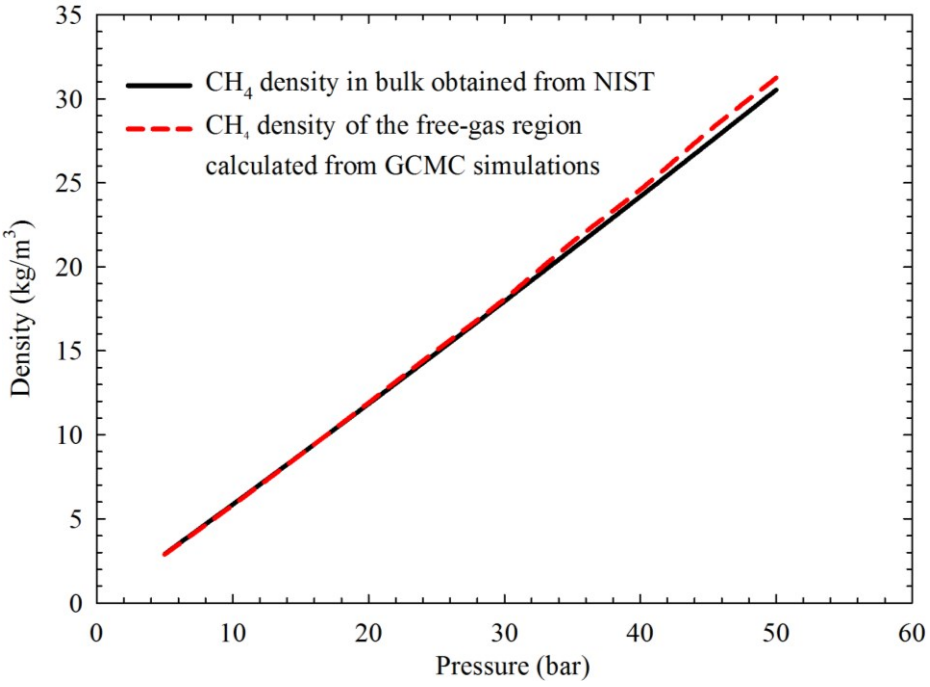

Figure 4-11 Comparisons of CH_4 density of the free-gas region at the carbon-slit pore of 4.2 nm at 333.15 K calculated by GCMC simulations with CH_4 density in bulk obtained from NIST.

4.4.3 Absolute Adsorption/Desorption Isotherms

Since the measured adsorption/desorption isotherms are surface excess quantities, the density of the adsorption phase is required to transform these excess values to absolute ones. Based on the density of the adsorption phase computed from GCMC simulations, we convert the excess adsorption/desorption isotherms to absolute ones. Figs. 4-12 and 4-13 present the converted absolute adsorption/desorption isotherms of CH_4 and *n*-C_4H_{10} on the two shale samples studied. We observe that the absolute adsorption of CH_4 or *n*-C_4H_{10} increases as pressure increases or as temperature decreases. At the same pressure and temperature, *n*-C_4H_{10} has relatively higher adsorption capacity compared to CH_4; it is because pore surface shows stronger attractions towards *n*-C_4H_{10} molecules than CH_4, indicating a higher affinity of *n*-C_4H_{10} towards shale. In shale reservoirs, the heavier hydrocarbons can be more easily to get adsorbed on the shale surface, forming liquid-phase-like structures and showing stronger storage capacity as the adsorbed state [35].

The difference in the adsorption and desorption isotherms is termed as the hysteresis phenomenon. This hysteresis behavior can be attributed to the capillary condensation taking place in nanopores as pressure changes at a given temperature [35,40]. With density functional theory (DFT), Li *et al.* (2014) [35] studied the adsorption/desorption hysteresis of pure CH_4 and pure *n*-C_4H_{10} in a single carbon-slit pore and found that the hysteresis phenomenon for pure component only occurs over a small pressure range at a given temperature. The measured results shown in Figs. 4-13 and 4-14 show that, however, in a real shale sample, the hysteresis phenomenon for CH_4 or *n*-C_4H_{10} appears over the entire pressure range at a given temperature. The real shale samples are porous medium, in which pore size distribution is presented. The hysteresis in shale samples is not as sharp as that in a carbon-slit pore because shale samples comprise of different pore sizes that may show hysteresis at different pressures. As for both CH_4 and *n*-$C_4H_{10,}$ the hysteresis phenomenon is getting more pronounced at a lower temperature. Comparatively speaking, *n*-C_4H_{10} exhibits stronger adsorption/desorption hysteresis than CH_4, which agrees well with the simulation studies based on the use of DFT [35].

Comparing Figs. 4-12 with 4-13, we observe CH_4 or *n*-C_4H_{10} exhibits a higher adsorption capacity on shale sample #1 than shale sample #2. Adsorption strongly correlates with the TOC content and surface area in the shale sample [22]. Thereof, such higher adsorption on shale sample #1 may be caused by the higher TOC content (3.17 wt%) and larger BET surface area (2.98 m^2/g) than those of shale sample #2 (a TOC content of 0.98 wt% and a BET surface area of 2.06 m^2/g). However, Xiong *et al.* (2017) [41] presented that the adsorption capacity does not correlate only with the TOC and surface area but shows a more complex dependence on the petro-physical and mineralogical properties; therefore, to understand the adsorption capacity of CH_4 or *n*-C_4H_{10}, more adsorption data should be measured and other factors, e.g., clay minerals,

should be considered to understand the adsorption behavior.

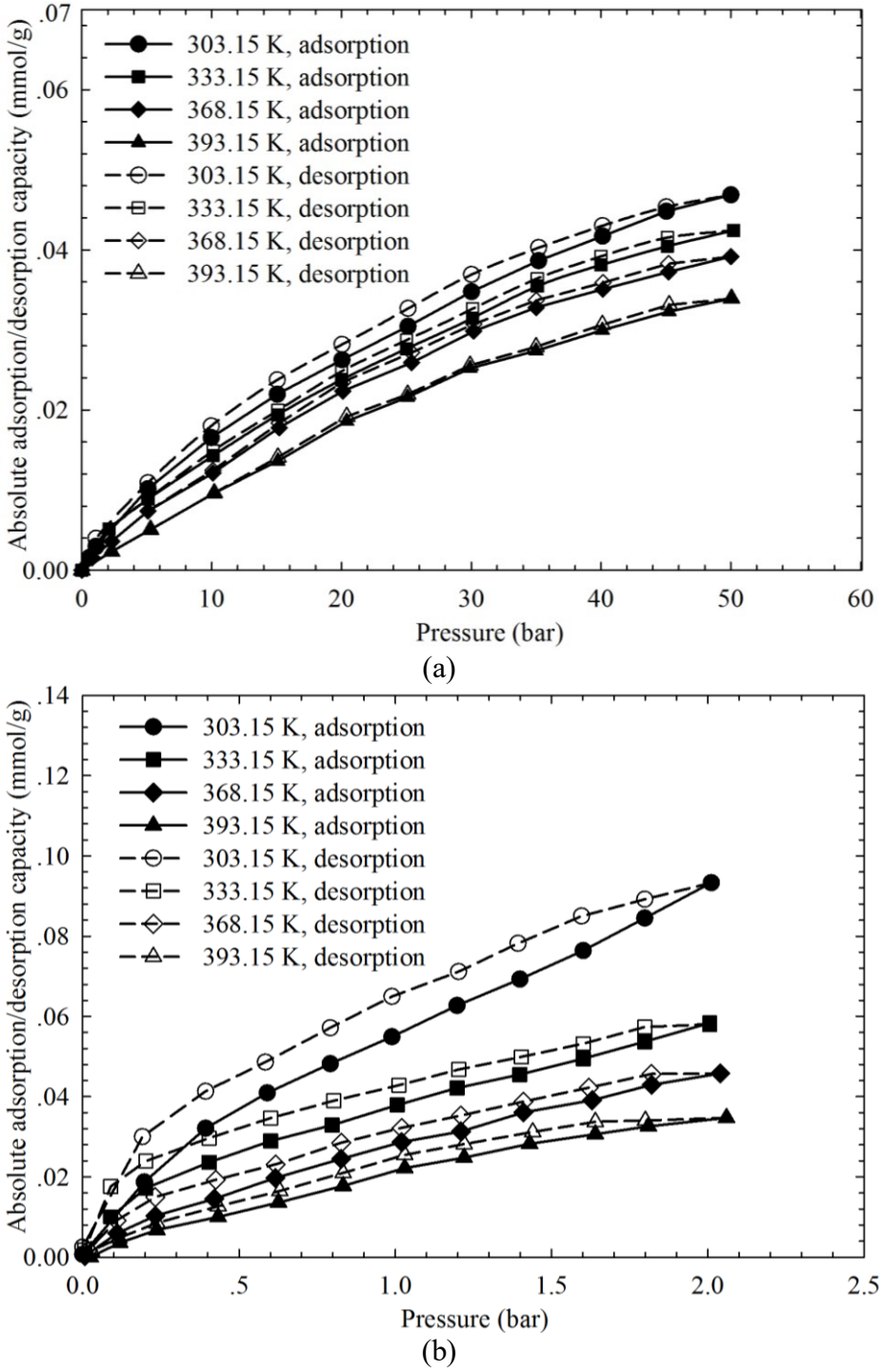

Figure 4-12 Absolute adsorption/desorption isotherms of (a) CH_4 and (b) n-C_4H_{10} on shale sample #1. These isotherms are obtained by converting the excess adsorption/desorption isotherms based on the average density of the adsorption phase calculated by GCMC simulations.

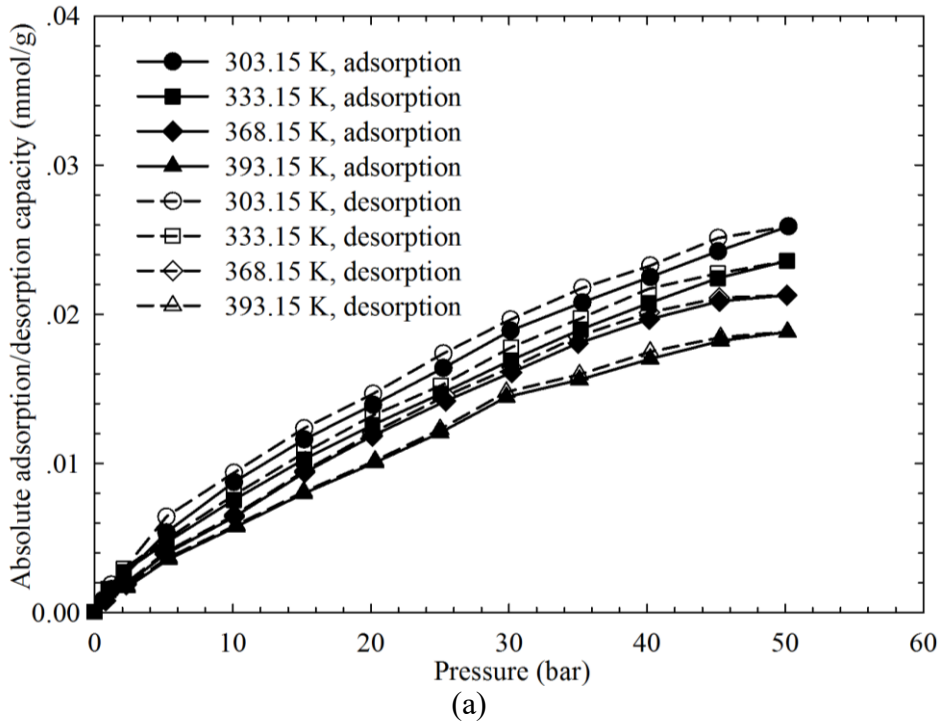

(a)

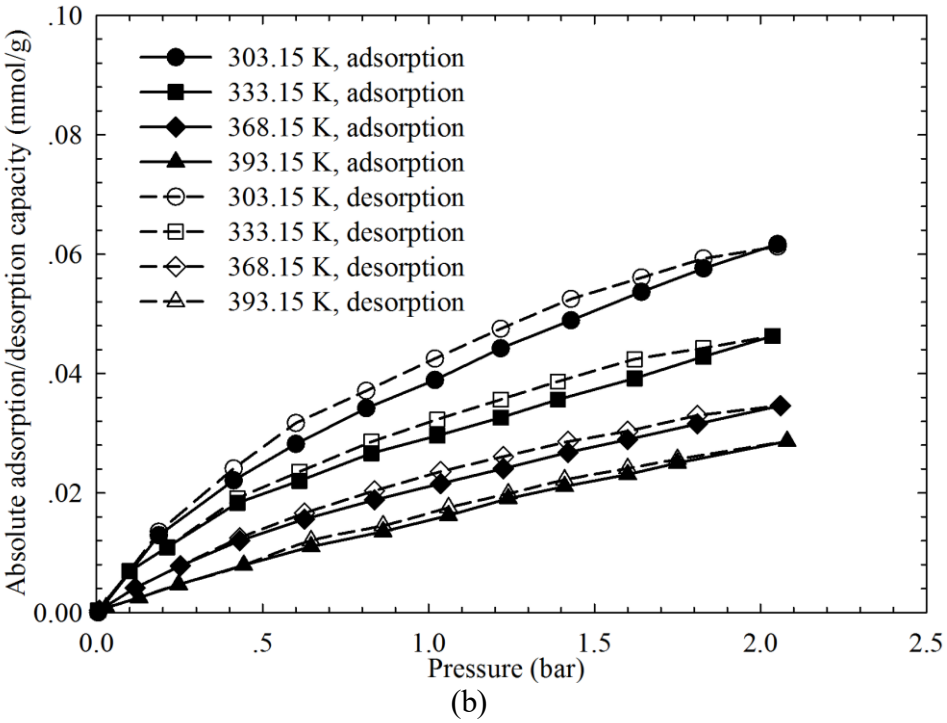

(b)

Figure 4-13 Absolute adsorption/desorption isotherms of (a) CH_4 and (b) n-C_4H_{10} on shale sample #2. These isotherms are obtained by converting the excess adsorption/desorption isotherms based on the average density of the adsorption phase calculated by GCMC simulations.

In Fig. 4-14, we compare the excess adsorption isotherms of CH_4 and n-C_4H_{10} against the

corresponding absolute adsorption isotherms. As mentioned above, the excess adsorption isotherms are converted to the absolute adsorption isotherms using the *in-situ* density of the adsorption phase which are calculated from GCMC simulations. It can be seen from Fig. 4-14a that, as for CH_4, the absolute adsorption is found to be always higher than the directly measured excess adsorption. A relatively large deviation is found to exist between the absolute adsorption isotherms and the excess adsorption isotherms for CH_4, which highlights the importance of using accurate density of the adsorption phase to obtain accurate absolute adsorption isotherms for CH_4. However, as for *n*-C_4H_{10}, the absolute adsorption isotherms are almost identical to the excess adsorption isotherms (See Fig. 4-14b). In this work, we measure the adsorption of *n*-C_4H_{10} on shale samples at pressures only up to 2 bar; under such low pressures, the bulk gas density is far less than the density of the adsorption phase, as seen from Fig. 4-5b. As a result, the term ρ/ρ_a is a value approaching zero. As such, the denominator in the right hand side of Equation 4-3 approaches 1, rendering the absolute adsorption being almost equal to the excess adsorption. This explains why the absolute adsorption isotherms for *n*-C_4H_{10} are almost identical to the excess adsorption isotherms, as shown in Fig. 5-14b.

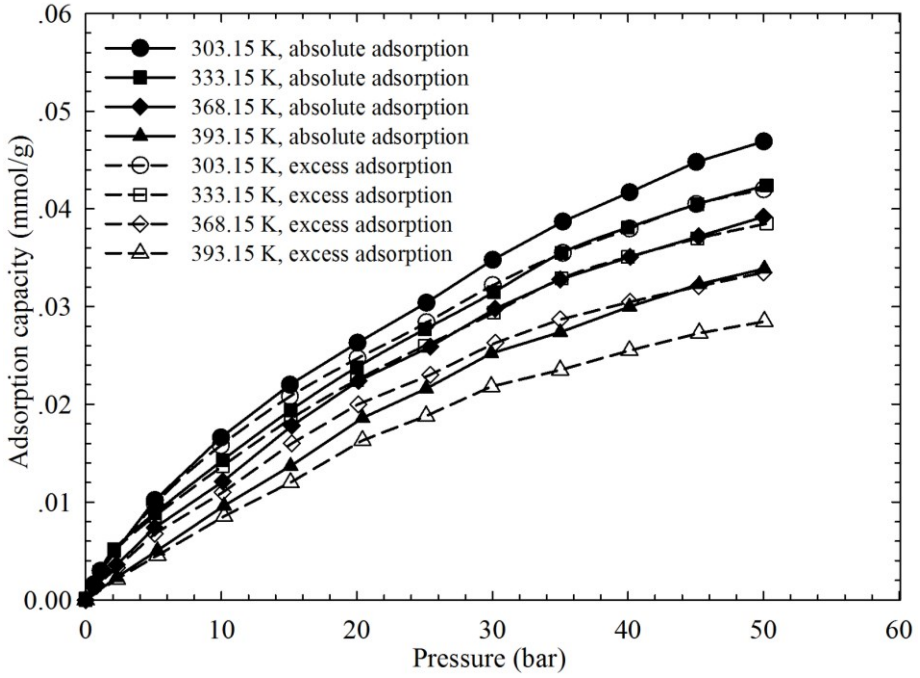

(a)

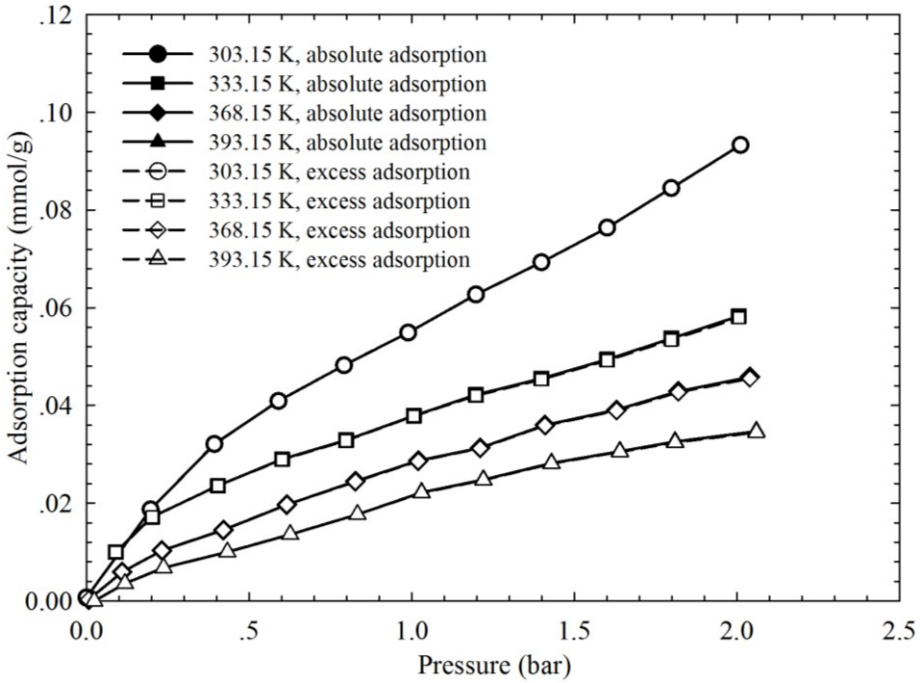

(b)

Figure 4-14 Comparisons of absolute adsorption isotherms with excess ones on shale sample #1: (a) CH_4 and (b) n-C_4H_{10}. The absolute adsorption isotherms have been converted from the excess adsorption isotherms based on density of the adsorption phase which is calculated by GCMC simulations.

4.4.4 Comparison of GCMC-based Approach with Conventional Approach

The liquid density and the density calculated from van der Waals constant *b* are commonly used to approximate the density of the adsorption phase. Herein, the densities calculated from these two conventional approaches are used to convert the measured excess adsorption isotherms to the absolute ones. Thereafter, we compare the absolute adsorption isotherms converted by the two conventional approaches with those calculated from the GCMC simulations. Fig. 4-15 compares the absolute adsorption capacity of CH_4 and *n*-C_4H_{10} on shale sample #1 calculated by GCMC-based approach against that calculated by using the liquid density of CH_4 or *n*-C_4H_{10}, while Fig. 4-16 compares the absolute adsorption capacity of CH_4 and *n*-C_4H_{10} on shale sample #1 calculated by GCMC-based approach against that calculated using the van der Waals constant *b*. As can be seen from Figs. 4-15b and 4-16b, as for *n*-C_4H_{10}, the conventional approaches and the GCMC-based approach provide almost the same conversion results. However, as seen from Figs. 4-15a and 4-16a, the two conventional approaches tend to underestimate the absolute adsorption for CH_4. These aforementioned findings highlight the importance of obtaining an accurate estimation of the adsorption-phase density, especially when one wants to accurately evaluate the total amount of gas-in-place in shale gas reservoirs.

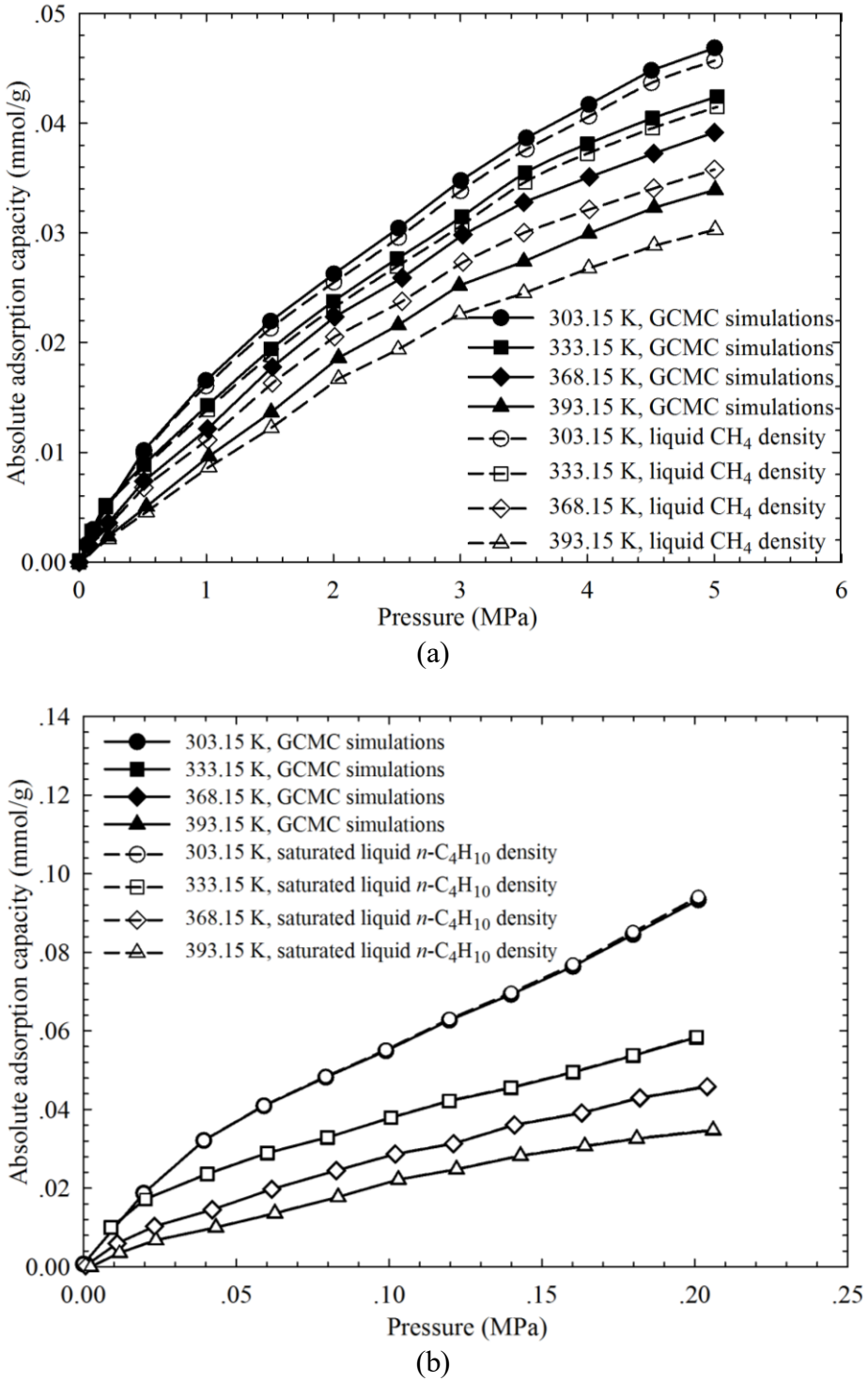

Figure 4-15 Comparisons of absolute adsorption capacity of (a) CH_4 and (b) n-C_4H_{10} on shale sample #1 calculated by GCMC-based approach with that obtained by the liquid density of CH_4 or n-C_4H_{10}.

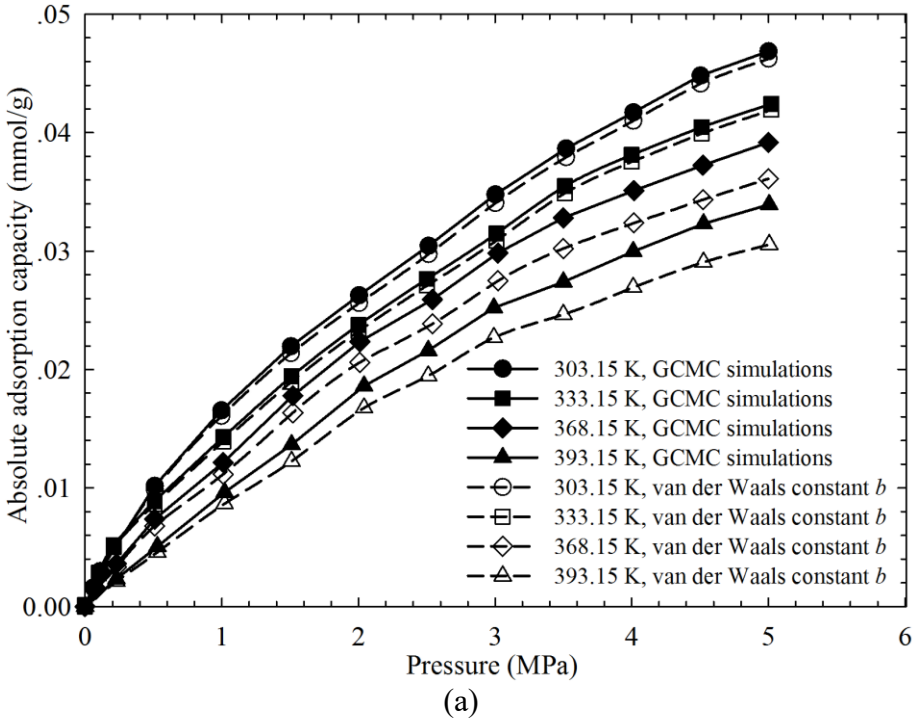

(a)

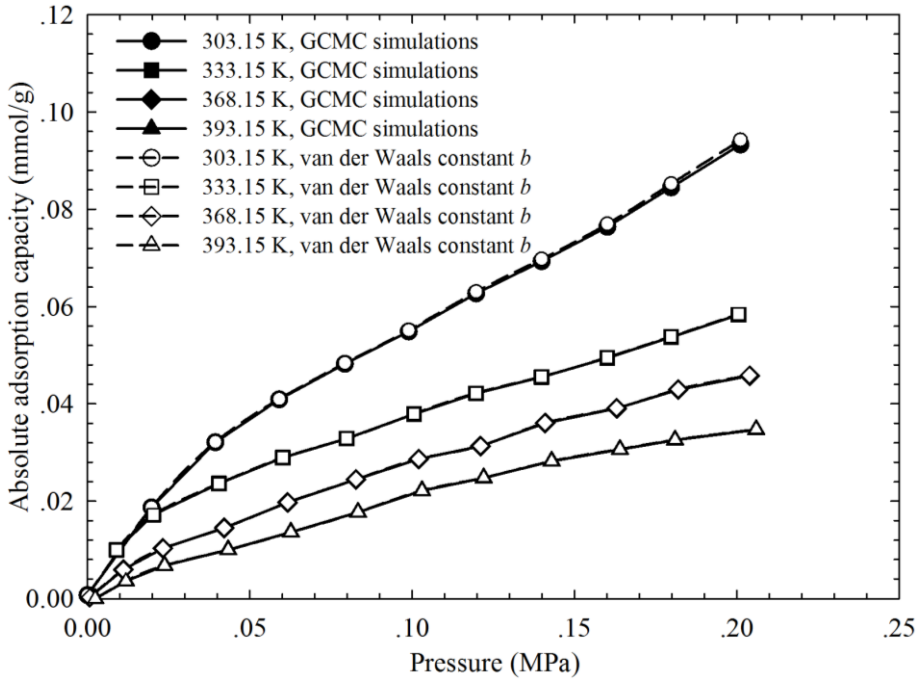

(b)

Figure 4-16 Comparisons of absolute adsorption capacity of (a) CH_4 and (b) *n*-C_4H_{10} on shale sample #1 calculated by GCMC-based approach with that obtained by the density calculated by van der Waals constant *b*.

4.5 Conclusions

In this study, we measure the excess adsorption/desorption isotherms of CH_4 and *n*-C_4H_{10} on two shale samples. Density distributions of CH_4 and *n*-C_4H_{10} in nanopores are investigated with the GCMC simulations. A pragmatic approach is used to estimate the adsorption-phase density based on the GCMC simulations, finding that the density of the adsorption phase correlates with system pressure, temperature, and pore size. Consequently, the *in-situ* density of the adsorption phase is used to convert the excess adsorption/desorption isotherms to the absolute adsorption/desorption isotherms. The following conclusions can be drawn:

- The GCMC simulations show that the density distributions of CH_4 or *n*-C_4H_{10} vary in response to the changes in system pressure, temperature, and pore size. The calculated density of the adsorption phase of CH_4 is always lower than the liquid CH_4 density and, at high pressures, the density of the adsorption phase is found to be very close but never equal or greater than the liquid phase density. The calculated density of the adsorption phase of *n*-C_4H_{10} can be higher than the liquid *n*-C_4H_{10} density.
- More obvious adsorption/desorption hysteresis and higher adsorption capacity are observed for *n*-C_4H_{10} than CH_4. This indicates a higher affinity of *n*-C_4H_{10} towards the two shale samples.
- GCMC simulations can faithfully capture the *in-situ* density of the adsorption phase by better honoring the carbon pore-surface/gas interactions. Compared with the GCMC-based approach, the conventional approaches, on the basis of using a constant density for the adsorption phase, are appropriate for obtaining the absolute adsorption isotherms for *n*-C_4H_{10}, but tend to significantly underestimate the absolute adsorption isotherms for CH_4.

- The adsorption capacity of CH_4 or *n*-C_4H_{10} on the shale sample #1 is much higher than that on the shale sample #2, which may be caused by the fact that the shale sample #1 has a higher TOC content and a larger BET surface area.

Although this work may provide an alternative to correct the measured excess adsorption, there are still some issues needed to be addressed in the future work. Firstly, we only measure the adsorption isotherms at the pressures up to 2 bar for *n*-C_4H_{10} considering the low vapor pressure of *n*-C_4H_{10} at room temperature. It is the drawback in this measurement. If possible, the testing pressures should be as high as the reservoir conditions, which would be more interesting to engineers. Secondly, we only measure the adsorption/desorption isotherms for CH_4 and *n*-C_4H_{10}. However, various hydrocarbon components (C_2H_6, and C_3H_8) and nonhydrocarbon components (CO_2, and N_2) may coexist in shale gas; thereby, more adsorption measurements should be conducted on the other components except CH_4 and *n*-C_4H_{10} to have a comprehensive understanding of the adsorption behavior of components in shale reservoirs. Additionally, shale gas is multi-component system, in which different components present distinct adsorption behavior on shale, exhibiting selective adsorption. Therefore, to better estimate shale gas-in-place storage, excess adsorption isotherms of gas mixtures should be measured and new techniques should be developed to correct the excess ones and obtain the accurate absolute adsorption of gas mixtures on shale.

4.6 References

[1] Ross, D.J.K., and Bustin, R.M. 2009. The Importance of Shale Composition and Pore Structure upon Gas Storage Potential of Shale Gas Reservoirs. *Mar. Pet. Geol.* **26**: 916-927.

[2] Wu, Y., Fan, T., and Jiang, S. *et al.* 2015. Methane Adsorption Capacities of the Lower

Paleozoic Marine Shales in the Yangtze Platform, South China. *Energy Fuels* **29**: 4160-4167.

[3] Gasparik, M., Ghanizadeh, A., Bertier, P. *et al.* 2012. High-pressure Methane Adsorption Isotherms of Black Shales from the Netherlands. *Energy Fuel.* **26**: 4995-5004.

[4] Duan, S., Gu, M., and Du, X. *et al.* 2016. Adsorption Equilibrium of CO_2 and Their Mixture on Sichuan Basin Shale. *Energy Fuels*. **30**: 2248-2256.

[5] Wang, Y., Zhu, Y., and Liu, S. *et al.* 2016. Methane Adsorption Measurements and Modeling for Organic-Rich Marine Shale Samples. *Fuel* **172**: 301-309.

[6] Wang, Y., Tsotsis, T.T., and Jessen, K. 2015. Competitive Adsorption of Methane/Ethane Mixtures on Shale: Measurements and Modeling. *Ind. Eng. Chem. Res*. **54**: 12187-12195.

[7] Pedram, E.O., Hines, A.L., and Cooney, D.O. 1984. Adsorption of Light Hydrocarbons on Spent Shale Produced in a Combustion Retort. *Chem. Eng. Commun*. **27**: 181-191.

[8] Heller, R., and Zoback, M. 2014. Adsorption of Methane and Carbon Dioxide on Gas Shale and Pure Mineral Samples. *J. Unconv. Oil Gas Res*. **8**: 14-24.

[9] Gasparik, M., Bertier, P., and Gensterblum, Y. *et al.* 2014. Geological Controls on the Methane Storage Capacity in Organic-Rich Shales. *Int. J. Coal Geol*. **123**: 34-51.

[10] Dubinin, M.M. 1960. The Potential Theory of Adsorption of Gases and Vapors for Adsorbents with Energetically Nonuniform Surfaces. *Chem. Rev*. **60** (2), 235-241.

[11] Menon, P.G. 1968. Adsorption at High Pressures. *J. Phys. Chem*. **72**: 2695-2696.

[12] Tsai, M.C., Chen, W.N., and Cen, P.L. *et al.* 1985. Adsorption of Gas Mixture on Activated Carbon. *Carbon*. **23** (2), 167-173.

[13] Li, M., Gu, A., and Lu, X. *et al.* 2002. Determination of the Adsorbate Density from Supercritical Gas Adsorption Equilibrium Data. *Carbon*. **41**: 579-625.

[14] Ambrose, R.J., Hartman, R.C., Diaz-Campos, M. *et al.* 2012. Shale Gas-in-place Calculations Part I: New Pore-scale Considerations. *SPE J*. **17** (1), 219-229.

[15] Groen, J.C. *et al.* 2003. Pore Size Determination in Modified Micro- and Mesoporous Materials. Pitfalls and Limitations in Gas Adsorption Data Analysis. *Micropor. Mesopor. Mat*. **60**: 1-17.

[16] Landers, J., Gor, G.Y., and Neimark, A.V. 2013. Density Functional Theory Methods for Characterization of Porous Materials. *Colloids Surf. A: Physicochem. Eng. Aspects* **437**: 3-32.

[17] Martin, M.G., and Siepmann, J.I. 1998. Transferable Potentials for Phase Equilibria. 1. United-Atom Description of n-Alkanes. *J. Phys. Chem. B*. **102** (14): 2569-2577.

[18] Errington, J.R., and Panagiotopoulos, A.Z. 1999. A New Intermolecular Potential Model for the n-Alkane Homologous Series. *J. Phys. Chem. B* **103** (30): 6314-6322.

[19] Singh, S.K., Sinha, A.K., and Deo, G. *et al.* 2009. Vapor-Liquid Phase Coexistence, Critical Properties, and Surface Tension of Confined Alkanes. *J. Phys. Chem. C.* **113** (17): 7170-7180.

[20] Smit, B., Karaborni, S., and Siepmann, J.I. 1995. Computer Simulations of Vapor-liquid Phase Equilibria of *n*-alkanes. *J. Chem. Physics* **102** (5): 2126-2140.

[21] van der Ploeg, P., and Berendsen, H.J.C. 1982. Molecular Dynamics Simulations of a Bilayer Membrane. *J. Chem. Physics* **76** (6): 3271-3276.

[22] Kim, J., Kim, D., Lee, W., Lee, Y. and Kim, H. 2017. Impact of Total Carbon and Specific Area on the Adsorption Capacity in Horn River Shale. *J. Petrol. Sci. Eng*. **149**: 331-339.

[23] Steele, W.A. 1973. The physical Interaction of Gases with Crystalline Solids: I. Gas-Solid Energies and Properties of Isolated Adsorbed Atoms. *Surf. Sci.* **36** (1): 317-352.

[24] Do, D.D., and Do, H.D. 2003. Adsorption of Supercritical Fluids in Non-porous and Porous Carbons: Analysis of Adsorbed Phase Volume and Density. *Carbon*. **41**: 1777-1791.

[25] Hensen, E.J.M., Tambach, T.J., and Bliek, A. *et al.* 2001. Adsorption Isotherms of Water in Li-, Na-, and K-montmorillonite by Molecular Simulations. *J. Chem. Phys.* **115** (7): 3322-3329.

[26] Widom, B. 1963. Some Topics in the Theory of Fluids. *J. Chem. Phys.* 39 (11): 2808-2812.

[27] Peng, D., Robinson, D.B. 1976. A New Two-Constant Equation of State. *Ind. Eng. Chem. Fund*. **15** (1): 59-64.

[28] Metropolis, N., Rosenbluth, A.W., and Rosenbluth, M.N. *et al.* 1953. Equation of State Calculations by Fast Computing Machines. *J. Chem. Phys*. **21** (6): 1087-1092.

[29] Jin, Z., and Firoozabadi, A. 2016. Phase Behavior and Flow in Shale Nanopores from Molecular Simulations. *Fluid Phase Equilibr.* **430**: 156-168.

[30] Lemmon, E.W., McLinden, M.O., and Friend, D.G. 2009. Thermophysical Properties of Fluid Systems. *In NIST Chemistry WebBook*, NIST Standard Reference Database Number 69; National Institute of Standards and Technology: Gaithersburg MD.

[31] Didar, B.R. and Akkutlu, I.Y. Pore-size Dependence of Fluid Phase Behavior and Properties in Organic-Rich Shale Reservoirs. *SPE International Symposium on Oilfield Chemistry*. Woodlands, Texas, USA, 2013.

[32] Liu, Y., Wilcox, J. 2012. Molecular Simulations of CO_2 adsorption in Micro- and Mesoporous Carbons with Surface Heterogeneity. *Int. J. Coal Geol*. **104**: 83-95.

[33] Chen, G., Zhang, J., Lu, S. *et al.* 2016. Adsorption Behavior of Hydrocarbon on Illite. *Energy Fuels*. **30**: 9114-9121.

[34] Tian, Y., Yan, C., and Jin, Z. 2017. Characterization of Methane Excess and Absolute

Adsorption in Various Clay Nanopores from Molecular Simulation. *Sci. Rep.* **7**: 12040.

[35] Li, Z.D., Jin, Z.H., and Firoozabadi, A. 2014. Phase Behavior and Adsorption of Pure Substances and Mixtures and Characterization in Nanopores Structures by Density Functional Theory. *SPE J*. **19** (6): 1096-1109.

[36] Dong, X., Liu, H., Hou, J., Wu, K., Chen, Z. 2016. Phase Equilibria of Confined Fluids in Nanopores of Tight and Shale Rocks Considering the Effect of Capillary Pressure and Adsorption Film. *Ind. Eng. Chem. Res*. **55**: 798-811.

[37] Rexer, T.F.T., Benham, M.J.; Aplin, A.C., and Thomas, K.M. 2013. Methane Adsorption on Shale under Simulated Geological Temperature and Pressure Conditions. *Energy Fuels*. **27**: 3099-3109.

[38] Weniger P., Kalkreuth, W., and Busch, A. *et al.* 2010. High-pressure Methane and Carbon Dioxide Sorption on Coal and Shale Samples from the Paraná Basin, Brazil. *Int. J. Coal. Geol*. **84**: 190-205.

[39] Yaws, C.L. 2003. Yaws' Handbook of Thermodynamic and Physical Properties of Chemical Compounds. Knovel Corporation, New York, NY.

[40] Bryan, W.P. 1987. Sorption Hysteresis and the Laws of Thermodynamics. *J. Chem. Educ*. **64** (3): 209-212.

[41] Xiong, F., Wang, X., and Amooie, N. *et al.* 2017. The Shale Gas Sorption Capacity of Transitional Shales in the Ordos Basin, NW China. *Fuel* **208**: 236-246.

[42] Firoozabadi, A. 2016. Thermodynamics and Applications in Hydrocarbon Energy Production, McGraw Hill, New York.

CHAPTER 5 PHASE BEHAVIOR OF N_2/n-C_4H_{10} IN A PARTIALLY CONFINED SPACE DERIVED FROM SHALE SAMPLE

A version of this chapter was presented at the SPE Annual Technical Conference and Exhibition held on 26-28 September 2016 in Dubai, UAE and has been accepted for publication in *Journal of Petroleum Science and Engineering*.

Abstract

Phase behavior of shale fluids in small pores is not well understood. One complexity comes from the fact that sorption of components by organic-rich shale can be significant and selective. In an attempt to elucidate the effect of sorption on phase behavior of shale fluids, we present a new experimental method that can be used to measure the bubble-point pressures of N_2/n-C_4H_{10} mixtures in the presence of an actual shale sample. Pressure/volume (P/V) isotherms for a given mixture were firstly measured in a PVT cell. Then, the measurements of the P/V isotherms for the same mixture were repeated in a partially confined space by opening a valve between the PVT cell and a shale container. The so-called partially confined space consists of the pore space inside the shale sample, the bulk space in the PVT cell and in the connecting tubing, and the non-cementing pore spaces among the shale particles. Results show that, the measured bubble-point pressure of the N_2/n-C_4H_{10} mixture in the partially confined space was higher than the corresponding bubble-point pressure in the bulk space. A detailed analysis indicates that, when loaded in the partially confined space, n-C_4H_{10} exhibits a higher level of sorption capacity on the shale sample than N_2, resulting in a higher concentration of N_2 left in the free fluid than that in the initial mixture, which is the so-called selective sorption. The higher concentration of N_2 led to the higher bubble-point pressure as observed in the measurements. The increase of the bubble-point pressure due to the selective sorption was observed to be greater at a lower temperature. This is because the sorption of n-C_4H_{10} relative to that of N_2 is more significant at a lower temperature. A higher temperature did not lead to a higher increment in the bubble-point pressure likely because bubble-point is more sensitive to composition than to temperature for these mixtures at the conditions tested. This emphasizes the importance of considering sorption in phase behavior for small pores.

Keywords: Partially confined space; Sorption; Bubble-point pressure; Shale sample

5.1 Introduction

Unlike conventional reservoirs, shale reservoir possesses unique characteristics, such as ultra-low permeability and strong heterogeneity. Nano-scale pores are dominant pores in shale reservoirs, and their diameters are normally between 1-20 nm (Nagarajan *et al.*, 2013). Thermodynamics and phase equilibria of fluids in nano-pores (called "confined spaces") are more complicated than those in bulk spaces. In such pores, the in-situ phase behavior in confined spaces is affected by pore wall-fluid interaction, capillary pressure, and sorption of hydrocarbon on shale material (Li *et al.*, 2014; Jin and Firoozabadi, 2016).

Extensive studies are devoted to understanding the phase behavior of shale fluids. Some modeling studies were conducted to describe phase behavior of shale fluids in confined spaces. Nojabaei *et al.* (2013) coupled capillary pressure with phase equilibrium relation to describe phase behavior of confined fluids by use of the Peng-Robinson equation (PR EOS) (Peng and Robinson, 1976). They reported that small pores decreased bubble-point pressures, and either decreased or increased dew-point pressures. Travalloni *et al.* (2014) modeled phase behavior of confined fluids in homogeneous and heterogeneous porous media using an extended PR EOS. Their modeling study showed that small pores may confine phases with very similar or very different densities and compositions. Dong *et al.* (2016) numerically studied phase equilibrium of pure components and their mixtures in cylindrical nano-pores using the PR EOS coupled with capillary pressure and adsorption theory. The reduction of pore diameter was considered in their model due to the existence of adsorption film. Wang *et al.* (2016) numerically investigated the effect of pore size distribution on phase transition of hydrocarbon mixtures in nano-porous media. They presented a procedure to simulate the sequence of phase transition in nano-porous

media, and found that a phase change always occurs firstly in the larger pores, and then in the smaller pores.

Experimental studies on the phase behavior of fluids contained in the nano-pore spaces of shale are, however, relatively scarce in the literature. Morishige *et al.* (1997) measured adsorption isotherms of pure gases on meso-porous MCM-41 molecular sieves with different pore sizes. Their experimental adsorption data showed that the critical temperatures of pure fluids in meso-pores were quite different from those in the bulk space. Yan *et al.* (2013) applied differential scanning calorimetry and temperature-dependent X-ray diffraction technology to obtain phase behavior of n-tridecane/n-tetradecane mixtures in the bulk and in the confined porous glass. The mixtures showed a similar phase behavior to the bulk, especially in larger pores than 30 nm. Under confinement, their phase behavior varied with pore size as well as temperature and composition. Wang *et al.* (2014) applied nano-fluidic devices to visualize phase changes of pure alkane and alkane mixtures under nano-confinement. The vaporization of liquid phase in nano-channels (5 μm wide by 100 nm deep) was remarkably suppressed in comparison to that in micro-channels (10 μm wide by 10 μm deep). Pure alkanes and alkane mixtures exhibited different vaporization behavior; this was because the liberation of lighter components from the liquid phase to the gas phase in the micro-channels increased the apparent molecular weight of the liquid in the nano-channels, suppressing its bubble point (Wang *et al.,* 2014). Alfi *et al.* (2016) investigated phase behavior of pure Hexane, Heptane, and Octane inside nano-channels of 50 nm using lab-on-a-chip technology integrated with high-resolution imaging techniques. They found that, in a nano-channel with a width of 50 nm, the confinement effect in the form of wall-molecule interactions was almost negligible. Luo *et al.* (2016) experimentally explored the relationship between saturation temperature and pore diameter for n-hexane, n-octane, and n-

decane that were confined in silicate nano-porous materials CPG-35 using differential scanning calorimetry. They observed that the saturation temperature in nano-pores was higher than that in a bulk space.

To summarize, extensive studies have been conducted to elucidate the effect of capillary pressure on the phase behavior of confined fluids. However, the effect of sorption on the phase equilibrium of shale fluids is scarcely investigated, although it is an important and common phenomenon in shale reservoirs. To our knowledge, no publications have reported experimental data on the phase behavior of fluids in the presence of real shale materials.

n-C_4H_{10}, as a nonvolatile hydrocarbon, is a common component present in the shale gas-condensate reservoirs; N_2, as a volatile non-hydrocarbon component, can be introduced into the reservoir as an energized fluid used during an energized fracturing treatment. Furthermore, N_2 has been found to be a main component that can be produced from some shale reservoirs, e.g., Antrim shale and Barnett shale. Hence, the N_2/n-C_4H_{10} binary is selected to elaborate the effect of sorption on the in-situ phase behavior of shale fluid. This paper presents an experimental study on the phase behavior of two binary mixtures in a partially confined space. Figure 5-1 illustrates the physical model representing a partially confined space, which consists of a bulk space and a confined space. The major objective is to explore the impact of sorption on fluid phase behavior. The experimental section shows the materials, the experimental setup and the procedures adopted in this study. Bubble-point pressures for the binary mixtures were measured firstly in a bulk space, and then in a partially confined space. The results and discussion section presents the experimental results and major findings in this study. We delineate the reasons leading to differences in bubble-point pressure between the bulk and the partially confined space. To our knowledge, this is the first time that the effect of sorption on the phase behavior of fluid

mixtures in the presence of real shale is measured.

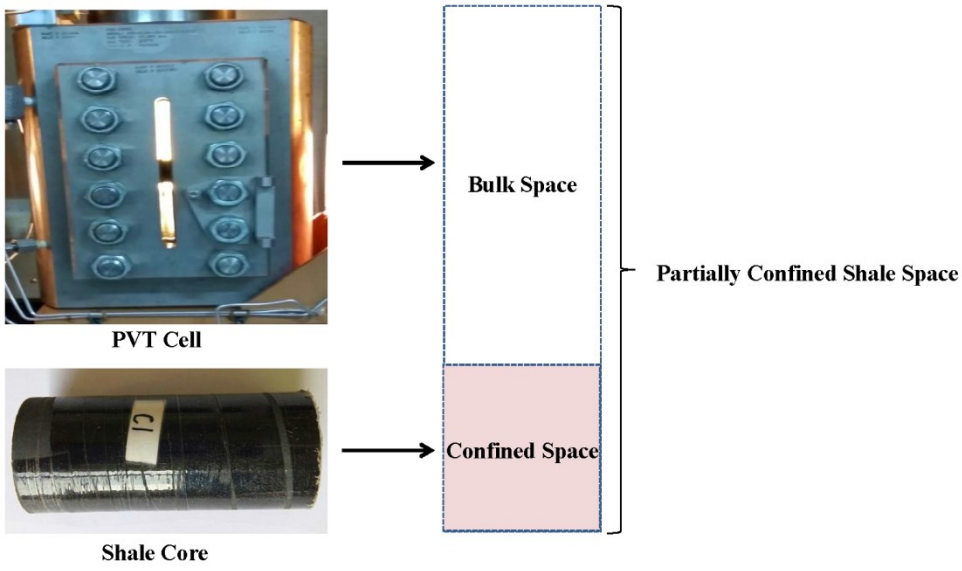

Figure 5-1 Schematic diagram of the partially confined space that consists of a bulk space and a confined shale space.

5.2 Experimental Section

5.2.1 Materials

The purities of N_2 and n-C_4H_{10} (Praxair, Canada) used in this research are 99.998 mol% and 99.99 wt%, respectively. Two hydrocarbon-wetting shale cores were used in the tests. Both shale cores (#1 and #2) were retrieved from Devonian formation in Canada.

5.2.2 Experimental Setup

Pressure/volume (P/V) isotherm measurements for N_2/n-C_4H_{10} mixtures were carried out with a conventional PVT apparatus (Schlumberger DBR, Edmonton, Canada). The operation limits for the PVT cell equipped in the PVT setup are 200,000 kPa and 473.15 K. The total sample capacity of the PVT cell is 124.0 cm^3. The pressure of the PVT cell is controlled by a high-pressure positive displacement pump (PMP-500-1-20-HB, Schlumberger DBR, Edmonton, Canada). The temperature of the system is controlled by an air bath with an accuracy of ±0.1 K.

A cathetometer directly measures a fluid volume in the PVT cell by the height of the fluid. The uncertainty of the volume measurement is ±0.016 cm^3. In order to obtain a highly accurate fluid pressure, a pressure gauge (901A-15K-232P-R5, Ashcroft Inc, Stratford, USA) was used to measure the fluid pressure with an accuracy of ±1 kPa.

5.2.3 Experimental Procedures

This section describes the N_2 adsorption/desorption test used for characterizing both shale cores (#1 and #2), the procedure of total organic carbon (TOC) measurement for shale cores, the measurement of system volumes, and the constant composition expansion (CCE) method for measuring P/V isotherms. Figure 5-2 shows the schematic diagram of the experimental setup for measuring P/V isotherms of N_2/n-C_4H_{10} mixtures.

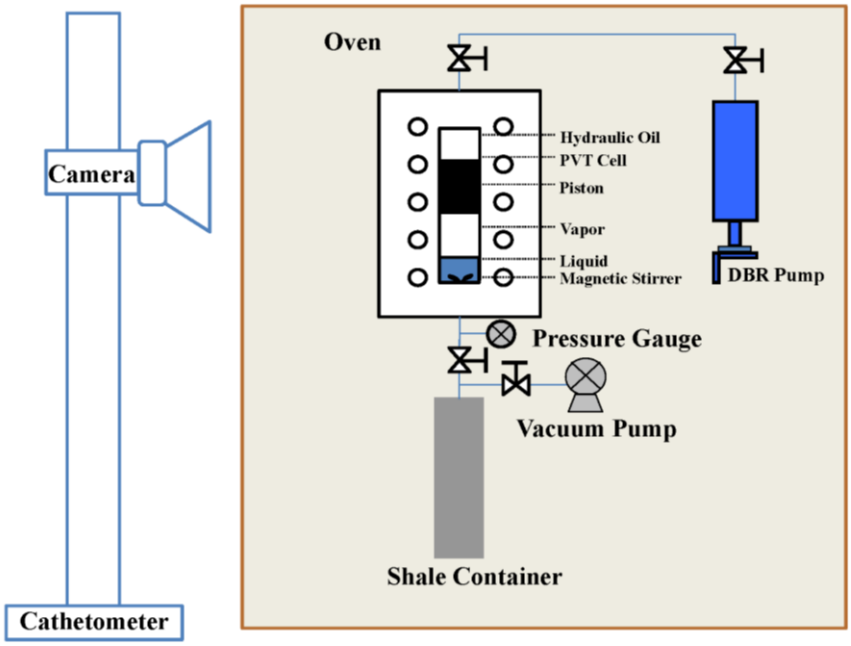

Figure 5-2 Schematic diagram of the experimental setup for measuring equilibrium P/V isotherms.

Before the measurement, both shale cores (#1 and #2) were placed in an oven, and vacuumed for 48 hours and heated at a constant temperature of 423.15 K with helium as a carrier gas to remove

moisture and other adsorbed gases. This pretreatment was called “degassing and drying treatment”. Helium within the shale samples was then evacuated before the subsequent steps. After this treatment, the surface area was artificially increased by crushing the shale cores into small particles with diameters in the range of 1.00-1.18 mm (US Mesh 16-18). The shale particles were then collected and stored in a zip-locked bag to avoid oxidation and water uptake. Pore size distribution of the shale particles was then characterized by N_2 adsorption/desorption test. The N_2 adsorption/desorption test on shale samples #1 and #2 was conducted with the Autosorb iQ-Chemisorption & Physi-sorption Gas Sorption Analyzer (Quantachrome Instruments, USA). The range of pore width that can be detected by this apparatus is 0.35-500 nm. It took about 3-4 hours for N_2 to reach adsorption/desorption equilibrium with the shale samples at a given temperature and pressure.

Furthermore, the pore volume of both shale samples was obtained with the Quantachrome Autosorb software installed for the gas sorption analyzer. Based on the assumption that the pores present in the solid particles are cylindrical, the software can figure out the total pore volume in the particles by measuring the total amount of N_2 take-up at 101.325 kPa and 77 K. From N_2 adsorption/desorption test, the pore volume, and pore size distribution for each shale core were obtained with an accuracy of ±0.6%.

Part of the shale particles were then used for the TOC test. The TOC of both shale cores was measured by a combustion elemental analyzer. During the measurement, H_2SO_4 (10 wt%) was added to the shale particles; then the solution was sparged with oxygen until the purgeable organic carbon and inorganic carbon were removed. The non-purgeable organic carbon was then placed in the combustion tube to form carbon dioxide, which can be detected by the non-dispersive infrared detector. Then, the TOC was obtained. Table 5-1 lists the mass, pore volume,

and TOC of the two shale samples.

Table 5-1 Mineral composition, TOC, pore volume, and the mass of shale sample used in this study.

Shale Sample	Mass, g	Pore Volume, cm^3/g	TOC, w/w%	Clay Composition, %		Other Minerals Composition, %			
				Illite	Smectite	Quartz	Potassium feldspar	Plagioclase	Calcite
#1	19.015	0.0211	0.988	31.0	32.0	26.0	1.6	3.0	6.4
#2	18.230	0.0140	2.217	25.0	34.0	18.0	3.2	9.7	10.1

The system volume was measured after shale core characterization. In order to obtain an accurate P/V isotherm for fluid mixtures in the partially confined space, it is crucial to obtain an accurate total volume of the mixture. The total volume of the mixture in the partially confined space is calculated as

$$V_{Total} = V_{Cell} + V_{Cell}^{Dead} + V_{Tubing} + V_{Container} + V_{Pore} - V_{Particle} \tag{5-1}$$

where V_{Total} is the total volume of the mixture in the partially confined space, cm^3; V_{Cell} is the volume of the mixture in the PVT cell, cm^3; V_{Cell}^{Dead} is the dead volume of the PVT cell; V_{Tubing} is the inner volume of stainless steel-tubing lying between the PVT cell and the shale container, cm^3; $V_{Container}$ is the total volume of the shale container, cm^3; V_{Pore} is the total pore volume in the shale particles, cm^3; and $V_{Particle}$ is the total volume of shale particles including both the pore volume and the solid volume, cm^3.

During the experiment, V_{Cell} was obtained by using a cathetometer through measuring the height of the fluid system with an accuracy of ±0.016 cm^3. V_{Cell}^{Dead} is 1.754 cm^3. By employing Boyle-Charles' law, V_{Tubing} was measured as 3.517 cm^3 with an accuracy of ±0.010 cm^3. $V_{Container}$ in this experiment is 10.000 cm^3. V_{Pore} was measured by N_2 adsorption/desorption test. After each P/V

isotherm measurement, $V_{Particle}$ was measured through a drainage method by immersing the shale particles into distilled water contained in a cylinder; the volume change before and after the immersion gave the total volume of the shale particles. Considering that the shale material was hydrocarbon-wetting, it is reasonable to assume the distilled water could not enter nano-pores in the shale particles. Thus, $V_{Particle}$ is approximately equal to the volume change of water in the cylinder.

Table 5-2 shows the compositions of two N_2/n-C_4H_{10} mixtures, molar numbers of each component injected and testing temperatures. Before each P/V isotherm measurement, the entire PVT system was tested for leakage with N_2 with testing pressure set as high as 20,000 kPa. Then, it was cleaned with acetone, and evacuated using a vacuum pump for 2 hours. Shale particles were then placed in the shale container and connected with the PVT cell. The whole system was evacuated again for 12 hours using a vacuum pump. In order to prevent shale particles from flowing away during evacuating, a steel mesh with mesh number 200 was used at the outlet of the shale container.

Table 5-2 Compositions and molar numbers for the N_2/n-C_4H_{10} mixtures tested. For each mixture, experiments were conducted at two temperatures, 299.15 K and 324. 15 K.

Molar Percentage		**Molar Numbers**	
N_2, mol%	**n-C_4H_{10}, mol%**	**N_2, mol**	**n-C_4H_{10}, mol**
5.40	94.60	0.0140	0.2452
5.01	94.99	0.0131	0.2476

A high-pressure cylinder containing a sufficient amount of n-C_4H_{10} was connected to the PVT cell, allowing direct withdrawal of the liquid n-C_4H_{10} into the PVT cell. A certain amount of liquid n-C_4H_{10} was injected into the PVT cell just above its vapor pressure at room temperature, the air bath temperature was set to be 303.15 K for 12 hours, enabling the n-C_4H_{10} sample in the PVT cell to reach thermal equilibrium. Then, the moles of the injected n-C_4H_{10} can be obtained

according to its density and its volume measured by the accurate cathetometer. Its density is obtained from the National Institute of Standards and Technology (NIST). Then, N_2 was added into the PVT cell without turning on the magnetic stirrer. The volume of N_2 injected can be determined to be the total volume minus the liquid n-C_4H_{10} volume. No volume change can be assumed since the volume measurement is conducted right after N_2 is injected into the PVT cell. Then, the mass of N_2 added can be determined. Finally, the composition of the binary mixture can be determined. After injection, the mixture was then pressurized into single-liquid state with the magnetic stirrer turned on for 6 hours. The mixture was maintained at 303.15 K for 12 hours to enable it to reach a thermal equilibrium. Bubble-point pressures for this mixture in the PVT cell were measured by the constant composition expansion (CCE) method. Because the vapor-liquid equilibrium of non-polar components is predicted quite well with the PR EOS (Robinson and Peng, 1978; Myers and Sandler, 2002), this EOS was applied to calculate the composition of the mixture. The physical properties of pure components and their binary interaction parameters used with the PR EOS are shown in Table 5-3. The measured bubble-point pressure was matched by adjusting the overall composition for the PR EOS model. Then, the matched composition was deemed to be the initial overall composition of the binary mixture; the former determined composition of the binary mixture was used to confirm the accuracy of the overall composition determined by the PR-EOS model. This method for determining the composition has an accuracy of ±0.3% on the basis of the crosschecking with the composition measured by gas chromatographic (GC) tests. After the determination of the overall composition, the system temperature was set to an operating temperature. Subsequently, we vigorously stirred the mixture for 6 hours by the magnetic stirrer at the selected operating temperature.

Table 5-3 Physical properties of pure components and their binary interaction parameters used in the PR EOS (1978) model.

Components	Critical Temperature, K	Critical Pressure, kPa	Acentric Factor	Binary Interaction Parameter	
				$n\text{-}C_4H_{10}$	N_2
$n\text{-}C_4H_{10}$	425.2	3799.6875	0.193	0.000	0.095
N_2	126.2	3394.3875	0.040	0.095	0.000

P/V isotherms of N_2/$n\text{-}C_4H_{10}$ mixtures were firstly measured in the PVT cell. Subsequently, another set of P/V isotherm for the same mixture were measured in the partially confined space by connecting the PVT cell with the shale container. Crushed shale particles with a certain mass were loaded in the shale container. The container and the tubing between the PVT cell and container were sufficiently vacuumed prior to being connected to the PVT cell. At each temperature, P/V isotherm measurement was initiated from a single-liquid phase state. Then, the pressure was gradually decreased to measure a P/V isotherm for the mixture. The mixture was sufficiently stirred for 30 min to ensure an equilibrium state prior to each volume measurement. After stirring, the magnetic stirrer was switched off and sufficient time, about 4-6 hours, was allowed to reach an equilibrium state. The equilibrium was indicated when no pressure changes were observed for a period of 2 hours. Thereafter, phase equilibrium of the mixture was visually identified, and the pressure and volume of each phase were measured and recorded. A phase boundary was confirmed by plotting the total volume with respect to pressure and locating the transition point in the curve. The P/V relationship often shows a clear slope change when the vapor phase appears as pressure reduces. The uncertainty in the measurement of the bubble-point pressure as well as the equilibrium pressure and volume is estimated to be ±2.5%. Each measurement is repeated twice to make sure the measured P/V isotherms are reliable and reproducible. The maximum deviation between two consecutive runs is found to be less than ±3.8%.

5.3 Results and Discussion

5.3.1 Characterization of Shale Samples

Figures 5-3 to 5-4 show the measured pore size distributions of the shale samples #1 and #2, respectively, as obtained through N_2 adsorption/desorption test. Figure 5-3 indicates that shale sample #1 contains pores in the range of 1-20 nm. The single sharp peak indicates that shale sample #1 has a narrow pore size distribution around 5.0 nm. In contrast, Figure 5-4 shows that shale sample #2 has a wider pore size distribution in the range of 1-70 nm.

It can be seen from Table 5-1 that the TOC content in shale sample #2 is 2.24 times higher than that in the shale sample #1. Previous studies showed that shale materials with a higher TOC content exhibited a higher sorption capacity (Lu *et al.*, 1995; Jarvie, 2004; Zhang *et al.*, 2012; Clarkson and Haghshenas, 2013). Hence, shale sample #2 is expected to possess a higher sorption capacity than the shale sample #1. In Section 5.3.3, we will present the sorbed molar numbers of N_2 and n-C_4H_{10} on the two shale samples, and in Section 5.3.4, we will explore the possible relationships between TOC content and sorption capacity of individual components.

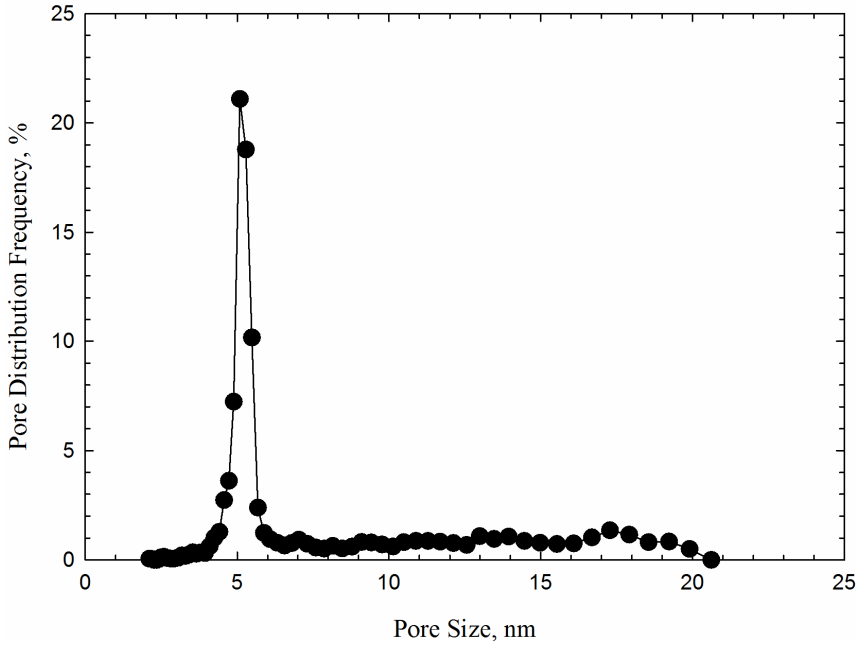

Figure 5-3 Pore size distribution of shale sample #1 as measured by the N_2 adsorption/desorption test.

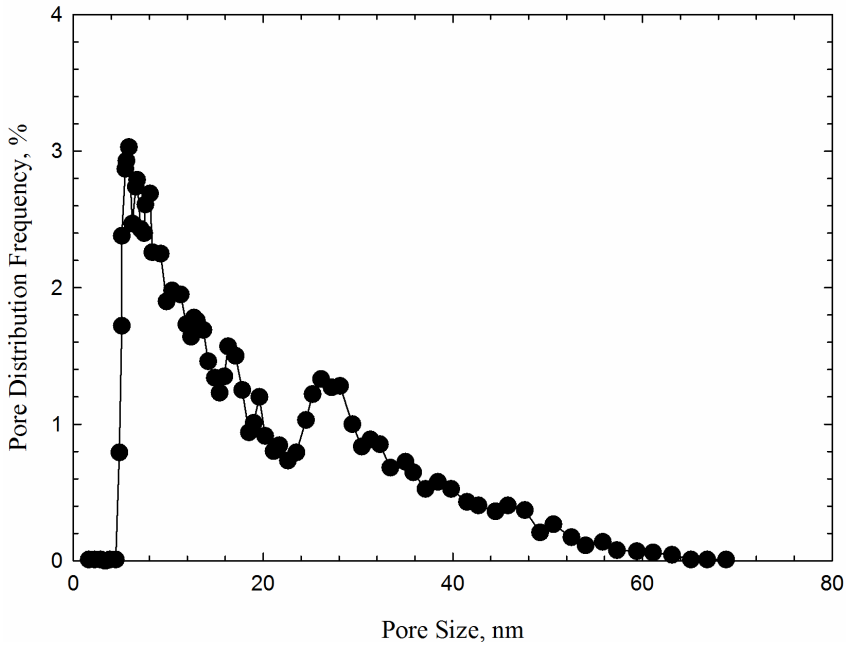

Figure 5-4 Pore size distribution of shale sample #2 as measured by the N_2 adsorption/desorption test.

5.3.2 Phase Behavior of N_2/*n*-C_4H_{10} Mixtures in the Partially Confined Space

The P/V isotherms for the N_2/n-C_4H_{10} mixtures, together with the measurement uncertainties, are

shown in Figures 5-5 to 5-8. In Figures 5-5 to 5-8, the solid squares represent the P/V isotherms measured in the PVT cell, and the solid circles represent the P/V isotherms measured in the partially confined space. As depicted in Figures 5-5 to 5-8, the phase boundary between single-phase region and two-phase region can be estimated by the intersection of two trend lines drawn to represent the two types of phase equilibrium. The dashed line in Figures 5-5 to 5-8 represents the bubble-point pressures of the N_2/n-C_4H_{10} mixtures that are calculated with the PR EOS (1978).

Figures 5-5 to 5-8 show that a good agreement is observed between the measured and calculated bubble-point pressures. We can observe the bubble-point pressures of the N_2/n-C_4H_{10} mixtures in the partially confined space are higher than those measured in the bulk space. Table 5-4 shows the detailed changes in the bubble-point pressure of the mixtures after being sorbed on the two shale samples. Previous studies reported that when a multi-component mixture contacts with a shale sample, different components in the mixture exhibit different levels of sorption on shale, leading to the so-called selective sorption phenomenon (Haghshenas *et al.*, 2014; Wang *et al.*, 2015). In this study, the shale particles were always immersed into the single liquid phase during the measurements. The liquid N_2 and n-C_4H_{10} were deemed to sorb on shale samples with different sorption levels at a given temperature and pressure. The selective sorption of N_2 and n-C_4H_{10} changes the initial composition of the N_2/n-C_4H_{10} mixtures, and thus results in an increase in bubble-point pressure, as demonstrated in Figures 5-5 to 5-8.

Previous studies demonstrated that bubble-point pressure can be reduced due to the capillary pressure present in small pores (Nojabaei *et al.*, 2013; Devegowda *et al.*, 2012; Teklu *et al.*, 2014). Capillary pressure is attributed to the interfacial tension that exists across the curved interface between the vapor/liquid phases in a tube (Firoozabadi, 2016). Wang *et al.* (2014,

2016) studied phase behavior of a fluid contained in a porous medium with a pore size distribution; they presented that if the fluid was initially a single-liquid phase during the constant composition expansion (CCE) process, the vapor phase would firstly appear in larger pores, and then appear in smaller pores when all the liquid vaporized in the larger pores. In this study, if we regard the PVT cell as a pore with an infinite pore radius, the first bubble is expected to arise from the PVT cell during the CCE test based on Wang *et al.* (2014 and 2016). During the measurements, the shale samples were always emerged in the single-liquid phase. At the bubble-point, therefore, the fluid contained in the shale pores was always a single-liquid phase and no capillary pressure was present in the shale pores. We deduced that the measured bubble-point pressure in the partially confined space should be influenced only by the effect of selective sorption between individual components (N_2 and *n*-C_4H_{10} in this study), without the effect of capillary pressure.

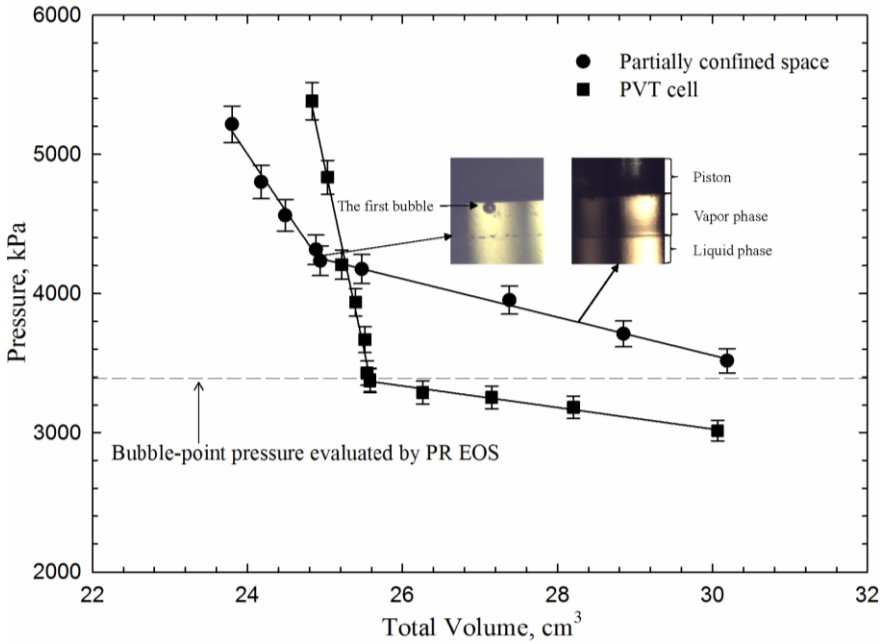

Figure 5-5 Measured P/V isotherms for the N_2/n-C_4H_{10} mixture with composition of (5.40 mol%, 94.60 mol%) in the PVT cell with and without shale sample #1 at 299.15 K.

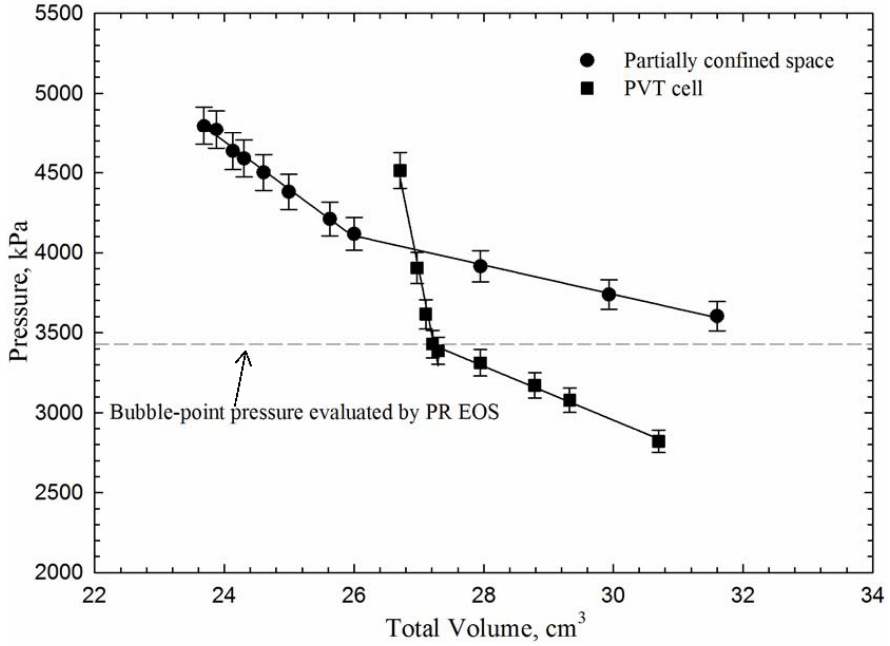

Figure 5-6 Measured P/V isotherms for the N_2/n-C_4H_{10} mixture with composition of (5.40 mol%, 94.60 mol%) in the PVT cell with and without shale sample #1 at 324.15 K.

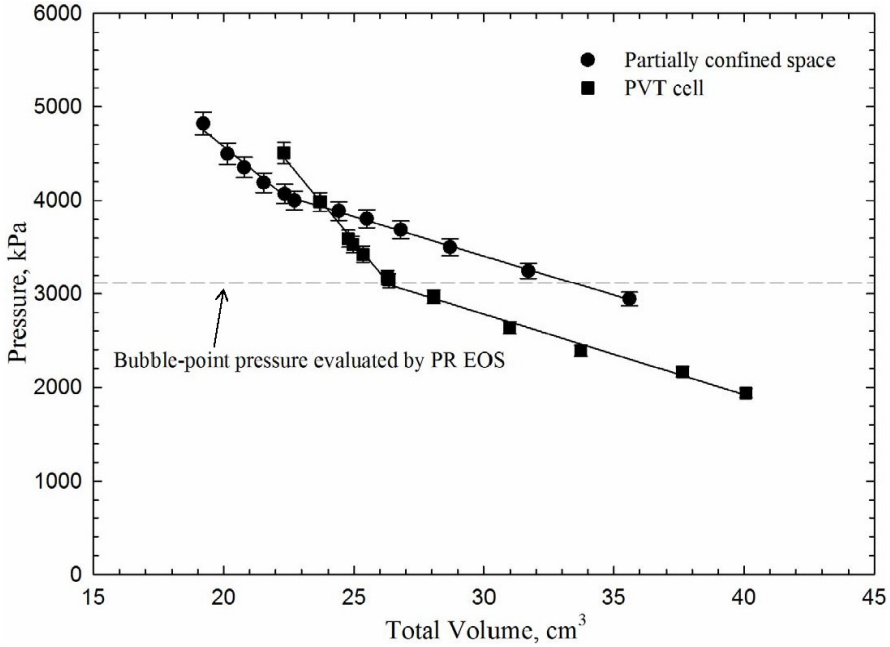

Figure 5-7 Measured P/V isotherms for the N_2/n-C_4H_{10} mixture with composition of (5.01 mol%, 94.99 mol%) in the PVT cell with and without shale sample #2 at 299.15 K.

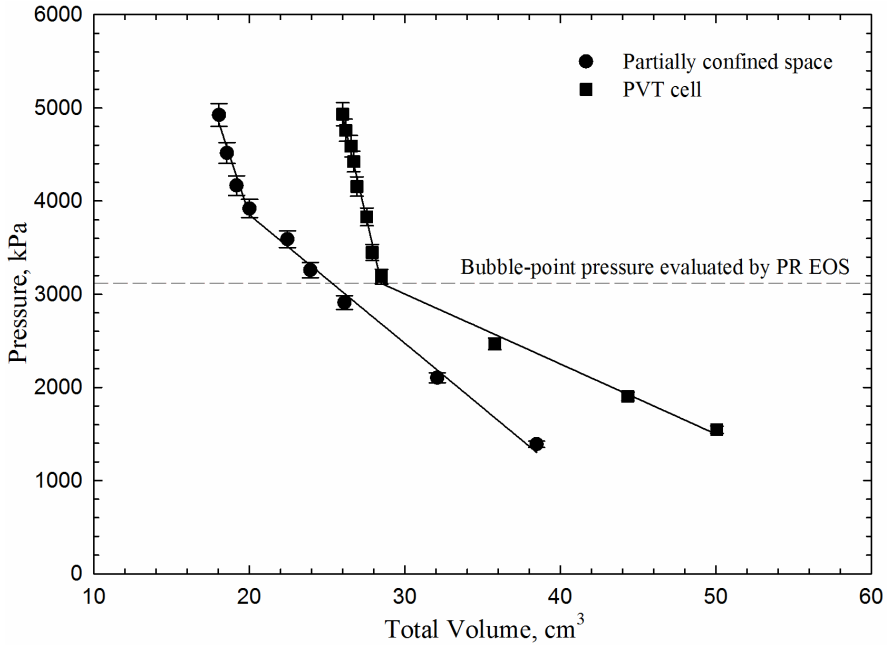

Figure 5-8 Measured P/V isotherms for the N_2/n-C_4H_{10} mixture with composition of (5.01 mol%, 94.99 mol%) in the PVT cell with and without shale sample #2 at 324.15 K.

Table 5-4 Changes in the bubble-point pressure of N_2/n-C_4H_{10} mixtures for two shale samples. Note that the experimental temperatures are above the supercritical temperature of N_2. The bubble-point pressure of n-C_4H_{10} at 299.15 K and 324.15 K are 241.0 kPa and 523.0 kPa, respectively.

Shale Sample	Molar Percentage		Temperature, K	Bubble-Point Pressure in the PVT cell, kPa	Bubble-Point Pressure in the Partially Confined Space, kPa	Percentage Change in Bubble-Point Pressure, %
	N_2, mol%	n-C_4H_{10}, mol%				
#1	5.4	94.60	299.15	3390.6	4268.5	25.89
	5.4	94.60	324.15	3429.5	4105.8	19.72
#2	5.01	94.99	299.15	3115.1	4035.5	29.55
	5.01	94.99	324.15	3189.6	3883.8	21.76

5.3.3 Sorption of Individual Components on Shale Samples

This section quantifies the selective sorption between the two components by calculating sorbed molar numbers on the two shale samples based on the results given in Table 5-4. It is explained how selective sorption is expected to affect the bubble-point pressure of a mixture in a partially confined space.

Shale gas-condensate reservoirs, which are normally organic-rich, are traditionally referred as "sorbed gas" reservoirs because a significant amount of shale gas is stored through physical adsorption onto the internal rock surface and through absorption within organic matter (Clarkson and Haghshenas, 2013). Based on the previous research findings, in this research, it can be reasonably deduced that N_2 and n-C_4H_{10} not only adsorb onto the shale rock surface, but also absorb within the organic matter at given temperature and pressure. In addition, Clarkson and Haghshenas (2013) proposed five mechanisms for gas storage in shale gas-condensate reservoirs: (1) Adsorption on internal surface area; (2) Compressed gas storage in natural and hydraulic fractures; (3) Compressed gas storage in matrix porosity; (4) Dissolved gas in formation water; and (5) Absorption in organic matter. Similarly, in our study, N_2 and n-C_4H_{10} in the partially confined space can exhibit two storage states; one is the sorbed gas including adsorption on shale rock surface and absorption in organic matter, and the other is the unsorbed gas which includes the compressed gas located in the pore space inside the shale sample, the bulk space in the PVT cell and in the connecting tubing, and the non-cementing pore spaces among the shale particles.

During the P/V isotherm measurements, as the fluid mixture in the partially confined space was depressurized, the first bubble liberated from the single-liquid phase (See Figure 5-5). At such a bubble-point, the composition of the N_2/n-C_4H_{10} mixture in the partially confined space was different from that of the initial mixture loaded in the bulk space. This difference was caused by the selective sorption between N_2 and n-C_4H_{10} on shale samples. In order to obtain the sorbed molar numbers of N_2 and n-C_4H_{10} on the shale samples, we firstly calculated the unsorbed moles of the mixture based on the following three assumptions: (1) The volume of the sorbed layers was negligible in comparison with V_{Total}; (2) The distribution of the unsorbed gas was homogeneous in all spaces; (3) The interactions of unsorbed/sorbed molecules and unsorbed

molecules/pore wall were neglected. Then, the following equation was employed to compute the total molar numbers of the unsorbed N_2/n-C_4H_{10} mixture in the partially confined space,

$$n_p = \frac{P_b V_{Total}}{Z_p RT} \tag{5-2}$$

where n_p is the total molar number of the unsorbed N_2/n-C_4H_{10} mixture in the partially confined space, mol; P_b represents the bubble-point pressure of the unsorbed N_2/n-C_4H_{10} mixture in the partially confined space, Pa; V_{Total} represents the total volume of the unsorbed N_2/n-C_4H_{10} mixture in the partially confined space, m^3, Z_p is the compressibility factor of the unsorbed N_2/n-C_4H_{10} mixture in the partially confined space that is calculated by the PR EOS; R is the universal gas constant, 8.314 $m^3 \cdot Pa \cdot K^{-1} \cdot mol^{-1}$; and T is the temperature, K.

After obtaining the total molar numbers of the unsorbed N_2/n-C_4H_{10} mixture in the partially confined space, the sorbed molar numbers of N_2 and n-C_4H_{10} can then be determined at the bubble point with the following equations, respectively,

$$n_{ad\_N_2} = n_o x_{N_2} - n_p x'_{N_2} \tag{5-3}$$

$$n_{ad\_C_4} = n_o x_{C_4} - n_p x'_{C_4} \tag{5-4}$$

where n_{ad_N2} and n_{ad_C4} are the sorbed molar numbers of N_2 and n-C_4H_{10} on shale samples, respectively, mol; n_o is the injected molar number of the N_2/n-C_4H_{10} mixture, mol; x_{N2} and x_{C4} are the molar percentage of N_2 and n-C_4H_{10} in the injected mixture in the PVT cell, respectively; x'_{N2} and x'_{C4} are the molar percentage of N_2 and n-C_4H_{10} when the mixture rests at the bubble-point in the partially confined space, respectively. Equations (5-3) and (5-4) are derived based on the assumption that the distribution of the unsorbed gas is uniform in all spaces as mentioned above.

Table 5-5 lists the calculated molar percentages of N_2 and n-C_4H_{10} in the mixture before and

after sorption, and sorbed molar numbers of N_2 and n-C_4H_{10} in the partially confined spaces. The higher sorption tendency of n-C_4H_{10} than that of N_2 is indicated in calculated sorbed molar numbers in Table 5-5. The molar percentage of N_2 in mixture in the partially confined space tends to increase in comparison to that in the bulk space. The higher N_2 concentration results in the higher bubble-point pressure of the N_2/n-C_4H_{10} mixture in the partially confined space, as observed in Figures 5-5 to 5-8.

Table 5-5 also shows that, for a given N_2/n-C_4H_{10} mixture, both N_2 and n-C_4H_{10} sorb more at a lower temperature. A higher temperature did not lead to a higher bubble-point pressure for a given mixture (Table 5-4) likely because bubble-point is more sensitive to composition than to temperature for these mixtures at the conditions tested. This emphasizes the importance of considering sorption in phase behavior calculation for small pores.

Table 5-5 Calculated molar percentages of N_2 and n-C_4H_{10} in the mixture before and after sorption, and sorbed molar numbers of N_2 and n-C_4H_{10} at the bubble-point in the partially confined spaces. Note that the molar concentrations of N_2 and n-C_4H_{10} have been determined by the PR EOS (1978) calibrated with the measured bubble-point.

Shale Sample	**Temperature, K**	**Molar Percentage before Sorption**		**Molar Percentage after Sorption**		**Adsorbed Molar Numbers**	
		N_2, mol%	**n-C_4H_{10}, mol%**	**N_2, mol%**	**n-C_4H_{10}, mol%**	**N_2, mol**	**n-C_4H_{10}, mol**
#1	299.15	5.40	94.60	7.00	93.00	0.0007	0.0683
#1	324.15	5.40	94.60	6.70	93.30	0.0006	0.0583
#2	299.15	5.01	94.99	6.59	93.41	0.0008	0.0728
#2	324.15	5.01	94.99	6.25	93.75	0.0007	0.0612

5.3.4 Effect of TOC on Sorption Capacity

In this study, sorption capacity is defined as the ability of gas storage on shale; quantitatively, it is equal to the sorbed molar numbers per gram of shale rocks. Organic matters present in shale rocks, generally represented by TOC content, can sorb and store shale components. Previous studies have investigated the relationship between TOC content and sorption capacity, showing that an increase in TOC content can lead to an approximately linear increase in the sorption capacity (Lu *et al.*, 1995; Jarvie, 2004; Zhang *et al.*, 2012). In this study, Table 5-5 also shows, given the fact that the two N_2/n-C_4H_{10} mixtures have a similar composition, much more N_2 and n-C_4H_{10} are sorbed onto the shale sample #2 than the shale sample #1 under similar temperature/pressure conditions. This can be attributed to a higher TOC content in the shale sample #2 than the shale sample #1.

Sorption capacities of N_2 and n-C_4H_{10} are closely correlated with the TOC content in the shale samples. Charoensuppanimit *et al.* (2016) measured N_2 and CH_4 sorption on shale materials and found both of their sorption capacities are positively correlated with TOC content. As for the sorption of n-C_4H_{10} on shale materials, however, there is no data available in the literature. Considering that CH_4 and n-C_4H_{10} are both hydrocarbons and have natural affinity with TOC content, it is conceivable that the sorption capacity for n-C_4H_{10} is correlated with TOC content positively.

After obtaining the sorbed molar numbers of individual components in each shale sample, the sorption capacities of N_2 and n-C_4H_{10} on two shale samples can be calculated by the following equation,

$$V_{ad} = \frac{n_{ad}}{m} \tag{5-5}$$

where V_{ad} represents the sorption capacity, mmol/g; n_{ad} is the sorbed molar numbers of individual components in each shale sample, mmol; m is the mass of the shale sample, g.

Figures 5-9 and 5-10, respectively, show the sorption capacities of N_2 and n-C_4H_{10} in terms of the TOC content in both shale samples. The sorption capacity for n-C_4H_{10} increases with the increasing TOC content, while the sorption capacity for N_2 only increases slightly with the TOC content. A shale sample with a higher TOC content is expected to have a higher sorption capacity, which is consistent with the findings by Nuttall *et al.* (2005) that sorption occurs primarily on active sites containing organic carbons. Besides, the natural affinity between hydrocarbon n-C_4H_{10} and TOC content leads to a higher sorption of n-C_4H_{10} as compared to non-hydrocarbon N_2. However, it seems that the sorption amounts are not affected much by the TOC content of shale sample #1 and #2. Recently, Xiong *et al.* (2017) conducted a series of methane sorption measurements for seven shale core samples collected from the Ordos Basin with depths over 3000 m and TOCs ranging from 0.49-3.82%. They then proposed that the sorption capacity did not correlate only with the TOC content but showed a more complex dependence on petrophysical and mineralogical properties. Therefore, to understand the sorption capacity of N_2 or n-C_4H_{10}, more sorption data should be measured and other factors, *e.g.*, clay minerals should be considered to have a better understanding on the sorption behavior.

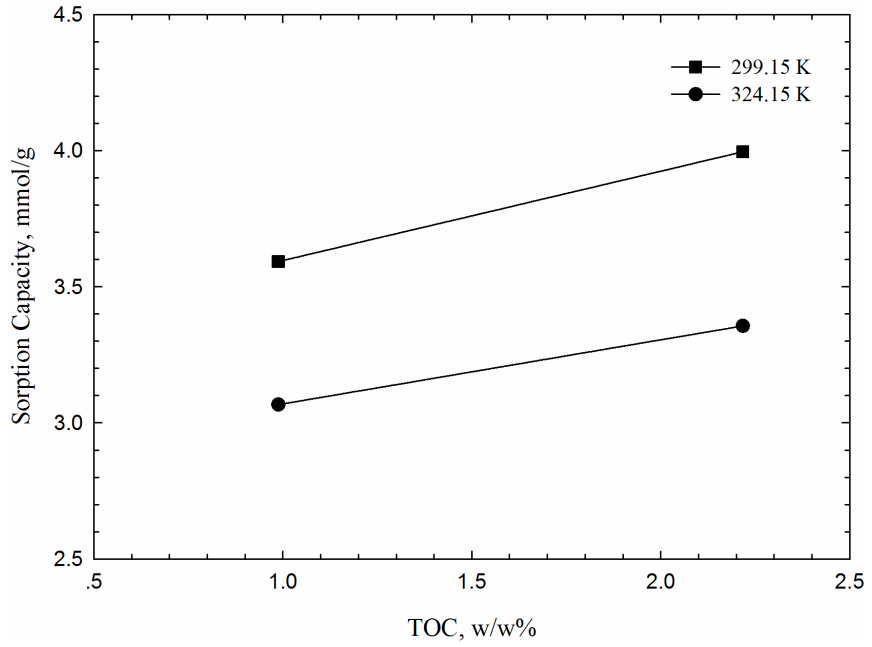

Figure 5-9 Sorption capacity of n-C_4H_{10} in terms of TOC content on the two shale samples.

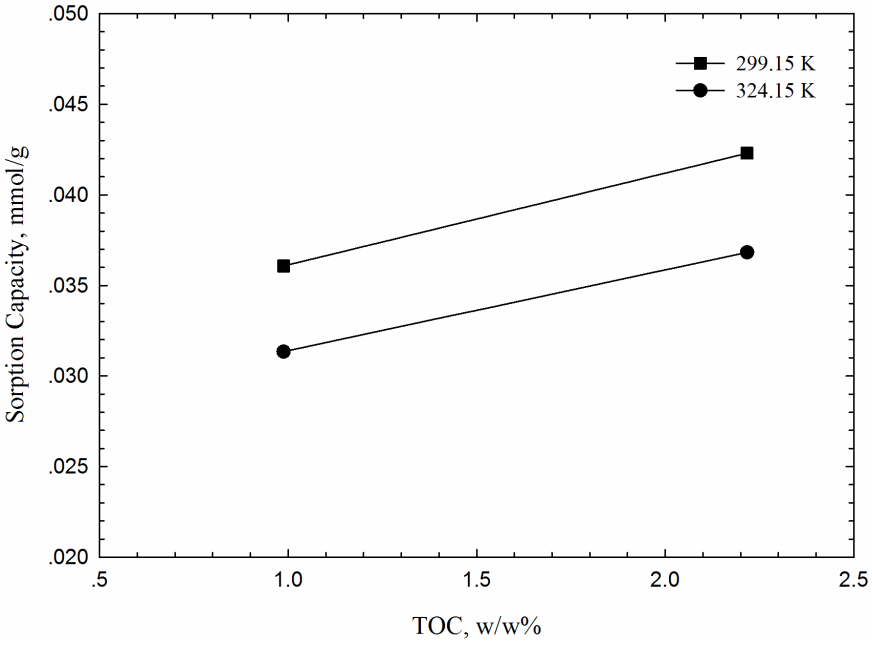

Figure 5-10 Sorption capacity of N_2 in terms of TOC content on the two shale samples.

5.4 Conclusions

This paper presented a novel experimental method to measure phase boundaries of a fluid

mixture in the presence of real shale sample retrieved from Devonian formation in Canada. In the new method, P/V isotherms were firstly measured as conventionally done with a PVT cell. Then, the P/V isotherm measurements were repeated in a partially confined space by opening a valve between the PVT cell and a shale container. In this study, P/V isotherms at two temperatures were measured for two N_2/n-C_4H_{10} mixtures in the PVT cell and in the partially confined space. Conclusions are as follows:

- It was observed that bubble-point pressures of the N_2/n-C_4H_{10} mixtures in the partially confined space were higher than those in the bulk space. A detailed analysis of results indicated that n-C_4H_{10} exhibited a higher level of sorption on the shale sample than N_2 in the partially confined space; therefore, the N_2 concentration in the free fluid was higher than that in the initial mixture. The higher N_2 concentration led to the higher bubble-point pressure as observed in the measurements.
- The increase in bubble-point pressure due to the selective sorption was observed to be greater at the lower temperature for the two mixtures tested. This is because the sorption of n-C_4H_{10} relative to that of N_2 is more significant at the lower temperature. The observed bubble-point increases are unlikely because of capillary pressure in the shale sample, because the shale sample was placed in a liquid phase at all times during the bubble-point measurements. It was visually confirmed that the bubble-points measured were associated with appearance of the first bubble in the PVT cell.
- It was found that a larger sorption amount of N_2 and n-C_4H_{10} for a given N_2/n-C_4H_{10} mixture occurred at the lower temperature. A higher temperature did not lead to a higher bubble-point pressure for a given mixture likely because bubble-point is more sensitive to composition than to temperature for these mixtures at the conditions tested. This

emphasizes the importance of considering sorption in phase behavior calculation for small pores.

- Shale sample #2 has a higher sorption capacity, especially for the hydrocarbon component n-C_4H_{10}, since its TOC content is much higher than the shale sample #1.

5.5 References

Alfi, M., Nasrabadi, H., Danerjee, D., 2016. Experimental investigation of confinement effect on phase behavior of hexane, heptane and octane using lab-on-a-chip technology. Fluid Phase Equilibr. 423, 25-33.

Charoensuppanimit, P., Mohammad, S.A., Gasem, K.A.M., 2016. Measurements and modeling of gas adsorption on shales. Energy Fuels 30, 2309-2319.

Clarkson, C.R., Haghshenas, B., 2013. Modeling of supercritical fluid adsorption on organic-rich shales and coal. In: SPE Unconv. Resour. Conf. Woodlands, Texas, USA.

Devegowda, D., Sapmanee, K., Civan, F., Sigal, R., 2012. Phase behavior of gas condensates in shale due to pore proximity effects: implications for transport, reserves and well productivity. In: SPE Annu. Tech. Conf. Exhib., San Antonio, Texas, USA.

Dong, X., Liu, H., Hou, J., Wu, K., Chen, Z., 2016. Phase equilibria of confined fluids in nanopores of tight and shale rocks considering the effect of capillary pressure and adsorption film. Ind. Eng. Chem. Res. 55, 798-811.

Firoozabadi, A., 2016. Thermodynamics and Applications in Hydrocarbon Energy Production, McGraw Hill, New York.

Haghshenas, B., Soroush, M., Brohi, I., Clarkson, C.R., 2014. Simulation of liquid-rich shale gas reservoirs with heavy hydrocarbon fraction desorption. In: SPE Unconv. Resour. Conf. Woodlands, Texas, USA.

Jarvie, D., 2004. Evaluation of Hydrocarbon Generation and Storage in Barnett Shale, Fort Worth Basin. Texas: The University of Texas at Austin, Bureau of Economic logy/PTTC.

Jin, Z., and Firoozabadi, A., 2016. Thermodynamic modeling of phase behavior in shale media. SPE J. 21, 190-207.

Linstrom, P.J., Mallard, W.G., NIST Chemistry WebBook, NIST Standard Reference Database Number 69, National Institute of Standards and technology, Gaithersburg, MD, 20899, http://webbook.nist.gov.

Li, Z., Jin, Z., and Firoozabadi, A., 2014. Phase behavior and adsorption of pure substances and mixtures and characterization in nanopore structures by density functional theory. SPE J. 19, 1096-1109.

Lu, X., Li, F., Watson, A.T., 1995. Adsorption measurements in Devonian shale. Fuel 74, 599-603.

Luo, S., Lutkenhaus, J.L., Nasrabadi, H., 2016. Confinement-induced supercriticality and phase equilibria of hydrocarbons in nanopores. Langmuir 32, 11506-11513.

Morishige, K., Fujii, H., Uga, M., Kinukawa, D., 1997. Capillary critical point of argon, nitrogen, oxygen, ethylene, and carbon dioxide in MCM-41. Langmuir 13, 3494-3498.

Myers, J.A., Sandler, S.I., 2002. An equation of state for electrolyte solutions covering wide ranges of temperature, pressure, and composition. Ind. Eng. Chem. Res. 41, 3282-3297.

Nagarajan, N.R., Hanapour, M.M., Arasteh, F., 2013. Critical role of rock and fluid impact on reservoir performance on unconventional shale reservoirs. In: Unconv. Resour. Tech. Conf. Denver, Colorado, USA.

Nojabaei, B., Johns, R.T., Chu, L., 2013. Effect of capillary pressure on phase behavior in tight rocks and shales. SPE Res. Eval. Eng. 16, 289-281.

Nuttall, B.C., Eble, C.F., Drahovzal, J.A., Bustin, M., 2005. Analysis of Devonian black shales in Kentucky for potential carbon dioxide sequestration and enhanced natural gas production, University of Kentucky.

Peng, D.Y., Robinson D.B., 1976. A new two-constant equation of state. Ind. Eng. Chem. Fundam. 15, 59-64.

Robinson, D.B., Peng, D.Y., 1978. The characterization of the heptanes and heavier fractions for the GPA Peng-Robinson programs, gas processors association. Research Report RR-28. (Booklet only sold by the Gas Processors Association, GPA)

Teklu, T.W., Alharthy, N., Kazemi, H., Yin, X., Graves, R.M., Alsumaiti, A.M., 2014. Phase behavior and minimum miscibility pressure in nanopores. SPE Res. Eval. & Eng. 17, 396-403.

Travalloni, L., Castier, M., Tavares, F.W., 2014. Phase equilibrium of fluids confined in pores media from an extended Peng-Robinson equation of state. Fluid Phase Equilibr. 362, 335-341.

Xiong, F., Wang, X., and Amooie, N. *et al.* 2017. The shale gas sorption capacity of transitional shales in the Ordos Basin, NW China. Fuel 208, 236-246.

Wang, L., Parsa, E., Gao, Y.F., Ok, J.T., Neeves, K., Yin, X.L., Ozkan, E., 2014. Experimental study and modeling of the effect of nanoconfinement on hydrocarbon phase behavior in unconventional reservoirs. In: SPE Western North American and Rocky and Rocky Mountain Joint Regional Meeting, Denver, Colorado, USA.

Wang, L., Yin, X.L., Neeves, K.B., Ozkan, E., 2016. Effect of pore-size distribution on phase transition of hydrocarbon mixtures in nanoporous media. SPE J. 19, 1096-1109.

Wang, Y., Tsotsis, T.T., Jessen, K., 2015. Competitive sorption of methane/ethane mixtures on

shale: measurements and modeling. Ind. Eng. Chem. Res. 54, 12178-12195.

Yan, X., Wang, T.B., Gao, C.F., Lan, X.Z., 2013. Mesoscopic phase behavior of tridecane-tetradecane mixtures confined in porous materials: effects of pore size and pore geometry. J. Phys. Chem. C 117, 17245-17255.

Zhang, T., Ellis, G.S., Ruppel, S.C., Milliken, K., Yang, R., 2012. Effect of organic-matter type and thermal maturity on methane adsorption in shale-gas systems. J. Org. Geochem. 47, 120-131.

CHAPTER 6 MEASUREMENTS AND MODELING OF INTERFACIAL TENSION FOR CO_2/CH_4/BRINE SYSTEMS UNDER RESERVOIR CONDITIONS

A version of this chapter has been accepted for publication in *Industry & Engineering Chemistry Research.*

Abstract

Supercritical CO_2 injection is a promising way to hydraulically fracture tight/shale gas formations as well as enhances gas recovery from these formations. Understanding of phase behaviour and interfacial tension (IFT) of CO_2/CH_4/brine (NaCl) systems is important, because they affect the performance of such a process in tight/shale gas formations. In this study, we employ the axisymmetric drop shape analysis (ADSA) method to measure the IFT between CO_2/CH_4 mixtures and brine over the temperature range from 77.0°F to 257.0°F and the pressure range from 15 psia to 5,027 psia. Test results show that the presence of CO_2 decreases the IFT of CH_4/H_2O or CH_4/brine (NaCl) systems, while the degree of reduction depends on the molar fraction of CO_2 in the gas mixture. Salinity tends to cause an increase in IFT of CO_2/CH_4/brine (NaCl) systems; a higher salinity leads to an increased IFT for a given system. On the basis of the Parachor model (Weinaug and Katz, 1943) and Firoozabadi's model (Firoozabadi and Ramey, 1988), we propose an improved IFT model to represent the measured IFT data for the CO_2/CH_4/brine systems. The new IFT model preserves the principle of zero IFT at a critical point. Comparison of the new IFT model with four commonly-used IFT correlations presented in the literature shows the superiority of the new model.

Keywords: Interfacial tension, axisymmetric drop shape analysis (ADSA) method, Parachor model, salinity, shale reservoirs

6.1 Introduction

Shale gas is playing an increasingly important role in global energy portfolio since 2010; it accounted for 23% of total world energy supply in 2010 and will reach 49% in 2035, according to the report on annual outlook of global energy from USA energy information administration (EIA). Recent years have witnessed an increasing trend in developing new technologies for

recovering the vast shale gas resources around the globe, such as hydraulic fracturing techniques. Water-less fracturing, such as CO_2 fracturing, has attracted an extensive attention because of the unique properties of CO_2, such as a higher Langmuir adsorption in shale matrix compared to CH_4[1], the compatibility between CO_2 and reservoir fluids (CH_4 and water), and large diffusivity of CO_2 in shale pores. These properties might enable CO_2-based fracturing technique to mitigate the formation damage issues that are otherwise caused by water-based fracturing, hence promoting a higher gas recovery post fracturing. Enhancing shale gas recovery through injecting CO_2 is also under investigation in some shale reservoirs[2]. Additional benefits of using CO_2 include storing CO_2 in shale formations. Either CO_2-based fracturing or CO_2-based enhanced gas recovery requires a profound understanding on the phase behavior and interfacial properties of the CO_2/CH_4/brine systems under reservoir conditions[3].

Interfacial tension (IFT) of gas-water or gas-brine is one of the most important properties affecting the performance of enhanced gas recovery. It significantly affects the movement, phase behavior and distribution of reservoir fluids in porous media[4]. Specifically, optimum operations of CO_2 flooding and sequestration in oil/gas reservoirs also depend on accurate knowledge of IFT of CO_2/brine systems, which affects the transport properties and capillary-sealing efficiency of CO_2 in the formation[5-8].

There have been extensive experimental and modeling studies on quantifying the IFT of various gas-water systems. Axisymmetric drop shape analysis method (ADSA) is the most-widely used technique to perform IFT measurement. With the ADSA method, IFT is measured by solving the Young-Laplace equation based on the geometry of a pendant drop captured by the measurement[9-10]. Table 6-1 summarizes some of the relevant gas-water IFT measurements and the range of laboratory conditions under which the measurements were conducted. It can be seen

from Table 6-1 that extensive experimental studies have been conducted on pure gas-pure water systems over wide ranges of pressures and temperatures. Most of the existing studies did not address the effects of non-hydrocarbon contaminants on gas-water IFT, especially at high pressure/temperature reservoir conditions. Moreover, most of the gas/water IFT measurements are only made for the pure hydrocarbon gases, rather than gas mixtures, with water or brine. Ren *et al.*[11] measured the interfacial tension of $CH_4/CO_2/H_2O$ systems. They covered the temperature range of 76.7-211.7^{o}F and pressure range of 145-4351 psia. But the salinity effect on the IFT was not addressed.

Table 6-1 Summary of previous laboratory measurements on gas-water IFT.

References	System compositions	Temperature range, °F	Pressure range, psia
Hocott[57], 1939	$CH_4/C_2H_6/C_3H_8/H_2O$	78.0-150.0	14.5-3,510
Hough *et al.*[53], 1951	CH_4/H_2O	74.0-280.0	15-15,000
Heuer[58], 1957	CO_2/H_2O	100.0, 280.0	up to 10,000
Jennings and Newman[54], 1971	CH_4/H_2O	74.0, 212.0, 350.0	14.7-12,000
Massoudi and King[27], 1974	CH_4/H_2O, CO_2/H_2O, N_2/H_2O	77.0	up to 1,000
Jho *et al.*[78], 1978	CO_2/H_2O	32.0-122.0	60-1,000
Wiegand and Franck[72], 1994	$CH_4/C_3H_8/C_6H_{14}/C_{10}H_{22}/N_2/H_2O$, etc.	77.0-571.0	14.5-37,710
Chun and Wilkinson[59], 1995	CO_2/H_2O/Ethanol	41.0-160.0	14.5-2,700
Sachs and Meyn[55], 1995	CH_4/H_2O	77.0	58-6,802
Lepski[79], 1997	CH_4/H_2O, N_2/H_2O	126.5-260.2	1,500-3,500
Tian *et al.*[80], 1997	CH_4/H_2O, C_6H_{14}/H_2O, C_7H_{16}/H_2O, N_2/H_2O, etc.	76.7-400.0	14.7-29,008
da Rocha *et al.*[60], 1999	CO_2/H_2O	95.0-149.0	1,000-4,000
Ren *et al.*[11], 2000	CH_4/H_2O, $CH_4/CO_2/H_2O$	77.0-212.0	145-4,351
Yan *et al.*[34], 2001	$CH_4/N_2/H_2O$, $CO_2/N_2/H_2O$	77.0-212.0	145-4,351
Hebach *et al.*[31], 2002	CO_2/H_2O	41.0-144.0	14.5-2,900
Zhao *et al.*[81], 2002	CH_4/H_2O	77.0-212.0	145-4,351
Tewes and Bourey[82], 2005	CO_2/H_2O	68.0, 86.0, 104.0	290-1,305
Park *et al.*[61], 2005	CO_2/H_2O	68.0, 77.0, 100.4, 159.8	up to 2,941
Yang *et al.*[20], 2005	CO_2/Brine	77.0, 136.0	14.5-4,351
Chiquet *et al.*[62], 2007	CO_2/H_2O	95.0-230.0	725-6,527
Akutsu *et al.*[83], 2007	CO_2/H_2O	77.0, 95.0, 113.0	1,088-2,393
Sutjiadi-Sia *et al.*[84], 2008	CO_2/H_2O	104.0	up to 3,916
Bennion and Bachu[21], 2008	CO_2/H_2O/Brine	105.0-257.0	290-3,916
Rushing *et al.*[76], 2008	$CH_4/C_2H_6/C_3H_8/N_2/CO_2/H_2O$	300.0-400.0	1,000-20,000
Bachu and Bennion[23], 2009	CO_2/H_2O/Brine	68.0-257.0	290-3,916
Aggelopoulos *et al.*[7], 2010	CO_2/Brine	81.0-212.0	725-3,626
Georgiadis *et al.*[63], 2010	CO_2/H_2O	77.0-214.0	145-4,351
Chalbaud *et al.*[22], 2010	CO_2/Brine	81.0-212.0	3,771
Shariat *et al.*[85], 2011	$CH_4/C_2H_6/C_3H_8/H_2O$	300.0-400.0	1,000-20,000
Aggelopoulos *et al.*[86], 2011	CO_2/Brine	80.6, 159.8, 212.0	725-3,626
Shariat *et al.*[87], 2012	CO_2/H_2O	up to 400.0	1,000-18,000
Li *et al.*[13], 2012	CO_2/Brine	76.7-346.7	290-7,252
Li *et al.*[14], 2012	CO_2/Brine	157.7-301.7	290-7,252
Khosharay and Varaminian[56], 2014	CH_4/H_2O, C_2H_6/H_2O, CO_2/H_2O,C_3H_8/H_2O	51.8-102.2	up to 870
Pereira *et al.*[88], 2015	CO_2/H_2O	76.7-384.5	49-10,028
Khashefi *et al.*[15], 2016	CH_4/H_2O, CH_4/Brine	100.1-391.7	0-13,343

In shale formations, the presence of salinity can affect the IFT of reservoir fluids to a large extent. It has been recognized that the addition of salts into the aqueous phase can significantly increase the IFT of gas/brine systems[12-14]. Some of the previous studies attributed the salinity effect to the change of the interface structure: the cations tend to accumulate in the aqueous phase due to the adsorption of the cations on the interface[15-19]. Another reason causing the IFT increase is the density increase of the aqueous phase because of salt addition. Yang *et al.*[20] reported IFT for CO_2/brine system over 77.0-136.0°F and 14.5-4351 psia. Bennion and Bachu[21] measured the IFT for CO_2/brine system over 105.0-257.0°F and 290-3916 psia. Aggelopoulos *et al.*[7] presented the IFT data of CO_2/brine system, with the consideration of different concentrations of NaCl and $CaCl_2$. Chalbaud *et al.*[22] measured the IFT for CO_2/brine systems at salinities of 0.085-2.75 mol/kg. Khashefi *et al.*[15] carried out IFT measurements on CH_4/brine and CH_4/pure water systems using the ADSA method in the temperature range 100.1-391.7°F and at pressures up to 13343 psia. Bachu and Bennion[23] conducted the IFT measurement of CO_2/water and CO_2/brine systems over 68.0-257.0°F and 290-3916 psia. Li *et al.*[13-14] measured the IFT between CO_2 with different salts in a wide range of total salt molality. Nonetheless, the experimental data for IFT of CH_4/brine mixtures are limited. Meanwhile, experimental data for IFT of CO_2/CH_4/brine mixtures are still scarce at reservoir conditions, albeit extensive IFT measurements have been conducted for CO_2/brine mixtures in the past decades.

An accurate IFT model is needed to predict the IFT of gas/brine systems under reservoir conditions. Up to now, numerous correlations were proposed and some of them have been used in commercial reservoir simulators for estimating IFT by petroleum engineering industry. The Parachor model[24, 25] and the scaling law[26] have gained more use than other predictive methods because of their simplicity[4]. However, both methods are not recommended for the IFT

predictions of hydrocarbon/water systems[4]. Massoudi and King[27] presented an IFT correlation for pure CO_2/water systems considering pressure and temperature; but it can be only applied at one temperature. Firoozabadi and Ramey[28] proposed an IFT model that can predict the IFT of hydrocarbon-gas/water mixtures. Argaud[29] and Sutton[30] developed new IFT correlations based on the Firoozabadi and Ramey[28] model by considering a broader class of compounds. Argaud[29] added the ratio of Parachor to molar mass of each compound to the Firoozabadi and Ramey[28] correlation as a corrective factor, while Sutton[30] considered more parameters in the improved correlation. Nonetheless, the predictive capabilities of these improved models are still limited[17]. Bennion and Bachu[21] presented an IFT correlation between CO_2 and brine as a function of salinity, which predicts the IFT of CO_2/brine systems based on the solubility of CO_2 in brine. However, the correlation of Bennion and Bachu[21] cannot predict IFT at pressures and temperatures higher than 3916 psia and 257.0°F. Meanwhile, the correlation was developed based on their own measured data, without being validated by other experimental data. Hebach *et al.*[31] and Kvamme *et al.*[32] presented IFT correlations for CO_2/water mixtures considering reservoir temperature, pressure, and density differences of pure component, but excluding the effect of mutual solubility. Furthermore, Li *et al.*[13-14] and Chalbaud *et al.*[33] developed correlations for IFT of CO_2/brine mixtures. Other methods based on statistical thermodynamics were also applied to predict IFT, such as linear gradient theory[34], perturbation theory[35], density gradient theory (DGT)[36-37], and integral and density functional theories[38-40]. In general, these methods have not been widely used in the petroleum industry likely due to their complexity.

In this study, previous IFT measurements of the gas/water or gas/brine mixtures are first reviewed and summarized. New experimental IFT data for CO_2/CH_4/brine systems with NaCl concentrations up to 200,000 ppm are presented over 77.0-257.0°F and 15-5,027 psia. IFT data

for CH_4/water and CO_2/water mixtures are found to be in good agreement with published data. The effects of temperature, pressure, CO_2 concentration, and salinity on IFT of CO_2/CH_4/brine mixtures are examined in detail. Based on the measured IFT data, a new IFT model is developed to determine IFT of CO_2/CH_4/brine mixtures. We examine this new model's performance by comparing it with other commonly used IFT correlations.

6.2 Experimental Section

6.2.1 Materials

Distilled water was used in the experiment. CO_2 and CH_4 (Praxair, Canada) had purities of 99.998 mol% and 99.99 wt%, respectively. Sodium chloride, ACS grade with a purity of greater than 99 wt%, was supplied by Sigma-Aldrich Company (Canada).

6.2.2 Experimental Setup

Figure 6-1 shows an image of the experimental setup used for the ADSA IFT measurements. The major component of this system is a visual high-pressure cell (TEMCO, Inc., U.S.A.) with a chamber volume of approximately 41.5cm^3. It can sustain pressure up to 10130.9 psia and temperature up to 350.0^{o}F. A light source was used to illuminate the pendant drop in the glass-windowed chamber. Nitrile O-rings were used in this experiment to reduce the corrosion of O-rings caused by CO_2 exposure. A band heater, together with an insulation jacket and a resistance temperature device (RTD) sensor, was used to heat the IFT cell and control its temperature within ±0.1 K. The IFT cell was placed on a vibration-free table (RS4000, USA) to remove the effect of constant low-frequency vibration. A needle valve was employed for controlling the formation of pendant drop, while several other valves were used to control the introduction of the different fluids (e.g., CO_2 or CH_4) into the pressure cell. The drain valve and a needle cleanout valve were used to flush and clean the cell chamber and needle without removal of the glass

windows. A high-resolution camera was used to observe the formation of the pendant drop, and capture its image. The stainless-steel needles could be changed to cover different IFT measurement ranges.

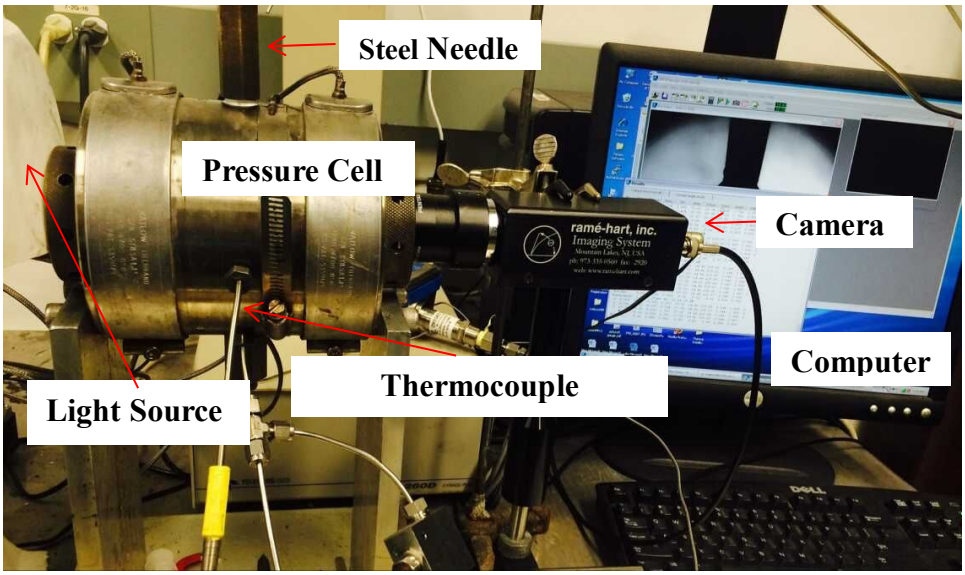

Figure 6-1 Digital image of the ADSA experimental setup.

Figure 6-2 shows the schematic of the ADSA experimental setup used in this study. The pressure of the high pressure IFT cell was measured with a digital precision testing gauge (DPG409-5.0kG, Ashcroft) with an accuracy of 0.05% of the full range. The temperature was measured with a thermocouple (JMQSS-125U-6, Omega) with an accuracy of ±0.1 K. The LED light source with a glass diffuser was used to provide a uniform illumination for the pendant drop. Two transfer cylinders, connected to the IFT cell, were used to pressurize and inject CH_4 and CO_2. The pressure of transfer cylinders was controlled by a syringe pump (500 HP, ISCO, Inc., Lincoln, NE). In this study, the pressure measurement, temperature measurement, and determination of mixture composition have accuracies of ±3 psia, ±0.1 K, and ±3.0 wt%, respectively. Considering the inaccuracies that arise from the ASDA method as well as from the estimated phase densities, a conservative uncertainty of ±5% can be applied to the

experimentally measured IFTs. The IFT of the CO_2/CH_4/brine systems is measured over 77.0-257.0°F, 15-5,027 psia and a salinity range of 0-200,000 ppm of NaCl. Each IFT measurement was repeated three times to ensure the repeatability of each measurement.

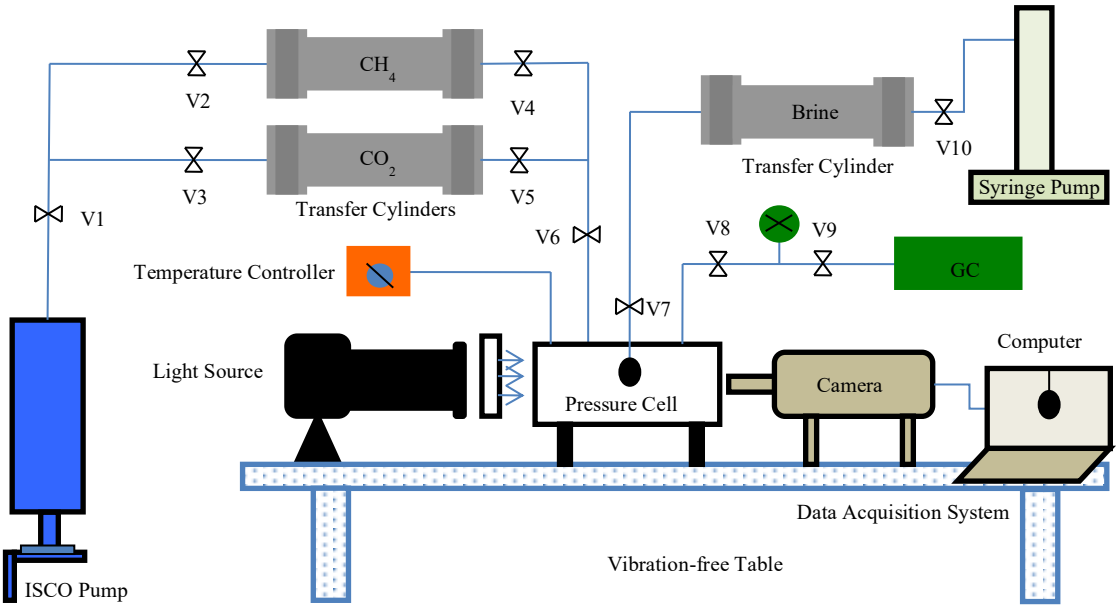

Figure 6-2 Schematic diagram of the experimental setup for measuring the equilibrium IFTs of CO_2/CH_4/brine systems using the ADSA technique for the pendant drop case.

6.2.3 Experimental Procedures

Before each measurement, the entire system was tested for leakage with N_2. Then it was cleaned with acetone, flushed with CH_4 or CO_2 and evacuated. The cell was pressurized with CH_4 or CO_2 to a pre-specified pressure. When measuring the IFT for gas mixtures, the pressure cell was first filled with a pure gas (e.g., CO_2) to a specified pressure at a given temperature; then another pure gas (e.g., CH_4) was injected into the pressure cell, resulting in a different pressure. A sampler (Swagelok, Canada) with a volume of 10 cm^3 was used to take the gas sample inside the pressure cell. The composition of the gas mixture was measured with a gas chromatography (GC) method. After the pressure and temperature in the pressure cell were stabilized, a pendant water/brine drop was introduced by a syringe pump (500 HP, ISCO, Inc., Lincoln, NE), of which pressure was maintained about 14-44 psia higher than that of gas phase inside the pressure cell. The

pendant water drop formed at the tip of the stainless-steel needle. After the gas was injected, usually 30-60 min were required for the system to reach an equilibrium state at given pressure and temperature.

After the pendant water drop was formed in the gas phase, its digital image was well-focused through the diffused light, acquired sequentially, and stored by the computer. For each digital water drop image, a standard grid image was used to calibrate the drop image and correct possible optical distortion. The ADSA program for the pendant drop case was then executed to determine the equilibrium IFT. The output data also included the radius of the curvature at the apex point, and the volume and surface area of the pendant water drop. Only the local gravitational acceleration and the gas-water density difference were required as the input data for this program. Knowing the pendant drop dimensions and the fluid densities enabled the calculations of IFT. During the IFT measurement, gas-phase and liquid-phase densities needed to be input into the software. In this study, as for CO_2/H_2O, CH_4/H_2O, and $CO_2/CH_4/H_2O$ systems, we calculated the densities of the liquid phase and vapor phase by an enhanced Peng-Robinson equation of state (PR EOS) model with temperature-dependent binary interaction parameters and constant volume shift parameters. More specifically, we used a new BIP correlation developed by Li and Yang[41] to estimate the BIP of CO_2/H_2O binary; this BIP correlation is a function of the reduced temperature of CO_2. Meanwhile, we used a BIP correlation developed by Søreide and Whitson[42] to estimate the BIP of CH_4/H_2O binary; this BIP correlation is a function of temperature and acentric factor of CH_4. Table 6-2 lists the physical properties of CO_2, CH_4 and H_2O used in the PR EOS model. As for CO_2/brine, CH_4/brine, and CO_2/CH_4/brine systems, in order to obtain an accurate phase density prediction, we used a modified PR EOS model by Søreide and Whitson[42] with constant volume shift parameters. This model considers salinity and

mutual solubility of CH_4/brine and CO_2/brine binaries.

Table 6-2 Physical properties of the three components used in the IFT model.

Component	P_c, psia	T_c, °F	Acentric factor	Molecular weight	Volume Shift	Parachor
CO_2	1069.9	87.89	0.225	44.01	-0.15400	78
CH_4	667.2	-116.59	0.008	16.04	-0.01478	77
H_2O	3197.8	705.47	0.344	18.02	0.23170	52

In this study, much care has been taken to eliminate possible error sources in IFT measurements. Firstly, as recommended by the manufacturer, the settings for KRÜSS software suitable for gas-water IFT measurements were set as (Light level=2, Brightness=31, Gain=10, Exposure=-11). Secondly, a steel needle with an outer needle diameter of 0.70 mm was used in the tests to control the droplet size. During the experiments, extra efforts were devoted to generating large droplets at the needle tip; larger droplet volumes created more accurate IFT measurements because the effect of the capillary tube tip diminished as the drop volume became larger[43]. In addition, all the IFT data were measured under equilibrium conditions.

6.3 Mathematical Formulation

Most of the previous IFT models originated from the Parachor model[6, 13-14, 44-49]. For example, Chalbaud *et al.*[6] developed a correlation on the basis of the Parachor model taking into account the influence of temperature, pressure, salt presence and chemical structure of CO_2. Ayirala and Rao[49] proposed a new mechanistic Parachor model based on mass transfer to predict IFT in multicomponent hydrocarbon systems.

Sudgen[50] proposed an equation including the new constant Parachor in the following form:

$$\sigma^{1/4} = \frac{P}{M}\Delta\rho \qquad (6\text{-}1).$$

where σ is the IFT between two phases; P is Parachor; M is molecular weight of the

component; and $\Delta\rho$ is density difference between two phases. Quayle[51] determined the Parachor for a large number of compounds considering their molecular structures. Weinaug and Katz[24] extended Sudgen's equation[50] to mixtures as follows:

$$\sigma^{1/4} = \sum_{i=1}^{n} P_i \left(\frac{\rho_L}{M_L} x_i - \frac{\rho_v}{M_v} y_i\right) \qquad (6\text{-}2).$$

where P_i is Parachor for component i; M_L is the average molecular weight of liquid phase; M_V is the average molecular weight of vapor phase; ρ_L is density of liquid phase; ρ_V is density of vapor phase; x_i is the mole fraction of component i in liquid phase; and y_i is the mole fraction of component i in vapor phase. The equation proposed by Weinaug and Katz[24] is used as a standard method of IFT prediction in the petroleum industry. It has been applied to some binary hydrocarbon systems and pure hydrocarbons successfully, but generally does not perform well for gas/water systems[28].

Firoozabadi and Ramey[28] presented a correlation for estimating the IFT of hydrocarbon gas or hydrocarbon liquid with water. The phase density difference and reduced temperature for the hydrocarbon phase were chosen to be two correlating parameters. It correlates the IFT to the density difference between gas phase and liquid phase with an exponent of 4 based on the assumption from the van der Waals equation,

$$\frac{\sigma_{hw}^{0.25}}{\rho_w - \rho_h} \left(\frac{T_{oR}}{T_c}\right)^{0.3125} = f\left(\Delta\rho\right) \qquad (6\text{-}3).$$

where σ_{hw} is IFT between hydrocarbon and water, dynes/cm; ρ_w is pure water density, g/cm^3; ρ_h is density of hydrocarbon, g/cm^3; T_c is critical temperature of water, ^{o}R; and T_{oR} is temperature, ^{o}R. One can plot the LHS of Equation (6-3) with respect to phase density difference

to find out their proper relationship. Danesh[4] presented a modified version of Equation (6-3) for modeling IFT of hydrocarbon/water systems as,

$$\sigma_{hw} = 111(\rho_w - \rho_h)^{1.024}(\frac{T_{oR}}{T_c})^{-1.25} \quad (6\text{-}4).$$

where σ_{hw} is IFT between hydrocarbon and water, dynes/cm; ρ_w is pure water density, g/cm^3; ρ_h is density of hydrocarbon, g/cm^3; T_c is critical temperature, K; and T_{oR} is temperature, ^{o}R.

Sutton[30] developed another empirical correlation for determining IFT of hydrocarbon-gas/water systems,

$$\sigma_{gw} = [\frac{1.53988(\rho_{w_{g/cc}} - \rho_{h_{g/cc}}) + 2.08339}{(\frac{T_{oR}}{T_c})^{(0.821976 - 1.83785\times10^{-3}T_{oR} + 1.34016\times10^{-6}T_{oR}^2)}}]^{3.6667} \quad (6\text{-}5).$$

where σ_{gw} is IFT between gas and water, dynes/cm; $\rho_{w_{g/cc}}$ is density of water phase, g/cm^3; and $\rho_{h_{g/cc}}$ is density of hydrocarbon-gas phase, g/cm^3; T_{oR} is temperature, ^{o}R; T_c is critical temperature of water, ^{o}R. As pointed out by Chalbaud *et al.*[22], Firoozabadi and Ramey's correlation[28] might not be applicable to some gases, such as CO_2, because the gas solubility in water can be large.

All of the correlations mentioned above were developed based on the IFT measurements and the phase density difference between hydrocarbon gases with water. From our experimental results, we observed that the IFT of gas mixtures with water has a strong correlation with gas composition in addition to the effect of temperature, pressure, and density difference. Considering these factors, we present a new IFT correlation,

$$\left(\frac{\sum_{i=1}^{n} z_i M_i}{M_H}\right)^{0.183361} \frac{\sigma_{gw}^{0.25}}{\left(\rho_M^L \sum_{i=1}^{n} x_i P_i - \rho_M^V \sum_{i=1}^{n} y_i P_i\right)} T_r^{0.3125} = f\left(\rho_M^L \sum_{i=1}^{n} x_i P_i - \rho_M^V \sum_{i=1}^{n} y_i P_i\right) \quad (6\text{-}6).$$

where z_i is the overall mole fraction of component i in the gas phase; M_i is molecular weight of component i, g/mol; M_H is the molecular weight of the heaviest component in the gas mixture, g/mol; T_r is reduced temperature of water; ρ_M^L is molar density of liquid phase, mol/m^3; ρ_M^V is molar density of vapor phase, mol/m^3; x_i is mole fraction of component i in liquid phase; and y_i is mole fraction of component i in vapor phase. This correlation takes into account the effects of pressure, temperature, individual compound's molecular weight, density difference, and gas composition on on IFT of gas-mixtures/water systems.

Also, at the same temperature and pressure, a different IFT can be found for a given gas mixture due to different water salinities. Argaud[29] presented a comprehensive review on salt's effect on IFT. Many scholars, such as Chalbaud *et al.*[6], Argaud[29], and Massoudi and King[12], have found that there exists a unique linear relationship between IFT increment and the salt concentration of NaCl; and the slope of this line is independent of temperature when an IFT plateau is reached. Analogous to previous works (such as Standing[52]), a linear relationship between IFT increment for CO_2/brine and CH_4/brine systems and the salt (NaCl) concentration is also provided as follows:

$$\sigma_{cor} = kC_s \quad (6\text{-}7).$$

where σ_{cor} represents the increase in IFT due to salinity effect, mN/m; and C_s represents the molar concentration of salt in water, mol/kg; and k is regression constant.

In this study, we find that the salt (NaCl) effects on IFT of the CO_2/brine and CH_4/brine systems are different from each other, although a linear relationship holds between IFT increment and NaCl concentration for both systems. The IFT of a given CO_2/CH_4/brine system can be determined by first calculating the IFT for CO_2/CH_4/water systems, and then applying the following correction:

$$\sigma_{gb} = \sigma_{gw} + y_{CH_4}\sigma_{cor-CH_4} + y_{CO_2}\sigma_{cor-CO_2} \quad (6\text{-}8).$$

where σ_{gb} represents IFT between gas and brine; σ_{gw} represents IFT between gas and pure water; σ_{cor-CH_4} represents the increase in IFT due to salinity effect for CH_4/brine system, mN/m; σ_{cor-CO_2} represents the increase in IFT due to salinity effect for CO_2/brine system, mN/m; y_{CH_4} is the mole fraction of CH_4 in the original gas mixture; and y_{CO_2} is the mole fraction of CO_2 in the original gas mixture.

6.4 Results and Discussion

6.4.1 Comparison with Published Data

In order to validate the reliability of IFT measurements made in this study, IFTs measured at 80.0°F, 81.0°F, 163.0°F and 257.0°F for CO_2/H_2O and CH_4/H_2O systems are compared with the published data given in Table 6-1. Figures 6-3 to 6-8 show the IFTs measured in this study, together with those measured previously at or close to these temperatures. For all plots, the color-filled (other than red) symbols represent published data, while the red-filled triangles are IFTs measured in this study. Figures 6-3 to 6-5 compare the IFT of CH_4/H_2O systems measured in this study with the published data by Hough *et al.*[53], Jennings and Newman[54], Sachs and Meyn[55], Ren *et al.*[11], Khosharay and Varaminian[56], and Khashefi *et al.*[15]. It can be seen from Figures 6-3 to 6-5 that our measurement results for CH_4/H_2O systems are comparable to the

published data. Our IFT data deviate much from those by Hocott[57]. This is because Hocott[57] used a gas phase that was dominated by CH_4, but also contained a small amount of C_2H_6 and C_3H_8. Figures 6-6 to 6-8 shows the comparison of IFTs of CO_2/H_2O systems measured in this study against the published IFT data by Hocott[57], Hough *et al.*[53], Heuer[58], Chun and Wilkinson[59], da Rocha *et al.*[60], Hebach *et al.*[31], Park *et al.*[61], Chiquet *et al.*[62], Bachu and Bennion[21], Chalbaud *et al.*[22], and Georgiadis *et al.*[63]. When pressure is low enough or equal to the saturation pressure of the aqueous phase, the water/gas IFT data should approach the surface tension of water at zero pressure and the temperature of interest. It has been found the surface tension of ordinary water at 257.0°F is 53.96 mN/m[64], as shown in Figure 6-8. The previous published and our measured IFT data deviate slightly from the constraint. This deviation may be caused by water vaporization at high temperatures.

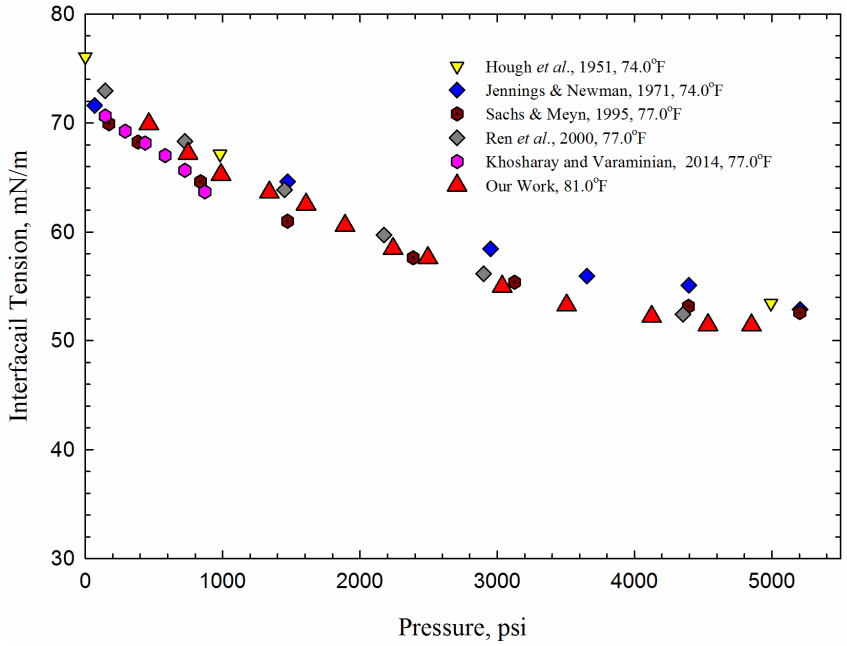

Figure 6-3 Comparison of CH_4/H_2O IFTs measured in this study at 81.0°F and IFTs measured previously over 74.0-81.0°F.

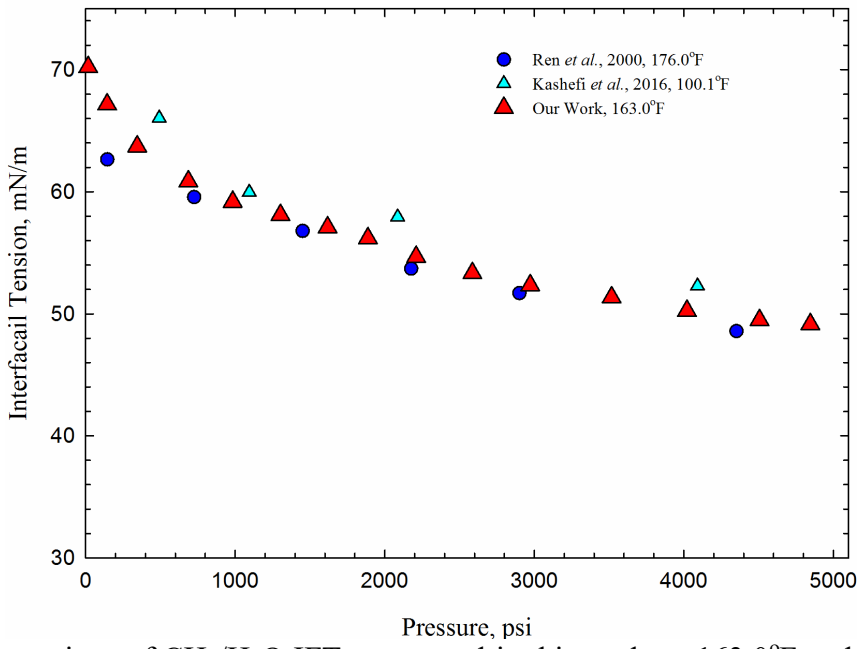

Figure 6-4 Comparison of CH_4/H_2O IFTs measured in this study at 163.0°F and IFTs measured previously over 100.1-176.0°F.

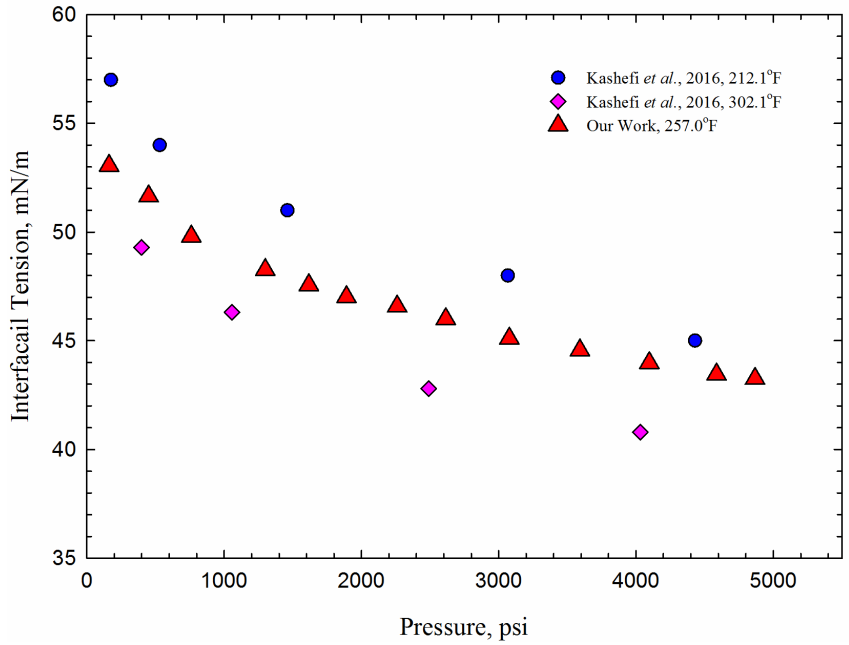

Figure 6-5 Comparison of CH_4/H_2O IFTs measured in this study at 257.0°F and IFTs measured previously over 212.1-302.1°F.

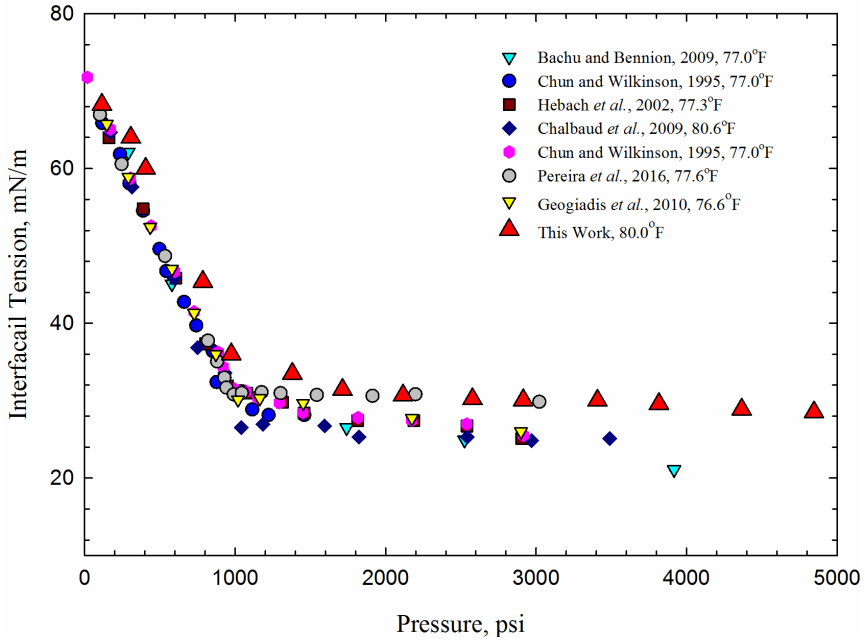

Figure 6-6 Comparison of CO_2/H_2O IFTs measured in this study at 80.0°F and IFTs measured previously over 76.6-80.6°F.

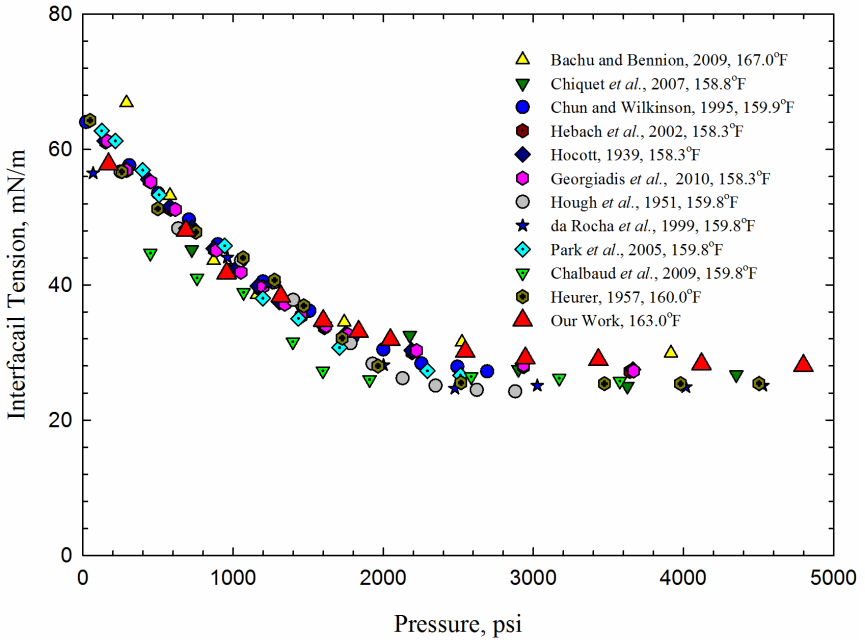

Figure 6-7 Comparison of CO_2/H_2O IFTs measured in this study at 163.0°F and IFTs measured previously over 158.3-167.0°F.

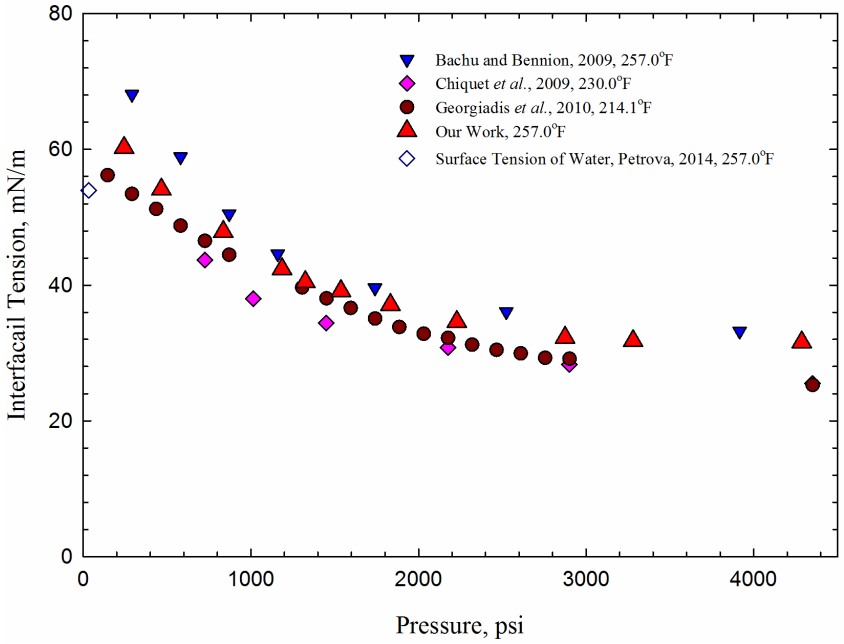

Figure 6-8 Comparison of CO_2/H_2O IFTs measured in this study at 257.0°F and IFTs measured previously over 214.1-257.0°F.

6.4.2 Effect of Pressure, Temperature and Salinity on IFT

In this section, we use the IFT measured for CO_2/brine (0-200,000ppm NaCl) (Figure 6-9) and CH_4/brine (0-200,000ppm NaCl) (Figure 6-10) at around 78.0°F, 167.0°F, and 257.0°F, respectively, to analyze the effect of pressure, temperature and salinity on IFT. Figure 6-9 presents the IFT isotherms of CO_2/brine system. It indicates that, at low pressures (below around 580.2-725.2 psia), IFTs decrease approximately linearly with increasing pressure at these three temperatures, corresponding to the so-called Henry regime[62]. Passing the Henry regime, pressure increase has less effect on the IFT reduction. When pressure increases to a high value, IFT levels off. In general, IFTs for CH_4/brine system are found to decrease with increasing temperature as shown in Figure 6-10. On the contrary, IFTs for CO_2/brine systems measured at higher temperatures are generally higher than those measured at lower temperatures. It is because the solubility of CO_2 in water varies significantly with temperature[20]. At a higher temperature, the solubility of CO_2 in water or brine is less than that at a lower temperature[65-67]. As salinity

increases, the solubility of CO_2 in brine decreases, leading to changes in the brine density and IFT. As seen from Figure 6-9, the IFT of CO_2/brine systems exhibits a more pronounced reduction with an increase in pressure at a lower temperature than that at a higher temperature. The plateau for CO_2/brine system is reached at about 1,400 psia at 78.0°F, about 2,000 psia at 167.0°F, and about 2,900 psia at 257.0°F, respectively.

The salinity of brine in shale formations can be quite high, up to 300,000 ppm[68]. Salts can affect the interfacial tension between gas and water. When ions dissolve into liquid water, electrostatic force from ions can change the original structure of water, usually forming water molecular layer around ions which is called "hydration". Indeed, water will always stride to maintain its hydrogen-bonded structure in order to maintain thermodynamic stability, while salts can affect such bonded structure formed by water, and thus affect the IFT between gas and water. In this study, IFT measurements are conducted at salinities up to 200,000 ppm of NaCl for both CO_2/brine and CH_4/brine systems, as shown in Figures 6-9 and 6-10. Similar to CH_4/H_2O and CO_2/H_2O systems, the IFT of CH_4/brine and CO_2/brine systems exhibits a decreasing trend with increasing pressure at a given temperature. Furthermore, at the same temperature, IFT increases as more NaCl is present in water. This is attributed to the fact that, as salinity increases, the specific gravity of brine also increases; this enlarges the density difference between gas phase and liquid phase, leading to a higher IFT of the gas/brine system. At lower pressures, the IFTs corresponding to different salinities usually cross with each other in the range of 15.0-725.2 psia. Such crossing behavior might be related to the complex gas solubility in liquid phase at different temperatures[20]. Chalbaud *et al.*[6] presented when NaCl concentration is lower than 5,000 ppm, salinity effect on IFT is negligible. For CO_2/brine systems at a low pressure, salinity shows a more obvious effect on IFT, while the salt effect on IFT reaches to a given value as the pressure

becomes higher. Meanwhile, at high pressures, the average IFT increment for different NaCl concentrations depends on neither pressure nor temperature. Some scholars[69-70] measured the solubility of CO_2 in water and brine as a function of pressure. They attributed the existence of a plateau to the solubility effect on the IFT reduction. Meanwhile, some studies[69-71] presented that the pressure-dependence of CO_2 solubility in brine exhibits a similar trend with that in pure water.

Our measurements were limited to the conditions of 77.0-257.0°F and 15-5,050 psia. Wiegand and Franck[72] measured the IFT of various gases and water systems covering much greater temperature and pressure ranges. They found the IFT levels off when pressure exceeds 2175.6-2900.8 psia, while it increases very slowly with pressures above 7251.9-14503.8 psia.

Regarding the IFT results of the CH_4/brine system as shown in Figure 6-10, similar conclusions can be made. The CH_4/brine IFT also decreases with an increasing pressure until it reaches at a plateau. At the same temperature, CH_4/brine system needs a higher pressure to reach the plateau compared to CO_2/brine system. At about 81.0°F, for example, the value of the plateau is reached at about 2,800 psia, and about 4,000 psia at 163.0°F. Figures 6-9 and 6-10 indicate that the CH_4/brine IFT is overall higher than that of CO_2/brine. The physical properties of CH_4 and CO_2 cause such difference; CH_4 has a lower solubility in water compared with CO_2 at the same temperature and pressure. Also, at the same pressure and temperature, the density difference between gas phase and liquid phase of the CH_4/brine system is larger than that of the CO_2/brine system.

As for the IFT between gas and brine, when pressure is low enough or equal to the saturation pressure of the aqueous phase, the brine/gas IFT data should approach the surface tension of

water at zero pressure and the temperature of interest. The surface tensions of ordinary brine at different temperatures were measured by Abramzon and Gaukhberg[73]; these surface tensions have been labeled in Figures 6-9 and 6-10.

For the experimental surface tension of salt solutions measured by Abramzon and Gaukhberg[73], we assumed that the surface tensions were measured at the saturation pressure of a specific salt solution because no specific operating pressures were reported in the paper. From Figures 6-9 and 6-10, this constraint is only satisfied at 77.0°F. However, at 167.0°F and at atmospheric pressure, the experimental IFTs tend to be higher than the brine surface tension. This can be explained as follows. At 77.0°F, the brine drop in the IFT cell can maintain as a single liquid phase because water's saturation pressure at 77.0°F is lower than the atmospheric pressure. Therefore, the reported gas-brine IFTs data should tend to be the exact brine surface tension at this temperature. However, at higher temperatures (such as 167.0°F), water molecules are more apt to escape form liquid phase into vapor phase, which leads to a higher salinity of the brine drop and also causes a larger density difference between the liquid phase and vapor phase. Hence, relatively higher IFTs could be resulted at higher temperatures.

When the temperature is higher than the saturation temperature at atmospheric pressure, such as 257.0°F, the drop cannot maintain as a single liquid phase, but vapor phase. In the literature, surface tensions of brine or pure water reported at higher temperatures mostly were measured using the differential maximum bubble pressure method[74]. For this method, a bubble chamber unit is applied, leading to a curved interface between gas and liquid phases. There may be a permanent state of metastability because of the negative pressure effect when the gas-liquid interface is curved[75]. As shown in Figures 6-8, 6-9(c), and 6-10(c), the deviation persists at higher temperatures; this may arise from the effect of water vaporization, as mentioned above.

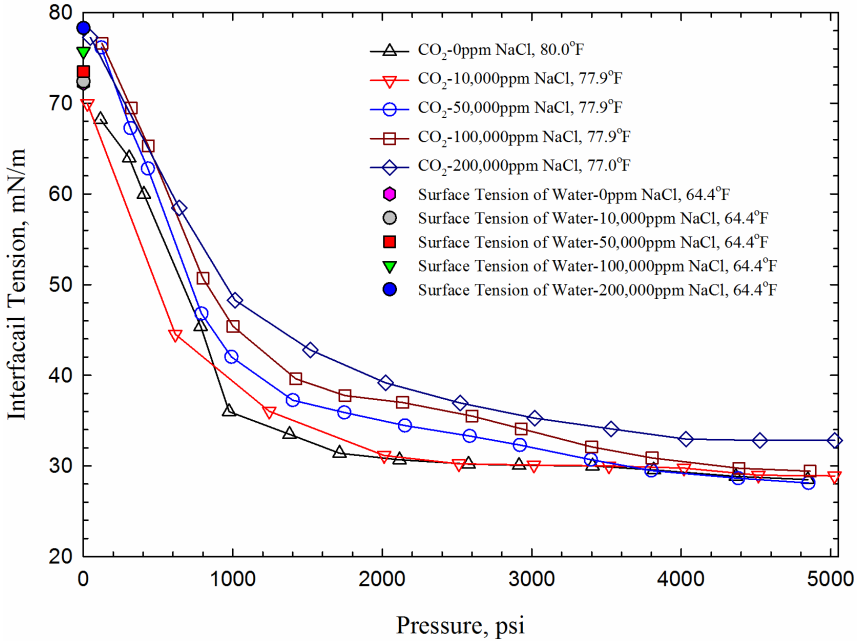
Interfacail Tension, mN/m
Pressure, psi
CO2-0ppm NaCl, 80.0°F
CO2-10,000ppm NaCl, 77.9°F
CO2-50,000ppm NaCl, 77.9°F
CO2-100,000ppm NaCl, 77.9°F
CO2-200,000ppm NaCl, 77.0°F
Surface Tension of Water-0ppm NaCl, 64.4°F
Surface Tension of Water-10,000ppm NaCl, 64.4°F
Surface Tension of Water-50,000ppm NaCl, 64.4°F
Surface Tension of Water-100,000ppm NaCl, 64.4°F
Surface Tension of Water-200,000ppm NaCl, 64.4°F

(a)

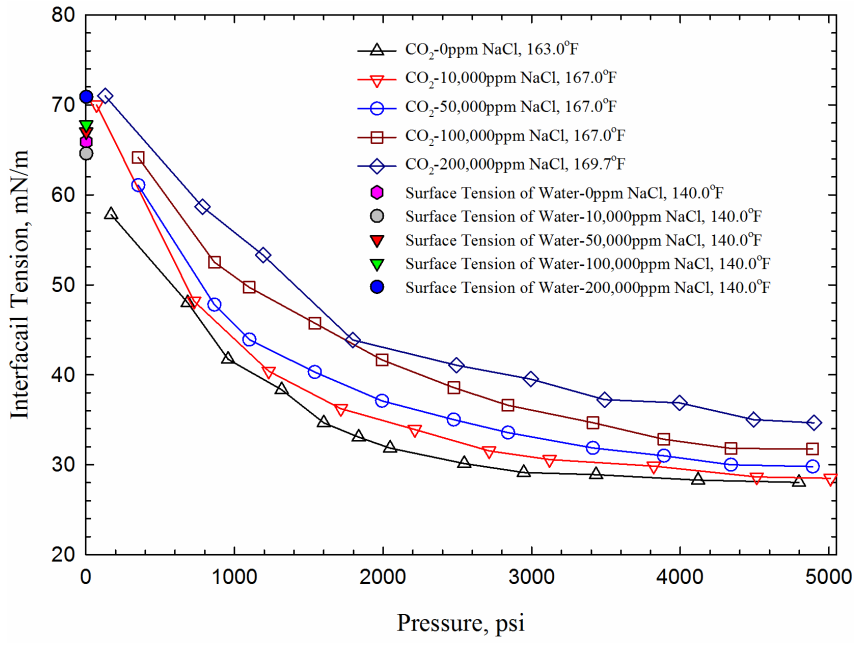
Interfacail Tension, mN/m
Pressure, psi
CO2-0ppm NaCl, 163.0°F
CO2-10,000ppm NaCl, 167.0°F
CO2-50,000ppm NaCl, 167.0°F
CO2-100,000ppm NaCl, 167.0°F
CO2-200,000ppm NaCl, 169.7°F
Surface Tension of Water-0ppm NaCl, 140.0°F
Surface Tension of Water-10,000ppm NaCl, 140.0°F
Surface Tension of Water-50,000ppm NaCl, 140.0°F
Surface Tension of Water-100,000ppm NaCl, 140.0°F
Surface Tension of Water-200,000ppm NaCl, 140.0°F

(b)

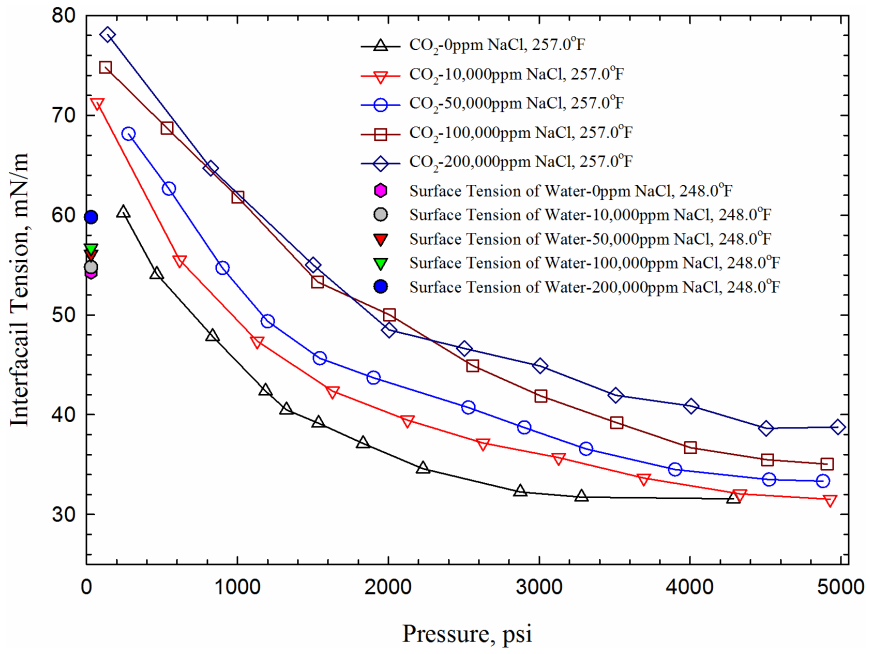

(c)

Figure 6-9 IFT of CO_2/brine system as a function of pressure at different temperatures and different salinities. The surface tension of brine was measured by Abramzon and Gaukhberg (1993).

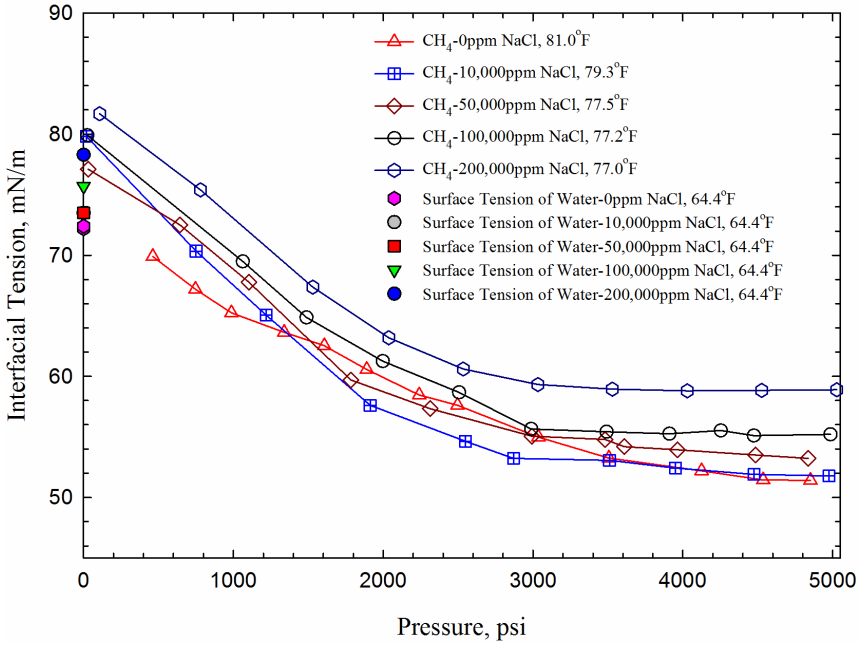
Interfacial Tension, mN/m
Pressure, psi
CH4-0ppm NaCl, 81.0°F
CH4-10,000ppm NaCl, 79.3°F
CH4-50,000ppm NaCl, 77.5°F
CH4-100,000ppm NaCl, 77.2°F
CH4-200,000ppm NaCl, 77.0°F
Surface Tension of Water-0ppm NaCl, 64.4°F
Surface Tension of Water-10,000ppm NaCl, 64.4°F
Surface Tension of Water-50,000ppm NaCl, 64.4°F
Surface Tension of Water-100,000ppm NaCl, 64.4°F
Surface Tension of Water-200,000ppm NaCl, 64.4°F

a)

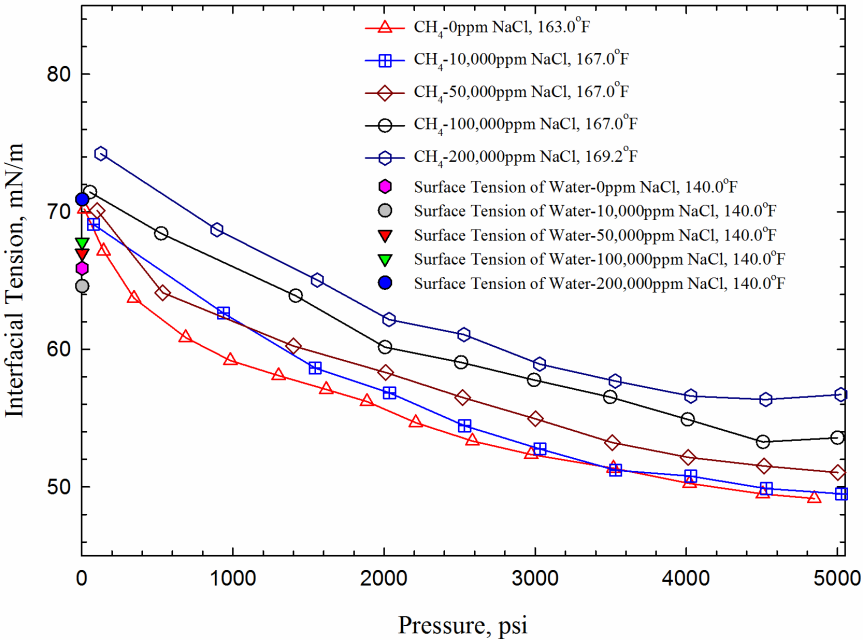
Interfacial Tension, mN/m
Pressure, psi
CH4-0ppm NaCl, 163.0°F
CH4-10,000ppm NaCl, 167.0°F
CH4-50,000ppm NaCl, 167.0°F
CH4-100,000ppm NaCl, 167.0°F
CH4-200,000ppm NaCl, 169.2°F
Surface Tension of Water-0ppm NaCl, 140.0°F
Surface Tension of Water-10,000ppm NaCl, 140.0°F
Surface Tension of Water-50,000ppm NaCl, 140.0°F
Surface Tension of Water-100,000ppm NaCl, 140.0°F
Surface Tension of Water-200,000ppm NaCl, 140.0°F

b)

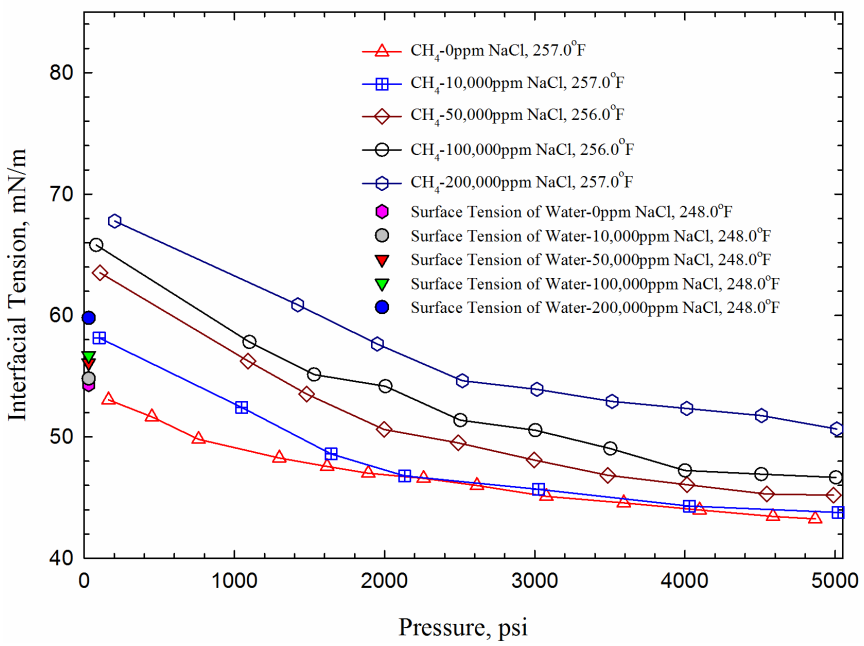

c)

Figure 6-10 IFT of CH_4/brine system as a function of pressure at different temperatures and different salinities. The surface tension of brine was measured by Abramzon and Gaukhberg (1993).

6.4.3 Effect of CO_2 Concentration on IFT

Supercritical CO_2 can be used as hydraulic fracturing fluid or enhanced gas recovery medium in shale reservoirs. Investigation on the CO_2 addition on IFT of CH_4/brine system is important for understanding the multiphase fluid flow within both the fracture and matrix. Figures 6-11 and 6-12 show the measurement results at different temperatures. The detailed data shown in Figure 6-11 and 6-12 are given in the Supporting Information (See Tables S1 and S2). It can be seen that the presence of CO_2 in CH_4 leads to reduction in IFT between gas mixtures and brine. A lower IFT can be expected if CO_2 is added into the gas phase, but the degree of IFT reduction depends on the amount of CO_2 added. With more CO_2 present in the gas mixture, the IFT reduction effect is more pronounced. As shown in Figure 6-11b, the IFT reduction ratio is more than 25% for the CH_4/H_2O system with 44.87 mol% CO_2 added at 163.0°F. Similarly, in Figures 6-12a and 6-12f,

the IFT reduction for the CH_4/brine systems is pronounced even at low concentrations of CO_2. The density difference between gas phase and liquid phase is reduced if CO_2 is added to CH_4, which is a major factor causing IFT reduction. Another reason is because CO_2 exhibits a higher solubility in water or brine compared to CH_4, further decreasing the density difference. The phase behavior of CO_2/CH_4 mixture with water or brine, together with the physical properties of the gas components, all contribute to the IFT reduction effect.

Rushing *et al.*[76] measured the effect of CO_2 concentration (up to 20.00 mol%) on IFT of gas-water system (gas: CH_4 with a small fraction of C_2H_6 and C_3H_8) at high pressure-temperature conditions. They suggested that a higher concentration of CO_2 resulted in a lower IFT over a much greater pressure range than that for gases with lower CO_2 concentrations. They found that CO_2 concentration in vapor phase tended to decrease IFT of CH_4/brine systems at lower pressures, but slightly increased the IFT or showed no effect at higher pressures. It is, however, shown in our study that the presence of CO_2 has a significant effect on the IFT at both high and low pressures. Shariat[43] measured IFT for gas mixtures containing up to 20.00 mol% CO_2 (or without CO_2) with water over a wider pressure range, showing that the presence of CO_2 up to 20.00 mol% in gas mixtures has no significant effect on gas-water IFTs at higher pressures. Ren *et al.*[11] measured the IFT of $CO_2/CH_4/H_2O$ systems with CO_2 concentrations of 0, 20.00, 40.00, 60.00, and 80.00 mol% at temperatures of 104.0°F, 140.0°F, 176.0°F, and 212.0°F, respectively. They found that: CO_2 concentration of 20.00 mol% leads to negligible IFT reduction, and CO_2 concentrations of 20.00-40.00 mol% lead to minor reduction in IFT. They also reported IFT reduction at higher concentrations of CO_2 in gas mixture for all temperatures. However, we observed pronounced IFT reduction even at low CO_2 concentrations in our study.

The aforementioned experimental results demonstrate that CO_2 decreases the IFT of CH_4/H_2O

systems, while salinity tends to increase the IFT of CH_4/H_2O systems. These IFT data are useful for assessing the engineering soundness of either using CO_2 for fracturing shale formations or CO_2 huff-and-puff for enhancing shale gas recovery. For a given shale reservoir, if the reservoir conditions such as reservoir temperature, pressure and salinity of formation water are given, the IFT between shale gas (mainly CH_4) and brine can be approximately determined.

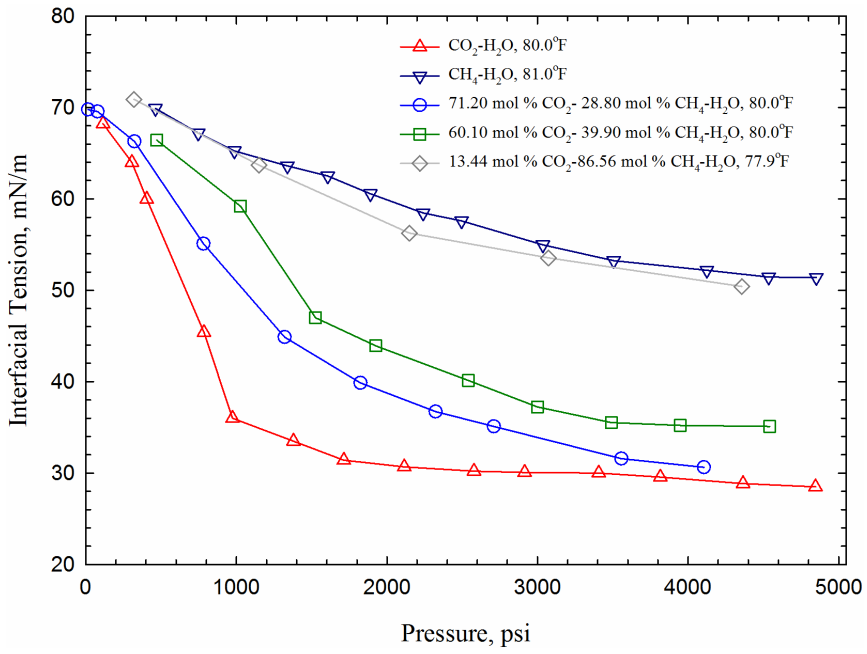
CO2-H2O, 80.0°F
CH4-H2O, 81.0°F
71.20 mol % CO2- 28.80 mol % CH4-H2O, 80.0°F
60.10 mol % CO2- 39.90 mol % CH4-H2O, 80.0°F
13.44 mol % CO2-86.56 mol % CH4-H2O, 77.9°F
Interfacial Tension, mN/m
Pressure, psi
80
70
60
50
40
30
20
0
1000
2000
3000
4000
5000

a)

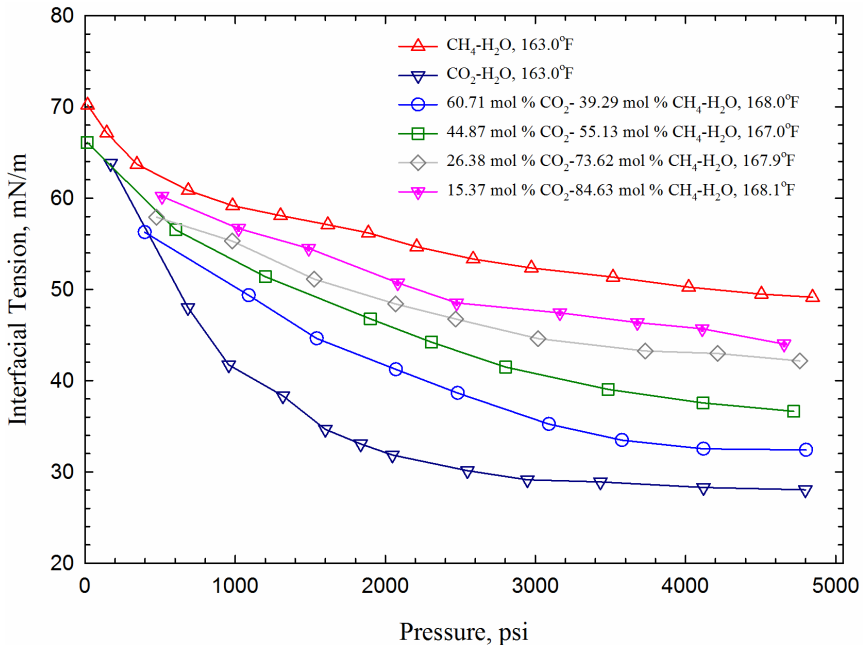
CH4-H2O, 163.0°F
CO2-H2O, 163.0°F
60.71 mol % CO2- 39.29 mol % CH4-H2O, 168.0°F
44.87 mol % CO2- 55.13 mol % CH4-H2O, 167.0°F
26.38 mol % CO2-73.62 mol % CH4-H2O, 167.9°F
15.37 mol % CO2-84.63 mol % CH4-H2O, 168.1°F
Interfacial Tension, mN/m
Pressure, psi
80
70
60
50
40
30
20
0
1000
2000
3000
4000
5000

b)

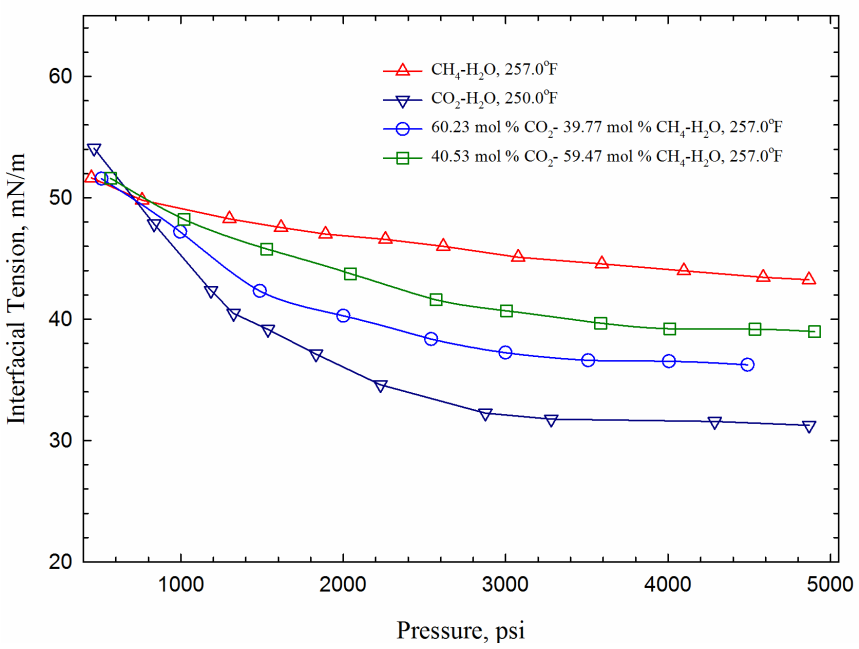

c)

Figure 6-11 IFT of $CO_2/CH_4/H_2O$ systems as a function of pressure at different temperatures.

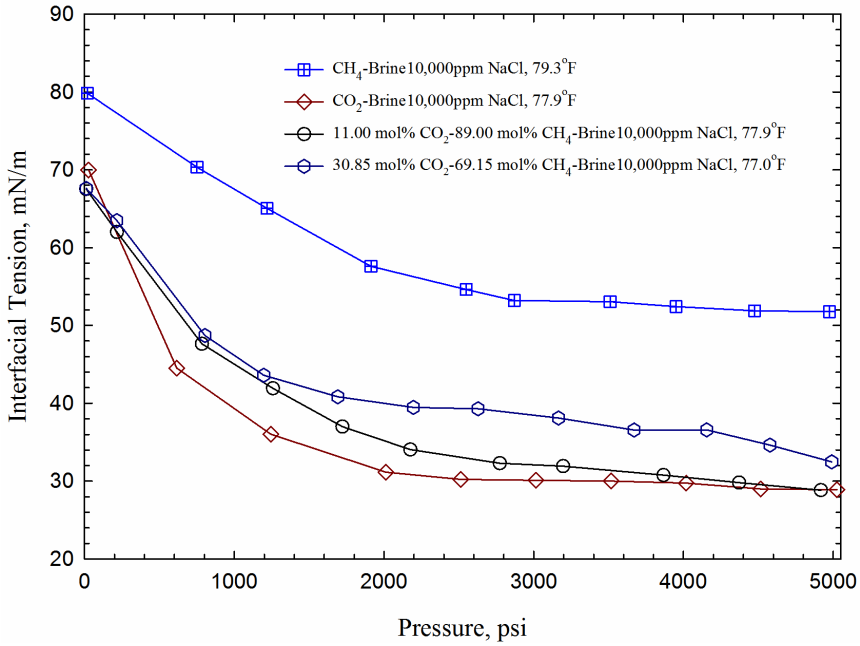
CH4-Brine10,000ppm NaCl, 79.3°F
CO2-Brine10,000ppm NaCl, 77.9°F
11.00 mol% CO2-89.00 mol% CH4-Brine10,000ppm NaCl, 77.9°F
30.85 mol% CO2-69.15 mol% CH4-Brine10,000ppm NaCl, 77.0°F
Interfacial Tension, mN/m
Pressure, psi
90
80
70
60
50
40
30
20
0
1000
2000
3000
4000
5000

a)

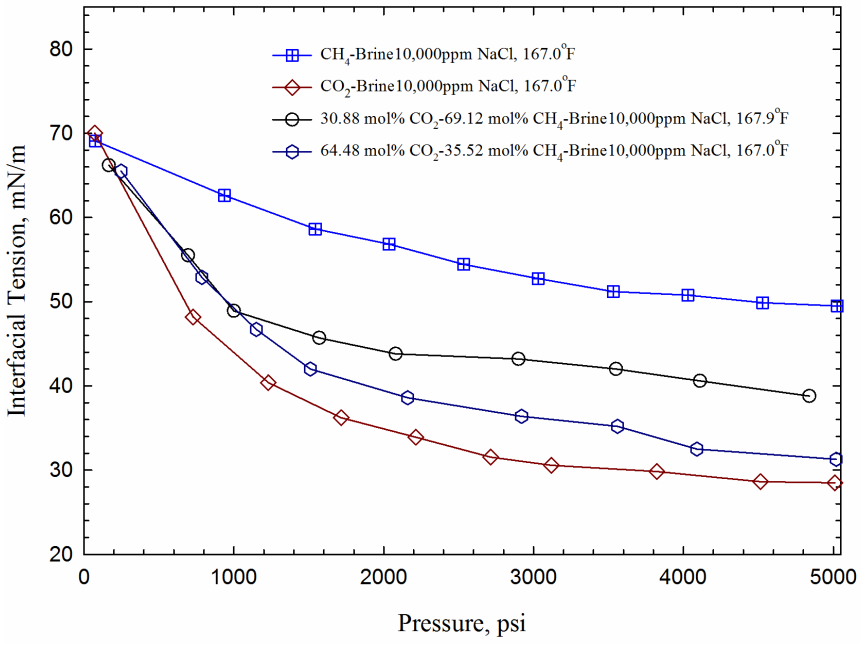
CH4-Brine10,000ppm NaCl, 167.0°F
CO2-Brine10,000ppm NaCl, 167.0°F
30.88 mol% CO2-69.12 mol% CH4-Brine10,000ppm NaCl, 167.9°F
64.48 mol% CO2-35.52 mol% CH4-Brine10,000ppm NaCl, 167.0°F
Interfacial Tension, mN/m
Pressure, psi
80
70
60
50
40
30
20
0
1000
2000
3000
4000
5000

b)

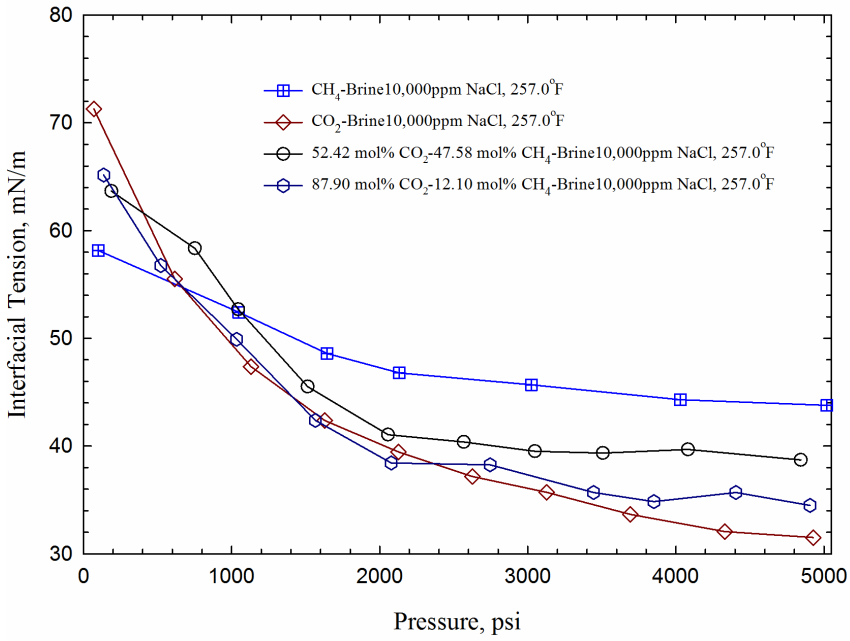
CH4-Brine10,000ppm NaCl, 257.0°F
CO2-Brine10,000ppm NaCl, 257.0°F
52.42 mol% CO2-47.58 mol% CH4-Brine10,000ppm NaCl, 257.0°F
87.90 mol% CO2-12.10 mol% CH4-Brine10,000ppm NaCl, 257.0°F
Interfacial Tension, mN/m
Pressure, psi
80
70
60
50
40
30
0
1000
2000
3000
4000
5000

c)

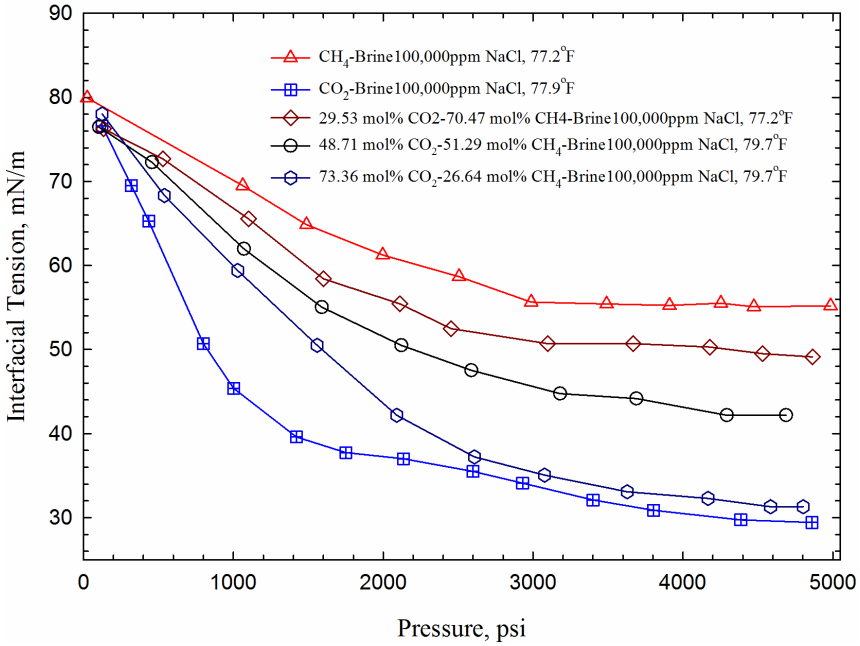
CH4-Brine100,000ppm NaCl, 77.2°F
CO2-Brine100,000ppm NaCl, 77.9°F
29.53 mol% CO2-70.47 mol% CH4-Brine100,000ppm NaCl, 77.2°F
48.71 mol% CO2-51.29 mol% CH4-Brine100,000ppm NaCl, 79.7°F
73.36 mol% CO2-26.64 mol% CH4-Brine100,000ppm NaCl, 79.7°F
Interfacial Tension, mN/m
Pressure, psi
90
80
70
60
50
40
30
0
1000
2000
3000
4000
5000

d)

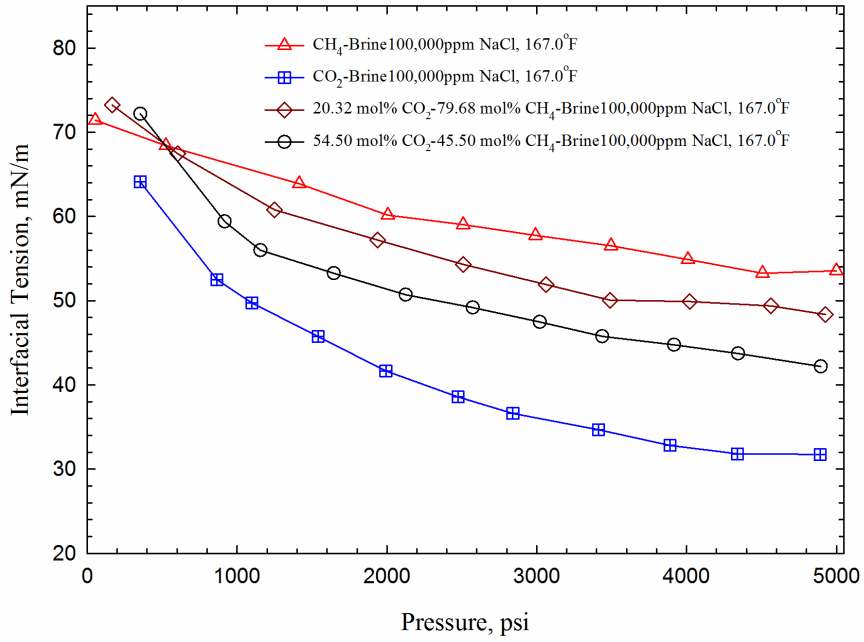
CH4-Brine100,000ppm NaCl, 167.0°F
CO2-Brine100,000ppm NaCl, 167.0°F
20.32 mol% CO2-79.68 mol% CH4-Brine100,000ppm NaCl, 167.0°F
54.50 mol% CO2-45.50 mol% CH4-Brine100,000ppm NaCl, 167.0°F
Interfacial Tension, mN/m
Pressure, psi
80
70
60
50
40
30
20
0
1000
2000
3000
4000
5000

e)

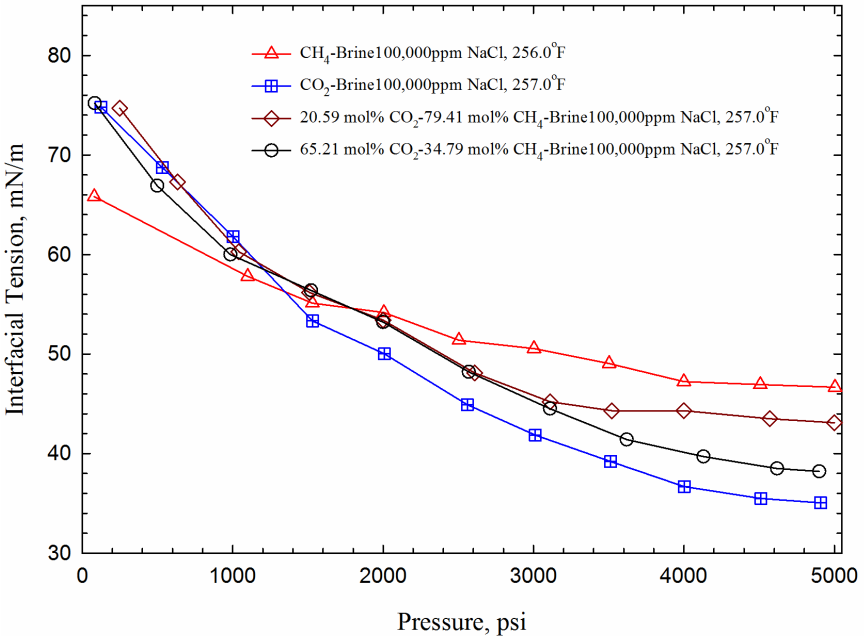
CH4-Brine100,000ppm NaCl, 256.0°F
CO2-Brine100,000ppm NaCl, 257.0°F
20.59 mol% CO2-79.41 mol% CH4-Brine100,000ppm NaCl, 257.0°F
65.21 mol% CO2-34.79 mol% CH4-Brine100,000ppm NaCl, 257.0°F
Interfacial Tension, mN/m
Pressure, psi
80
70
60
50
40
30
0
1000
2000
3000
4000
5000

f)

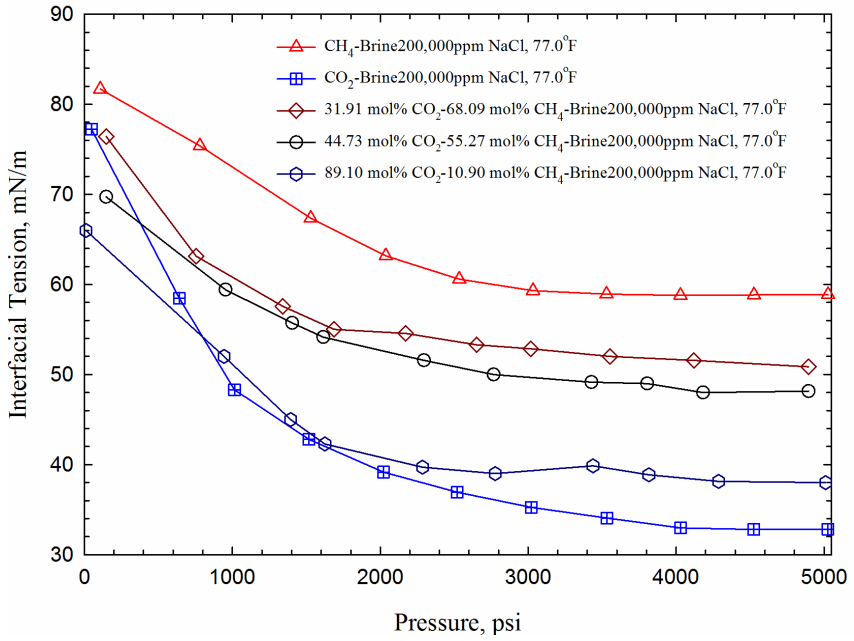
CH4-Brine200,000ppm NaCl, 77.0°F
CO2-Brine200,000ppm NaCl, 77.0°F
31.91 mol% CO2-68.09 mol% CH4-Brine200,000ppm NaCl, 77.0°F
44.73 mol% CO2-55.27 mol% CH4-Brine200,000ppm NaCl, 77.0°F
89.10 mol% CO2-10.90 mol% CH4-Brine200,000ppm NaCl, 77.0°F
Interfacial Tension, mN/m
Pressure, psi
90
80
70
60
50
40
30
0
1000
2000
3000
4000
5000

g)

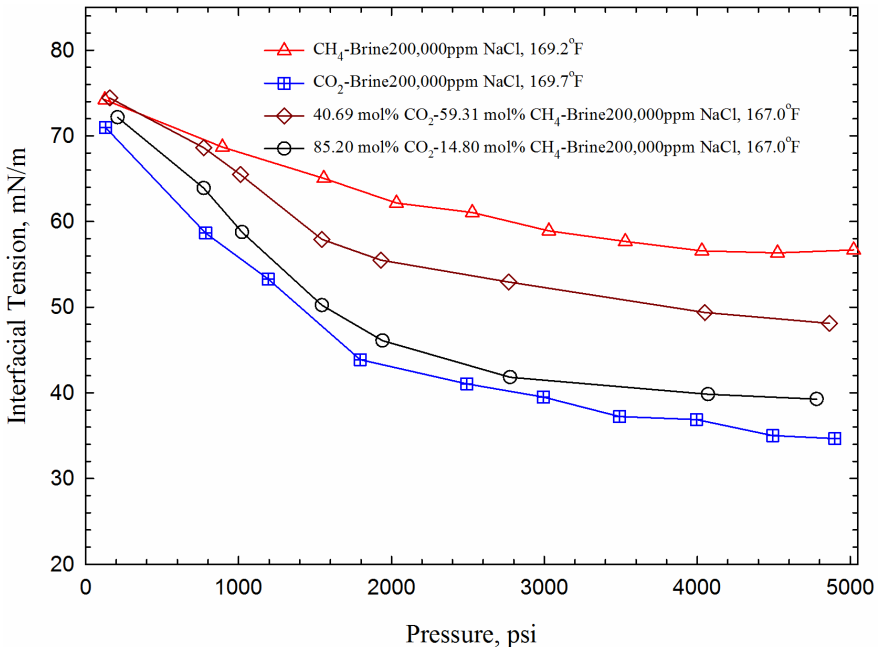
CH4-Brine200,000ppm NaCl, 169.2°F
CO2-Brine200,000ppm NaCl, 169.7°F
40.69 mol% CO2-59.31 mol% CH4-Brine200,000ppm NaCl, 167.0°F
85.20 mol% CO2-14.80 mol% CH4-Brine200,000ppm NaCl, 167.0°F
Interfacial Tension, mN/m
Pressure, psi
80
70
60
50
40
30
20
0
1000
2000
3000
4000
5000

h)

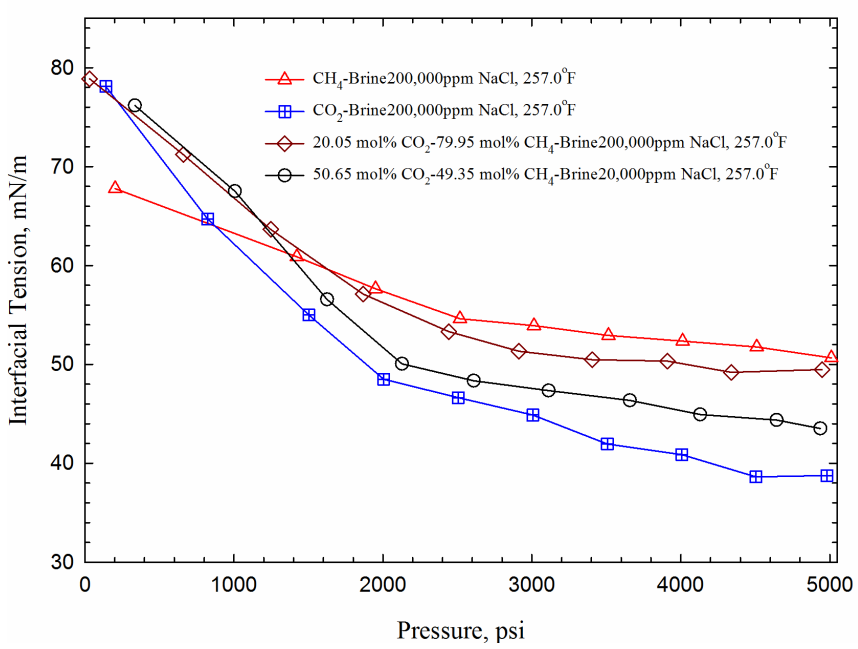

i)

Figure 6-12 IFT of CO_2/CH_4/brine as a function of pressure at different temperatures and NaCl concentrations.

Taking reservoir conditions, 167.0°F and 4,351 psia, for example, the IFT between shale gas (mainly CH_4) with brine (with a salinity of 100,000 ppm NaCl) is about 54.50 mN/m, about 4.00 mN/m higher than that of CH_4/H_2O system (See Figure 6-13). IFT significantly affects the in-situ capillary pressure and entrapment of gas in shale matrix; in order to enhance the shale gas recovery, gas/water IFT should be as low as possible. To reduce the IFT of CH_4/brine (with a salinity of 100,000 ppm NaCl) system to a value of 45.50 mN/m, CO_2 concentration in the gas has to be around 50.00 mol%. Similarly, if the salinity of reservoir brine is 200,000 ppm, the concentration of CO_2 should be around 20.05 mol%-50.65 mol% to obtain the same level of IFT at the NaCl concentration of 50,000 ppm at the pressure of 4,351 psia and temperature of 257.0°F, as shown in Figure 6-14.

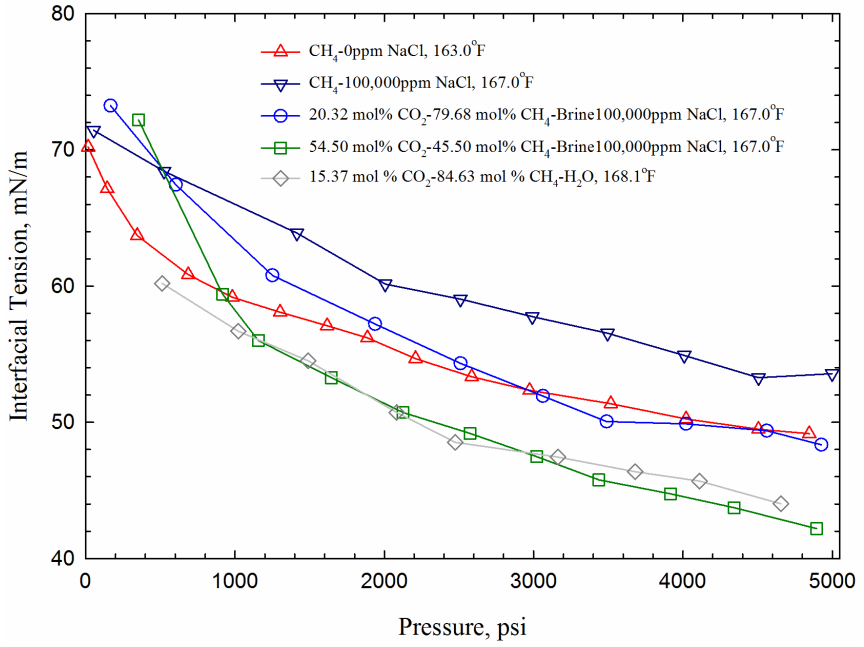

Figure 6-13 IFT of CH_4/CO_2/brine systems as a function of pressure.

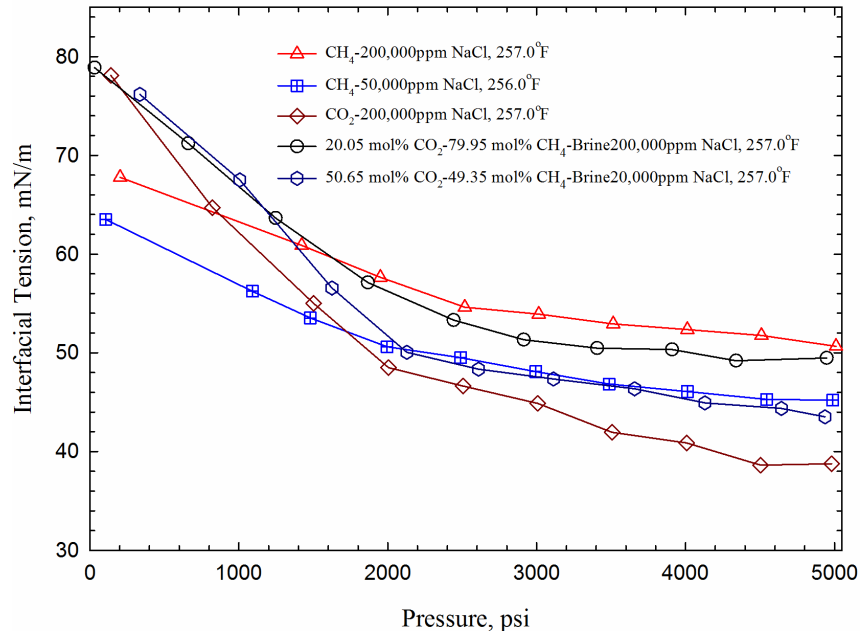

Figure 6-14 IFT of CO_2/CH_4/brine systems as a function of pressure.

6.4.4 IFT Modeling for $CO_2/CH_4/H_2O$ and CO_2/CH_4/Brine Systems

6.4.4.1 Improved IFT Model for $CO_2/CH_4/H_2O$ Systems

The IFT data for $CO_2/CH_4/H_2O$ systems are used to regress the coefficients appearing in

Equation (6-6). We obtain the following correlation based on regression analysis as indicated by Figure 6-15 (R^2=0.9658),

$$\sigma_{gw}^{0.25} = \frac{2.068}{T_r^{0.3125}} \left(\frac{M_H}{\sum_{i=1}^{n} z_i M_i} \right)^{0.183361} \left(\rho_M^L \sum_{i=1}^{n} x_i P_i - \rho_M^V \sum_{i=1}^{n} y_i P_i \right)^{0.2921} \quad (6\text{-}9).$$

Figure 6-16 presents a parity chart that plots the measured IFTs versus the calculated ones with Equation (6-9), while Figure 6-17 shows the distribution of errors versus the number of data points. Both figures illustrate that a good match is obtained between the measured and calculated IFTs, demonstrating the accuracy of Equation (6-9) in correlating the IFTs for $CO_2/CH_4/H_2O$ systems. Figure 6-17 indicates that the difference between predicted and measured data is mostly less than ±5.00 mN/m. Table 6-3 summarizes the statistical analysis results on using the improved correlation. As shown in Table 6-3, the average absolute relative error (AARE) and standard deviation (SD) are found to be 9.42% and 11.33%, respectively.

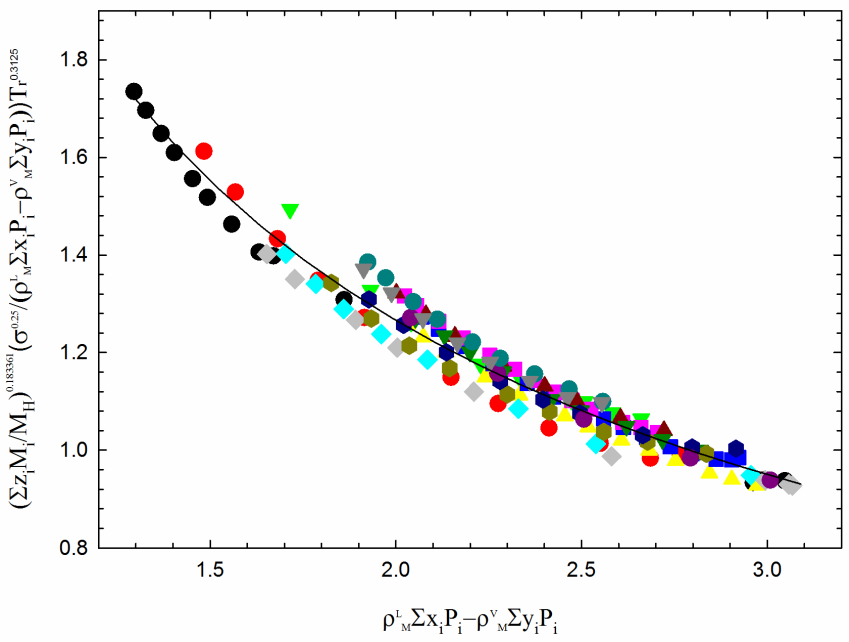

Figure 6-15 Regression of IFT model parameters using measured data in this study for $CO_2/CH_4/H_2O$ systems: ●, CO_2/H_2O, 80.0°F; ●, CO_2/H_2O, 163.0 °F; ▼, CO_2/H_2O, 250.0°F; ▲, CH_4/H_2O, 81.0°F; ■, CH_4/H_2O, 163.0°F; ■, CH_4/H_2O, 257.0°F; ◆, 60.10mol% CO_2/39.90mol% CH_4/H_2O, 80.0°F; ◆, 71.20mol% CO_2/28.80mol% CH_4/H_2O, 80.0°F; ▲, 26.40mol% CO_2/73.60mol% CH_4/H_2O, 168.0°F; ▼, 15.40mol% CO_2/84.60mol% CH_4/H_2O, 168.0°F; ⬢, 60.70mol% CO_2/39.30mol% CH_4/H_2O, 168.0°F; ●, 44.90mol% CO_2/55.10mol% CH_4/H_2O, 167.0°F; ●, 13.40mol% CO_2/86.60mol% CH_4/H_2O, 78.0°F; ●, 40.50mol% CO_2/59.50mol% CH_4/H_2O, 257.0°F; ▼, 60.20mol% CO_2/39.80mol% CH_4/H_2O, 257.0°F.

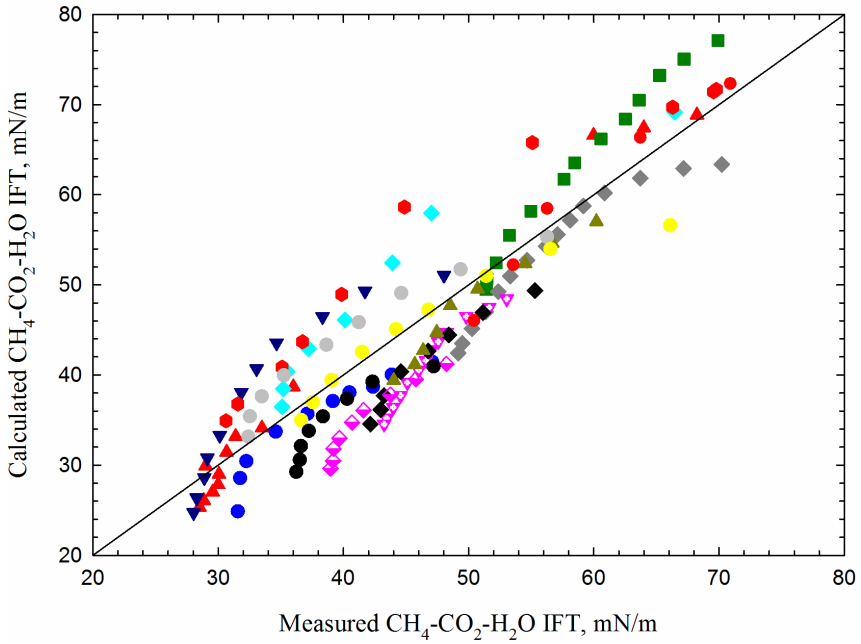

Figure 6-16 Comparison between predicted IFTs with Equation (6-9) versus measured IFTs for $CO_2/CH_4/H_2O$ systems: ●, CO_2/H_2O, 80.0°F; ●, CO_2/H_2O, 163.0°F; ▼, CO_2/H_2O, 250.0°F; ▲, CH_4/H_2O, 81.0°F; ■, CH_4/H_2O, 163.0°F; ■, CH_4/H_2O, 257.0°F; ◆, 60.10mol% CO_2/39.90mol% CH_4/H_2O, 80.0°F; ◆ , 71.20mol% CO_2/28.80mol% CH_4/H_2O, 80.0°F; ▲ , 26.40mol% CO_2/73.60mol% CH_4/H_2O, 168.0°F; ▼ , 15.40mol% CO_2/84.60mol% CH_4/H_2O, 168.0°F; ● , 60.70mol% CO_2/39.30mol% CH_4/H_2O, 168.0°F; ● , 44.90mol% CO_2/55.10mol% CH_4/H_2O, 167.0°F; ● , 13.40mol% CO_2/86.60mol% CH_4/H_2O, 78.0°F; ● , 40.50mol% CO_2/59.50mol% CH_4/H_2O, 257.0°F; ▼, 60.20mol% CO_2/39.80mol% CH_4/H_2O, 257.0°F.

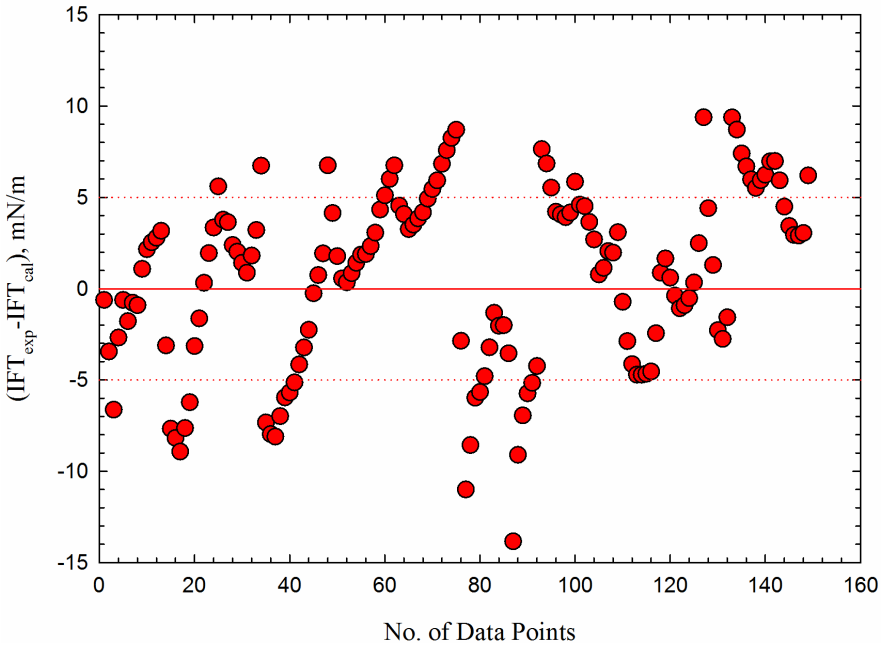

Figure 6-17 Difference between measured IFTs and predicted IFT with Equation (6-9) for $CO_2/CH_4/H_2O$ systems.

Table 6-3 Performance of different IFT models in reproducing the IFTs of $CO_2/CH_4/H_2O$ systems.

Model	Number of data points obtained by this study	AARE, %	SD, %
New Model	156	9.42	11.33
Danesh *et al.*[4], 1998	156	28.28	38.48
Sutton[30], 2009	156	23.13	40.39
Firoozabadi and Ramey[28], 1988	156	25.52	29.08
Weinaug and Katz[24], 1943	156	35.98	44.11

6.4.4.2 Comparison with Existing Correlations

The improved model is compared with four commonly used hydrocarbon gas/H_2O IFT correlations in the literature. As for the Firoozabadi and Ramey[28] correlation, a relationship between $\frac{\sigma_{gw}^{0.25}}{(\rho_L-\rho_V)}T_r^{0.3125}$ and $(\rho_L-\rho_V)$ can be obtained by plotting these two terms together, and then applying proper regression, as done in Figure 6-18. The following equation is obtained,

$$\sigma_{gw}^{0.25}=\frac{2.978}{T_r^{0.3125}}(\rho_L-\rho_V)^{0.1382} \quad (6\text{-}10).$$

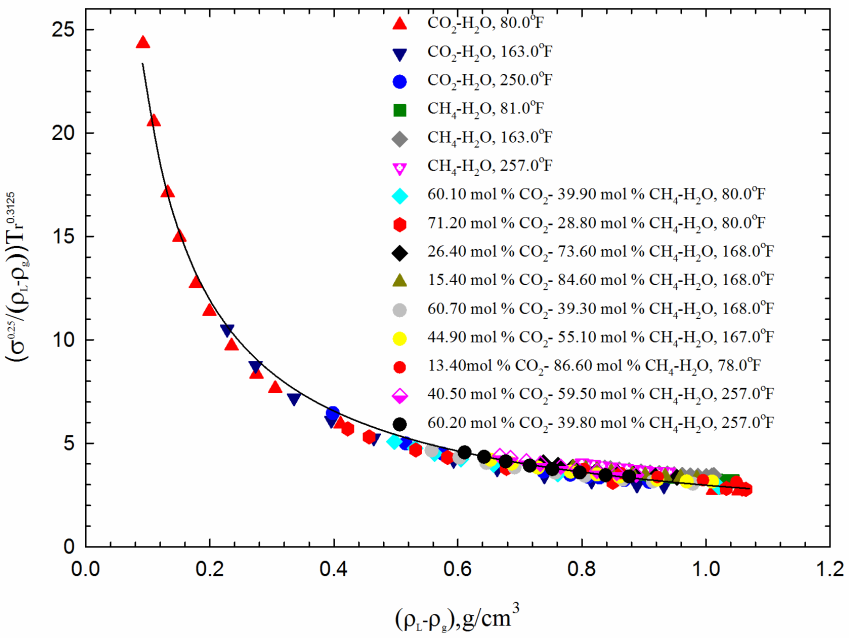

Figure 6-18 Application of Firoozabadi and Ramey[28] correlation to the IFT data of $CO_2/CH_4/H_2O$ systems.

Figure 6-19 shows a parity chart that compares the measured and calculated IFTs with Equation (6-10). Similarly, three commonly-used correlations (Sutton[30], Danesh[4], and Weinaug and Katz[24]) are also used to correlate the IFT data, as shown in Figures 6-20 to 6-22. Table 6-3 summarizes the overall comparison results, while Table S2 (shown in Supporting Information) provides detailed comparison results between the measured IFTs and calculated IFTs with these correlations. As can be seen from Figures 6-19 to 6-22 and Table 6-3, there is a large discrepancy between the measured IFTs and calculated IFTs with these four models. Compared with these four correlations, Equation (6-9) provides more accurate IFT prediction for the $CO_2/CH_4/H_2O$ systems.

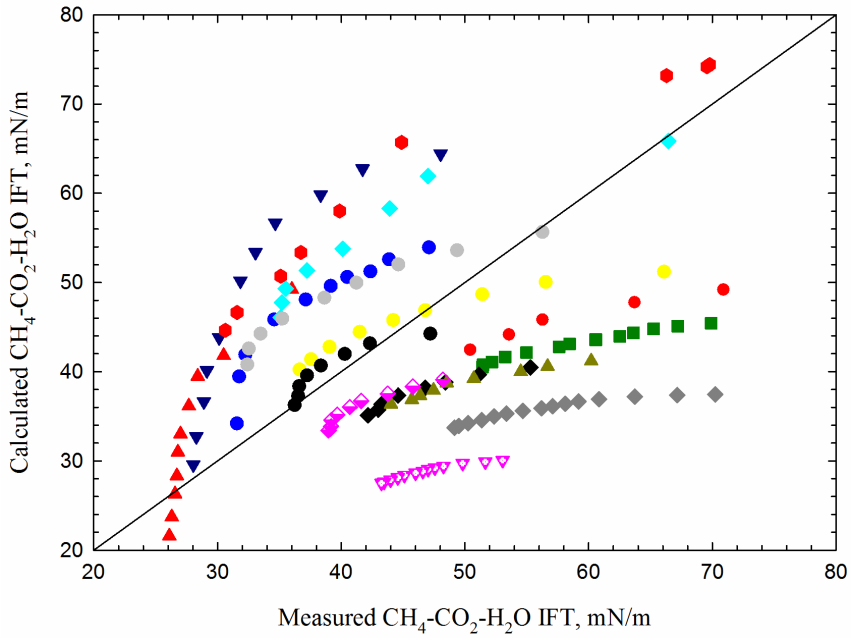

Figure 6-19 Comparison between the measured IFTs and calculated ones with Firoozabadi and Ramey[28] correlation for $CO_2/CH_4/H_2O$ systems.

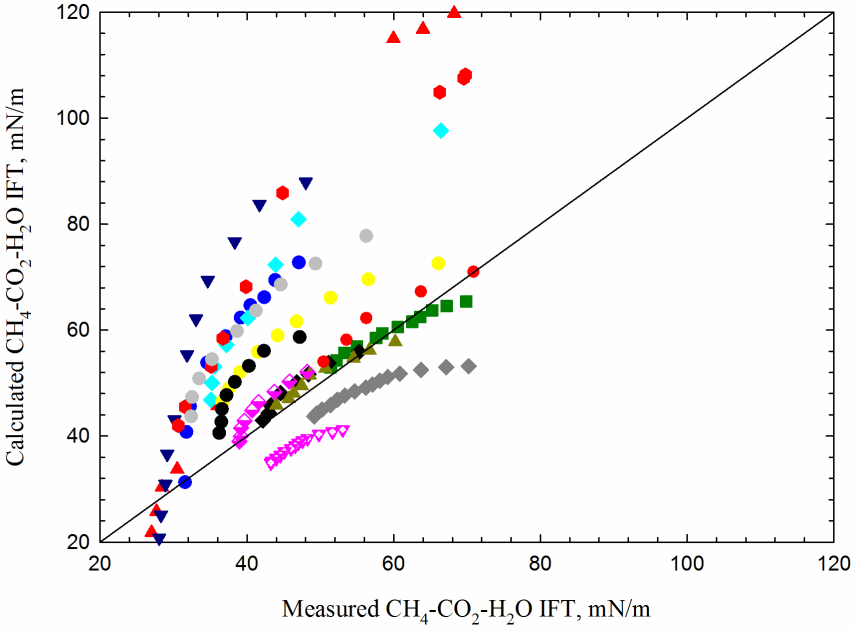

Figure 6-20 Comparison between the measured IFTs and calculated ones with Danesh[4] correlation for $CO_2/CH_4/H_2O$ systems.

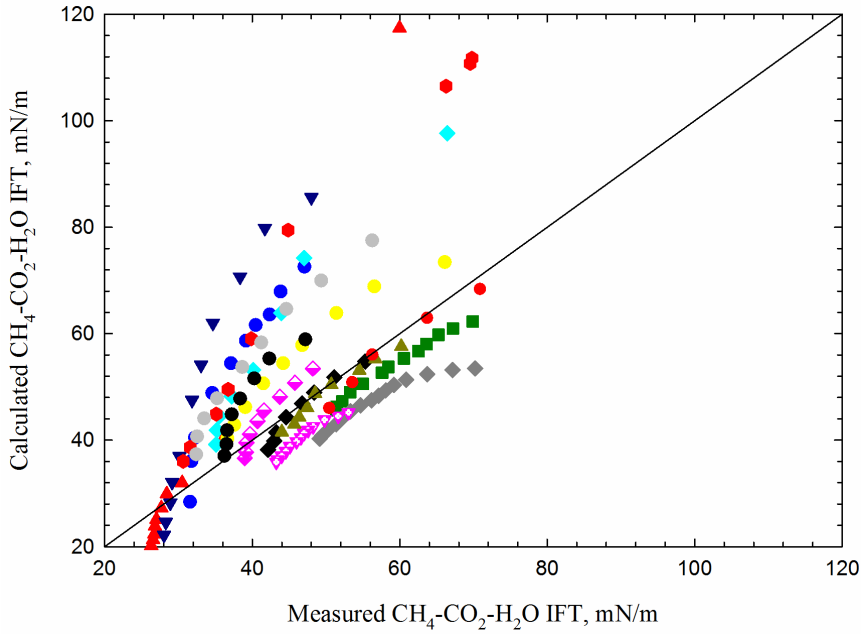

Figure 6-21 Comparison between the measured IFTs and calculated ones with Sutton[30] correlation for $CO_2/CH_4/H_2O$ systems.

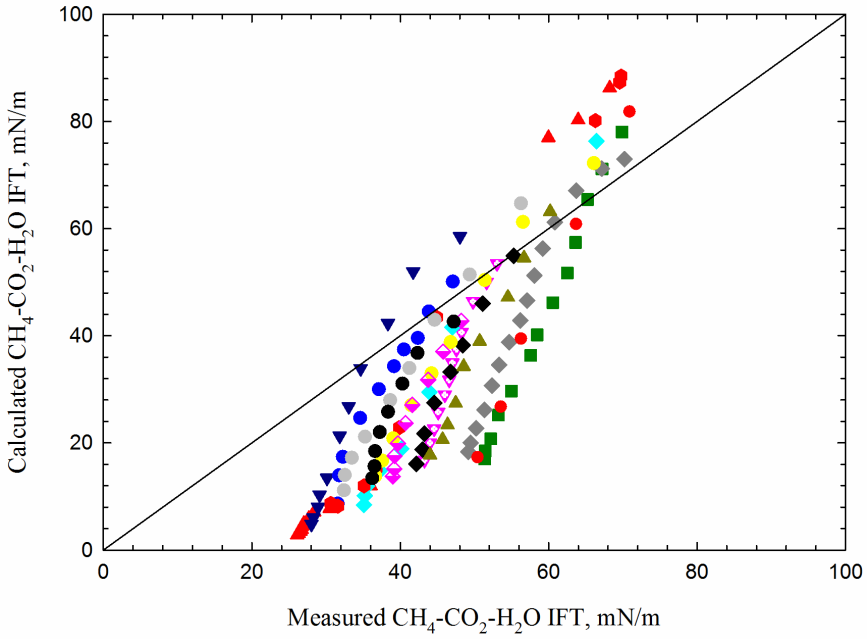

Figure 6-22 Comparison between the measured IFTs and predicted ones with Weinaug and Katz[24] correlation for $CO_2/CH_4/H_2O$ systems.

6.4.4.3 Validation of the Improved Model

In order to further test the predictive ability of the newly developed IFT model, Equation (6-9) is tested with 150 IFT data presented by Ren *et al.*[11] that are not used in developing the new IFT

model. The comparison between the calculated and measured IFT values is presented in Figure 6-23. It indicates that the new IFT model provides a good prediction on $CO_2/CH_4/H_2O$ IFT. Deviations between the measured and predicted IFTs are mostly less than ±5.00 mN/m. Table 6-4 shows the validation results. Compared to other models, the improved model provides more accurate IFT prediction for $CO_2/CH_4/H_2O$ systems, with AARE and SD of 10.19% and 14.01%, respectively.

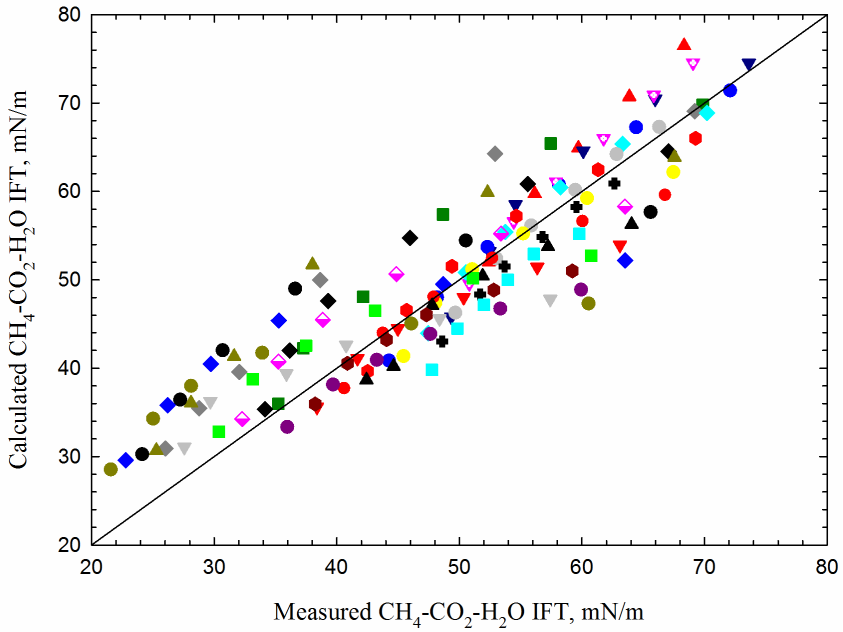

Figure 6-23 Comparison between the measured data by Ren *et al.*[11] and predicted IFTs with the new correlation for $CO_2/CH_4/H_2O$ systems: ▲, CH_4/H_2O, 77.0°F; ▼, 20.00mol% CO_2/80.00mol% CH_4/H_2O, 77.0°F; ● ,40.00mol% CO_2/60.00mol% CH_4/H_2O, 77.0°F; ■ , 60.00mol% CO_2/40.00mol% CH_4/H_2O, 77.0°F; ◆,80.00mol% CO_2/20.00mol% CH_4/H_2O, 77.0°F; ▽,CH_4/H_2O, 104.0°F; ◆ ,20.00mol% CO_2/80.00mol% CH_4/H_2O, 104.0°F; ● ,40.00mol% CO_2/60.00mol% CH_4/H_2O, 104.0°F; ◆ ,60.00mol% CO_2/40.00mol% CH_4/H_2O, 104.0°F; ▲ , 80.00mol% CO_2/20.00mol% CH_4/H_2O, 104.0°F; ● , CH_4/H_2O, 140.0°F; ● , 20.00mol% CO_2/80.00mol% CH_4/H_2O, 140.0°F; ● ,40.00mol% CO_2/60.00mol% CH_4/H_2O, 140.0°F; ◆ , 60.00mol% CO_2/40.00mol% CH_4/H_2O, 140.0°F; ● , 80.00mol% CO_2/20.00mol% CH_4/H_2O, 140.0°F; ✚ , CH_4/H_2O, 176.0°F; ▲ , 20.00mol% CO_2/80.00mol% CH_4/H_2O, 176.0°F; ▼ , 40.00mol% CO_2/60.00mol% CH_4/H_2O, 176.0°F; ■ , 60.00mol% CO_2/40.00mol% CH_4/H_2O, 176.0°F; ◆ , 80.00mol% CO_2/20.00mol% CH_4/H_2O, 176.0°F; ■ , CH_4/H_2O, 212.0 °F; ● , 20.00mol% CO_2/80.00mol% CH_4/H_2O, 212.0°F; ● , 40.00mol% CO_2/60.00mol% CH_4/H_2O, 212.0°F; ▼ , 60.00mol% CO_2/40.00mol% CH_4/H_2O, 212.0°F; ● , 80.00mol% CO_2/20.00mol% CH_4/H_2O, 212.0°F.

Table 6-4 Performance of the improved IFT model in predicting the IFTs of $CO_2/CH_4/H_2O$ systems published by Ren *et al.*[11]

Model	Number of data pointsmeasuredby Ren *et al.*[11]	AARE (%)	SD (%)
This study	150	10.19	14.01
Danesh*et al.*[4] (1998)	150	57.92	62.82
Sutton[30] (2009)	150	45.83	50.08
Firoozabadi and Ramey[28] (1988)	150	26.56	30.40
Weinaug and Katz[24] (1943)	150	26.45	32.67

6.4.4.4 IFT Modeling for CO_2/CH_4/Brine Systems

The preceding discussion shows that salinity can increase the IFT of $CO_2/CH_4/H_2O$ systems. Some researchers[6,29] proposed to use a linear relationship to account for the IFT increase as a function of salinity. It can be seen from Figures 6-9 and 6-10 that, after the IFT levels off, the IFT increase due to salinity effect tends to be independent of temperature and pressure. As for the CO_2/brine (NaCl) systems, the following linear relationship is found to be adequate to account for the salinity effect, as shown in Figure 6-24:

$$\sigma_{cor-CO_2} = 3.45\times10^{-5} C_S \qquad (6\text{-}11).$$

As for the CH_4/brine (NaCl) systems, the following linear relationship is obtained, as shown in Figure 6-24:

$$\sigma_{cor-CH_4} = 3.65\times10^{-5} C_S \qquad (6\text{-}12).$$

The ratio of 3.600×10^{-5} obtained for CO_2/brine (NaCl) system is slightly different from the values reported in the literature. Chalbaud *et al.*[6] reported a ratio of 2.550×10^{-5} instead of 3.600×10^{-5} for the CO_2/brine system (up to 16,071 ppm of NaCl). Massoudi and King[14] reported a ratio of 2.704×10^{-5}, while Argaud[29] obtained a ratio of 2.789×10^{-5} for the CO_2/brine system. The ratio of 3.950×10^{-5} obtained in this study for CH_4/brine systems is larger than that of

CO_2/brine systems. It indicates that an increase in salinity (NaCl) results in a more pronounced increase in the IFT for CH_4/brine systems than for CO_2/brine systems. Cai *et al.*[77] (1996) measured IFT of salt solutions containing NaCl, $CaCl_2$ and $MgCl_2$ with *n*-C_8H_{18}. They showed that the degree of IFT increase is sensitive to salt species. For salts such as KCl, $CaCl_2$ and $MgCl_2$, the effect of salt on IFT has been widely studied, and such increase in IFT is not linear at salt concentrations higher than 1.0 mol/kg. It is noted that one can first calculate the IFT of CO_2/CH_4/H_2O system with Equation (6-9), and then apply Equations (6-8), (6-11) and (6-12) to obtain the IFT of a given CO_2/CH_4/brine (NaCl) system.

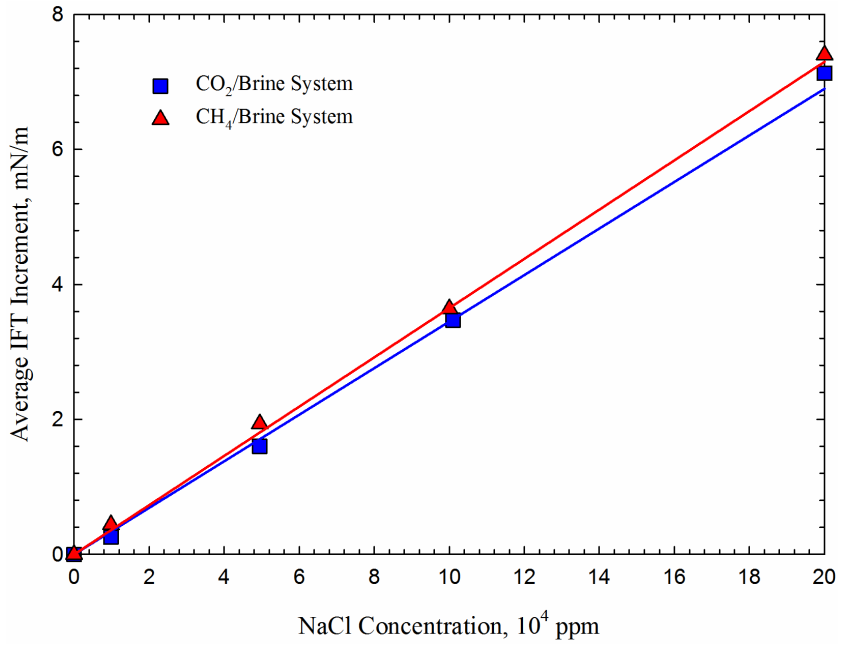

Figure 6-24 Average IFT increment for CO_2/brine and CH_4/brine systems as a function of NaCl concentration.

6.5 Conclusions

Experiments were conducted to measure IFTs for the CO_2/CH_4/brine system along three isotherms between 77.0 and 257.0°F, at pressures up to 5,027 psia and salinities up to 200,000 ppm. Different CH_4/CO_2 ratios in the gas mixture were considered in the measurements. The IFT

data measured for CO_2/H_2O and CH_4/H_2O mixtures were shown to be in good agreement with the published data, validating the reliability of our IFT measurements.

A detailed analysis of the CO_2 and salt effect on IFT was carried out based on the measured IFT data. The presence of CO_2 decreases the IFT, but the degree of reduction in IFT depends on the amount of CO_2 added. The presence of salt in pure water increases the IFT between gas and liquid. IFT reduction of the CH_4/brine system due to the addition of CO_2 can possibly result in an increased capillary number, which may be beneficial for enhancing shale gas recovery if CO_2 is used as a recovery medium.

Based on the IFT data measured in this research, an improved IFT correlation was developed based on the Parachor model[1] and Firoozabadi and Ramey's model[2]. Unlike other correlations, the improved IFT correlation accounts for all major parameters that affect $CO_2/CH_4/H_2O$ IFT, including pressure, temperature, individual compound's molecular weight, density difference, and gas composition on IFT of gas-mixture/H_2O systems. For the $CO_2/CH_4/H_2O$ mixtures, the improved correlation provides a more accurate prediction of $CO_2/CH_4/H_2O$ IFT data measured by Ren *et al.*[13] in comparison to other four existing correlations. Improved correlations used for predicting IFT of CO_2/CH_4/brine systems have been also presented, showing a good performance in correlating the measured IFTs.

6.6 References

(1) Heller, R.; Zoback, M. Adsorption of Methane and Carbon Dioxide on Gas Shale and Pure Mineral Samples. *J. Unconv. Oil Gas Resour*. **2014**, *8*, 14.

(2) Hussen, C.; Amin, R.; Madden, G.; Evans, B. Reservoir Simulation for Enhanced Gas Recovery: An Economic Evaluation. *J. Nat. Gas Sci. Eng*. **2012**, *5*, 42.

(3) Li, X.; Elsworth, D. Geomechanics of CO_2 Enhanced Shale Gas Recovery. *J. Nat. Gas Sci. Eng*. **2014**, *26*, 1607.

(4) Danesh, A. PVT and Phase Behaviour of Petroleum Reservoir Fluids. Ph.D. Dissertation, Herriot Watt University, Edinburgh, SCO, 1998.

(5) Li, Z.; Wang, S.; Li, S.; Liu, W.; Li, B.; Lv, Q. C. Accurate Determination of the CO_2-Brine Interfacial Tension Using Graphical Alternating Conditional Expectation. *Energy Fuels* **2013**, *28*, 624.

(6) Chalbaud, C.; Robin, M.; Egermann, P. Interfacial Tension Data and Correlations of Brine/CO_2 Systems under Reservoir Conditions. Presented at the SPE Annual Technical Conference and Exhibition, San Antonio, September 2006; SPE 102918.

(7) Aggelopoulos, C. A.; Robin, M.; Perfetti, M.; Vizika, O. CO_2/$CaCl_2$ Solution Interfacial Tensions under CO_2 Geological Storage Conditions: Influence of Cation Valence on Interfacial Tension. *Adv. Water Resour*. **2010**, *33*, 691.

(8) Shah, V.; Broseta, D.; Mouronval, G.; Montel, F. Water/acid Gas Interfacial Tensions and Their Impact on Acid Gas Geological Storage. *Int. J. Greenh. Gas Control.* **2008**, *2*, 594.

(9) Bahramian, A.; Danesh, A. Prediction of Liquid-Liquid Interfacial Tension in Multi-Component Systems. *Fluid Phase Equilibr*. **2004**, *221*, 197.

(10) Bahramian, A.; Danesh, A. Prediction of Liquid-Vapour Surface Tension in Multi-Component Systems. *Fluid Phase Equilibr*. **2005**, *236*, 156.

(11) Ren, Q. Y.; Chen, G. J.; Yan, W.; Guo, T. M. Interfacial Tension of (CO_2+CH_4)+Water from 298 K to 373 K and Pressures up to 30 MPa. *J. Chem. Eng. Data* **2000**, *45*, 610.

(12) Massoudi, R.; King Jr., A. D. Effect of Pressure on the Surface Tension of Aqueous Solutions. Adsorption of Hydrocarbon Gases, Carbon Dioxide, and Nitrous Oxide on

Aqueous Solutions of Sodium Chloride and Tetra-n-Butylammonium Bromide at 25°C. *J. Phys. Chem.* **1975**, *79*, 1670.

(13) Li, X.; Boek, E.; Maitland, G. C.; Trusler, J. P. M. Interfacial Tension of (Brines+CO_2): (0.864 NaCl+0.136 KCl) at Temperatures between (298 and 448) K, Pressures between (2 and 50) MPa, and Total Molarities of (1 to 5) mol·kg^{-1}. *J. Chem. Eng. Data* **2012**, *57*, 1078.

(14) Li, X.; Boek, E.; Maitland, G. C.; Trusler, J. P. M. Interfacial Tension of (Brines+CO_2): $CaCl_2$(aq), $MgCl_2$(aq), and Na_2SO_4(aq) at Temperatures between (343 and 423) K, Pressures between (2 and 50) MPa, and Molarities of (0.5 to 5) mol·kg^{-1}. *J. Chem. Eng. Data* **2012**, *57*, 1369.

(15) Khashefi, K.; Pereira, L. M. C.; Chapoy, A.; Burgass, R.; Tohidi, B. Measurement and Modelling of Interfacial Tension in Methane/Water and Methane/Brine Systems at Reservoir Conditions. *Fluid Phase Equilibr*. **2016**, *409*, 301.

(16) Ralston, J.; Healy, T. Specific Cation Effects on Water Structure at the Air-Water and Air-Octadecanol Monolayer-Water Interface. *J. Colloid Interface Sci*. **1973**, *42*, 629.

(17) Johansson, K.; Eriksson, J. C. γ and dγ/dT Measurements on Aqueous Solutions of 1,1-Electrolyte. *J. Colloid Interface Sci*. **1974**, *49*, 469.

(18) Pegram, L. M.; Record, M. T. The Thermodynamic Origin of Hofmeister Ion Effects. *J. Phys. Chem. B* **2008**, *112*, 9428.

(19) Levin, Y.; dos Santos, A. P.; Diehl, A. Ions at the Air-Water Interface: An End to a Hundred-Year-Old Mystery? *Phys. Rev. Lett*. **2009**, *103*, 1.

(20) Yang, D. Y.; Tontiwachwuthikul, P.; Gu, Y. A. Interfacial Interactions between Reservoir Brine and CO_2 at High Pressures and Elevated Temperatures. *Energy Fuels* **2005**, *19*, 216.

(21) Bennion, D. B.; Bachu, S. A Correlation of the Interfacial Tension between Supercritical

Phase CO_2 and Equilibrium Brine as a Function of Salinity, Temperature and Pressure. Presented at the SPE Annual Technical Conference and Exhibition. Colorado, September **2008**; SPE 114479.

(22) Chalbaud, C.; Robin, M.; Lombard, J. M.; Bertin, H.; Egermann, P. Brine/CO_2 Interfacial Properties and Effects on CO_2 Storage in Deep Saline Aquifers. *Oil Gas Sci. and Technol.* **2010**, *65*, 541.

(23) Bachu, S.; Bennion, D. B. Interfacial Tension between CO_2, Freshwater, and Brine in the Range of Pressure from (2 to 27) MPa, Temperature from (20 to 125) ^{o}C, and Water Salinity from (0 to 334 000) $mg \cdot L^{-1}$. *J. Chem. Eng. Data* **2009**, *54*, 765.

(24) Weinaug, C. F.; Katz, D. L. Surface Tension of Methane-Propane Mixtures. *J. Ind. Eng. Chem.* **1943**, *35*, 239.

(25) Macleod, D. B. On a Relation between Surface Tension and Density. *Trans. Faraday. Soc.* **1923**, *19*, 38.

(26) Lee, S. T.; Chien, M. C. H. A New Multicomponent Surface Tension Correlation Based on Scaling Theory. Presented at the SPE/DOE Improved Oil Recovery Conference. Tulsa, April 1984, SPE/DOE 12643.

(27) Massoudi, R.; King Jr., A. D., Effect of Pressure on the Surface Tension of Water Adsorption of Low Molecular Weight Gases on Water at 25^{o}C. *J. Phys. Chem*. **1974**, *78*, 2262.

(28) Firoozabadi, A.; Ramey, Jr., H. J. Surface Tension of Water-Hydrocarbon Systems at Reservoir Conditions. *J. Can. Pet. Technol.* **1988**, *27*, 41.

(29) Argaud, M. J. Predicting the Interfacial Tension of Brine/Gas (or Condensate) Systems. Presented at the SCA European Core Analysis Symposium. Paris, September, 1992.

(30) Sutton, R. P. An Improved Model for Water-Hydrocarbon Surface Tension at Reservoir Conditions. Presented at the SPE Annual Technical Conference and Exhibition. New Orleans, October 2009; SPE 124968.

(31) Hebach, A.; Oberhof, A.; Dahmen, N.; Kogel, A.; Ederer, H.; Dinjus, E. Interfacial Tension at Elevated Pressures-Measurements and Correlations in the Water+Carbon Dioxide System. *J. Chem. Eng. Data* **2002**, *47*, 1540.

(32) Kvamme, B.; Kuznetsova, T.; Hebach, A.; Oberhof, A.; Lunde, E. Measurements and Modelling of Interfacial Tension for Water+Carbon Dioxide Systems at Elevated Pressures. *Comput. Mater. Sci.* **2007**, *38*, 506.

(33) Chalbaud, C.; Robin, M.; Lombard, J. M.; Martin, F.; Egermann, P.; Bertin, H. Interfacial Tension Measurement and Wettability Evaluation for Geological CO_2 Storage. *Adv. Water Resour.* **2009**, *32*, 98.

(34) Yan, W.; Zhao, G.; Chen, G.; Guo, T. Interfacial Tension of (Methane+Nitrogen)+Water and (Carbon Dioxide+Nitrogen)+Water Systems. *J. Chem. Eng. Data* **2001**, *46*, 1544.

(35) Nordholm, S.; Johnson, M.; Freasier, B. C. Generalized van der Waals Theory. III. The Prediction of Hard Sphere Structure. *Aust. J. Chem*. **1980**, *33*, 2139.

(36) Cahn, J. W.; Hilliard, J. E. Free Energy of a Nonuniform System. I. Interfacial Free Energy. *J. Chem. Phys*. **1958**, *28*, 258.

(37) Rowlinson, J. S. Translation of J. D. van der Waals' "The Thermodynamic Theory of Capillarity under the Hypothesis of a Continuous Variation of Density". *J. Stat. Phys.* **1979**, *20*, 197.

(38) Evans, R. The Nature of the Liquid-Vapor Interface and Other Topics in the Statistical Mechanics of Non-Uniform, Classical Fluids. *Adv. Phys*. **1979**, *28*, 143.

(39) Almeida, B. S.; Telo da Gama, M. M. Surface Tension of Simple Mixtures: Comparison between Theory and Experiment. *J. Phys. Chem*. **1989**, *93*, 4132.

(40) Bongiorno, V.; Davis, H. T. Modified van der Waals Theory of Fluid Interfaces. *Phys. Rev. A*. **1975**, *12*, 2213.

(41) Li, X.; Yang, D. Determination of Mutual Solubility between CO_2 and Water by Using the Peng-Robinson Equation of State with Modified Alpha Function and binary Interaction Parameter. *Ind. Eng. Chem. Res*. **2013**, *52*, 13829.

(42) Søreide, I.; Whitson, C. H. Peng-Robinson prediction for hydrocarbons, CO_2, N_2, and H_2S with pure water and NaCl brine. *Fluid Phase Equilibr*. **1992**, *77*, 217.

(43) Shariat, A. Measurement and Modelling of Interfacial Tension at High Pressure/High Temperature Conditions. Ph.D. Dissertation, University of Calgary, Calgary, AB, 2014.

(44) Zuo, Y. X.; Stenby, E. H. Corresponding-States and Parachor Models for the Calculation of Interfacial Tensions. *Can. J. Chem. Eng.* **1997***, 75*, 1130.

(45) Sato, K. Sensitivity of Interfacial-tension Predictions to Parachor-method Parameters. *J. Jpn. Pet. Inst*. **2003**, *46*, 148.

(46) Ayirala, S. C.; Rao, D. N. Application of a New Mechanistic Parachor Model to Predict Dynamic Gas-Oil Miscibility in Reservoir Crude Oil-Solvent Systems. Presented at the SPE International Petroleum Conference. Puebla, November 2004; SPE 91920.

(47) Fawcett, M. J. Evaluation of Correlations and Parachors to Predict Low Interfacial Tensions in Condensate Systems. Presented at the SPE 69th Annual Technical Conference and Exhibition. New Orleans, September 1994; SPE 28611.

(48) Hough, E. W.; Stegemeier, G. L. Correlation of Surface and Interfacial Tension of Light Hydrocarbons in the Critical Region. *SPE J*. **1961**, *1*, 259.

(49) Ayirala, S. C.; Rao, D. N. A New Mechanistic Parachor Model to Predict Dynamic Interfacial Tension and Miscibility in Multicomponent Hydrocarbon Systems. *J. Colloid Interface Sci*. **2006,** *299*, 321.

(50) Sudgen, S. Capillary Rise. *J. Chem. Soc*. **1921**, *119*, 1483.

(51) Quayle, O. R. The Parachors of Organic Compounds. An Interpretation and Catalogue. *Chem. Rev*. **1953**, *53*, 439.

(52) Standing, M. B. *Volumetric and Phase Behaviour of Oil Hydrocarbon Systems*. California Research Corp.: Dallas, 1951.

(53) Hough, E. W.; Rzasa, M. J.; Wood, B. B. Interfacial Tensions at Reservoir Pressures and Temperatures; Apparatus and the Water-Methane Systems. *Petrol. Trans. AIME.* **1951**, *192*, 57.

(54) Jennings, H. Y.; Newman, G. H. The Effect of Temperature and Pressure on the Interfacial Tension of Water against Methane-Normal Decane Mixtures. *SPE J.* **1971**, *11*, 171.

(55) Sachs, W.; Meyn, V. Pressure and Temperature Dependence of the Surface Tension in the System Natural Gas/Water: Principles of Investigation and the First Precise Experimental Data for Pure Methane/Water at 25^{o}C up to 48.8 MPa. *J. Colloids Surf. A.* **1995**, *94*, 291.

(56) Khosharay, S.; Varaminian, F. Experimental and Modeling Investigation on Surface Tension and Surface Properties of (CH_4+H_2O), (C_2H_6+H_2O), (CO_2+H_2O) and (C_3H_8+H_2O) from 284.15 K to 312.15 K and Pressures up to 60 Bar. *Int. J. Refrig.* **2014**, *47*, 26.

(57) Hocott, C. R. Interfacial Tension between Water and Oil under Reservoir Conditions. *Petrol. Trans. AIME.* **1939***, 132*, 184.

(58) Heuer, G. J. Interfacial Tension of Water against Hydrocarbons and Other Gases and Adsorption of Methane on Solids at Reservoir Temperatures and Pressures. Ph.D.

Dissertation, University of Texas, Austin, TX, 1957.

(59) Chun, B. S.; Wilkinson, G. T. Interfacial Tension in High-Pressure Carbon Dioxide Mixtures. *Ind. Eng. Chem. Res*. **1995**, *34*, 4371.

(60) da Rocha, S. R. P.; Harrison, K. L.; Johnston, K. P. Effect of Surfactants on the Interfacial Tension and Emulsion Formation between Water and Carbon Dioxide. *Langmuir.* **1999***, 15*, 419.

(61) Park, J. Y.; Lim, J. S.; Yoon, C. H.; Lee, C. H.; Park, K. P. Effect of a Fluorinated Sodium Bis (2-Ethylhexyl) Sulfosuccinate (Aerosol-OT, AOT) Analogue Surfactant on the Interfacial Tension of CO_2+Water and CO_2+Ni-Plating Solution in Near- and Supercritical CO_2. *J. Chem. Eng. Data* **2005***, 50*, 299.

(62) Chiquet, P.; Daridon, J.; Broseta, D.; Thibeau, S. CO_2/Water Interfacial Tensions under Pressure and Temperature Conditions of CO_2 Geological Storage. *Energy Convers. Manage.* **2007***, 48*, 736.

(63) Georgiadis, A.; Maitland, G.; Trusler, J. P. M.; Bismarck, A. Interfacial Tension Measurements of the (H_2O+CO_2) System at Elevated Pressures and Temperatures. *J. Chem. Eng. Data* **2010**, *55*, 4168.

(64) Petrova, T. Revised Release on Surface Tension of Ordinary Water Substance. Presented at the International Association for the Properties of Water and Steam. Moscow, 2014.

(65) Duan, Z.; Rui, S. An Improved Model Calculating CO_2 Solubility in Pure Water and Aqueous NaCl Solutions from 273 to 533 K and from 0 to 2000 bar. *Chem. Geol*. **2003**, *193*, 257.

(66) Bando, S.; Takemura, F.; Nishio, M.; Hihara, E.; Akai, M. Solubility of CO_2 in Aqueous Solutions of NaCl at (30 to 60) °C and (10 to 20) MPa. *J. Chem. Eng. Data* **2003**, *48*, 576.

(67) Koschel, D.; Coxam, J. Y.; Majer, V. Enthalpy and Solubility Data of CO_2 in Water and NaCl (aq) at Conditions of Interest for Geological Sequestration. *Fluid Phase Equilibr*. **2006**, *247*, 107.

(68) Whitson, C. H.; Brulé, M.R. *Phase Behavior*. Henry L. Doherty Memorial Fund of AIME Society of Petroleum Engineers Inc.: Richardson, Texas, 2000.

(69) Wiebe, R. The Brine System Carbon Dioxide-Water under Pressure. *Chem. Rev.* **1941**, *29*, 475.

(70) Malinin, S. D.; Kurovskaya, N. A. Solubility of CO_2 in Chloride Solutions at Elevated Temperatures and CO_2 Pressures. *Geochem. Int.* **1975**, *2*, 199.

(71) Malinin, S. D.; Savelyeva, N.I. The Solubility of CO_2 in NaCl and $CaCl_2$ Solutions at 25, 50 and 75^{o}C under Elevated CO_2 Pressures. *Geochem. Int.* **1972**, *9*, 410.

(72) Wiegand, G.; Franck, E. U. Interfacial Tension between Water and Non-polar Fluids up to 473 K and 2800 bar. *Ber. Bunsenges. Phys. Chem.* **1994**, *98*, 809.

(73) Abramzon, A. A.; Gaukhberg, R. D. Surface Tension of Salt Solutions. *Russian J. Appl. Chem*. **1993**, *66*, 1428.

(74) Chen, Z.; Xia, S.; Ma, P. Measuring Surface Tension of Liquids at High Temperature and Elevated Pressure. *J. Chem. Eng. Data* **2008**, *53*, 742.

(75) Firoozabadi, A. Thermodynamics and Applications in Hydrocarbon Energy Production. Mc Graw Hill Education: New York, 2016.

(76) Rushing, J. A.; Newsham, K. E.; Van Fraassen, K. C.; Mehta, S. A.; Moore, G. R. Laboratory Measurements of Gas-Water Interfacial Tension at HP/HT Reservoir Conditions. Presented at the CIPC/SPE Gas Technology Symposium. Calgary, June 2008; SPE 114516.

(77) Cai, B. Y.; Yang, J. T.; Guo, T. M. Interfacial Tension of Hydrocarbon+Water/Brines

Systems under High Pressure. *J. Chem. Eng. Data* **1996**, *41*, 493.

(78) Jho, C.; Nealon, D.; Shogbola, S.; King, A. D. Effect of Pressure on the Surface Tension of Water: Adsorption of Hydrocarbon Gases and Carbon Dioxide on Water at Temperatures between 0 and 50°C. *J. Colloid Interface Sci*. **1978**, *65*, 141.

(79) Lepski, B. Gravity Assisted Tertiary Gas Injection Process In Water Drive Oil Reservoirs. Ph.D. Dissertation, Louisiana State University, Baton Rouge, USA, 1997.

(80) Tian, Y.; Xiao, Y.; Zhu, H.; Dong, X.; Ren, X.; Zhang, F. Interfacial Tension between Water and Non-Polar Fluids at High Pressures and High Temperatures. *Acta Physico-Chimica Sinica*. **1997**, *13*, 89.

(81) Zhao, G. Y. Measurement and Calculation of High Pressure Interfacial Tension of Methane Nitrogen/Water System. *J. Univ. Pet*. **2002**, *26*, 75.

(82) Tewes, F.; Boury, F. Formation and Rheological Properties of the Supercritical CO_2-Water Pure Interface. *J. Phys. Chem. B*. **2005**, *109*, 3990.

(83) Akutsu, T.; Yoshinori, Y.; Hirokazu, Y.; Masaru, W.; Richard, L. S. J.; Hiroshi, I. Interfacial Tension between Water and High Pressure CO_2 in the Presence of Hydrocarbon Surfactants. *Fluid Phase Equilibr*. **2007**, *257*, 163.

(84) Sutjiadi-Sia, Y.; Jaeger, P.; Eggers, R. Interfacial Phenomena of Aqueous Systems in Dense Carbon Dioxide. *J. Supercrit. Fluids* **2008**, *46*, 272.

(85) Shariat, A.; Moore, R. G.; Mehta, S. A.; Van Fraassen, K. C.; Newsham, K. E.; Rushing, J. A. A Laboratory Study of the Effects of Fluid Compositions on Gas-Water Interfacial Tension at HP/HT Reservoir Conditions. Presented at the SPE Annual Technical Conference and Exhibition. Denver, October 30-November 2, 2011; SPE 146178.

(86) Aggelopoulos, C. A.; Robin, M.; Vizika, O. Interfacial Tension between CO_2 and Brine

($NaCl+CaCl_2$) at Elevated Pressures and Temperatures: The Additive Effect of Different Salts. *Adv. Water Res*. **2011**, *34*, 505.

(87) Shariat, A.; Moore, R. G.; Mehta, S. A.; Fraassen, K.; Newsham, K.; Rushing, J. A. Laboratory Measurement of CO_2-H_2O Interfacial Tension at HP/HT Conditions: Implications for CO_2 Sequestration in Deep Aquifers. Presented at the Carbon Management Technology Conference. Orlando, February 2012; Paper 150010.

(88) Pereira, L. M. C.; Chapoy, A.; Burgass, R.; Oliveira, M. B.; Coutinho, J. A. P.; Tohidi, B. Study of the Impact of High Temperature and Pressures on the Equilibrium Densities and Interfacial Tension of the Carbon Dioxide/Water System. *J. Chem. Thermodyn*. **2016**, *93*, 404.

Supporting Information

Table S1. IFT data for CO_2/CH_4/brine systems at different temperatures and pressures.

Salinity, 10,000 ppm			50,000 ppm			100,000 ppm			200,000 ppm		
Pressure,	**IFT/Δρ**	**IFT**	**Pressure,**	**IFT/Δρ**	**IFT**	**Pressure,**	**IFT/Δρ**	**IFT,**	**Pressure,**	**IFT/Δρ**	**IFT**
psi	**mN·m²/Kg**	**mN/m**	**psi**	**mN·m²/Kg**	**mN/m**	**psi**	**mN·m²/Kg**	**mN/m**	**psi**	**mN·m²/Kg**	**mN/m**
CO_2/Brine, 77.9°F			CH_4/Brine, 77.2°F			CH_4/Brine, 77.2°F			CH_4/Brine, 77.0°F		
27	0.0696	69.97	30	0.0743	77.12	25	0.0744	79.91	107	0.0720	81.69
615	0.0488	44.52	644	0.0720	72.50	1063	0.0681	69.50	780	0.0685	75.40
1243	0.1512	36.03	1104	0.0690	67.78	1488	0.0651	64.86	1530	0.0636	67.37
2012	0.2085	31.16	1785	0.0633	59.69	1997	0.0633	61.25	2037	0.0613	63.18
2512	0.2655	30.23	2313	0.0628	57.33	2506	0.0624	58.67	2533	0.0604	60.60
3015	0.3507	30.10	2994	0.0626	55.05	2988	0.0607	55.65	3033	0.0605	59.32
3516	0.4770	30.00	3480	0.0638	54.79	3491	0.0619	55.42	3530	0.0614	58.94
4018	0.6857	29.76	3610	0.0634	54.19	3910	0.0628	55.26	4029	0.0624	58.80
4516	1.0891	28.99	3964	0.0641	53.93	4253	0.0639	55.52	4526	0.0635	58.84
5025	2.5120	28.90	4485	0.0648	53.50	4474	0.0639	55.10	5027	0.0645	58.89
CH_4/Brine, 79.3°F			4836	0.0653	53.23	4985	0.0651	55.20	CO_2/Brine, 77.0°F		
18	0.0793	79.83	CO_2/Brine, 77.9°F			CO_2/Brine, 77.9°F			48	0.0681	77.24
751	0.0725	70.34	121	0.0743	76.15	125	0.0723	76.60	642	0.0566	58.46
1218	0.0689	65.06	315	0.0674	67.25	320	0.0673	69.50	1014	0.1097	48.29
1912	0.0637	57.60	432	0.0641	62.80	435	0.0645	65.30	1518	0.1234	42.79
2550	0.0628	54.63	790	0.0526	46.80	800	0.0549	50.70	2021	0.1324	39.17
2870	0.0623	53.23	990	0.1265	42.03	1001	0.1162	45.40	2520	0.1424	36.94
3510	0.0641	53.06	1400	0.1494	37.25	1421	0.1332	39.60	3021	0.1527	35.26
3950	0.0646	52.43	1745	0.1722	35.90	1750	0.1472	37.75	3532	0.1648	34.08
4475	0.0653	51.90	2150	0.1989	34.45	2135	0.1672	37.00	4031	0.1766	32.97
4975	0.0663	51.78	2585	0.2317	33.30	2600	0.1884	35.50	4525	0.1937	32.81
30.85 mol% CO_2/69.15 mol% CH_4/Brine, 77.0°F			2920	0.2588	32.30	2930	0.2014	34.10	5026	0.2134	32.83
15	0.0671	67.61	3395	0.3009	30.69	3400	0.2199	32.10	31.91 mol% CO2/68.09 mol% CH4/Brine, 77.0°F		
220	0.0638	63.47	3800	0.3461	29.50	3805	0.2399	30.88	150	0.0677	76.43
800	0.0514	48.69	4380	0.4444	28.65	4386	0.2772	29.75	749	0.0585	63.14
1190	0.0480	43.60	4850	0.5646	28.12	4861	0.3197	29.43	1336	0.0564	57.57
1686	0.0477	40.83	CH_4/Brine, 167.0°F			73.36 mol% CO_2/26.64 mol% CH_4/Brine, 79.7°F			1700	0.0561	55.00
2191	0.0492	39.47	102	0.0710	70.10	127	0.0735	78.02	2190	0.0568	54.57
2625	0.0517	39.29	535	0.0661	64.13	536	0.0675	68.32	2668	0.0605	53.29

3164	0.0532	38.11	1399	0.0645	60.25	1042	0.0646	59.41	3024	0.0620	52.86
3663	0.0535	36.57	2010	0.0642	58.32	1561	0.0674	50.50	3550	0.0637	52.00
4150	0.0557	36.59	2521	0.0637	56.50	2090	0.0706	42.18	4101	0.0657	51.57
4562	0.0543	34.63	3001	0.0632	54.95	2620	0.0720	37.23	4901	0.0679	50.86
4983	0.0524	32.47	3510	0.0626	53.23	3079	0.0745	35.07	44.73 mol% CO_2/55.27 mol% CH_4/Brine, 77.0°F		
11.00 mol% CO_2/89.00 mol% CH_4/Brine, 77.9°F			4012	0.0625	52.15	3628	0.0771	33.09	150	0.0618	69.71
15	0.0670	67.53	4515	0.0629	51.52	4168	0.0813	32.30	945	0.0568	59.43
215	0.0622	62.01	5002	0.0633	51.05	4582	0.0830	31.31	1399	0.0565	55.71
784	0.0484	47.62	CO_2/Brine, 167.0°F			4802	0.0852	31.31	1617	0.0568	54.14
1260	0.0451	41.92	352	0.0641	61.08	48.71 mol% CO_2/51.29 mol% CH_4/Brine, 79.7°F			2290	0.0601	51.57
1720	0.0413	37.00	865	0.0542	47.80	106	0.0718	76.46	2780	0.0624	50.00
2175	0.0394	34.06	1100	0.0523	43.91	474	0.0700	72.28	3430	0.0659	49.14
2765	0.0391	32.31	1540	0.0548	40.29	1066	0.0644	61.98	3803	0.0680	49.00
3187	0.0398	31.93	1992	0.0625	37.10	1586	0.0623	55.05	4200	0.0688	48.00
3850	0.0399	30.77	2475	0.0760	35.01	2118	0.0632	50.50	4890	0.0724	48.14
4368	0.0398	29.80	2841	0.0861	33.57	2582	0.0645	47.52	89.10 mol% CO_2/10.90 mol% CH_4/Brine, 77.0°F		
4905	0.0394	28.84	3412	0.1019	31.86	3178	0.0661	44.75	15	0.0580	66.00
CH_4/Brine, 167.0°F			3890	0.1166	31.00	3700	0.0693	44.16	946	0.0541	52.00
76	0.0721	69.10	4340	0.1300	30.00	4285	0.0701	42.18	1400	0.0774	45.00
937	0.0678	62.63	4890	0.1456	29.80	4672	0.0724	42.18	1620	0.0816	42.29
1543	0.0653	58.64	CH4/Brine, 256.0°F			29.53 mol% CO_2/70.47 mol% CH_4/Brine, 77.2°F			2289	0.0943	39.71
2035	0.0648	56.84	105	0.0296	63.53	146	0.0716	76.26	2783	0.1031	39.00
2533	0.0636	54.44	1090	0.0682	56.25	522	0.0701	72.67	3434	0.1184	39.86
3031	0.0630	52.76	1480	0.0626	53.53	1099	0.0665	65.54	3805	0.1224	38.86
3532	0.0625	51.22	1995	0.0605	50.61	1603	0.0626	58.42	4280	0.1287	38.14
4029	0.0632	50.79	2489	0.0584	49.51	2118	0.0631	55.45	4989	0.1408	38.00
4528	0.0633	49.88	2995	0.0582	48.10	2447	0.0619	52.48	CH_4/Brine, 169.2°F		
5026	0.0639	49.50	3487	0.0576	46.84	3106	0.0639	50.69	126	0.0684	74.23
CO_2/Brine, 167.0°F			4012	0.0571	46.07	3676	0.0670	50.69	894	0.0651	68.70
72	0.0734	70.02	4545	0.0572	45.29	4195	0.0690	50.30	1557	0.0633	65.05
728	0.0552	48.18	4989	0.0572	45.20	4532	0.0694	49.51	2032	0.0617	62.17
1230	0.0517	40.40	CO_2/Brine, 257.0°F			4868	0.0702	49.11	2529	0.0618	61.07
1715	0.0555	36.23	278	0.0748	68.14	CH_4/Brine, 167.0°F			3030	0.0608	58.93
2213	0.0684	33.92	545	0.0709	62.65	54	0.0697	71.44	3530	0.0606	57.70
2714	0.0830	31.54	901	0.0647	54.71	525	0.0680	68.43	4030	0.0605	56.60
3120	0.0967	30.58	1200	0.0610	49.35	1415	0.0659	63.90	4525	0.0611	56.35

3821	0.1245	29.84	1545	0.0598	45.66	2006	0.0637	60.16	5023	0.0624	56.71
4514	0.1536	28.64	1901	0.0614	43.70	2510	0.0639	59.05	CO_2/Brine, 169.7°F		
5011	0.1823	28.50	2530	0.0663	40.71	2992	0.0638	57.77	130	0.0659	71.00
30.88 mol% CO_2/69.12 mol% CH_4/Brine, 167.9°F			2901	0.0695	38.71	3496	0.0637	56.53	785	0.0591	58.67
166	0.0696	66.20	3310	0.0734	36.57	4009	0.0630	54.91	1193	0.0580	53.30
704	0.0605	55.50	3900	0.0812	34.51	4507	0.0622	53.27	1795	0.0574	43.87
1011	0.0545	48.90	4523	0.0927	33.50	4999	0.0635	53.57	2493	0.0714	41.06
1578	0.0534	45.70	4880	0.1009	33.35	CO_2/Brine, 167.0°F			2994	0.0812	39.51
2090	0.0535	43.80				352	0.0649	64.15	3492	0.0877	37.23
2893	0.0566	43.20				865	0.0573	52.52	3995	0.0979	36.88
3548	0.0581	42.00				1100	0.0569	49.73	4493	0.1033	35.02
4098	0.0586	40.60				1540	0.0594	45.74	4900	0.1107	34.66
4836	0.0589	38.80				1992	0.0660	41.65	40.69 mol% CO_2/59.31 mol% CH_4/Brine, 167.0°F		
64.48 mol% CO_2/35.52 mol% CH_4/Brine, 167.0°F						2475	0.0772	38.57	156	0.0688	74.44
245	0.0696	65.50				2841	0.0851	36.61	756	0.0661	68.62
782	0.0593	52.90				3412	0.0982	34.68	998	0.0642	65.49
1150	0.0548	46.70				3890	0.1071	32.82	1537	0.0594	57.94
1512	0.0519	42.00				4340	0.1173	31.82	1930	0.0589	55.52
2160	0.0531	38.60				4890	0.1346	31.75	2766	0.0606	52.95
2925	0.0575	36.40				20.32 mol% CO_2/79.68 mol% CH_4/Brine, 167.0°F			4041	0.0628	49.39
3552	0.0619	35.20				160	0.0719	73.24	4866	0.0647	48.11
4091	0.0622	32.50				605	0.0678	67.44	85.20 mol%CO_2/14.80 mol% CH_4/Brine, 167.0°F		
5024	0.0680	31.30				1250	0.0635	60.80	203	0.0673	72.17
CH_4/Brine, 257.0°F						1930	0.0625	57.22	778	0.0635	63.91
100	0.0646	58.16				2521	0.0617	54.32	1015	0.0604	58.78
1048	0.0604	52.43				3050	0.0610	51.93	1539	0.0566	50.23
1643	0.0573	48.59				3510	0.0605	50.06	1932	0.0569	46.10
2132	0.0563	46.79				4012	0.0620	49.89	2769	0.0637	41.83
3025	0.0569	45.69				4541	0.0631	49.38	4047	0.0783	39.83
4030	0.0573	44.30				4930	0.0630	48.35	4788	0.0865	39.27
5020	0.0585	43.78				54.50 mol% CO_2/45.50 mol% CH_4/Brine, 167.0°F			CH_4/Brine, 257.0°F		
CO_2/Brine, 257.0°F						358	0.0722	72.19	203	0.0660	67.78
70	0.0792	71.29				901	0.0623	59.41	1422	0.0617	60.89
616	0.0655	55.51				1150	0.0602	56.00	1950	0.0595	57.65
1130	0.0601	47.38				1635	0.0606	53.27	2517	0.0574	54.62

1629	0.0587	42.37				2110	0.0612	50.72	3014	0.0576	53.92
2126	0.0610	39.46				2561	0.0629	49.18	3514	0.0574	52.92
2628	0.0654	37.17				3000	0.0643	47.48	4012	0.0577	52.34
3128	0.0725	35.71				3432	0.0654	45.77	4510	0.0578	51.76
3693	0.0807	33.66				3902	0.0675	44.75	5010	0.0573	50.65
4330	0.0923	32.07				4351	0.0691	43.73	CO_2/Brine, 257°F		
4927	0.1071	31.52				4910	0.0704	42.19	140	0.0763	78.10
52.42 mol% CO_2/47.58 mol% CH_4/Brine, 257.0°F						CH_4/Brine, 256.0°F			822	0.0679	64.72
190	0.0713	63.66				80	0.0680	65.82	1502	0.0633	55.01
753	0.0682	58.36				1100	0.0619	57.81	2005	0.0609	48.49
1041	0.0631	52.71				1530	0.0600	55.13	2504	0.0646	46.63
1508	0.0568	45.51				2005	0.0600	54.17	3006	0.0692	44.88
2055	0.0540	41.06				2503	0.0580	51.38	3507	0.0720	41.95
2580	0.0560	40.38				3003	0.0581	50.55	4007	0.0777	40.88
3035	0.0575	39.52				3503	0.0573	49.04	4505	0.0809	38.63
3508	0.0601	39.35				4000	0.0561	47.23	4980	0.0885	38.76
4075	0.0642	39.69				4508	0.0566	46.93	20.05 mol% CO_2/79.95 mol% CH_4/Brine, 257.0°F		
4856	0.0675	38.72				5004	0.0571	46.66	37	0.0752	78.88
87.90 mol% CO_2/12.10 mol% CH_4/Brine, 257.0°F						CO_2/Brine, 257.0°F			667	0.0709	71.20
149	0.0729	65.16				125	0.0779	74.80	1235	0.0651	63.65
546	0.0661	56.76				533	0.0746	68.72	1860	0.0602	57.13
1031	0.0616	49.91				1002	0.0711	61.80	2445	0.0578	53.31
1558	0.0564	42.38				1530	0.0666	53.33	2896	0.0569	51.32
2081	0.0560	38.44				2008	0.0684	50.02	3422	0.0574	50.47
2755	0.0636	38.27				2560	0.0695	44.91	3910	0.0585	50.32
3444	0.0687	35.70				3012	0.0724	41.86	4360	0.0583	49.19
3850	0.0731	34.84				3513	0.0768	39.20	4960	0.0601	49.47
4415	0.0843	35.70				4002	0.0809	36.69	50.65 mol% CO_2/49.35 mol% CH_4/Brine, 257.0°F		
4900	0.0898	34.50				4512	0.0881	35.48	346	0.0752	76.17
						4908	0.0950	35.05	1010	0.0697	67.52
						20.59 mol% CO_2/79.41 mol% CH_4/Brine, 257.0°F			1605	0.0611	56.57
						259	0.0779	74.70	2140	0.0564	50.05
						630	0.0714	67.30	2604	0.0566	48.34
						1040	0.0654	60.30	3100	0.0577	47.35
						1520	0.0625	56.20	3642	0.0590	46.35
						2005	0.0609	53.40	4120	0.0594	44.93

						2620	0.0567	48.10	4630	0.0609	44.36
						3111	0.0547	45.20	4910	0.0609	43.51
						3520	0.0548	44.30			
						4005	0.0561	44.30			
						4560	0.0566	43.50			
						4980	0.0571	43.10			
						65.21 mol% CO_2/34.79 mol% CH_4 /Brine, 257.0°F					
						74	0.0778	75.20			
						494	0.0879	66.90			
						975	0.0668	60.00			
						1530	0.0663	56.40			
						2011	0.0658	53.20			
						2570	0.0636	48.20			
						3100	0.0624	44.50			
						3630	0.0618	41.40			
						4120	0.0626	39.70			
						4605	0.0640	38.50			
						4910	0.0656	38.20			

Table S2. Comparison of the measured IFTs for $CO_2/CH_4/H_2O$ systems with the IFTs calculated by Equation (9) as well as other four existing correlations.

Pressure, psi	IFT/Δρ, mN·m²/Kg	Exp. IFT, mN/m	This Work		Danesh *et al.*[6]		Sutton[39]		Firoozabadi and Ramey[2]		Weinaug and Katz[1]	
			IFT, mN/m	ARE, %	IFT, mN/m	ARE, %	IFT, mN/m	ARE, %	IFT, mN/m	ARE, %	IFT, mN/m	ARE, %
CO_2/H_2O, 80.0°F												
114	0.0687	68.23	68.85	0.90	119.77	75.54	125.03	83.25	82.84	21.42	86.23	26.38
306	0.0662	63.98	67.42	5.38	116.78	82.52	120.21	87.89	81.72	27.73	80.29	25.49
405	0.0630	59.97	66.60	11.06	114.99	91.75	117.39	95.75	81.04	35.14	76.99	28.38
974	0.1027	36.00	38.69	7.46	45.69	26.92	40.07	11.31	49.24	36.78	11.99	66.70
1379	0.1364	33.49	34.11	1.85	33.74	0.76	31.98	4.51	41.81	24.84	7.79	76.74
1713	0.1459	31.40	33.19	5.70	30.33	3.41	29.89	4.80	39.47	25.70	7.09	77.41
2115	0.1754	30.67	31.44	2.52	25.78	15.94	27.26	11.11	36.15	17.88	5.89	80.78
2577	0.2083	29.00	29.91	3.13	21.78	24.88	25.09	13.50	33.01	13.83	4.97	82.88
2915	0.2554	30.07	28.98	3.62	19.38	35.56	23.83	20.74	30.99	3.05	4.46	85.17
3407	0.3296	30.00	27.84	7.21	16.40	45.32	22.35	25.52	28.32	5.59	3.89	87.05
3816	0.4110	29.56	27.02	8.59	14.28	51.68	21.32	27.87	26.28	11.08	3.51	88.13
4365	0.5820	28.85	26.07	9.64	11.81	59.06	20.17	30.09	23.72	17.78	3.10	89.25
4846	0.8803	28.50	25.34	11.10	9.92	65.21	19.31	32.23	21.58	24.27	2.81	90.12
CO_2/H_2O, 163.0°F												
170	0.0618	57.81	54.00	6.59	94.16	62.88	94.74	63.88	80.36	80.36	69.80	20.75
685	0.0551	48.02	51.14	6.50	87.96	83.17	85.60	78.26	64.43	64.43	58.55	21.93
957	0.0503	41.72	49.39	18.39	83.79	100.83	79.81	91.31	62.76	62.76	51.98	24.60
1317	0.0507	38.33	46.51	21.35	76.73	100.18	70.67	84.36	59.85	59.85	42.32	10.40
1600	0.0510	34.66	43.58	25.75	69.40	100.24	61.99	78.84	56.69	56.69	33.87	2.27
1835	0.0548	33.06	40.70	23.11	62.09	87.82	54.11	63.67	53.39	53.39	26.79	18.95
2047	0.0597	31.84	38.06	19.54	55.36	73.87	47.50	49.20	50.18	50.18	21.30	33.09
2547	0.0746	30.13	33.28	10.47	43.08	42.96	36.95	22.63	43.82	43.82	13.46	55.34
2947	0.0868	29.14	30.78	5.62	36.60	25.59	32.11	10.18	40.13	40.13	10.29	64.68
3433	0.1048	28.90	28.58	1.10	30.91	6.95	28.24	2.29	36.63	36.63	7.99	72.35
4120	0.1323	28.29	26.34	6.88	25.09	11.31	24.63	12.95	32.73	32.73	6.04	78.64
4798	0.1670	28.04	24.69	11.94	20.80	25.84	22.17	20.92	29.58	29.58	4.84	82.73
CO_2/H_2O, 257.0°F												
246	0.0578	50.23	42.72	14.95	74.48	48.28	75.07	49.45	77.35	53.99	53.27	6.04
464	0.0555	47.08	41.49	11.88	72.75	54.53	72.55	54.11	53.93	14.55	50.10	6.42
845	0.0543	43.85	40.08	8.61	69.44	58.35	67.91	54.87	52.59	19.93	44.51	1.50
1182	0.0551	42.36	38.72	8.59	66.18	56.23	63.55	50.03	51.24	20.97	39.56	6.60
1325	0.0540	40.48	38.09	5.90	64.66	59.74	61.60	52.16	50.61	25.02	37.41	7.59
1538	0.0543	39.15	37.13	5.16	62.32	59.18	58.65	49.81	49.61	26.71	34.27	12.46

1836	0.0547	37.12	35.71	3.81	58.81	58.42	54.43	46.63	48.08	29.52	29.98	19.24
2230	0.0561	34.59	33.71	2.53	53.84	55.64	48.83	41.18	45.84	32.53	24.63	28.79
2873	0.0626	32.25	30.44	5.62	45.57	41.31	40.45	25.42	41.90	29.91	17.36	46.17
3280	0.0696	31.75	28.54	10.10	40.75	28.36	36.06	13.57	39.44	24.23	13.93	56.12
4280	0.0933	31.57	24.84	21.33	31.26	0.97	28.41	10.02	34.18	8.28	8.65	72.60
CH_4/H_2O, 81.0°F												
462	0.0703	69.90	77.23	10.49	65.43	6.40	62.29	10.89	45.43	35.00	45.43	35.00
747	0.0686	67.20	75.16	11.85	64.52	3.99	60.94	9.31	45.09	32.90	45.09	32.90
987	0.0675	65.25	73.35	12.41	63.72	2.35	59.78	8.39	44.79	31.36	44.79	31.36
1339	0.0671	63.62	70.60	10.98	62.50	1.77	58.04	8.77	44.32	30.33	44.32	30.33
1607	0.0670	62.52	68.48	9.54	61.55	1.55	56.72	9.28	43.96	29.69	43.96	29.69
1890	0.0660	60.57	66.26	9.39	60.56	0.02	55.35	8.62	43.57	28.06	43.57	28.06
2240	0.0650	58.46	63.60	8.80	59.37	1.55	53.74	8.08	43.11	26.26	43.11	26.26
2495	0.0650	57.61	61.77	7.21	58.54	1.61	52.64	8.63	42.78	25.74	42.78	25.74
3036	0.0638	54.98	58.21	5.87	56.92	3.54	50.54	8.07	42.14	23.35	42.14	23.35
3506	0.0633	53.25	55.51	4.24	55.69	4.59	48.99	8.01	41.65	21.79	41.65	21.79
4125	0.0637	52.20	52.46	0.49	54.29	4.01	47.25	9.47	41.08	21.31	41.08	21.31
4535	0.0637	51.45	50.70	1.45	53.48	3.95	46.28	10.06	40.75	20.80	40.75	20.80
4851	0.0644	51.41	49.48	3.76	52.91	2.92	45.60	11.31	40.51	21.20	40.51	21.20
CH_4/H_2O, 163.0°F												
17	0.0729	70.21	63.47	9.61	53.17	24.27	53.45	23.87	37.45	46.66	37.45	3.90
144	0.0700	67.16	63.02	6.16	52.98	21.12	53.15	20.86	37.38	44.35	37.38	6.03
345	0.0671	63.72	61.94	2.80	52.50	17.61	52.43	17.72	37.19	41.63	37.19	5.32
687	0.0650	60.85	60.29	0.92	51.78	14.91	51.33	15.64	36.92	39.33	36.92	0.57
983	0.0640	59.18	58.84	0.59	51.13	13.60	50.38	14.88	36.67	38.04	36.67	4.90
1302	0.0637	58.10	57.25	1.46	50.43	13.19	49.35	15.06	36.40	37.35	36.40	11.79
1617	0.0635	57.09	55.67	2.48	49.73	12.89	48.34	15.33	36.12	36.73	36.12	18.40
1887	0.0633	56.20	54.34	3.31	49.14	12.57	47.49	15.50	35.89	36.14	35.89	23.71
2209	0.0625	54.67	52.78	3.46	48.44	11.40	46.51	14.93	35.61	34.86	35.61	29.03
2585	0.0620	53.34	51.02	4.36	47.65	10.67	45.41	14.87	35.30	33.83	35.30	35.24
2973	0.0619	52.35	49.29	5.85	46.87	10.47	44.35	15.28	34.98	33.17	34.98	41.37
3517	0.0622	51.36	47.04	8.42	45.85	10.73	42.99	16.30	34.57	32.69	34.57	49.07
4021	0.0620	50.25	45.14	10.17	44.98	10.48	41.86	16.69	34.22	31.90	34.22	54.78
4506	0.0622	49.49	43.48	12.14	44.23	10.63	40.89	17.38	33.91	31.49	33.91	59.60
4846	0.0625	49.16	42.41	13.72	43.74	11.03	40.27	18.09	33.70	31.44	33.70	62.66
CH_4/H_2O, 257.0°F												
162	0.0596	53.05	48.51	8.57	41.21	22.32	45.18	14.83	30.07	43.32	53.49	0.83
450	0.0587	51.65	47.56	7.91	40.80	21.02	44.52	13.81	29.90	42.10	50.02	3.16
761	0.0572	49.80	46.54	6.55	40.34	18.99	43.80	12.05	29.72	40.31	46.42	6.78

1299	0.0566	48.26	44.76	7.26	39.55	18.04	42.57	11.79	29.41	39.06	40.62	15.83
1617	0.0565	47.56	43.71	8.09	39.09	17.82	41.86	11.99	29.22	38.56	37.46	21.23
1891	0.0564	47.01	42.82	8.91	38.69	17.70	41.25	12.24	29.06	38.18	34.92	25.73
2259	0.0567	46.58	41.65	10.58	38.16	18.07	40.47	13.12	28.85	38.07	31.75	31.84
2615	0.0567	46.00	40.55	11.85	37.67	18.11	39.73	13.62	28.64	37.73	28.97	37.03
3077	0.0566	45.10	39.18	13.14	37.05	17.85	38.83	13.90	28.39	37.05	25.74	42.93
3592	0.0570	44.56	37.73	15.33	36.39	18.33	37.89	14.96	28.12	36.90	22.63	49.22
4097	0.0572	43.98	36.40	17.23	35.79	18.62	37.05	15.77	27.86	36.64	20.02	54.48
4586	0.0574	43.45	35.20	18.98	35.25	18.88	36.29	16.48	27.63	36.40	17.85	58.91
4867	0.0577	43.25	34.56	20.10	34.95	19.19	35.88	17.04	27.51	36.40	16.75	61.27
60.10 mol% CO_2/39.90 mol% CH_4/H_2O, 80.0°F												
472	0.0685	66.43	69.30	4.31	97.65	47.00	97.63	46.96	65.85	0.87	76.30	14.85
1028	0.0661	59.19	64.22	8.50	90.33	52.62	86.82	46.68	43.97	25.72	58.82	0.63
1525	0.0588	47.01	58.01	23.41	80.93	72.15	74.22	57.87	61.93	31.75	41.52	11.67
1925	0.0618	43.92	52.49	19.51	72.36	64.75	63.91	45.52	58.30	32.74	29.48	32.89
2540	0.0660	40.12	46.10	14.91	62.30	55.28	53.17	32.52	53.78	34.04	18.90	52.88
3000	0.0671	37.23	42.90	15.22	57.20	53.63	48.24	29.57	51.35	37.93	14.77	60.32
3491	0.0693	35.52	40.32	13.53	53.08	49.44	44.50	25.29	49.32	38.86	11.95	66.35
3947	0.0732	35.21	38.43	9.14	50.03	42.09	41.87	18.92	47.77	35.68	10.14	71.21
4542	0.0785	35.10	36.42	3.77	46.79	33.30	39.19	11.66	46.07	31.27	8.44	75.96
71.20 mol% CO_2/28.80 mol% CH_4/H_2O, 80.0°F												
15	0.0688	69.78	71.82	2.93	108.16	55.00	111.75	60.15	74.42	6.64	88.48	26.80
78	0.0690	69.56	71.56	2.88	107.54	54.60	110.74	59.21	74.19	6.65	87.35	25.57
323	0.0674	66.29	69.84	5.35	104.88	58.22	106.50	60.66	73.19	10.41	80.17	20.93
781	0.0598	55.10	65.88	19.56	98.42	78.61	96.67	75.44	70.72	28.35	65.29	18.50
1320	0.0561	44.87	58.71	30.83	85.88	91.40	79.47	77.10	65.70	46.43	43.46	3.15
1824	0.0634	39.86	48.97	22.84	68.19	71.08	59.05	48.14	58.01	45.54	22.85	42.68
2323	0.0689	36.73	43.67	18.90	58.42	59.05	49.53	34.84	53.36	45.29	15.21	58.60
2711	0.0728	35.10	40.84	16.35	53.15	51.44	44.88	27.85	50.71	44.48	11.97	65.88
3557	0.0776	31.58	36.74	16.35	45.49	44.05	38.67	22.44	46.62	47.64	8.21	73.99
4105	0.0823	30.63	34.87	13.84	41.96	36.99	36.02	17.59	44.63	45.72	8.70	71.60
26.38 mol% CO_2/73.62 mol% CH_4/H_2O, 167.9°F												
476	0.0456	57.93	52.83	8.80	57.67	0.45	57.45	0.82	41.18	28.92	63.71	9.98
981	0.0481	55.30	49.45	10.58	55.85	0.99	54.76	0.97	40.47	26.82	54.90	0.72
1527	0.0504	51.13	46.97	8.14	53.76	5.14	51.79	1.29	39.65	22.46	46.03	9.98
2068	0.0542	48.40	44.49	8.08	51.65	6.71	48.90	1.04	38.80	19.84	38.23	21.02
2468	0.0586	46.77	42.70	8.69	50.11	7.15	46.88	0.24	38.17	18.38	33.23	28.95
3019	0.0633	44.60	40.39	9.44	48.11	7.87	44.33	0.61	37.34	16.28	27.46	38.43
3732	0.0705	43.25	37.72	12.79	45.77	5.83	41.48	4.10	36.35	15.96	21.72	49.77

4214	0.0788	42.98	36.13	15.94	44.37	3.23	39.83	7.33	35.74	16.84	18.75	56.38
4761	0.0855	42.16	34.52	18.12	42.95	1.86	38.20	9.38	35.12	16.70	16.04	61.94
15.37 mol% CO_2/84.63 mol% CH_4/H_2O, 168.1°F												
513	0.0476	60.20	57.11	5.14	57.74	4.09	57.58	4.35	41.20	31.57	63.17	4.94
1023	0.0508	56.68	54.71	3.48	56.16	0.91	55.25	2.53	40.59	28.39	54.54	3.77
1490	0.0531	54.51	52.45	3.78	54.67	0.29	53.09	2.61	40.00	26.62	47.21	13.40
2083	0.0563	50.72	49.59	2.24	52.75	4.00	50.42	0.60	39.24	22.64	38.96	23.20
2475	0.0591	48.53	47.75	1.60	51.52	6.15	48.75	0.44	38.74	20.18	34.25	29.43
3163	0.0644	47.45	44.75	5.68	49.48	4.27	46.07	2.90	37.90	20.12	27.43	42.20
3680	0.0713	46.37	42.72	7.87	48.08	3.69	44.31	4.44	37.32	19.51	23.39	49.56
4112	0.0760	45.69	41.18	9.88	47.02	2.91	42.99	5.90	36.87	19.30	20.62	54.88
4656	0.0829	44.01	39.41	10.44	45.80	4.06	41.52	5.66	36.35	17.40	17.75	59.66
60.71 mol% CO_2/39.29 mol% CH_4/H_2O, 168.0°F												
400	0.0353	56.27	55.40	1.55	77.77	38.21	77.50	37.74	55.66	1.08	64.71	14.99
1089	0.0381	49.35	51.80	4.96	72.55	47.01	69.96	41.77	53.62	8.64	51.41	4.18
1545	0.0415	44.61	49.15	10.17	68.60	53.78	64.61	44.83	52.02	16.61	42.94	3.73
2072	0.0473	41.22	45.88	11.31	63.65	54.42	58.33	41.50	49.96	21.20	33.94	17.66
2485	0.0554	38.64	43.36	12.21	59.77	54.69	53.71	39.01	48.29	24.97	27.96	27.64
3092	0.0653	35.24	39.95	13.38	54.49	54.62	47.86	35.80	45.94	30.35	21.14	40.02
3580	0.0761	33.48	37.62	12.36	50.83	51.81	44.07	31.64	44.24	32.15	17.20	48.64
4123	0.0909	32.53	35.41	8.85	47.34	45.53	40.67	25.03	42.58	30.89	13.98	57.02
4805	0.1131	32.40	33.12	2.23	43.70	34.89	37.32	15.20	40.78	25.86	11.12	65.67
44.87 mol% CO_2/55.13 mol% CH_4/H_2O, 167.0°F												
14	0.0386	66.10	56.72	14.19	72.60	9.84	73.45	11.12	51.21	22.53	72.22	9.26
603	0.0413	56.54	54.05	4.40	69.58	23.07	68.88	21.82	50.04	11.49	61.24	8.32
1200	0.0453	51.40	51.06	0.66	66.10	28.60	63.86	24.24	48.68	5.30	50.40	1.95
1900	0.0518	46.78	47.30	1.11	61.62	31.73	57.80	23.56	46.87	0.19	38.78	17.10
2307	0.0578	44.20	45.10	2.05	58.97	33.42	54.41	23.10	45.77	3.55	32.96	25.43
2801	0.0648	41.49	42.56	2.59	55.87	34.66	50.63	22.03	44.45	7.14	27.03	34.86
3483	0.0768	39.05	39.43	0.98	52.01	33.20	46.19	18.29	42.77	9.52	20.81	46.72
4118	0.0902	37.56	36.96	1.59	48.94	30.29	42.85	14.09	41.38	10.18	16.67	55.61
4720	0.1115	36.63	34.97	4.52	46.44	26.79	40.28	9.95	40.23	9.83	13.80	62.33
13.44 mol% CO_2/86.56 mol% CH_4/H_2O, 77.9°F												
320	0.0510	70.89	72.46	2.22	71.02	0.19	68.40	3.51	49.20	30.60	81.84	15.45
1149	0.0573	63.70	66.46	4.33	67.29	5.63	62.93	1.20	47.78	24.99	60.86	4.45
2148	0.0653	56.27	58.54	4.04	62.23	10.60	56.05	0.40	45.81	18.59	39.43	29.92
3073	0.0793	53.56	52.26	2.43	58.14	8.55	50.88	5.01	44.16	17.55	26.73	50.09
4358	0.0954	50.43	46.03	8.72	54.02	7.12	46.02	8.74	42.44	15.84	17.31	65.67
40.53 mol% CO_2/59.47 mol% CH_4/H_2O, 257.0°F												

568	0.0456	49.60	43.73	11.83	53.74	8.36	55.79	12.48	39.73	19.90	48.25	2.72
1020	0.0473	48.22	41.25	14.46	52.14	8.13	53.43	10.80	39.09	18.94	42.77	11.30
1530	0.0492	45.78	39.54	13.62	50.27	9.81	50.76	10.87	38.32	16.29	37.02	19.14
2045	0.0519	43.75	37.82	13.56	48.35	10.52	48.12	9.99	37.53	14.22	31.77	27.39
2570	0.0556	41.60	36.09	13.25	46.42	11.58	45.56	9.51	36.71	11.76	27.07	34.93
3006	0.0589	40.69	34.71	14.70	44.86	10.24	43.56	7.06	36.04	11.44	23.69	41.79
3585	0.0650	39.67	32.98	16.86	42.89	8.11	41.14	3.70	35.17	11.33	19.89	49.86
4011	0.0704	39.20	31.80	18.87	41.53	5.95	39.53	0.83	34.57	11.81	17.56	55.21
4535	0.0772	39.16	30.46	22.22	39.98	2.10	37.74	3.63	33.87	13.51	15.14	61.33
4901	0.0456	38.96	29.59	24.05	38.98	0.04	36.61	6.04	33.40	14.26	13.72	64.79
60.23 mol% CO_2/39.77 mol% CH_4/H_2O, 257.0°F												
996	0.0608	47.20	41.00	13.14	58.65	24.27	58.91	24.81	44.23	6.28	42.61	9.73
1486	0.0466	42.32	39.27	7.21	56.05	32.44	55.30	30.68	43.16	1.99	36.76	13.13
2000	0.0496	40.28	37.38	7.20	53.21	32.11	51.57	28.02	41.97	4.19	31.04	22.93
2541	0.0529	38.35	35.41	7.67	50.20	30.90	47.79	24.63	40.67	6.05	25.79	32.74
2999	0.0568	37.23	33.80	9.22	47.71	28.14	44.83	20.40	39.57	6.27	21.99	40.93
3508	0.0621	36.60	32.11	12.27	45.07	23.15	41.83	14.30	38.37	4.84	18.45	49.58
4005	0.0692	36.52	30.59	16.24	42.69	16.89	39.25	7.46	37.26	2.03	15.63	57.20
4489	0.0768	36.23	29.24	19.29	40.56	11.94	37.03	2.22	36.25	0.04	13.40	63.03
% AARE				9.42		28.28		23.13		25.52		35.98
% SD				11.33		38.48		40.39		29.08		44.11

Error Analysis

The accuracy of the new model is assessed by performing statistical error analysis. The following three parameters are evaluated for such purpose:

1) Absolute Relative Error

$$ARE(\%) = \frac{\left|IFT_{\exp,i} - IFT_{cal,i}\right|}{IFT_{\exp,i}} \times 100$$

2) Average Absolute Relative Error

$$AARE(\%) = \frac{1}{n}\sum_{i=1}^{n}\left(\frac{\left|IFT_{\exp,i} - IFT_{cal,i}\right|}{IFT_{\exp,i}}\right) \times 100$$

3) Standard Deviation

$$SD = \sqrt{\frac{\sum_{i=1}^{n}\left[\left(\frac{\left|IFT_{\exp,i} - IFT_{cal,i}\right|}{IFT_{\exp,i}}\right) \times 100\right]^2}{n-1}}$$

CHAPTER 7 CONCLUSIONS, CONTRIBUTIONS AND RECOMMENDATIONS

7.1 Conclusions and Scientific Contributions to the Literature

Understanding of the phase behavior, adsorption behavior, and interfacial properties of fluids in shale reservoirs is of critical importance for more accurately determining the macroscopic and microscopic distribution of fluids in shale reservoirs as well as revealing the mechanisms that govern the fluid transport in shale reservoirs. In this thesis, the engineering DFT and the PR-EOS with capillary pressure model are first employed to investigate phase behavior of pure hydrocarbon and hydrocarbon mixtures in single nanopores. We compare the confined fluid phase behavior calculated with the engineering DFT to that calculated with the PR-EOS with capillary pressure model. Then, MD simulation is applied to investigate the competitive adsorption behavior of hydrocarbon(s)/CO_2 mixtures in a double-nanopore system considering that shale matrix generally contains pores with different sizes.

In nanopores, fluid-pore wall interactions are strong, which can thus result in significant adsorption on pore surface. Excess adsorption isotherms of pure hydrocarbons are measured on shale samples; we then use GCMC simulations to obtain the absolute adsorption isotherms by correcting the excess adsorption isotherms with the adsorption phase density. Next, an experimental method is designed to measure the fluid phase behavior with the presence of shale samples, revealing the effect of competitive adsorption on phase behavior. In addition to the fluid-pore wall interactions, capillary pressure due to the interfacial tension between two equilibrating vapor-liquid phases comes into play a key role in affecting the two-phase equilibria, whenever two-phase equilibrium appears in tiny pores in shale. Thereby, the IFTs of CO_2/CH_4/brine systems are finally measured under reservoir conditions using the ADSA method. Based on the above-mentioned efforts, the following conclusions can be obtained in this thesis:

Chapter 2:

- Phase behavior of fluid is described in nanopores using engineering DFT and PR-EOS with capillary pressure model. The performance of PR-EOS with capillary pressure model is evaluated by comparing with engineering DFT; through this comparison, the limitations of the PR-EOS with capillary pressure model are revealed.
- It is found that as for pure nC_8, both engineering DFT and PR-EOS with capillary pressure model predicts that, at isobaric conditions, as nanopore size increases, the dew-point temperature approaches the bulk saturation temperature. The difference in the dew-point temperature calculated by PR-EOS with capillary pressure model and engineering DFT model decreases as the system pressure approaches the critical pressure. At low pressure conditions, the PR-EOS with capillary pressure model becomes unreliable.
- Under different isobaric conditions, engineering DFT predicts that the confined dew-point of pure nC_8 approaches the bulk saturation point when pore size is 30 nm, while the PR-EOS with capillary pressure model predicts that the confined dew-point approaches the bulk only when the pore size is as large as 1,000 nm. It emphasizes the importance of considering the fluid-pore surface interactions and surface adsorption for accurately describing the phase behavior of confined fluids.
- Under different isobaric conditions, engineering DFT predicts that the confined lower dew-point of C_1-nC_6 mixture approaches the bulk saturation point when pore size is 20 nm, while for this pore size the upper dew-point shows larger deviation from the bulk value. On the other hand, the dew-point obtained from the PR-EOS with capillary pressure model approaches the bulk only when the pore size is as large as 100 nm.
- As for the C_1-nC_6 mixture tested, both PR-EOS with capillary pressure model and

engineering DFT predict that the confined fluids can have phase transition at temperature higher than the cricondentherm point. Engineering DFT also predicts that supercriticality of the upper dew-point can occur when temperature is lower than a certain point.

Chapter 3:

- Competitive adsorption behavior of hydrocarbon(s)/CO_2 mixtures is studied in a double-nanopore system using MD simulations. The dynamic distribution characteristics of hydrocarbon(s) and CO_2 molecules are obtained in the double-nanopore system with a depressurization process. CO_2 injection for enhanced shale lighter (or heavier) hydrocarbon recovery is thus illustrated.
- The dynamic distributions of C_1/nC_4 mixture in the double-nanopore system illustrates that as pressure decreases, adsorption of C_1 tends to decrease, while adsorption of nC_4 is improved. It indicates that lighter components may be readily produced from nanopores as pressure drops, while heavier components will concentrate in organic pores and are difficult to be produced.
- The dynamic distributions of C_1/CO_2 mixture in the double-nanopore system shows that as pressure drops, the adsorbed C_1 molecules can be replaced by CO_2 from nanopores due to the stronger adsorption capacity of CO_2 on organic pore surface.
- As observed from the dynamic distributions of nC_4/CO_2 mixture in the double-nanopore system, adsorption of CO_2 decreases with decreasing pressure, while adsorption of nC_4 increases; it indicates that CO_2 injection may be not efficient to recover nC_4 with the depressurization approach.

- Based on the calculated adsorption selectivity, nC_4 and CO_2 exhibit stronger adsorption capacity on organic pore surface than C_1, while the adsorption capacity of CO_2 is smaller than that of nC_4.
- Based on the calculated molar fraction of C_1 (and nC_4) in C_1/CO_2 (and nC_4/CO_2) mixture in nanopores in terms of pressure, CO_2 is considered as a suitable agent to recover the lighter hydrocarbons from organic pores but may be less efficient to recover the heavier hydrocarbons; it depends on the competitive adsorption between hydrocarbon(s) and CO_2 on organic pore surface.

Chapter 4:

- By using TGA method, excess adsorption isotherms are measured for CH_4 or n-C_4H_{10} on shale samples. We then use the GCMC simulation to obtain the adsorption phase density of hydrocarbons on shale sample. The calculated adsorption-phase density is then used to correct the measured excess adsorption isotherm to obtain the absolute adsorption isotherms. This molecular simulation method is more accurate than these conventional approaches in obtaining the absolute adsorption.
- The GCMC simulations show that the density distributions of CH_4 or n-C_4H_{10} vary in response to the changes in system pressure, temperature, and pore size. The calculated density of the adsorption phase of CH_4 is always lower than the liquid CH_4 density and, at high pressures, the density of the adsorption phase is found to be very close to but never equal or greater than the liquid phase density. The calculated density of the adsorption phase of n-C_4H_{10} can be higher than the liquid n-C_4H_{10} density.

- More obvious adsorption/desorption hysteresis and higher adsorption capacity are observed for *n*-C_4H_{10} than CH_4. This indicates a higher affinity of *n*-C_4H_{10} towards the two shale samples.
- GCMC simulations can faithfully capture the *in-situ* density of the adsorption phase by better honoring the carbon pore-surface/gas interactions. Compared with the GCMC-based approach, the conventional approaches, on the basis of using a constant density for the adsorption phase, are appropriate for obtaining the absolute adsorption isotherms for *n*-C_4H_{10}, but tend to significantly underestimate the absolute adsorption isotherms for CH_4.

Chapter 5:

- A new experimental approach is designed to measure the phase behavior of fluid mixtures with the presence of shale samples. With this experiment, the effect of competitive adsorption on phase behavior is illustrated.
- It was observed that bubble-point pressures of the N_2/n-C_4H_{10} mixtures with the presence of shale samples were higher than those in the bulk space. A detailed analysis of results indicated that n-C_4H_{10} exhibited a higher level of adsorption on shale sample than N_2; therefore, the N_2 concentration in the free fluid was higher than that in the initial mixture. The higher N_2 concentration led to the higher bubble-point pressure as observed in the measurements.
- The increase in bubble-point pressure due to the competitive adsorption was observed to be greater at the lower temperature for the two mixtures tested. This is because the adsorption of n-C_4H_{10} relative to that of N_2 is more significant at the lower temperature.

- It was found that a higher adsorption amount of N_2 and n-C_4H_{10} for a given N_2/n-C_4H_{10} mixture occurred at a lower temperature. A higher temperature did not lead to a higher bubble-point pressure for a given mixture likely because bubble-point is more sensitive to composition than to temperature for these mixtures at the conditions tested. This emphasizes the importance of considering adsorption in phase behavior calculation for small pores.

Chapter 6:

- Experiments were conducted to measure IFT for the CO_2/CH_4/brine system along three isotherms between 77.0 and 257.0^oF, at pressures up to 5,027 psia and salinities up to 200,000 ppm. Different CH_4/CO_2 ratios in the gas mixture were considered in the measurements. This is the first time that the IFTs for the CO_2/CH_4/brine system are measured.
- A detailed analysis of the presence of CO_2 and salt effect on IFT was carried out based on the measured IFT data. The presence of CO_2 decreases the IFT, but the degree of reduction in IFT depends on the amount of CO_2 added. The presence of salt in pure water increases the IFT between gas and liquid. IFT reduction of the CH_4/brine system due to the addition of CO_2 can possibly result in an increased capillary number, which may be beneficial for enhancing shale gas recovery if CO_2 is used as a recovery medium.
- Based on the IFT data measured in this research, an improved IFT correlation was developed based on the Parachor model (Weinaug and Katz, 1943) and Firoozabadi and Ramey's model (Firoozabadi and Ramey, 1988). Unlike other correlations, the improved IFT correlation accounts for all major parameters that affect CO_2/CH_4/H_2O IFT, including pressure, temperature, individual compound's molecular weight, density

difference, and gas composition on IFT of gas-mixture/H_2O systems. For the $CO_2/CH_4/H_2O$ mixtures, the improved correlation provides a more accurate prediction of $CO_2/CH_4/H_2O$ IFT data measured by Ren *et al.* (2000) in comparison to other four existing correlations. Improved correlations used for predicting IFT of CO_2/CH_4/brine systems have been also presented, showing a good performance in correlating the measured IFTs.

7.2 Suggested Future Work

- Conventional EOS modeling approach ignores the inhomogeneous density distributions and surface adsorption that are prevalent in nanopores, while engineering DFT can capture these two effects in nanopores. It is meaningful for researchers and engineers to further improve the conventional EOS models based on the phase behavior results computed using the engineering DFT model. One could also use engineering DFT model in reservoir simulations by adopting the following procedure: first exhaustively run the engineering DFT model to obtain phase behavior of confined fluids with varied compositions at different pressure/temperature conditions; then tabulate these results; and finally create look-up tables that can be called by the numerical simulator at different timesteps.
- Phase behavior modeling works are extensively conducted in slit-shaped pores. However, the SEM imaging of shale samples reveals that pore structures may also include cylindrical and ink-bottle shapes (de Boer and Lippens 1964; Sing *et al.* 2008). In these cylindrical and ink-bottle shapes pores, the phase behavior and adsorption-desorption behavior of hydrocarbons can be quite different from that in the slit-shaped pores. For instance, by using ink-bottle model, due to pore-blocking and cavitation effects (Fan *et*

al. 2011; Klomkliang *et al.* 2013), nitrogen adsorption-desorption isotherms may behave differently depending on the pore diameter ratio of "ink" and "bottle". In future works, the effect of pore geometry on the phase behavior and adsorption-desorption behavior of pure and hydrocarbon mixtures should be explored.

- We investigate the competitive adsorption behavior of hydrocarbon(s)/CO_2 mixtures in a double-nanopore system using MD simulations. The dynamic distributions of individual species are revealed in different pores with a depressurization process. This double-nanopore system, however, comprises of only two pores with different sizes. In shale reservoirs, real shale samples generally have pores with a given pore size distribution. Thereby, to better understand the competitive adsorption in shale samples, adsorption behavior of different species should be studied using porous media with actual pore size distributions. Moreover, in addition to organic matters, clay minerals are also vastly present in real shale samples (Tian *et al.*, 2017). Due to the high specific surface area exhibited by clay minerals, shale gas can also strongly adsorb onto the surface of clay minerals. Further works should be done to study the adsorption behavior of hydrocarbons on clay minerals (e.g., montmorillonite, illite, and kaolinite *etc*.).
- In our previous work, considering the low vapor pressure of *n*-C_4H_{10} at room temperature, we only measure the excess adsorption isotherms at the pressures up to 2 bar. Pressures in shale reservoir are generally significantly higher than 2 bar. In future works, the testing pressures/temperatures should be chosen according to true reservoir conditions. In addition, we only measure the excess adsorption/desorption isotherms for pure CH_4 and *n*-C_4H_{10}. In reality, various hydrocarbon components (e.g., C_2H_6, and C_3H_8) and nonhydrocarbon components (e.g., CO_2, and N_2) may coexist in shale condensate

reservoirs. Thereby, to have a comprehensive understanding of the adsorption behavior of fluid mixtures in shale reservoirs, adsorption measurements should also be conducted on the other species besides CH_4 and *n*-C_4H_{10} as well as their mixtures.

- In this thesis, we measure the bubble-point pressure of N_2/*n*-C_4H_{10} mixtures to investigate the effect of competitive adsorption on fluid phase behavior. We select the N_2/*n*-C_4H_{10} binary based on the following considerations: *n*-C_4H_{10}, as a nonvolatile hydrocarbon, is a common component present in the shale gas-condensate reservoirs; N_2, as a volatile non-hydrocarbon component, can be introduced into shale reservoir as an energized fluid used during an energized fracturing treatment. Furthermore, N_2 has been found to be an abundant component that can be produced from some shale reservoirs. However, in shale reservoirs, CH_4 is the dominant component in shale fluid. In the future works, the effect of competitive adsorption between CH_4 and heavier hydrocarbons on phase behavior should be studied.
- In this thesis, we measure and model the IFTs of CO_2/CH_4/brine system under reservoir conditions considering that capillary pressure due to the interfacial tension between two equilibrating vapor-liquid phases comes into play a key role in affecting the two-phase equilibria. These IFT values are measured in a bulk environment where the fluid interface is flat. But, in shale reservoirs, IFT between two phases can be quite different from that captured in such bulk condition due to strong fluid/pore wall interactions. Thereof, more sophisticated techniques are recommended to be proposed to measure the IFT in confined space.

7.3 References

de Boer, J.H., and Lippens, B.C. 1964. Studies on pore systems in catalysts II. The shapes of

pores in aluminum oxide systems. *J. Catal.* 3 (1): 38-43.

Fan, C., Do, D.D., and Nicholson, D. 2011. On the cavitation and pore blocking in slit-shaped ink-bottle pores. *Langmuir* 27 (7): 3511-3526.

Firoozabadi, A., and Ramey Jr., H.J. 1988. Surface tension of water-hydrocarbon systems at reservoir conditions. *J. Can. Pet. Technol.* 27: 41-48.

Jin, B., Bi, R., and Nasrabadi, H. 2017. Molecular simulation of the pore size distribution effect on phase behavior of methane confined in nanopores. *Fluid Phase Equilibr.* 452: 94-102.

Klomkliang, N., Do, D.D., and Nicholson, D. 2013. On the hysteresis loop and equilibrium transition in slit-shaped ink-bottle pores. *Adsorption* 19 (6): 1273-1290.

Luo, S., Lutkenhaus, J.L., and Nasrabadi, H. 2017. Multi-scale fluid phase behavior simulation in shale reservoirs by a pore-size-dependent equation of state. Presented at the SPE Annual Technical Conference and Exhibition, San Antonio, USA, 9-11 October.

Sing, K.S.W., Everett, D.H., Haul, R.A.W. *et al.* 2008. Reporting physisorption data for gas/solid systems. Handbook of Heterogeneous Catalysis, Wiley-VCH Verlag GmbH & Co. KGaA.

Tian, Y., Yan, C., and Jin, Z. 2017. Characterization of methane excess and absolute adsorption in various clay nanopores from molecular simulation. *Sci. Rep.* 7: 12040.

Wang, L., Yin, X., Neeves, K.B. *et al.* 2016. Effect of pore-size distribution on phase transition of hydrocarbon mixtures in nanoporous media. *SPE J.* 21 (6): 1981-1995.

Weinaug, C.F., and Katz, D.L. 1943. Surface tensions of methane-propane mixtures. *Ind. Eng. Chem.* 35 (2): 239-246.

BIBLIOGRAPHY

Abramzon, A.A., and Gaukhberg, R.D. 1993. Surface tension of salt solutions. *Russian J. Appl. Chem.* 66: 1428.

Aggelopoulos, C.A., Robin, M., and Perfetti, M., *et al.* 2010. $CO_2/CaCl_2$ solution interfacial tensions under CO_2 geological storage conditions: influence of cation valence on interfacial tension. *Adv. Water Resour.* 33: 691-697.

Aggelopoulos, C.A., Robin, M., and Vizika, O. 2011. Interfacial tension between CO_2 and brine ($NaCl+CaCl_2$) at elevated pressures and temperatures: the additive effect of different salts. *Adv. Water Res.* 34: 505-511.

Akutsu, T., Yoshinori, Y., and Hirokazu, Y., *et al.* 2007. Interfacial tension between water and high pressure CO_2 in the presence of hydrocarbon surfactants. *Fluid Phase Equilibr.* 257: 163-168.

Alfi, M., Nasrabadi, H., and Banerjee, D. 2016. Experimental investigation of confinement effect on phase behavior of hexane, heptane and octane using lab-on-a-chip technology. *Fluid Phase Equilibr.* 423: 25-33.

Alharthy, N.S., Nguyen, T., and Teklu, T., *et al.* 2013. Multiphase compositional modeling in small-scale pores of unconventional shale reservoirs. SPE Annual Technical Conference and Exhibition. New Orleans, Louisiana, Society of Petroleum Engineers.

Almeida, B.S., and Telo da Gama, M.M. 1989. Surface tension of simple mixtures: comparison between theory and experiment. *J. Phys. Chem.* 93: 4132-4138.

Ambrose, R.J., Hartman R.C., and Campos, M.D., *et al.* 2010. New pore-scale considerations for shale gas in place calculations. Presented at the SPE Unconventional Gas Conference, Pittsburgh, Pennsylvania, USA.

Ambrose, R.J., Hartman, R.C., and Diaz-Campos, M. *et al.* 2012. Shale gas-in-place calculations Part I: new pore-scale considerations. *SPE J.* 17 (1): 219-229.

Andersen, H.C. 1980. Molecular dynamics at constant pressure and/or temperature. *J. Chem. Phys.* 72: 2384-2393.

Argaud, M.J. 1992. Predicting the interfacial tension of brine/gas (or condensate) Systems. Presented at the SCA European Core Analysis Symposium. Paris.

Ayirala, S.C., and Rao, D.N. 2004. Application of a new mechanistic Parachor model to predict dynamic gas-oil miscibility in reservoir crude oil-solvent systems. Presented at the SPE International Petroleum Conference. Puebla.

Ayirala, S.C., and Rao, D.N. 2006. A new mechanistic Parachor model to predict dynamic interfacial tension and miscibility in multicomponent hydrocarbon systems. *J. Colloid Interface Sci.* 299: 321-331.

Bachu, S., and Bennion, D.B. 2009. Interfacial tension between CO_2, freshwater, and brine in the range of pressure from (2 to 27) MPa, temperature from (20 to 125)^{o}C, and water salinity from (0 to 334 000) mg·L^{-1}. *J. Chem. Eng. Data* 54: 765-775.

Bahramian, A., and Danesh, A. 2004. Prediction of liquid-liquid interfacial tension in multi-component systems. *Fluid Phase Equilibr.* 221: 197-205.

Bahramian, A., and Danesh, A. 2005. Prediction of liquid-vapour surface tension in multi-component systems. *Fluid Phase Equilibr.* 236: 156-161.

Balbuena, P.B., and Gubbins, K.E. 1993. Theoretical interpretation of adsorption behavior of simple fluids in slit pores. *Langmuir* 9 (7): 1801-1814.

Bando, S., Takemura, F., and Nishio, M., *et al.* 2003. Solubility of CO_2 in aqueous solutions of NaCl at (30 to 60)°C and (10 to 20) MPa. *J. Chem. Eng. Data* 48: 576-579.

Basaldella, E.I., Tara, J.C., and Armenta, G.A., *et al.* 2007. Cu/SBA-15 as adsorbent for propane/propylene separation. *J. Porous Mat.* 14 (3): 273-278.

Bennion, D.B., and Bachu, S.A. 2008. Correlation of the interfacial tension between supercritical phase CO_2 and equilibrium brine as a function of salinity, temperature and pressure. Presented at the SPE Annual Technical Conference and Exhibition. Colorado.

Bhowmik, S., and Dutta P. 2011. Investigation into the methane displacement behavior by cyclic, pure carbon dioxide injection in dry, powdered, bituminous Indian coals. *Energy Fuels* 25 (6): 2730-2740.

Bongiorno, V., and Davis, H.T. 1975. Modified van der Waals theory of fluid interfaces. *Phys. Rev. A* 12: 2213-2224.

Brochard, L., Vandamme, M., and Pellenq, R., *et al.* 2011. Adsorption-induced deformation of microporous materials: coal swelling induced by CO_2-CH_4 competitive adsorption. *Langmuir* 28: 2659-2670.

Brunauer, S., Emmett, P.H., and Teller, E. 1938. Adsorption of gases in multimolecular layers. *J. Am. Chem. Soc*. 60 (2): 309-319.

Bruot, N., and Caupin, F. 2016. Curvature dependence of the liquid-vapor surface tension beyond the Tolman approximation. *Phys. Rev. Lett.* 116 (5): 056102.

Bryan, W.P. 1987. Sorption hysteresis and the laws of thermodynamics. *J. Chem. Educ*. 64 (3): 209-212.

Bui, K., and Akkutlu, I.Y. 2015. Nanopore wall effect on surface tension of methane. *Mol. Phys.* 113 (22): 3506-3513.

Busch, A., Gensterblum, Y., and Krooss, B.M. 2003. Methane and CO_2 sorption and desorption measurements on dry argonne premium coals: pure components and mixtures. *Int. J. Coal*

Geol. 55 (2): 205-224.

Cabral, V.F., Alfradique, M.F., and Tavares, F.W., *et al.* 2005. Thermodynamic equilibrium of adsorbed phases. *Fluid Phase Equilibr.* 233 (1): 66-72.

Cahn, J.W., and Hilliard, J.E. 1958. Free energy of a nonuniform system. I. Interfacial free energy. *J. Chem. Phys.* 28: 258-267.

Cai, B.Y., Yang, J.T., and Guo, T.M. 1996. Interfacial tension of hydrocarbon+water/brines systems under high pressure. *J. Chem. Eng. Data* 41: 493-496.

Cervilla, A., Corma, A., and Fornes, V., *et al.* 1994. Intercalation of $[MoVIO_2(O_2CC(S)Ph_2)_2]_2$- in a Zn(II)-Al(III) layered double hydroxide host: a strategy for the heterogeneous catalysis of the air oxidation of thiols. *J. Am. Chem. Soc.* 116 (4): 1595-1596.

Cessford, N., Seaton, N., and Düren, T. 2012. Evaluation of ideal adsorbed solution theory as a tool for the design of metal-organic framework materials. *Ind. Eng. Chem. Res*. 51: 4911-4921.

Chalbaud, C., Robin, M., and Egermann, P. 2006. Interfacial tension data and correlations of brine/CO_2 systems under reservoir conditions. Presented at the SPE Annual Technical Conference and Exhibition, San Antonio.

Chalbaud, C., Robin, M., and Lombard, J.M., *et al.* 2010. Brine/CO_2 interfacial properties and effects on CO_2 storage in deep saline aquifers. *Oil Gas Sci. and Technol.* 65: 541-555.

Chalbaud, C., Robin, M., and Lombard, J. M., *et al.* 2009. Interfacial tension measurement and wettability evaluation for geological CO_2 storage. *Adv. Water Resour.* 32: 98-109.

Charoensuppanimit, P., Mohammad, S.A., and Gasem, K.A.M. 2016. Measurements and modeling of gas adsorption on shales. *Energy Fuels* 30: 2309-2319.

Chatterjee, R., and Paul, S. 2013. Classification of coal seams for coal bed methane exploitation

in central part of Jharia coalfield, India statistical approach. *Fuel* 111: 20-29.

Chen, G., Zhang, J., and Lu, S., *et al.* 2016. Adsorption behavior of hydrocarbon on illite. *Energy Fuels* 30: 9114-9121.

Chen, Z., Xia, S., and Ma, P. 2008. Measuring surface tension of liquids at high temperature and elevated pressure. *J. Chem. Eng. Data* 53: 742-744.

Chiquet, P., Daridon, J., and Broseta, D., *et al.* 2007. CO_2/water interfacial tensions under pressure and temperature conditions of CO_2 geological storage. *Energy Convers. Manage.* 48: 736-744.

Chun, B.S., and Wilkinson, G.T. 1995. Interfacial tension in high-pressure carbon dioxide mixtures. *Ind. Eng. Chem. Res.* 34: 4371-4377.

Civan, F., Devegowda, D., and Sigal, R., *et al.* 2012. Theoretical fundamentals, critical issues, and adequate formulation of effective shale gas and condensate reservoir simulation. AIP Conference Proceedings 1453 (1): 155-160.

Clarkson, C.R., and Haghshenas, B. 2013. Modeling of supercritical fluid adsorption on organic-rich shales and coal. Presented at the Unconventional Resources Technology Conference, Texas, USA.

de Boer, J. H., and Lippens, B.C. 1964. Studies on pore systems in catalysts II. The shapes of pores in aluminum oxide systems. *J. Catal.* 3 (1): 38-43.

da Rocha, S.R.P., Harrison, K.L., and Johnston, K.P. 1999. Effect of surfactants on the interfacial tension and emulsion formation between water and carbon dioxide. *Langmuir* 15: 419-428.

Danesh, A. 1998. PVT and phase behaviour of petroleum reservoir fluids. Ph.D. Dissertation, Herriot Watt University, Edinburgh, SCO.

Devegowda, D., Sapmanee, K., and Civan, F., *et al.* 2012. Phase behavior of gas condensates in shale due to pore proximity effects: implications for transport, reserves and well productivity. Paper SPE 160099 presented at the *SPE Annual Technical Conference and Exhibition*, 8-10 October, San Antonio, Texas, USA.

Didar, B.R., and Akkutlu, I.Y. 2013. Pore-size dependence of fluid phase behavior and properties in organic-rich shale reservoirs. SPE International Symposium on Oilfield Chemistry. The Woodlands, Texas, USA Society of Petroleum Engineers.

Do, D.D., and Do, H.D. 2003. Adsorption of supercritical fluids in non-porous and porous carbons: analysis of adsorbed phase volume and density. *Carbon* 41: 1777-1791.

Dong, X., Liu, H., and Hou, J., *et al.* 2016. Phase equilibria of confined fluids in nanopores of tight and shale rocks considering the effect of capillary pressure and adsorption film. *Ind. Eng. Chem. Res.* 55: 798-811.

Duan, S., Gu, M., and Du, X., *et al.* 2016. Adsorption equilibrium of CO_2 and their mixture on Sichuan Basin Shale. *Energy Fuels* 30: 2248-2256.

Duan, Z., and Rui, S. 2003. An improved model calculating CO_2 solubility in pure water and aqueous NaCl solutions from 273 to 533 K and from 0 to 2000 bar. *Chem. Geol.* 193: 257-271.

Dubinin, M.M. 1960. The potential theory of adsorption of gases and vapors for adsorbents with energetically nonuniform surfaces. *Chem. Rev*. 60 (2): 235-241.

Ebner, C., and Saam, W.F. 1977. New phase-transition phenomena in thin argon films. *Phys. Rev. Lett.* 38 (25): 1486-1489.

Ebner, C., Saam, W.F., and Stroud, D. 1976. Density-functional theory of simple classical fluids. I. Surfaces. *Phys. Rev. A* 14 (6): 2264-2273.

Errington, J.R., and Panagiotopoulos, A.Z. 1999. A new intermolecular potential model for the n-alkane homologous series. *J. Phys. Chem. B* 103 (30): 6314-6322.

Evans, R. 1979. The nature of the liquid-vapor interface and other topics in the statistical mechanics of non-uniform, classical fluids. *Adv. Phys.* 28: 143-200.

Faiz, M.M., Saghafi, A., and Barclay, S.A., *et al.* 2007. Evaluating geological sequestration of CO_2 in bituminous coals: the southern Sydney Basin, Australia as a natural analogue. *Int. J. Greenhouse Gas Control* 1 (2):223-235.

Fan, C., Do, D.D., and Nicholson, D. 2011. On the cavitation and pore blocking in slit-shaped ink-bottle pores. *Langmuir* 27 (7): 3511-3526.

Fawcett, M. J. 1994. Evaluation of correlations and Parachors to predict low interfacial tensions in condensate systems. Paper SPE 28611 presented at the *SPE Annual Technical Conference and Exhibition*, 25-28 September, New Orleans, Louisiana.

Firoozabadi, A., 2016. Thermodynamics and Applications in Hydrocarbon Energy Production, McGraw Hill, New York.

Firoozabadi, A., and Ramey Jr., H.J. 1988. Surface tension of water-hydrocarbon systems at reservoir conditions. *J. Can. Pet. Technol.* 27: 41-48.

Gasparik, M., Bertier, P., and Gensterblum, Y., *et al.* 2014. Geological controls on the methane storage capacity in organic-rich shales. *Int. J. Coal Geol*. 123: 34-51.

Gensterblum, Y., Busch, A., and Krooss, B.M. 2014. Molecular concept and experimental evidence of competitive adsorption of H_2O, CO_2 and CH_4 on organic material. *Fuel* 115: 581-588.

Gensterblum, Y., Hemert, P., and Billemont, P., *et al.* 2009. European inter-laboratory comparison of high pressure CO_2 sorption isotherms. I: activated carbon. *Carbon* 47:

2958-2969.

Gensterblum, Y., Hemert, P., and Billemont, P., *et al.* 2010. European inter-laboratory comparison of high pressure CO_2 sorption isotherms II: natural coals. *Int. J. Coal Geol.* 84: 115-124.

Gasparik, M., Ghanizadeh, A., and Bertier, P., *et al.* 2012. High-pressure methane adsorption isotherms of black shales from the Netherlands. *Energy Fuel* 26: 4995-5004.

Gasparik, M., Ghanizadeh, A., and Gensterblum, Y., *et al.* 2012. The methane storage capacity of black shales. 3rd EAGE Shale Wrokshop.

Gelb, L.D., Gubbins, K.E., and Radhakrishnan, R., *et al.* 1999. Phase Separation in Confined Systems. *Rep. Prog. Phys.* 62: 1573-1659.

Georgiadis, A., Maitland, G., and Trusler, J.P.M., *et al.* 2010. Interfacial tension measurements of the (H_2O+CO_2) system at elevated pressures and temperatures. *J. Chem. Eng. Data* 55: 4168-4175.

Godec, M., Koperna, G., and Petrusak, R., *et al.* 2013. Potential for enhanced gas recovery and CO_2 storage in the Marcellus shale in the Eastern United States. *Int. J. Coal Geol.* 118: 95-104.

Groen, J.C., Peffer, L., and Pérez-Ramírez, J. 2003. Pore size determination in modified micro- and mesoporous materials. Pitfalls and limitations in gas adsorption data analysis. *Micropor. Mesopor. Mat*. 60: 1-17.

Grant, R.J., and Manes, M. 1964. Correlation of some gas adsorption data extending to low pressures and supercritical temperatures. *Ind. Eng. Chem. Fundam.* 3: 221-224.

Haghshenas, B., Soroush, M., and Brohi, I., *et al.* 2014. Simulation of liquid-rich shale gas reservoirs with heavy hydrocarbon fraction desorption. Paper SPE 168968 presented at the

SPE Unconventional Resources Conference, 1-3 April, The Woodlands, Texas, USA.

Halsey, G.D. 1948. Physical adsorption on non-uniform surfaces. *J. Chem. Phys.* 16: 931-937.

Hebach, A., Oberhof, A., and Dahmen, N., *et al.* 2002. Interfacial tension at elevated pressures-measurements and correlations in the water+carbon dioxide system. *J. Chem. Eng. Data* 47: 1540-1546.

Heller, R., and Zoback, M. 2014. Adsorption of methane and carbon dioxide on gas shale and pure mineral samples. *J. Unconv. Oil Gas Resour.* 8: 14-24.

Hensen, E.J.M., Tambach, T.J., and Bliek, A., *et al.* 2001. Adsorption isotherms of water in Li-, Na-, and K-montmorillonite by molecular simulations. *J. Chem. Phys.* 115 (7): 3322-3329.

Heuer, G.J. 1957. Interfacial tension of water against hydrocarbons and other gases and adsorption of methane on solids at reservoir temperatures and pressures. Ph.D. Dissertation, University of Texas, Austin, TX.

Hocott, C.R. 1939. Interfacial tension between water and oil under reservoir conditions. *Petrol. Trans. AIME.* 132: 184-190.

Hough, E.W., and Stegemeier, G.L. 1961. Correlation of surface and interfacial tension of light hydrocarbons in the critical region. *SPE J.* 1: 259-263.

Hough, E.W., Rzasa, M.J., and Wood, B.B. 1951. Interfacial tensions at reservoir pressures and temperatures; apparatus and the water-methane systems. *Petrol. Trans. AIME.* 192: 57-60.

Huang, L., Ning, Z., and Wang, Q., *et al.* 2018. Molecular simulation of adsorption behaviors of methane, carbon dioxide and their mixtures on kerogen: effect of kerogen maturity and moisture content. *Fuel* 211: 159-172.

Huang, L., Ning, Z., and Wang, Q., *et al.* 2018. Effect of organic type and moisture on CO_2/CH_4 competitive adsorption in kerogen with implications for CO_2 sequestration and enhance CH_4

recovery. *Appl. Energy* 210: 28-43.

Hussen, C., Amin, R., and Madden, G., *et al.* 2012. Reservoir simulation for enhanced gas recovery: an economic evaluation. *J. Nat. Gas Sci. Eng.* 5: 42-50.

Jarvie, D. 2004. Evaluation of Hydrocarbon Generation and Storage in Barnett Shale, Fort Worth Basin. Texas: The University of Texas at Austin, Bureau of Economic logy/PTTC.

Jennings Jr., H.Y., and Newman, G.H. 1971. The effect of temperature and pressure on the interfacial tension of water against methane-normal decane mixtures. *SPE J.* 11: 171-175.

Jhaveri, B.S., and Youngren, G.K. 1988. Three-parameter modification of the Peng-Robinson equation of state to improve volumetric predictions. *SPE Res. Eng.* 3 (3): 1033-1040.

Jho, C., Nealon, D., and Shogbola, S., *et al.* 1978. Effect of pressure on the surface tension of water: adsorption of hydrocarbon gases and carbon dioxide on water at temperatures between 0 and 50°C. *J. Colloid Interface Sci.* 65: 141-154.

Jiang, J., Shao, Y., and Younis, R.M. 2014. Development of a multi-continuum multicomponent model for enhanced gas recovery and CO_2 storage in fractured shale gas reservoirs. Paper SPE 169114 presented at the *SPE Improved Oil Recovery Symposium*, 12-16 April, Tulsa, Oklahoma, USA.

Jiang, X. 2011. A review of physical modelling and numerical simulation of long-term geological storage of CO_2. *Appl. Energy* 88 (11): 3557-3566.

Jin, B., Bi, R., and Nasrabadi, H. 2017. Molecular simulation of the pore size distribution effect on phase behavior of methane confined in nanopores. *Fluid Phase Equilibr.* 452 (Supplement C): 94-102.

Jin, B., and Nasrabadi, H. 2016. Phase behavior of multi-component hydrocarbon systems in nano-pores using gauge-GCMC molecular simulation. *Fluid Phase Equilibr.* 425: 324-334.

Jin, L., Ma, Y., and Jamili, A. 2013. Investigating the effect of pore proximity on phase behavior and fluid properties in shale formations. Paper SPE 166192 presented at SPE Annual Technical Conference and Exhibition, 30 September-2 October, New Orleans, Louisiana, USA.

Jin, Z. 2017. Bubble/dew point and hysteresis of hydrocarbons in nanopores from molecular perspective. *Fluid Phase Equilibr.* 458: 177-185.

Jin, Z., and Firoozabadi, A. 2013. Methane and carbon dioxide adsorption in clay-like slit pores by Monte Carlo simulations. *Fluid Phase Equilibr.* 360: 456-465.

Jin, Z., and Firoozabadi, A. 2015. Phase behavior and flow in shale nanopores from molecular simulations. Paper SPE 175151 presented at SPE Annual Technical Conference and Exhibition, 28-30 September, Houston, Texas, USA.

Jin, Z., and Firoozabadi, A. 2016. Thermodynamic modeling of phase behavior in shale media. *SPE J.* 21 (1): 190-207.

Jin, Z., and Firoozabadi, A. 2016. Phase behavior and flow in shale nanopores from molecular simulations. *Fluid Phase Equilibr.* 430: 156-168.

Johansson, K., and Eriksson, J.C. 1974. γ and dγ/dT measurements on aqueous solutions of 1,1-electrolyte. *J. Colloid Interface Sci.* 49: 469-480.

Jones, J.E. 1924. On the determination of molecular field-OII from the equation of state of a gas. *Proc. R. Soc. Lond. Ser. A* 106: 463-477.

Karacan, CÖ., Ruiz, F.A., and Cotè, M., *et al.* 2011. Coal mine methane: a review of capture and utilization practices with benefits to mining safety and to greenhouse gas reduction. *Int. J. Coal Geol.* 86: 121-156.

Kazemi, M., and Takbiri-Borujeni, A. 2016. Molecular dynamics study of carbon dioxide storage

in carbon-based organic nanopores. Paper SPE 181705 presented at the *SPE Annual Technical Conference and Exhibition*, 26-28 September, Dubai, UAE.

Khashefi, K., Pereira, L.M.C., and Chapoy, A., *et al.* 2016. Measurement and modelling of interfacial tension in methane/water and methane/brine systems at reservoir conditions. *Fluid Phase Equilibr.* 409: 301-311.

Khosharay, S., and Varaminian, F. 2014. Experimental and modeling investigation on surface tension and surface properties of (CH_4+H_2O), (C_2H_6+H_2O), (CO_2+H_2O) and (C_3H_8+H_2O) from 284.15 K to 312.15 K and Pressures up to 60 Bar. *Int. J. Refrig.* 47: 26-35.

Khosrokhavar, R., Wolf, K.H., and Bruining, H. 2014. Sorption of CH_4 and CO_2 on a carboniferous shale from Belgium using a manometric setup. *Int. J. Coal Geol.* 128: 153-161.

Kim, J., Kim, D., and Lee, W., *et al.* 2017. Impact of total carbon and specific area on the adsorption capacity in Horn River Shale. *J. Petrol. Sci. Eng*. 149: 331-339.

Kim, T.H., Cho, J., and Lee, K.S. 2017. Evaluation of CO_2 injection in shale gas reservoirs with multi-component transport and geomechanical effects. *Appl. Energy* 190: 1195-1206.

Klomkliang, N., Do, D.D., and Nicholson, D. 2013. On the hysteresis loop and equilibrium transition in slit-shaped ink-bottle pores. *Adsorption* 19 (6): 1273-1290.

Koschel, D., Coxam, J.Y., and Majer, V. 2006. Enthalpy and solubility data of CO_2 in water and NaCl (aq) at conditions of interest for geological sequestration. *Fluid Phase Equilibr.* 247: 107-120.

Kowalczyk, P., Gauden, P.A., and Terzyk, A.P., *et al.* 2012. Displacement of methane by coadsorbed carbon dioxide is facilitated in narrow carbon nanopores. *J. Phys. Chem. C* 116 (25):13640-13649.

Kurniawan, Y., Bhatia, S.K., and Rudolph, V. 2006. Simulation of binary mixture adsorption of methane and CO_2 at supercritical conditions in carbons. *AIChE J.* 52 (3): 957-967.

Kvamme, B., Kuznetsova, T., and Hebach, A., *et al.* 2007. Measurements and modelling of interfacial tension for water+carbon dioxide systems at elevated pressures. *Comput. Mater. Sci.* 38: 506-513.

Landers, J., Gor, G.Y., and Neimark, A.V. 2013. Density functional theory methods for characterization of porous materials. *Colloids Surf. A: Physicochem. Eng. Aspects* 437: 3-32.

Langmuir, I. 1916. The Constitution and fundamental properties of solids and liquids. Part I. solids. *J. Am. Chem. Soc*. 38 (11): 2221-2295.

Lee, S.T., and Chien, M.C.H. 1984. A new multicomponent surface tension correlation based on scaling theory. Presented at the SPE/DOE Improved Oil Recovery Conference. Tulsa.

Lemmon, E.W., McLinden, M.O., and Friend, D.G. 2009. Thermophysical properties of fluid systems. *In NIST Chemistry WebBook*, NIST Standard Reference Database Number 69; National Institute of Standards and Technology: Gaithersburg MD.

Lepski, B. 1997. Gravity assisted tertiary gas injection process in water drive oil reservoirs. Ph.D. Dissertation, Louisiana State University, Baton Rouge, USA.

Levin, Y., dos Santos, A.P., and Diehl, A. 2009. Ions at the air-water interface: an end to a hundred-year-old mystery? *Phys. Rev. Lett.* 103: 18-25.

Lewis, W.K., Gilliland, E.R., and Chertow, B., *et al.* 1950. Pure Gas Isotherms. *Ind. Eng. Chem.* 42: 1326-1332.

Li, M., Gu, A., and Lu, X., *et al.* 2002. Determination of the adsorbate density from supercritical gas adsorption equilibrium data. *Carbon* 41: 579-625.

Liu, F., Ellett, K., and Xiao, Y., *et al.* 2013. Assessing the feasibility of CO_2 storage in the New

Albany Shale (Devonian-Mississippian) with potential enhanced gas recovery using reservoir simulation. *Int. J. Greenhouse Gas Control* 17: 111-126.

Liu, X., He, X., Qiu, N., *et al.* 2016. Molecular simulation of CH_4, CO_2, H_2O and N_2 molecules adsorption on heterogeneous surface models of coal. *Appl. Surf. Sci.* 389: 894-905.

Liu, Y., Jin, Z., and Li, H. 2017. Comparison of PR-EOS with capillary pressure model with engineering density functional theory on describing the phase behavior of confined hydrocarbons. Paper SPE 187405 presented at the *SPE Annual Technical Conference and Exhibition*, 9-11 October, San Antonio, Texas, USA.

Liu, Y., Li, H., and Tian, Y., *et al.* 2018. Determination of the absolute adsorption/desorption isotherms of CH_4 and *n*-C_4H_{10} on Shale from a Nano-scale Perspective. *Fuels* 218: 67-77.

Liu, Y., and Wilcox, J. 2012. Molecular simulations of CO_2 adsorption in Micro- and mesoporous carbons with surface heterogeneity. *Int. J. Coal Geol*. 104: 83-95.

Li, W.Z., Liu, Z.Y., and Chen, Y.L., *et al.* 2007. Molecular simulation of adsorption and separation of mixtures of short linear alkanes in pillared layered materials at ambient temperature. *J. Colloid Interface Sci.* 312 (2): 179-185.

Li, X., Boek, E., and Maitland, G.C., *et al.* 2012. Interfacial tension of (brines+CO_2): (0.864 NaCl+0.136 KCl) at temperatures between (298 and 448) K, pressures between (2 and 50) MPa, and total molarities of (1 to 5) mol·kg^{-1}. *J. Chem. Eng. Data* 57: 1078-1088.

Li, X., Boek, E., and Maitland, G.C., *et al.* 2012. Interfacial tension of (brines+CO_2): $CaCl_2$(aq), $MgCl_2$(aq), and Na_2SO_4(aq) at temperatures between (343 and 423) K, Pressures between (2 and 50) MPa, and molarities of (0.5 to 5) mol·kg^{-1}. *J. Chem. Eng. Data* 57: 1369-1375.

Li, X., and Elsworth, D. 2014. Geomechanics of CO_2 enhanced shale gas recovery. *J. Nat. Gas Sci. Eng.* 26: 1607-1619.

Li, X., and Yang, D. 2013. Determination of mutual solubility between CO_2 and water by using the Peng-Robinson equation of state with modified alpha function and binary interaction parameter. *Ind. Eng. Chem. Res.* 52: 13829-13838.

Li, Y., Wang, S., and Wang, Q., *et al.* 2016. Molecular dynamics simulations of tribology properties of NBR (nitrile-butadiene rubber)/carbon nanotube composites. *Compos. Part B* 97: 62-67.

Li, Z., and Firoozabadi, A. 2009. Interfacial tension of nonassociating pure substances and binary mixtures by density functional theory combined with Peng-Robinson equation of state. *J. Chem. Phys.* 130 (15): 154108.

Li, Z., Jin, Z., and Firoozabadi, A. 2014. Phase behavior and adsorption of pure substances and mixtures and characterization in nanopores structures by density functional theory. *SPE J.* 19 (6): 1096-1109.

Li, Z., Wang, S., and Li, S., *et al.* 2013. Accurate determination of the CO_2-brine interfacial tension using graphical alternating conditional expectation. *Energy Fuels* 28: 624-635.

Lu, L., Wang, Q., and Liu, Y. 2003. Adsorption and separation of ternary and quaternary mixtures of short linear alkanes in zeolites by molecular simulation. *Langmuir* 19 (25): 10617-10623.

Luo, F., Xu, R.N., and Jiang, P.X. 2013. Numerical investigation of the influence of vertical permeability heterogeneity in stratified formation and of injection/production well perforation placement on CO_2 geological storage with enhanced CH_4 recovery. *Appl. Energy* 102: 1314-1323.

Luo, S., Lutkenhaus, J.L., and Nasrabadi, H. 2016. Confinement-induced supercriticality and phase equilibria of hydrocarbons in nanopores. *Langmuir* 32 (44): 11506-11513.

Luo, S., Lutkenhaus, J.L., and Nasrabadi, H. 2017. Use of differential scanning calorimetry to study phase behavior of hydrocarbon mixtures in nano-scale porous media. *J. Petrol. Sci. Eng.* 163: 731-738.

Luo, S., Lutkenhaus, J.L., and Nasrabadi, H. 2017. Multi-scale fluid phase behavior simulation in shale reservoirs by a pore-size-dependent equation of state. Paper SPE 187422 presented at the *SPE Annual Technical Conference and Exhibition*, 9-11 October, San Antonio, Texas, USA.

Luo, S., Nasrabadi, H., and Lutkenhaus, J.L. 2016. Effect of confinement on the bubble points of hydrocarbons in nanoporous media. *AIChE J.* 62 (5): 1772-1780.

Luo, X., Wang, S., and Wang, Z., *et al.* 2015. Adsorption of methane, carbon dioxide and their binary mixtures on Jurassic shale from the Qaidam Basin in China. *International J. Coal Geology* 150-151: 210-223.

Lu, X., Li, F., and Watson, A.T. 1995. Adsorption measurements in Devonian shale. *Fuel* 74: 599-603.

Lu, X., Jin, D., and Wei, S., *et al.* 2015. Competitive adsorption of a binary CO_2-CH_4 mixture in nanoporous carbons: effects of edge-functionalization. *Nanoscale* 7 (3): 1002-1012.

Macleod, D.B. 1923. On a relation between surface tension and density. *Trans. Faraday. Soc.* 19: 38-41.

Majewska, Z., Ceglarska-Stefańska, G., and Majewski, S., *et al.* 2009. Binary gas sorption/desorption experiments on a bituminous coal: simultaneous measurements on sorption kinetics, volumetric strain and acoustic emission. *Int. J. Coal Geol.* 77 (1): 90-102.

Malinin, S.D., and Kurovskaya, N.A. 1975. Solubility of CO_2 in chloride solutions at elevated temperatures and CO_2 pressures. *Geochem. Int.* 12: 199-201.

Malinin, S.D., and Savelyeva, N.I. 1972. The solubility of CO_2 in NaCl and $CaCl_2$ solutions at 25, 50 and 75°C under elevated CO_2 pressures. *Geochem. Int.* 6: 643-653.

Martin, M.G., and Siepmann, J.I. 1998. Transferable potentials for phase equilibria. 1. united-atom description of n-alkanes. *J. Phys. Chem. B* 102 (14): 2569-2577.

Massoudi, R., and King Jr., A.D. 1974. Effect of pressure on the surface tension of water adsorption of low molecular weight gases on water at 25°C. *J. Phys. Chem.* 78: 2262-2266.

Massoudi, R., and King Jr., A.D. 1975. Effect of pressure on the surface tension of aqueous solutions. Adsorption of hydrocarbon gases, carbon dioxide, and nitrous oxide on aqueous solutions of sodium chloride and tetra-n-butylammonium bromide at 25°C. *J. Phys. Chem.* 79: 1670-1675.

Menon, P.G. 1968. Adsorption at high pressures. *J. Phys. Chem*. 72: 2695-2696.

Metropolis, N., Rosenbluth, A.W., and Rosenbluth, M.N., *et al.* 1953. Equation of state calculations by fast computing machines. *J. Chem. Phys*. 21 (6): 1087-1092.

Morishige, K., Fujii, H., and Uga, M., *et al.* 1997. Capillary critical point of argon, nitrogen, oxygen, ethylene, and carbon dioxide in MCM-41. *Langmuir* 13: 3494-3498.

Myers, A.L., and Prausnitz, J.M. 1965. Thermodynamics of mixed-gas adsorption. *AIChE J.* 11 (1): 121-127.

Myers, J.A., and Sandler, S.I. 2002. An equation of state for electrolyte solutions covering wide ranges of temperature, pressure, and composition. *Ind. Eng. Chem. Res.* 41: 3282-3297.

Nagarajan, N.R., Hanapour, M.M., and Arasteh, F. 2013. Critical role of rock and fluid impact on reservoir performance on unconventional shale reservoirs. Paper URTEC 1585730 presented at the *Unconventional Resources Technology Conference*, 12-14 August, Denver, Colorado, USA.

Neimark, A.V., and Vishnyakov, A. 2000. Gauge cell method for simulation studies of phase transitions in confined systems. *Phys. Rev. E* 62 (4): 4611-4622.

Nojabaei, B., Johns, R.T., and Chu, L. 2013. Effect of capillary pressure on phase behavior in tight rocks and shales. *SPE Res. Eval. Eng.* 16 (3): 281-289.

Nordholm, S., Johnson, M., and Freasier, B.C. 1980. Generalized van der Waals theory. III. The prediction of hard sphere structure. *Aust. J. Chem.* 33: 2139-2150.

Nuttall, B.C., Eble, C.F., and Drahovzal, J.A., *et al.* 2005. Analysis of Devonian black shales in Kentucky for potential carbon dioxide sequestration and enhanced natural gas production. *Greenhouse Gas Control Technologies* Volume II: 2225-2228.

Ottiger, S., Pini, R., and Storti, G., *et al.* 2008. Measuring and modeling the competitive adsorption of CO_2, CH_4, and N_2 on a dry coal. *Langmuir* 24 (17): 9531-9540.

Park, J.Y., Lim, J.S., and Yoon, C.H., *et al.* 2005. Effect of a fluorinated sodium bis (2-Ethylhexyl) sulfosuccinate (Aerosol-OT, AOT) analogue surfactant on the interfacial tension of CO_2+water and CO_2+Ni-plating solution in near- and supercritical CO_2. *J. Chem. Eng. Data* 50: 299-308.

Parsa, E., Yin, X., and Ozkan, E. 2015. Direct observation of the impact of nanopore confinement on petroleum gas condensation. Paper SPE 175118 presented at the *SPE Annual Technical Conference and Exhibition*, 28-30 September, Houston, Texas, USA.

Pedram, E.O., Hines, A.L., and Cooney, D.O. 1984. Adsorption of light hydrocarbons on spent shale produced in a combustion retort. *Chem. Eng. Commun*. 27: 181-191.

Pegram, L.M., and Record, M.T. 2008. The thermodynamic origin of Hofmeister ion effects. *J. Phys. Chem. B* 112: 9428-9436.

Peng, D., and Robinsion, D.B. 1976. A new two-constant equation of state. *Ind. Eng. Chem.*

Fund. 15 (1): 59-64.

Pereira, L.M.C., Chapoy, A., and Burgass, R., *et al.* 2016. Study of the impact of high temperature and pressures on the equilibrium densities and interfacial tension of the carbon dioxide/water system. *J. Chem. Thermodyn.* 93: 404-415.

Petrova, T. 2014. Revised release on surface tension of ordinary water substance. Presented at the International Association for the Properties of Water and Steam. Moscow.

Quayle, O.R. 1953. The Parachors of organic compounds. An interpretation and catalogue. *Chem. Rev.* 53: 439-589.

Ralston, J., and Healy, T. 1973. Specific cation effects on water structure at the air-water and air-octadecanol monolayer-water interface. *J. Colloid Interface Sci.* 42: 629-644.

Ren, Q.Y., Chen, G.J., and Yan, W., *et al.* 2000. Interfacial tension of (CO_2+CH_4)+Water from 298 K to 373 K and pressures up to 30 MPa. *J. Chem. Eng. Data.* 45: 610-612.

Ren, W., Li, G., and Tian, S., *et al.* 2017. Adsorption and surface diffusion of supercritical methane in shale. *Ind. Eng. Chem. Res.* 56: 3446-3455.

Rexer, T.F.T., Benham, M.J., and Aplin, A.C., *et al.* 2013. Methane adsorption on shale under simulated geological temperature and pressure conditions. *Energy Fuels* 27: 3099-3109.

Rigby, D., Sun, H., and Eichinger, B.E. 1997. *Polym. Int.* 44 (3): 311-330.

Robinson, D.B., and Peng, D.Y. 1978. The characterization of the heptanes and heavier fractions for the GPA Peng-Robinson programs, gas processors association. Research Report RR-28. (Booklet only sold by the Gas Processors Association, GPA)

Robinson, D.B., Peng, D.Y., and Chung, S.Y.K. 1985. The development of the Peng-Robinson equation and its application to phase equilibrium in a system containing methanol. *Fluid Phase Equilibr.* 24 (1-2): 25-41.

Roque-Malherbe, R.M.A. 2007. Adsorption and diffusion in nanoporous materials. Boca Raton, Florida: CRC Press.

Rosenfeld, Y. 1989. Free-energy model for the inhomogeneous hard-sphere fluid mixture and density-functional theory of freezing. *Phys. Rev. Lett.* 63 (9): 980-983.

Ross, D.J., and Bustin, R.M. 2007. Impact of mass balance calculations on adsorption capacities in microporous shale gas reservoirs. *Fuel* 86 (17): 2696-2706.

Ross, D.J., and Bustin, R.M. 2009. The importance of shale composition and pore structure upon gas storage potential of shale gas reservoirs. *Mar. Pet. Geol*. 26: 916-927.

Rowlinson, J.S. 1979. Translation of J.D. van der Waals' "The Thermodynamic Theory of Capillarity under the Hypothesis of a Continuous Variation of Density". *J. Stat. Phys.* 20: 197-200.

Rowlinson, J.S., and Swinton, F.L. 1982. Liquids and liquid mixtures. London, U.K., Butterworth.

Rowlinson, J.S., and Widom, B. 1982. Molecular theory of capillarity. Oxford, U.K., Clarendon.

Rushing, J.A., Newsham, K.E., and Van Fraassen, K.C., *et al.* 2008. Laboratory measurements of gas-water interfacial tension at the *CIPC/SPE Gas Technology Symposium 2008 Joint Conference*, 16-19 June, Calgary, Alberta, Canada.

Sachs, W., and Meyn, V. 1995. Pressure and temperature dependence of the surface tension in the system natural gas/water: principles of investigation and the first precise experimental data for pure methane/water at 25^{o}C up to 48.8 MPa. *J. Colloids Surf. A* 94: 291-301.

Sandoval, D.R., Yan, W., and Michelsen, M.L., *et al.* 2016. The phase envelope of multicomponent mixtures in the presence of a capillary pressure difference. *Ind. Eng. Chem. Res.* 55 (22): 6530-6538.

Santiso, E., and Firoozabadi, A. 2006. Curvature dependency of surface tension in multicomponent systems. *AIChE J.* 52 (1): 311-322.

Sapmanee, K. 2011. Effects of pore proximity on behavior and production prediction of gas/condensate, University of Oklahoma.

Sato, K. 2003. Sensitivity of interfacial-tension predictions to Parachor-method parameters. *J. Jpn. Pet. Inst.* 46: 148-153.

Shirono, K., and Daiguiji, H. 2007. Molecular simulation of the phase behavior of water confined in silica nanopores. *J. Phys. Chem. C* 111 (22): 7938-7946.

Shah, V., Broseta, D., and Mouronval, G., *et al.* 2008. Water/acid gas interfacial tensions and their impact on acid gas geological storage. *Int. J. Greenh. Gas Control.* 2: 594-604.

Shariat, A. 2014. Measurement and modelling of interfacial tension at high pressure/high temperature conditions. Ph.D. Dissertation, University of Calgary, Calgary, AB.

Shariat, A., Moore, R.G., and Mehta, S.A., *et al.* 2012. Laboratory measurement of CO_2-H_2O interfacial tension at HP/HT conditions: implications for CO_2 sequestration in deep aquifers. Paper CMTC 150010 presented at the *Carbon Management Technology Conference*, 7-9 February, Orlando, Florida, USA.

Shariat, A., Moore, R.G., and Mehta, S.A., *et al.* 2011. A laboratory study of the effects of fluid compositions on gas-water interfacial tension at HP/HT reservoir conditions. Paper SPE 146178 presented at the *SPE Annual Technical Conference and Exhibition*, 30 October-2 November, Denver, Colorado, USA.

Singh, J.K., and Kwak, S.K. 2007. Surface tension and vapor-liquid phase coexistence of confined square-well fluid. *J. Chem. Phys.* 126 (2): 024702.

Sing, K.S.W., Everett, D.H., and Haul, R.A.W., *et al.* 2008. Reporting physisorption data for

gas/solid systems. Handbook of Heterogeneous Catalysis, Wiley-VCH Verlag GmbH & Co. KGaA.

Singh, S.K., Sinha, A., and Deo, G., *et al.* 2009. Vapor−liquid phase coexistence, critical properties, and surface tension of confined Alkanes. *J. Phys. Chem. C* 113 (17): 7170-7180.

Smit, B., Karaborni, S., and Siepmann, J.I. 1995. Computer simulations of vapor-liquid phase equilibria of *n*-alkanes. *J. Chem. Physics* 102 (5): 2126-2140.

Song, Y., Jiang, B., and Li, W. 2017. Molecular simulations of $CH_4/CO_2/H_2O$ competitive adsorption on low rank coal vitrinite. *Phys. Chem. Chem. Phys*. 19: 17773-17788.

Sudgen, S. 1921. Capillary rise. *J. Chem. Soc.* 119: 1483.

Sun, H., Zhao, H., and Qi, N., *et al.* 2017. Molecular insights into the enhanced shale gas recovery by carbon dioxide in kerogen slit nanopores. *J. Phys. Chem. C* 121 (18): 10233-10241.

Sutjiadi-Sia, Y., Jaeger, P., and Eggers, R. 2008. Interfacial phenomena of aqueous systems in dense carbon dioxide. *J. Supercrit. Fluids* 46: 272-279.

Sutton, R.P. 2009. An improved model for water-hydrocarbon surface tension at reservoir conditions. Paper SPE 124968 presented at the *SPE Annual Technical Conference and Exhibition*, 4-7 October, New Orleans, Louisiana.

Standing, M.B. 1951. Volumetric and phase behaviour of oil hydrocarbon systems. California Research Corp.: Dallas.

Steele, W.A. 1973. The physical interaction of gases with crystalline solids: I. Gas-solid energies and properties of isolated adsorbed atoms. *Surf. Sci.* 36 (1): 317-352.

Sweatman, M.B., and Quirke, N. 2002. Predicting the adsorption of gas mixtures: adsorbed solution theory versus classical density functional theory. *Langmuir* 18 (26): 10443-10454.

Søreide, I., and Whitson, C.H. 1992. Peng-Robinson prediction for hydrocarbons, CO_2, N_2, and H_2S with pure water and NaCl brine. *Fluid Phase Equilibr.* 77: 217-240.

Tan, S.P., and Piri, M. 2015. Equation-of-state modeling of confined-fluid phase equilibria in nanopores. *Fluid Phase Equilibr.* 393: 48-63.

Teklu, T.W., Alharthy, N., and Kazemi, H., *et al.* 2014. Phase behavior and minimum miscibility pressure in nanopores. *SPE Res. Eval. Eng.* 17: 396-403.

Tewes, F., and Boury, F. 2005. Formation and rheological properties of the supercritical CO_2-water pure interface. *J. Phys. Chem. B* 109: 3990-3997.

Tian, Y., Xiao, Y., and Zhu, H., *et al.* 1997. Interfacial tension between water and non-polar fluids at high pressures and high temperatures. *Acta Physico-Chimica Sinica.* 13: 89-95.

Tian, Y., Yan, C., and Jin, Z. 2017. Characterization of methane excess and absolute adsorption in various clay nanopores from molecular simulation. *Sci. Rep.* 7: 12040.

Travalloni, L., Castier, M., and Tavares, F.W., *et al.* 2010. Critical behavior of pure confined fluids from an extension of the van der Waals equation of state. *J. Supercrit. Fluids* 55 (2): 455-461.

Travalloni, L., Castier, M., and Tavares, F.W., *et al.* 2010. Thermodynamic modeling of confined fluids using an extension of the generalized van der Waals theory. *Chem. Eng. Sci.* 65 (10): 3088-3099.

Travalloni, L., Castier, M., and Tavares, F.W. 2014. Phase equilibrium of fluids confined in pores media from an extended Peng-Robinson equation of state. *Fluid Phase Equilibr.* 362: 335-341.

Tsai, M.C., Chen, W.N., and Cen, P.L., *et al.* 1985. Adsorption of gas mixture on activated carbon. *Carbon* 23 (2): 167-173.

van der Ploeg, P., and Berendsen, H.J.C. 1982. Molecular dynamics simulations of a bilayer membrane. *J. Chem. Physics* 76 (6): 3271-3276.

Valentini, P., Schwartzentruber, T.E., and Cozmuta, I. 2011. ReaxFF grand canonical Monte Carlo simulation of adsorption and dissociation of oxygen on platinum (111). *Surf. Sci.* 605 (23): 1941-1950.

Vishal, V., Singh, T.N., and Ranjith, P.G. 2015. Influence of sorption time in CO_2-ECBM process in Indian coals using coupled numerical simulation. *Fuel* 139: 51-58.

Volzone, C. 2007. Retention of pollutant gases: comparison between clay minerals and their modified products. *Appl. Clay Sci.* 36 (1-3): 191-196.

Walton, J.P.R.B., and Quirke, N. 1989. Capillary condensation: a molecular simulation study. *Mol. Simul.* 2 (4-6): 361-391.

Wang, L., Parsa, E., and Gao, Y.F., *et al.* 2014. Experimental study and modeling of the effect of nanoconfinement on hydrocarbon phase behavior in unconventional reservoirs. Paper SPE 169581 presented at the *SPE Western North American and Rocky Mountain Joint Meeting*, 17-18 April, Denver, Colorado.

Wang, L., Yin, X., and Neeves, K.B., *et al.* 2016. Effect of pore-size distribution on phase transition of hydrocarbon mixtures in nanoporous media. *SPE J.* 21 (6): 1981-1995.

Wang, X., Zhai, Z., and Jin, X., *et al.* 2016. Molecular simulation of CO_2/CH_4 competitive adsorption in organic matter pores in shale under certain geological conditions. *Petrol. Explor. Dev.* 43 (5): 841-848.

Wang, Y., Tsotsis, T.T., and Jessen, K. 2015. Competitive sorption of methane/ethane mixtures on shale: measurements and modeling. *Ind. Eng. Chem. Res.* 54: 12178-12195.

Wang, Y., Zhu, Y., and Liu, S., *et al.* 2016. Methane adsorption measurements and modeling for

organic-rich marine shale samples. *Fuel* 172: 301-309.

Weijermars, R. 2013. Economic appraisal of shale gas plays in Continental Europe. *Appl. Energy* 106: 100-115.

Weijermars, R. 2014. US shale gas production outlook based on well roll-out rate scenarios. *Appl. Energy* 124: 283-297.

Weinaug, C.F., and Katz, D.L. 1943. Surface tensions of methane-propane mixtures. *Ind. Eng. Chem.* 35 (2): 239-246.

Weniger, P., Kalkreuth, W., and Busch, A., *et al.* 2010. High-pressure methane and carbon dioxide sorption on coal and shale samples from the Paraná Basin, Brazil. *Int. J. Coal. Geol*. 84 (3-4): 190-205.

White, C.M., Smith, D.H., and Jones, K.L., *et al.* 2005. Sequestration of carbon dioxide in coal with enhanced coalbed methane recovery-a review. *Energy Fuels* 19 (3): 659-724.

Whitson, C.H., and Brulé, M.R. 2000. Phase behavior. Henry L. Doherty Memorial Fund of AIME Society of Petroleum Engineers Inc.: Richardson, Texas.

Widom, B. 1963. Some topics in the theory of fluids. *J. Chem. Phys.* 39 (11): 2808-2812.

Wiebe, R. 1941. The brine system carbon dioxide-water under pressure. *Chem. Rev.* 29: 475-481.

Wiegand, G., and Franck, E.U. 1994. Interfacial tension between water and non-polar fluids up to 473 K and 2800 bar. *Ber. Bunsenges. Phys. Chem.* 98: 809-817.

Wongkoblap, A., Do, D.D., and Birkett, G., *et al.* 2011. A critical assessment of capillary condensation and evaporation equations: A computer simulation study. *J. Colloid Interface Sci.* 356 (2): 672-680.

Wu, H., Chen, J., and Liu, H. 2015. Molecular dynamics simulations about adsorption and displacement of methane in carbon nanochannels. *J. Phys. Chem. C* 119 (24): 13652-13657.

Wu, Y., Fan, T., and Jiang, S., *et al.* 2015. Methane adsorption capacities of the lower Paleozoic marine shales in the Yangtze Platform, South China. *Energy Fuels* 29: 4160-4167.

Xiong, F., Wang, X., and Amooie, N., *et al.* 2017. The shale gas sorption capacity of transitional shales in the Ordos Basin, NW China. *Fuel* 208: 236-246.

Yamazaki, T., Aso, K., and Chinju, J. 2006. Japanese potential of CO_2 sequestration in coal seams. *Appl. Energy* 83 (9): 911-920.

Yan, W., Zhao, G., and Chen, G., *et al.* 2001. Interfacial tension of (methane+nitrogen)+water and (carbon dioxide+nitrogen)+water systems. *J. Chem. Eng. Data* 46: 1544-1548.

Yang, D.Y., Tontiwachwuthikul, P., and Gu, Y.A. 2005. Interfacial interactions between reservoir brine and CO_2 at high pressures and elevated temperatures. *Energy Fuels* 19: 216-223.

Yan, X., Wang, T.B., and Gao, C.F., *et al.* 2013. Mesoscopic phase behavior of tridecane-tetradecane mixtures confined in porous materials: effects of pore size and pore geometry. *J. Phys. Chem. C* 117: 17245-17255.

Yaws, C.L. 2003. Yaws' handbook of thermodynamic and physical properties of chemical compounds. Knovel Corporation, New York, NY.

Yuan, J., Luo, D., and Feng L. 2015. A review of the technical and economic evaluation techniques for shale gas development. *Appl. Energy* 148: 49-65.

Yuan, Q., Zhu, X., and Lin, K., *et al.* 2015. Molecular dynamics simulations of the enhanced recovery of confined methane with carbon dioxide. *Phys. Chem. Chem. Phys.* 17: 31887-31893.

Yu, S., Yanming, Z., and Wu, L. 2017. Macromolecule simulation and CH_4 adsorption mechanism of coal vitrinite. *Appl. Surf. Sci.* 396: 291-302.

Yu, W., Al-Shalabi, E.W., and Sepehrnoori, K. 2014. A sensitivity study of potential CO_2 injection for enhanced gas recovery in Barnett shale reservoirs. Paper SPE 169012 presented at the *SPE Unconventional Resources Conference*, 1-3 April, The Woodlands, Texas, USA.

Zhang, J., Liu, K., and Clennell, M.B., *et al.* 2015. Molecular simulation of CO_2-CH_4 competitive adsorption and induced coal swelling. *Fuel* 160: 309-17.

Zhang, T., Ellis, G.S., and Ruppel, S.C., *et al.* 2012. Effect of organic-matter type and thermal maturity on methane adsorption in shale-gas systems. *J. Org. Geochem.* 47: 120-131.

Zhang, Y., Civan, F., and Devegowda, D., *et al.* 2013. Improved prediction of multi-component hydrocarbon fluid properties in organic rich shale reservoirs. Paper SPE 166290 presented at the *SPE Annual Technical Conference and Exhibition*, 30 September-2 October, New Orleans, Louisiana, USA.

Zhao, G.Y. 2002. Measurement and calculation of high pressure interfacial tension of methane nitrogen/water system. *J. Univ. Pet.* 26: 75-78.

Zhao, Y., Feng, Y., and Zhang, X. 2016. Molecular simulation of CO_2/CH_4 self- and transport diffusion coefficients in coal, *Fuel* 165: 19-27.

Zhong, J., Zandavi, S.H., and Li, H., *et al.* 2017. Condensation in one-dimensional dead-end nanochannels. *ACS Nano* 11 (1): 304-313.

Zuo, Y.X., and Stenby, E.H. 1997. Corresponding-states and Parachor models for the calculation of interfacial tensions. *Can. J. Chem. Eng.* 75: 1130-1137.